PENNSTATE

Inhibiting Corrosion in Gr/Al and Gr/Mg Metal Matrix Composites Using Nonequilibrium Alloying Techniques

Final Report
September 1995

Submitted to:
Office of Naval Research
800 North Quincy Street
Arlington, VA   22217-5000

Submitted by:

B.A. Shaw[1], R.G. Wendt[2], W.C. Moshier[3], P.L. Miller[1], K.L. Heidersbach[1], T.R. Schrecengost[1], and D.J. Ciscon[1]

[1] Penn State University, University Park, PA   16802

[2] Martin Marietta Astronautics Group, Denver CO 80201
(currently employed by ITN Energy Systems)

[3] Martin Marietta Astronautics Group, Denver CO   80201
(currently employed by Bettis Atomic Power Lab)

PENNSTATE

1855

Inhibiting Corrosion in Gr/Al and Gr/Mg Metal Matrix Composites Using Nonequilibrium Alloying Techniques

Final Report
September 1995

Submitted to:
Office of Naval Research
800 North Quincy Street
Arlington, VA   22217-5000

Submitted by:

B.A. Shaw[1], R.G. Wendt[2], W.C. Moshier[3], P.L. Miller[1],
K.L. Heidersbach[1], T.R. Schrecengost[1], and D.J. Ciscon[1]

[1] Penn State University, University Park, PA   16802

[2] Martin Marietta Astronautics Group, Denver CO 80201
(currently employed by ITN Energy Systems)

[3] Martin Marietta Astronautics Group, Denver CO 80201
(currently employed by Bettis Atomic Power Lab)

REPORT DOCUMENTATION PAGE

Form Approved
OMB No. 0704-0188

1a. REPORT SECURITY CLASSIFICATION Unclassified	1b. RESTRICTIVE MARKINGS None
2a. SECURITY CLASSIFICATION AUTHORITY	3. DISTRIBUTION / AVAILABILITY OF REPORT Unrestricted/
2b. DECLASSIFICATION / DOWNGRADING SCHEDULE	

4. PERFORMING ORGANIZATION REPORT NUMBER(S)	5. MONITORING ORGANIZATION REPORT NUMBER(S)

DISTRIBUTION STATEMENT A
Approved for public release;

6a. NAME OF PERFORMING ORGANIZATION Penn State University	6b. OFFICE SYMBOL (If applicable) Code 3312	7a. NAME OF MONITORING ORGANIZATION
6c. ADDRESS (City, State, and ZIP Code) Dept. of Engineering Science and Mechanics 227 Hammond Bldg., University Park, PA 16802		7b. ADDRESS (City, State, and ZIP Code)

8a. NAME OF FUNDING / SPONSORING ORGANIZATION Office of Naval Research	8b. OFFICE SYMBOL (If applicable) Code	9. PROCUREMENT INSTRUMENT IDENTIFICATION NUMBER

8c. ADDRESS (City, State, and ZIP Code) 800 North Quincy St. Arlington, VA 22217-5000	10. SOURCE OF FUNDING NUMBERS			
	PROGRAM ELEMENT NO.	PROJECT NO. N00014- 91-J-1196	TASK NO.	WORK UNIT ACCESSION NO.

11. TITLE (Include Security Classification)
Inhibiting Corrosion in Gr/Al and Gr/Mg Metal Matrix Composites Using Nonequilibrium Alloying - Final Report

12. PERSONAL AUTHOR(S)   B.A. Shaw, R.G. Wendt, W.C. Moshier, P.L Miller, K.L. Heidersbach, T.R. Schrecengost, and D.J. Ciscon

13a. TYPE OF REPORT Technical	13b. TIME COVERED FROM 4/1/91 TO 7/31/95	14. DATE OF REPORT (Year, Month, Day) September 11, 1995	15. PAGE COUNT

16. SUPPLEMENTARY NOTATION

17. COSATI CODES			18. SUBJECT TERMS (Continue on reverse if necessary and identify by block number)
FIELD	GROUP	SUB-GROUP	Metal Matrix Composites, Gr/Al Composites, Gr/Mg Composites, Nonequilibrium Alloying

19. ABSTRACT (Continue on reverse if necessary and identify by block number)

Metal matrix composites (MMCs) have been heavily studied over the past thirty years. During that period, many proposals have been made to develop a matrix alloy that was compatible with the reinforcing phase. However, for one reason or another, the technology has continued to focus on conventional alloys and fabrication practices. Although tremendous advances have been made on composite materials, the basic technoloby remains similar to systems studied twenty years ago. This work presents the first program where new alloys were developed for graphite reinforced composites which were tailored to a novel processing technology for manufacturing corrosion resistant graphite-reinforced composites.

20. DISTRIBUTION / AVAILABILITY OF ABSTRACT ☒ UNCLASSIFIED/UNLIMITED ☐ SAME AS RPT. ☐ DTIC USERS	21. ABSTRACT SECURITY CLASSIFICATION
22a. NAME OF RESPONSIBLE INDIVIDUAL B.A. Shaw	22b. TELEPHONE (Include Area Code) (814) 865-7828	22c. OFFICE SYMBOL

DD Form 1473, JUN 86   Previous editions are obsolete.   SECURITY CLASSIFICATION OF THIS PAGE

Abstract

High modulus graphite fiber-reinforced metal matrix composites offer a wide variety of attractive properties including high specific modulus and strength (E/r and UTS/r), tailorable or zero coefficient of thermal expansion (CTE), and high thermal conductivity. With these properties, structures can be designed and fabricated from MMCs that are dimensionally stable when subjected to both thermal and mechanical perturbations.

However previous research has revealed that several problems are associated with the use of graphite/magnesium (Gr/Mg) and graphite/aluminum (Gr/Al) MMCs. These problems can be grouped into four major categories:

- poor corrosion resistance,

- significant fiber/matrix reaction during processing that can lead to embrittlement,

- excessive thermal and strain hysteresis due to low matrix strength, and

- limited processing capabilities restricted to simple shapes and fiber architectures.

In this program, nonequilibrium alloying by sputter vapor deposition was investigated since it offers the potential to eliminate all of these shortcomings. Although the emphasis of this research was on improving the corrosion resistance of MMCs, the vapor deposition approach to producing these composites will also enhance fabrication capability, eliminate fiber/matrix reactions, and reduce thermal hysteresis.

Binary alloys consisting of Mg-Cr, Mg-Mo, Mg-Ta, Mg-W, Mg-Ti, Mg-Y, Al-Cr, Al-Mo, Al-Ta, and Al-W as well as ternary alloys composed Mg-Ta-W, Mg-Al-W, Mg-Ti-Al, Mg-Ti-Y and Al-Mg-W were successfully fabricated and evaluated. While a few of the Mg-based alloys and all of the Al-based alloys exhibited improved corrosion resistance over pure Al and Mg, detailed testing indicated that the Al-W, Al-Mo, and Mg-Y alloys showed the best potential for use as matrix alloys in graphite-reinforced composites. Each of these alloys exhibited marked increases in pitting potential and reduced galvanic interaction at nominal composite processing temperatures.

An Al-17Mo alloy was chosen for use in the processing phase of the program. Following deposition, the fibers remained flexible enough for further processing and growth of the deposit on the fibers was very columnar. Despite the columnar morphology of the deposit, the alloy coated fibers revealed enhanced corrosion resistance; however, this performance was not as good as that noted for the lab deposited alloy of the same composition. Composites with pure Al surface foils and inter-layers were produced at Martin Marietta and at Cordec Inc.. Unfortunately, the best hot-pressed composites contained a void content exceeding 9%, damage to the Al surface foils and graphite fibers exposed at the surface of the composite. As a result of these defects, anodic polarization of the composites in 0.1M NaCl revealed less than optimal performance. SEM analysis of the pitted composite after anodic polarization showed that diffusion bonding of the alloy coated fibers was not achieved. In fact, the alloy coating on the graphite fibers appeared to have undergone no change during either diffusion bonding or anodic polarization. While the lack of diffusion bonding within the composite was disappointing, the fact that the alloy coated fibers underwent no discernible degradation after anodic polarization was very promising. With the use of an alternative consolidation approach, such as hot isostatic pressing with no surface foils or Al-Mo surface foils, it is likely that a fully consolidated, corrosion resistant composite could be produced.

Several inhibitive treatments for magnesium were also studied to determine if Mg and/or Mg-based composites could be protected by the use of stand-alone inhibitive treatment.

Table of Contents

Abstract

1.0 Introduction

Metal matrix composites (MMCs) have been intensively studied over the past thirty years due to their unique combination of stiffness and thermal stability. During this period, many proposals have been made to develop matrix alloys that were compatible with the reinforcing phase. However, for one reason or another, the technology has continued to focus on conventional alloys and fabrication practices. Although tremendous advances have been made on composite materials, the basic technology remains similar to systems studied twenty years ago. This work represents the first program where new alloys are being developed for graphite reinforced composites which are tailored to a novel processing technology for manufacturing corrosion resistant graphite reinforced composites.

Previous research has revealed that graphite/magnesium (Gr/Mg) and graphite/aluminum (Gr/Al) MMC's are subject to several problems which can be grouped into four major categories:

- poor corrosion resistance,

- significant reactivity between the Gr fiber and metal matrix during processing that can lead to embrittlement,

- excessive thermal and strain hysteresis due to low cast matrix strength, and

- limited processing capabilities restricted to simple shapes and fiber architectures.

Graphite fiber reinforced aluminum metal matrix composites are susceptible to rapid corrosion, especially in chloride environments [1-16], which has, in part, limited the use of these materials in aircraft, spacecraft, and Naval applications. Attempts have been made to improve the corrosion resistance of graphite/aluminum composites through the use of: coatings or some other form of electrical isolation between the fiber and matrix [4,5,7,9], cathodic protection, or cathodic inhibitors [3,13]. However, each of these protection techniques often adversely affect composite properties and in the long term only delay pitting and subsequent galvanic interaction between the matrix and fiber. In addition, none of these corrosion prevention processes address the real problem -- poor corrosion resistance of the aluminum matrix, especially when coupled to graphite fibers in a chloride-containing environment. In this program, the approach taken was to develop a corrosion resistant matrix alloy that was more electrochemically compatible with graphite than pure Al or commercially available Al alloys.

One study of the corrosion of graphite/aluminum MMCs reported that these composites corroded at rates up to fifteen times greater than monolithic aluminum alloys in a sodium chloride (NaCl) electrolyte at room temperature [13]. Corrosion of conventionally processed graphite/aluminum composites initiates as a result of pitting of the facesheet foils. Once these foils have been penetrated, corrosion is accelerated by the following mechanisms [4,5,13-16]:

- Residual microstructural chlorides within the composite at precursor wire interfaces lead to rapid internal composite corrosion, and

- Exposure of the graphite fibers creates a galvanic couple with the aluminum matrix leading to rapid matrix dissolution.

One of the key problems leading to rapid corrosion of graphite/aluminum composites stems from the fabrication process, which introduces residual microstructural chlorides. Current

1

state-of-the-art (SOA) manufacturing of graphite/aluminum MMCs utilizes the liquid metal infiltration (LMI) process. The basic steps in the LMI process are as follows [13,17-21]:

- Titanium diboride (TiB_2) is deposited onto the graphite fibers to promote fiber/matrix wetting and bonding. This coating is deposited by chemical vapor deposition using titanium tetrachloride ($TiCl_4$) and boron trichloride (BCl_3) as the sources of titanium and boron irrespectively, while zinc gas is used as the reducing agent.

- Prior to exposure to air, the TiB_2 coated graphite fibers are passed through molten aluminum with an argon cover gas that also contains $TiCl_4$, BCl_3 (g), and zinc (g) to create straight composite wires. These wires are extremely stiff and susceptible to fracture.

- The fiber wires are then consolidated into the composite by diffusion bonding or hot isostatic pressing of the wires between aluminum matrix facesheet foils.

A new process has been recently developed and is in commercial practice that does not rely on the titanium diboride coating or the cast aluminum matrix [21,22]. In this process, the matrix alloy is deposited onto each individual fiber by a physical vapor deposition (PVD) method such as sputtering. The very nature of the PVD process allows virtually any matrix alloy to be deposited on to graphite fibers.

Using the PVD approach, composite processing involves the following steps:

- Deposit metal alloy onto fibers using automated magnetron sputtering (a process developed at Naval Research Laboratory and now in commercial practice).

- Configure the flexible graphite fibers by automated processes such as filament winding, braiding, or weaving.

- Consolidate the composite by low temperature diffusion bonding or hot isostatic pressing (HIP'ing).

Sputtering of metal alloys onto graphite fibers has several potential advantages over the current liquid metal infiltration process used to fabricate graphite/aluminum composites. The three most significant advantages of the physical vapor deposition method of fabricating graphite/aluminum composites are described in the following paragraphs.

Sputtering eliminates unwanted reactions at the fiber/matrix interface- Reaction between the molten aluminum matrix and graphite fiber often result in the formation of aluminum carbide (Al_4C_3) at the metal-graphite interface when the composites are produced using the liquid metal infiltration process [23-30]. Deleterious effects of this carbide are two-fold: (1) mechanical properties of the composite are decreased because the brittle carbide forms in a non-uniform manner and readily cracks upon loading; thereby beginning the failure process, and (2) the aluminum carbide can react with water to form aluminum hydroxide, which has no mechanical integrity; further reducing the strength of the composite [24]. Conversely, the sputtered alloys should be able to be consolidated at relatively low temperatures (~400°C) for a shorter time, thereby avoiding the potential fiber-matrix reaction.

Sputtering minimizes thermal strain hysteresis - Graphite fiber reinforced metal matrix composites typically exhibit strain hysteresis and residual strain during thermal cycling. This has been attributed to the low yield strength of the cast aluminum matrix plastically deforming to compensate for the large coefficient of thermal expansion mismatch between the fiber and matrix [21]. Sputtered alloys should exhibit yield strength values much greater than cast alloys due to the extremely small grain size (<0.2 μm) [21]. Thus, the strength of sputtered aluminum alloys should be sufficient to avoid plastic deformation during thermal cycling, thereby eliminating strain hysteresis and residual strain.

Sputter coated graphite fibers provides near-net shape processing capability
- Due to the brittle nature of LMI fiber wires, only fairly simple shapes such as flat plates and tubes can be fabricated. However, using the sputtering process, the fibers remain flexible after deposition of the matrix alloy, and can be configured into complex shapes by automated processes such as filament winding, weaving, or braiding. Thus complex shaped preforms can be fabricated and subsequently consolidated, resulting in near net shape graphite/aluminum components.

Program Objectives

The primary goal of this program was to determine if nonequilibrium alloying could be used to improve the corrosion resistance of graphite-reinforced MMCs. Of specific interest was improving the inherent corrosion resistance of the matrix metal and improving galvanic compatibility between the matrix and the graphite reinforcement. The nonequilibrium alloys improve corrosion behavior and do not introduce residual chlorides as does the liquid metal infiltration process, further improving the composites' inherent corrosion performance. Transition of the corrosion resistant nonequilibrium alloys into commercial practice only requires incorporation of these new alloys as the sputtering target material.

To accomplish the primary goal of the program the following major tasks were undertaken.

- Determine whether enhanced corrosion behavior could be achieved through the nonequilibrium alloying of aluminum and magnesium with molybdenum, tantalum, tungsten, chromium, and yttrium.

- Determine if enhanced corrosion behavior could be maintained for these nonequilibrium alloys after heat treating at typical composite consolidation temperatures.

- Determine the galvanic corrosion compatibility of the most promising candidate alloys with graphite fibers.

- Fabricate ternary alloys (containing Al, Mg, and one of the alloying additions cited above) to reduce alloy density and to determine whether improved corrosion resistance can be achieved and maintained for these alloys after heat treating to nominal composite consolidation temperatures.

- Develop the parameters to deposit the corrosion resistant nonequilibrium alloys onto graphite fibers and consolidate the fibers into composite panels.

A secondary objective of this research program was to determine if an inhibitive treatment (similar to the one developed by Mansfeld for Al) could be developed which would further enhance the corrosion resistance of Mg and Mg-based composites.

3

2.0 Background

2.1 Fabrication of Traditional Graphite/Aluminum Composites

Corrosion of graphite/aluminum composites is strongly dependent on contaminants introduced during processing, therefore understanding the corrosion behavior first requires an understanding of the composite fabrication process. The most widely used process is the liquid metal infiltration process [13,17-20]. In this process graphite fiber tows are coated with TiB_2, passed through molten aluminum and consolidated between matrix foils by diffusion bonding. TiB_2 is deposited onto the graphite fibers to promote wetting between the fiber and aluminum matrix and to prevent a fiber/matrix reaction which forms aluminum carbide, Al_4C_3. TiB_2 is deposited onto the fibers by reduction of $TiCl_4$ and BCl_3 using zinc gas in a chemical vapor deposition chamber as illustrated in Figure 2-1. Unfortunately, TiB_2 rapidly oxidizes when exposed to air and looses the ability to promote wetting between molten aluminum and the fiber. Therefore, the TiB_2 coated fibers are immediately passed through molten aluminum, under an argon cover gas that also contains $TiCl_4$, BCl_3, and zinc gas; thus forming composite wires. These wires are then cleaned by solvent rinsing, placed between aluminum matrix facesheet foils, and consolidated into a composite by diffusion bonding, pultrusion, or hot isostatic pressing (HIP'ing).
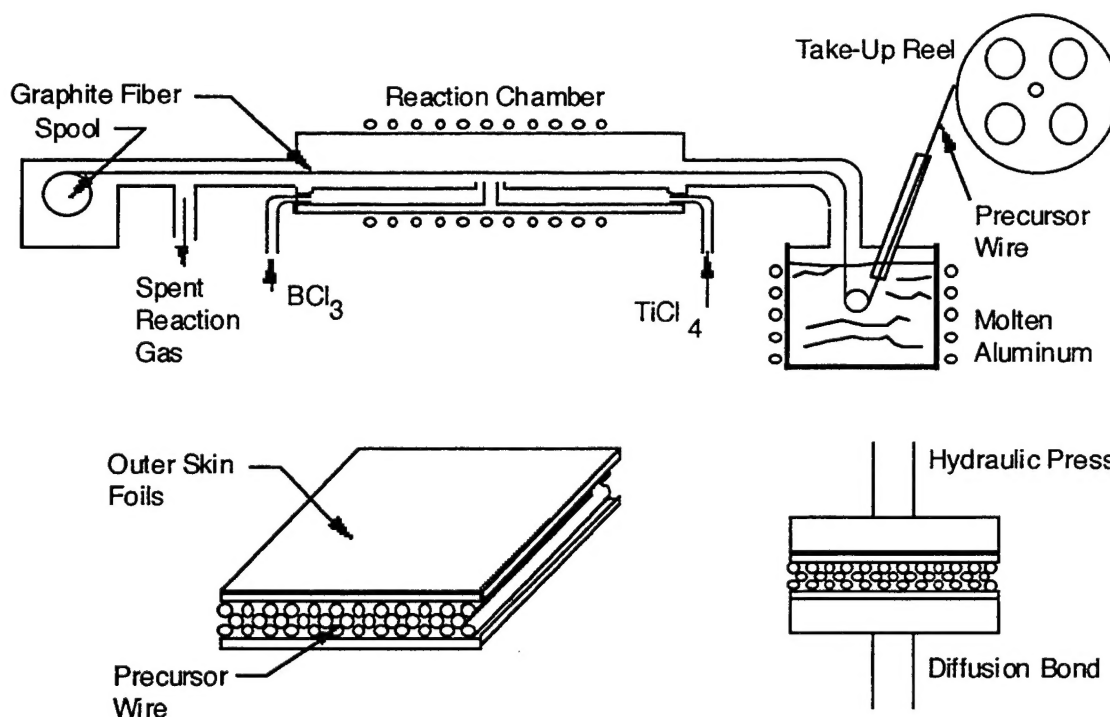
Figure 2-1. *Schematic of the liquid metal infiltration process for the production of a Gr/Al composite showing (a) deposition of TiB₂ on the graphite Fibers and directly passing through molten aluminum to create composite wires, (b) lay-up of the composite wires between facesheet foils, and (c) diffusion bonding of the composite.*

A new process has been developed that eliminated the need for the TiB_2 coating step [21,22]. In this process, the aluminum alloy matrix is directly deposited onto graphite fibers by physical vapor deposition (PVD), and the coated fibers are subsequently

4

consolidated into composites by diffusion bonding, pultrusion, or hot isostatic pressing. The first step in this process is to spread the fiber tows into monofilament layers and deposit the matrix metal onto each individual fiber by passing them through a vapor deposition system to form fiber tapes. Fiber tapes are then wrapped onto a take-up reel for later processing. The sputtered alloys coat the fibers fairly uniformly and the volume of the fiber in the composite is controlled by adjusting the thickness of the matrix on each fiber. The fiber tapes can then be consolidated.
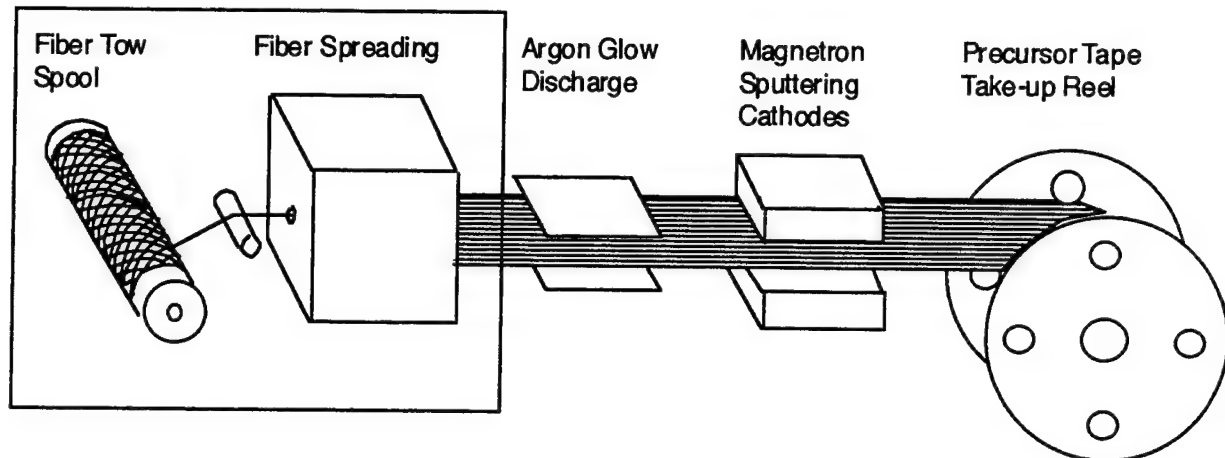

Figure 2-2. *Schematic of the physical vapor deposition (PVD) composite fabrication process [22].*

The advantages of the physical vapor deposition process are:

- Due to lack of contaminants or residuals, matrix strength is much higher than the cast liquid metal infiltration matrix, which increases the overall composite strength and minimizes thermal hysteresis during thermal cycling that is a result of plastic deformation of the matrix.

- Residual chlorides from the TiB_2 deposition process are eliminated. These residual chlorides have been shown to be a key factor in the rapid corrosion of conventionally processed Al-Gr composites.

- Fiber tapes are much more flexible than the liquid metal infiltration precursor wires and can be configured into complex near-net shaped components and consolidated by diffusion bonding, pultrusion, or hot isostatic pressing.

2.2 Corrosion Resistance of Graphite-Reinforced MMCs

2.2.1 Graphite/Aluminum MMC Corrosion

A number of researchers have found that the liquid metal infiltration of graphite/aluminum MMCs is at least partially responsible for the severe corrosion of these composites in chloride environments [1-16]. Corrosion can initiate on either the panel edges where fibers are exposed or by pitting through the aluminum facesheet foil. Once the outer foil of the composite has been penetrated, residual chlorides on the surface of the precursor liquid metal infiltration wires (introduced during fabrication of the composite) have been reported to greatly accelerate localized corrosion of the matrix, especially at internal wire-wire interfaces and wire-foil interfaces [13]. Formation of corrosion products at the wire-wire

5

and wire-foil interfaces cause volumetric expansion of the composite and subsequent loss of mechanical integrity. Dissolution of the matrix also exposes the graphite fibers, allowing galvanic corrosion to occur, further accelerating the dissolution of the matrix and leading to the rapid degradation of the composite. It has been reported that the corrosion rate of aluminum can be increased eighty-fold when equal areas of graphite and aluminum are coupled and exposed to aerated sea water [13].

Al immersed in an aerated aqueous chloride solution buffered to a near neutral pH, dissolves locally by an anodic reaction:

$$Al \rightarrow Al^{+3} + 3e^-$$

with oxygen reduction at cathodic sites:

$$O_2 + 2H_2O + 4e^- \rightarrow 4OH^-$$

Corrosion of Al under these conditions is in the form of pits, with the majority of the surface remaining passive. . Once the electrochemically noble Gr is exposed, corrosion of the Al matrix is accelerated due to galvanic corrosion as illustrated by the galvanic diagram for pure Al coupled to graphite shown in Figure 2-3. The dissolution of Al is dramatically increased as a result of oxygen reduction taking place on the exposed Gr fibers, as the relatively high value for $I_{galv:Gr/Al}$ indicates. The rate of dissolution increases as the amount of exposed Gr fiber increases, and extensive dissolution can occur in a very short period of time.

The addition of several atomic percent of W, Ta, Cr, or Mo to Al has been shown to substantially increase its pitting potential as illustrated in Figure 2-4.[31-40] For example, alloying with 1.5 atomic percent W resulted in an breakdown voltage of -111 mV$_{SCE}$ in a 0.1 M chloride solution. Pitting in this alloy is suppressed when exposed to an air saturated solution or as a result of galvanic coupling to another metal whose open circuit potential is less than -111 mV.

By superimposing the cathodic polarization data for Gr on the anodic polarization data for the Al-1.5 atomic percent W alloy, the effects of the galvanic coupling on the corrosion behavior of the Al matrix can be estimated. Figure 2-5 shows cathodic polarization data for P100 Gr fibers generated in aerated 3.15 weight percent NaCl, superimposed on the anodic polarization curve for the Al-1.5 atomic percent W (Al-1.5W) alloy. This figure reveals that even at a Gr:Al area ratio of 1-to-1, corrosion of the nonequilibrium Al-1.5 W alloy was not accelerated as a result of galvanic coupling.

The addition of certain transition metals to Al shifts the open circuit potential, E_{oc}, of the alloy several hundred millivolts in the positive direction. Table 2-1 shows this effect for Al-Mo alloys [32] in deaerated 0.1M KCl. In each case, the Mo in the alloy was in solid solution with the Al.

6
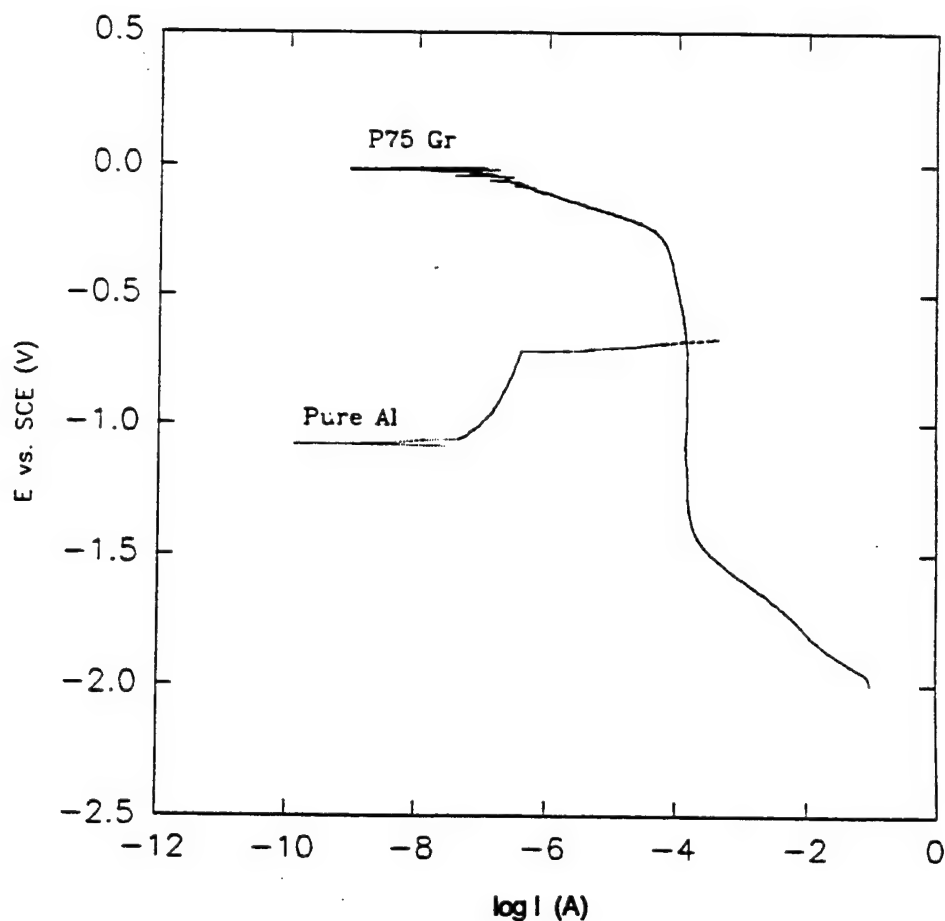
Figure 2-3. *Galvanic diagram for Al coupled to graphite in 0.1M NaCl (initially adjusted to a pH of 8) under ambient laboratory conditions. A potentiodynamic scan rate of 0.2mV/s was used to produce each of the curves.*

Table 2-1. *Effect of Molybdenum Concentration on Open Circuit Potential of Nonequilibrium Al Alloys.*

Atomic Percent Molybdenum	Open Circuit Potential (mV v. SCE)
0.0	-1405
2.8	-1002
5.4	-953
7.1	-877
10.4	-833

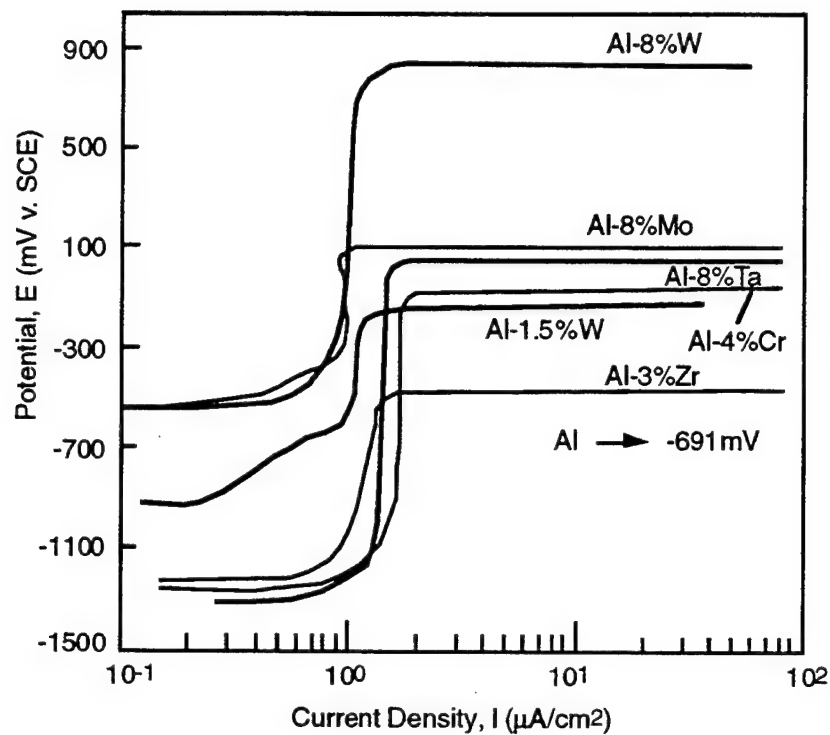**Figure 2-4.** *Anodic polarization behavior of a variety of nonequilibrium Al alloys in aerated 0.1 M KCl compared to the spontaneous pitting potential for Al (-691 mV v. SCE).*
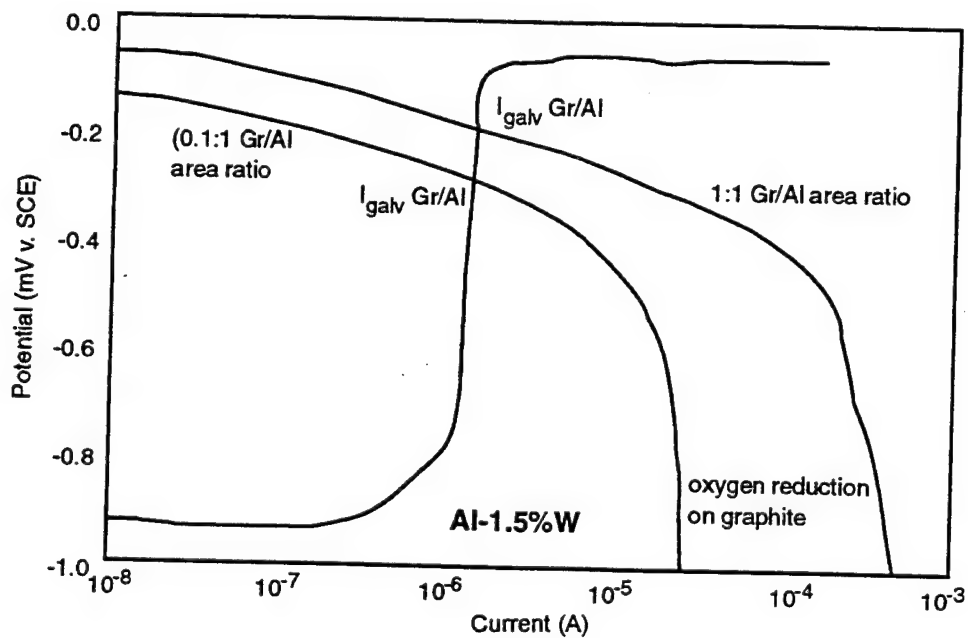

Figure 2-5. *Mixed potential analysis of Gr/Al-1.5 atomic percent W galvanic couple (cathodic data derived form Ref. 13).*

8

2.2.2 Corrosion Prevention for Graphite/Aluminum MMCs

During the past decade a variety of methods for improving the corrosion resistance of graphite/aluminum metal matrix composites has been investigated. These methods include: cathodic protection [13], electrical insulation between the graphite fiber and metal matrix [13], use of cathodic inhibitors [13], and barrier coatings [5,7,9,13]. Cathodic protection, which promotes the formation of hydroxyl ions, can be damaging and is not recommended because aluminum is susceptible to corrosion in alkaline environments. Electrical insulation of the graphite fibers from the matrix by a continuous coating may be possible, but it is impractical because holidays in the coating can never be totally eliminated. Cathodic inhibitors, such as $ZnCl_2$ or mixtures of Na_2CrO_4 and $ZnCl_2$, show promise for decreasing the galvanic corrosion [13] through the precipitation of $Zn(OH)_2$ on the cathodic sites, effectively reducing the cathodic area and subsequent galvanic corrosion. However, the use of cathodic inhibitors is difficult to put into practice for composites. Protective coatings such as electroplated [7] or electroless nickel [5,9], anodization [5,9], chemical vapor deposition of either nickel [5,9] or chromium carbide [13], or organic coatings [13] have all been used to inhibit localized corrosion by sealing surface flaws in composites. Although these coatings can extend the life of the composite, the corrosion resistance of the Al when coupled to the graphite is still poor and the composite is very susceptible to degradation if the coating is damaged. Furthermore, these coatings will increase the density of the component and may alter the thermal dimensional stability of the composite.

2.2.3 Graphite/Magnesium MMC Corrosion

Magnesium, in Gr/Mg composites, experiences more severe corrosion degradation than Al in Gr/Al composites because unlike Al, which can form a passive film that limits attack, the film that forms on Mg is not nearly as protective as the one that formed on Al. For example, high purity Mg in a benign solution of sodium borate/boric acid (pH 9.3) exhibits a passive current density of 1-2 mA/cm^2 [41]; whereas, a typical current density for Al in a near neutral pH solution is on the order of several $\mu A/cm^2$. In addition, the quasi-protective $Mg(OH)_2$ film is only stable in basic pH values above 11.

For Mg and Mg alloy corrosion, the rate controlling reaction is the evolution of hydrogen rather than the reduction of oxygen. Mg dissolves by the following reaction:

$$Mg \rightarrow Mg^{+2} + 2e^-$$

and in near neutral aqueous solutions, water is reduced to form hydrogen gas and hydroxyl ions:

$$2H_2O + 2e^- \rightarrow H_2 + 2OH^-$$
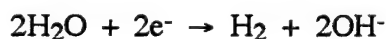
Efforts to reduce the corrosion of Mg and its alloys have focused on eliminating trace element impurities, of particular interest are Fe, Ni, and Cu. These impurities increase corrosion by establishing microgalvanic cells within the Mg alloy since they are more noble than Mg by several hundred millivolts. Limits of 170, 1000, and 5 ppm for Fe, Cu, and Ni, respectively, have been set to decrease the corrosion rate of Mg.[42] However, not all elements are deleterious to the corrosion behavior of Mg. Small concentrations of Zn and Mn have also been found to increase corrosion resistance of Mg by minimizing the deleterious effect of Fe since they react to form a compound less galvanically active than pure iron precipitates.[43] The addition of 1 weight percent Zn or Mn effectively decreases the corrosion rate of Fe-contaminated Mg by almost three orders of magnitude as revealed in Figure 2-6. Another example of an alloying addition which improves the corrosion

9

resistance of Mg is Al. A study of nonequilibrium melt spun Mg alloys a decrease in the corrosion current of two orders of magnitude [44] with the addition of 10 to 23 weight percent Al. The decrease in corrosion rate with the addition of Al was attributed to the formation of an aluminum-rich passive film. These efforts improve the corrosion resistance of Mg but they do not improve it enough to make the alloys galvanically compatible with graphite. In order to drastically improve the galvanic compatibility with graphite, either the open circuit potential of the alloy must be moved to a value close to that of graphite or the quasi-passive film must be enhanced significantly. Ideally, a combination of both a large shift in E_{oc} and significantly enhanced passivity are desired.
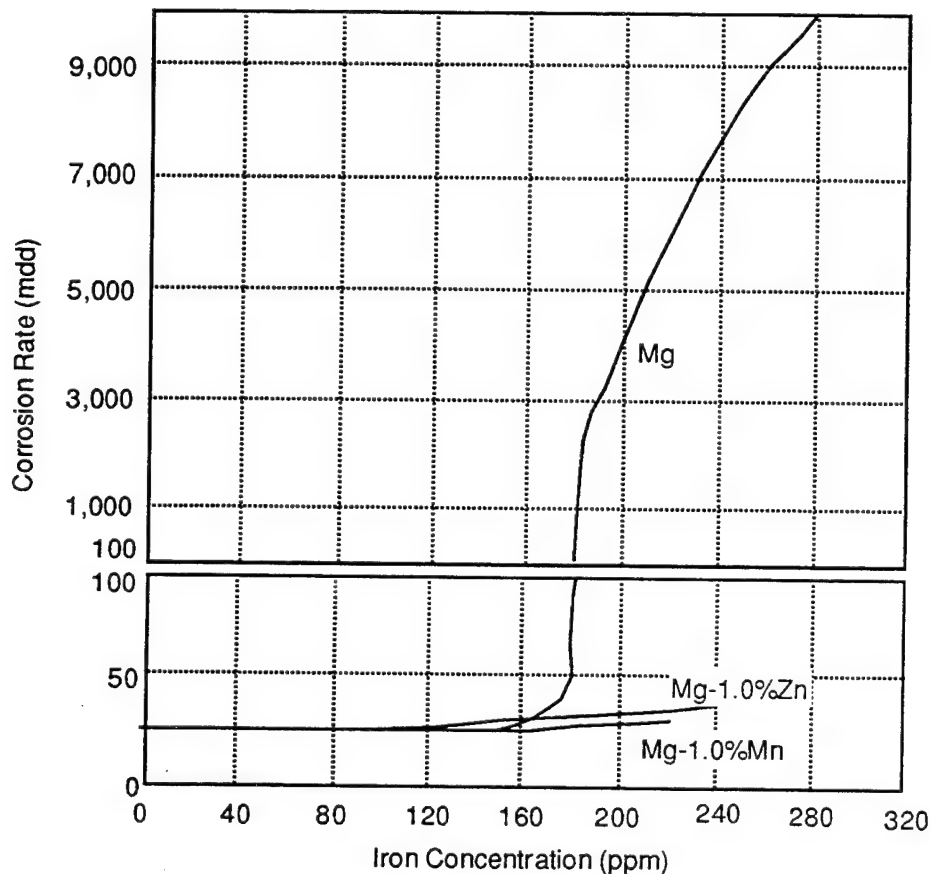
Figure 2-6. *The corrosion of Mg in 3 weight percent NaCl, alternate immersion, 16 weeks, showing tolerance limit for Fe and the beneficial effect of alloying with zinc and manganese [taken from reference 43].*

2.2.4 Prevention of Graphite/Magnesium MMC Corrosion

In the case of Al-based composites, the focus of this research was on improving the passivity of the alloy to eliminate, or at least minimize, galvanic attack. Magnesium on the other hand is extremely reactive, and its passive film is easily dissolved. Hence, for this metal it is necessary to add elements that not only improve passivity but also raise E_{oc}.

One method to increase the passivity of Mg is to alloy it with Cr, Mo, Ta, Y, and W in nonequilibrium concentrations. A key to this method is to maintain the solute elements in solid solution in order to alter the overall composition of the passive film. Precipitates of a second phase would not only decrease the amount of alloying addition available for incorporation into the passive film, but it would also lead to the establishment of microgalvanic cells within the alloy.

Al and Mg both have low exchange current densities, whereas the exchange current densities of Mo, Ta, Y, and W are several orders of magnitude higher. If the open circuit potential of Mg could be shifted through solid solution alloying with elements such as Mo, Ta, Y, or W, then the galvanic compatibility of Mg with Gr could be significantly enhanced.

Yttrium was originally added to Mg because of the age hardening capabilities of Mg-Y alloys.[45] As a result, its corrosion performance was also investigated and found to be better than that of other Mg alloys.[46, 47] Since the E_{oc} of Y is approximately 300 mV higher than that of Mg and yttrium exhibits a stable passive region at pH values lower than Mg, it is good candidate for consideration in the development of a corrosion resistant Mg alloy for possible use in a graphite-reinforced composite.

3.0 Experimental Details

Nonequilibrium aluminum and magnesium alloys were prepared by co-sputtering the two (or three) elements onto single crystal silicon or sapphire wafers. The temperature of the silicon or sapphire wafer substrates was not controlled during sputtering and reached a maximum temperature of approximately 100°C. The composition of the alloys was varied by holding the primary aluminum or magnesium target at a constant power, generally 480 or 240 watts (W), while the power for the solute cathodes was varied between 10 and 100 watts. By spacing the sputtering heads approximately 100-mm (4-in.) from the substrate at angles of 60° from the substrate normal and rotating the substrate at 30 RPM, the alloy composition could be maintained to within one atomic percent across the 100 mm diameter wafer.

The wafers were cleaved into approximately 16 pieces for alloy characterization and corrosion testing. Compositional analysis was conducted using either semi-quantitative energy dispersive x-ray spectroscopy (EDS) or direct coupled plasma (ICP) emission. Following deposition, x-ray diffraction (XRD) of each film was conducted to determine 1) whether the solute was in solid solution in the aluminum or magnesium and 2) whether precipitation occurred after heat treating. One thick alloy (0.1mm) was produced for tensile and hardness testing. Anodic polarization testing, in a 0.1 M NaCl solution which was adjusted to a pH of 8, was conducted to determine the corrosion behavior of each alloy before and after heat treatment. Long-term galvanic couple experiments, in which the alloys were coupled to p75 graphite, were also conducted.

3.1 Target Materials

Targets were manufactured by machining bulk metals to 76 mm diameter circles 3.2 mm thick (3.0 x 0.125-in.). Nominal composition for each element was 99.95 percent pure (by weight).

3.2 Sputter Deposition System

A 602RS Loadlock Thin Film Deposition System was used to produced the sputter-deposited binary and ternary alloys. The 45 x 70 x 60 cm box sputtering chamber contained three co-focused cathodes that allowed for a large range of alloy compositions. Each cathode held a 76-mm-dia. x 3.2-mm-thick target focused toward a 100-mm-diameter rotating substrate holder. Power for cathode one was regulated with an Advanced Energy (AE) MDX 1.5K power supply that provided 1500 watts at a maximum of 700 volts direct current (V DC). Power for cathode two was switchable for either DC or RF operation. DC power was supplied by an AE MDX1.5K power supply which regulated power up to 1500 watts (W) at 500 V DC. RF power for cathode two was supplied by an AE RFX-600 supply which was tuned with an AE ATX-600. An in-line blocking filter was installed to prevent RF power from translating back to the DC power supply. The third cathode was supplied with an AE RFX-600 RF power supply and the power conditions were tuned with the AE ATX-600. The substrate holder was also connected to an AE RFX-600 power supply for RF etch cleaning of the substrates prior to sputtering.

Vacuum for the main chamber was maintained by using a CTI Cyrotorr-8 vacuum pump with an Alcatel-Drytel 100 diaphragm/turbomolecular drag backing pump. Low contamination levels in the alloys were achieved because both vacuum pumps were oil-free and substrates were transferred into the main chamber through a load-lock that was

evacuated with the backing pump. In this system, the load lock could be evacuated to approximately 10^{-5} torr within three minutes which allowed for rapid transfer of specimens into the sputter chamber, thereby avoiding any possible contamination that could have been experienced by opening the chamber.

During sputtering, gas was introduced into the chamber through flow controllers and the sputtering pressure was controlled between 1.0 and 100 millitorr with a VAT, Inc. series 64 pressure controller. The sputtering pressure was regulated by adjusting the conductance of the high vacuum valve between the cyropump and chamber.

All systems and subsystems were controlled by an IBM PS/2 50Z computer that allowed for fully automatic operation.

3.3   Alloy Development and Characterization

3.3.1   Sputtering Rates

Sputtering rates for all of the materials were determined by depositing films onto glass slides and measuring the step height between the coated and uncoated regions using a Sloan Dektak II profilometer which had an accuracy of ± 5.0 nm. Three profilometer scans, each three millimeters in length, were conducted on each glass slide to obtain an average sputtering rate. Each element was sputtered at different power settings to obtain sputter rate versus power curve. The sputtering rate was then calculated by dividing film thickness by total deposition time, assuming the films were 100 percent dense.

3.3.2   Nonequilibrium Alloy Fabrication and Heat Treatment

The sputtering rates for the Al, the Mg, and the Mo were used to predict alloy compositions prior to actual fabrication of the binary Al-Mo and ternary Al-Mg-Mo alloys. These alloys were sputtered by holding the Al power at 480 W (RF) while the Mo power was varied between 7 and 40 W and the Mg power was varied between 95 and 120 W (DC).

Heat treatments were conducted in a laboratory-scale resistive-element tube furnace interfaced with an Omega temperature controller. A heat treatment matrix was generated to determine the onset of precipitation as a function of time and temperature. Each alloy was heat treated at 400, 500 and 600°C for times of one, two and eight hours. Commercial grade argon gas was purged through the furnace at a rate of approximately one liter per minute to prevent oxidation of the aluminum alloy. The tube furnace was allowed to reach the above specific temperature and stabilize before the specimens were inserted. After heat treating for the specified time, the specimens were removed and allowed to cool in air.

3.3.3   Alloy Structure and Morphology

Upon removal from the sputtering system load-lock chamber, each alloy was visually inspected and the appearance recorded. Distinguishing features such as reflectivity, cloudiness, color, and surface roughness were noted.

A JOEL 840 scanning electron microscope (SEM) was used to examine the morphology of each alloy and to perform EDS compositional analysis. The alloys were examined in three conditions: (1) as-sputtered, (2) after heat treating to determine if any recognizable grain growth had occurred, and (3) after polarization testing to examine pit morphology and determine whether one of the alloy constituents had preferentially dissolved.

A semi-quantitative EDS computer program was used to analyze x-ray spectra to determine alloy composition by comparing the acquired peaks to a library of references peaks. The computer program used a multiple squares analysis to accurately measure peak intensities, remove background, and to unfold overlapping peaks.

The conditions used during the EDS analysis were kept constant for all the alloys and were as follows:

Voltage:	15 kV
Magnification:	350 X
Working Distance:	35 mm
Counts/s In:	1400 to 1800
Acquisition Time:	100

Each alloy was analyzed in three locations to obtain an average composition and to determine if the composition varied with position. In addition, compositions of several alloys were measured by direct current plasma emission, DCP, using the Beckman Spectraspan VI. In this analysis, the alloys were dissolved in a hydrofluoric/nitric acid solution, brought to a required volume, and then atomized and injected into the plasma.

X-ray diffraction (XRD) spectra were acquired for each of the alloys using a Rigaku Rotoflex 12 kW rotating anode diffractometer with a monochromatic Cu Kα x-ray source. XRD spectra for as-sputtered and heat treated alloys were compared with each other and with a data base of possible products (including reactions that may have occurred with the silicon or sapphire substrates) to determine whether precipitation had occurred.

Transmission Electron Microscopy (TEM) examination was performed using a Phillips CM-30 microscope with the electrons accelerated to 200 keV. Planar specimens were prepared by polishing the silicon wafer to approximately 0.1 mm and then ion milling the remainder of the silicon (using a cold stage) to provide a film thin enough for electron transmission.

3.3.4 Mechanical Properties

Tensile and hardness properties were measured on a thick free-standing Al-Mo alloy film. The alloy was sputtered onto a copper foil coated with a thin (0.5 μm) molybdenum layer to prevent the copper from reacting with the Al-Mo alloy. A stainless steel mask pattern was placed over the copper substrate to provide three tensile dog-bone specimens and various other specimens for hardness and corrosion testing. After sputtering, the mask was removed and the copper substrate was etched away in a 50% nitric acid solution leaving a free standing alloy foil.

Ends of the dog-bone specimens were potted with epoxy to prevent damage to the film from the tensile machine grips. Tensile testing was performed using a 45,000 kg$_f$ (100 kip) MTS universal testing machine fitted with a secondary hydraulic actuator and a 45 kg$_f$ load cell. This was necessary to achieve load sensitivity for the thin film specimens. Portions of the thick film specimen were mounted in plastic with the surface and edge exposed for microhardness tests.

3.3.5 Corrosion Testing

Polarization specimens were prepared by sectioning the alloys that had been sputtered onto silicon or sapphire wafers into approximately 10 mm x 10 mm specimens. Alligator clips were used to attach the specimens to the leads on the potentiostat and the edges, the back and the alligator clip attachment were coated with a marine epoxy paint (Interlux 404/414) leaving approximately 100 mm^2 of the alloy surface exposed for testing. The epoxy was allowed to cure for 24 to 48 hours before electrochemical testing.

The electrolyte was made by mixing reagent grade NaCl with distilled water to obtain a 0.1 M solution. The initial pH was adjusted by adding HCl to lower the pH or NaOH to raise the pH. Some drop in the pH 8 solution did occur during the course of most experiments but for the short term experiments this did not affect the results. Anodic polarization tests were conducted under ambient pressure and lab conditions without aeration.

Prior to polarization, the potential was monitored for approximately 1 hr or until the potential reached a steady state value. The specimens were then polarized using a Princeton Applied Research PAR Model 273 potentiostat/galvanostat starting a few millivolts below the corrosion potential until pitting occurred. Scan rates of 0.2 mV/s and 0.05 mV/s were used. At least two specimens of each alloy were tested. Following anodic potentiodynamic polarization, anodic potentiostatic experiments were conducted on the most promising alloys. The conditions for these tests were the same as those for the dynamic tests. All references to potential in this report are versus a saturated calomel electrode.

Assuming an insignificant IR drop between the metal and graphite, no contributions from reverse reactions, and uniform current distribution, the intersection of the anodic and cathodic curves provides an estimate of the current present in the galvanic couple. The galvanic corrosion resistance of the alloys was estimated in this fashion, using galvanic diagrams [43,48,49]. In these diagrams, the anodic data for the nonequilibrium alloys were superimposed on the cathodic curve for P75 graphite fiber.

In order to confirm the predictions made with the galvanic diagrams, galvanic current measurements were taken on alloys coupled to graphite. These experiments were performed on alloys coupled to P75 graphite fibers embedded in a dielectric consisting of either polyetheretherketone (PEEK) thermoplastic or an epoxy thermoset. One edge of the graphite/polymer composite specimen was polished to reveal the P75 graphite fibers while the remainder of the composite was coated with the Interlux epoxy. The surface area of the exposed P75 graphite fibers was measured using a Buehler Omnimet II image analyzer. Individual graphite and thin-film specimens were coupled through an ESC Model 440 mulitchannel potentiostat/zero resistance ammeter (operating in the ZRA mode) and immersed. The galvanic current was monitored as a function of time. Again, the electrolyte was a 0.1 M NaCl aqueous solution (initially adjusted to a pH of 8).

The purpose of using the composites in this application were two-fold: 1) the dielectric provided rigidity for the fibers with a known volume fraction, and hence area density, and 2) the fibers were identical to the material used later in the program to make the composites.

3.3.6 Inhibitive Treatments for Enhancing the Corrosion Resistance of Mg

Substrate metals employed in this segment of the study were 99.98% pure magnesium and WE43 (a commercial magnesium alloy considered to be one of the most corrosion resistant magnesium alloys available). The inhibitive treatments evaluated are listed in Table 3-1. This table indicates the variations in concentration, length of immersion, temperature, and solution pH that were investigated. The compounds used to prepare the inhibitive solution were dissolved in de-ionized water and heated to the specified temperature. Initially, the Mg specimens were polished with 600 grit SiC sandpaper to ensure surface smoothness. This surface preparation step was followed by immersion of the specimen in the inhibitor for the times/temperatures listed in Table 3-1. As part of the inhibitive treatment, some of the specimens were polarized for 2 hours in a 0.1 M sodium molybdate solution, adjusted to a pH of 12, prior to corrosion testing. As in the other experiments, the pH was adjusted by adding hydrochloric acid to lower the pH or sodium hydroxide to increase the pH.

Table 3-1. *Inhibitive Treatments Evaluated for Enhancing the Corrosion Resistance of Mg.*

Inhibitor	$Ce(NO_3)_3$	$Y(NO_3)_3$	CeF_3	Na_2MoO_4
Solution conc. (mM)	5 10	5 10	1 5	100
Solution temp (∞C)	room 60-70 100	room 60-70 100	room 60-70 100	room
Solution pH	natural 10 12	natural 12	natural 12	natural 12
Immersion time (h)	2 4	2 4	2 4	2

3.3.7 Corrosion Evaluation of Treated Mg

Following the inhibitive treatments, the specimens were anodically polarized at room temperature in quiescent 0.1 M NaCl (with the initial pH adjusted to 8) to assess the effectiveness of the various treatments in altering magnesium's corrosion resistance. Treated specimens were tested in a flat cell where the specimen was exposed vertically with an o-ring seal to avoid edge effects and to select a portion of the sample, with a known area (1 cm² in this research), for testing. The cell utilized a platinum/niobium counter electrode and a SCE (saturated calomel electrode) reference electrode. As before, the specimens were polarized using a Princeton Applied Research PAR Model 273 potentiostat/galvanistat. Specimens were allowed to stabilize for one hour or until the potential reached a steady state value. A scan rate of 0.2mV/s was used for these polarization experiments.

EIS was used to monitor the corrosion process of the treated specimens in a 0.1 M NaCl solution (with initial pH adjusted to 8 using NaOH). EIS spectra were collected using EG&G SoftCorr Model 398 Electrochemical Impedance Software, an IBM personal computer, an EG&G PAR model 5210 lock-in amplifier, and an EG&G PAR 273 Potentiostat. Initial and final frequencies of 10 mHz and 5 kHz were used with 5 data points taken per decade and an AC amplitude of 5 mV. In these experiments, the spectra were collected at the open-circuit potential, E_{oc}. Before starting a test, a delay of 10 minutes was allowed to give the system time to stabilize. EIS spectra were acquired after exposure of the specimens for periods of 1 hour, 1 day, and 1 week. Data comparing the effect of exposure time were evaluated using Boukamp equivalent circuit software. EIS spectra were collected for magnesium and WE43 in the untreated state and after treatment with the most effective inhibitor for that material (cerium fluoride for both magnesium and WE43). The same flat cell setup and same treatment steps utilized in the potentiodynamic tests were also used in the EIS experiments.

Cathodic polarization scans were conducted on magnesium to verify whether the best inhibitive treatment identified in this research functioned as an anodic, a cathodic, or a mixed inhibitor. This was done by examining the cathodic polarization behavior of both treated and untreated specimens. These cathodic polarization experiments were conducted using the same conditions outlined earlier for the anodic polarization experiments.

Scribed sample testing was conducted to determine the effectiveness of the coating when damaged (scratched). After completion of the treatment steps and prior to the corrosion experiments, panels with the best treatment identified from anodic polarization were scratched with the sharp point of a glass rod. The scribe was made in the shape of an "X" and cut deep enough into the surface to reach the untreated metal underneath. These samples were then polarized as outlined above.

4.0 Results

4.1 Phase 1: Preliminary Alloy Development and Testing

4.1.1 Sputter Deposition Rate Evaluation

Sputtering rates for Al, Mg, Cr, Mo, Ta, and W determined using a Dektak profilometer are plotted in Figures 4-1 and 4-2. For the Al and Mg, the sputtering rates were determined using both DC and RF power. Comparing the Al and Mg data at similar power settings, it was observed that the rate for DC sputtering was at least double the rate for RF sputtering. For example, at ~240 W, the Al sputtered at rates of 0.29 nm/s with DC power and 0.16 nm/s with RF power. Similarly, the Mg sputtered at rates of 1.07 nm/s with DC power and 0.43 nm/s with RF power. This figure also shows that the deposition rate for Mg is approximately triple the rate of Al (for both DC and RF sputtering). The DC sputtered films were very cloudy for the Mg and less specular for the Al. Therefore, although the sputtering rate was higher for DC, RF was selected to fabricate the alloys. If higher rates for Al or Mg were needed, two sources were used.

Comparing the sputtering rates at similar power settings indicated that the Cr sputtered at the slowest rate, and the Mo sputtered at the highest rate. For example, for a power setting of 241 W, deposition rates were measured at 0.23 nm/s, 0.39 nm/s, 0.35 nm/s, and 0.37 nm/s for Cr, Mo, Ta, and W, respectively. To achieve concentrations between 1 and 10 atomic percent, deposition rates were also measured at much lower cathode power settings. Sputtering rates at 38 W DC were determined to be 0.037 nm/s, 0.064 nm/s, 0.10 nm/s, and 0.063 nm/s for Cr, Mo, Ta, and W, respectively.
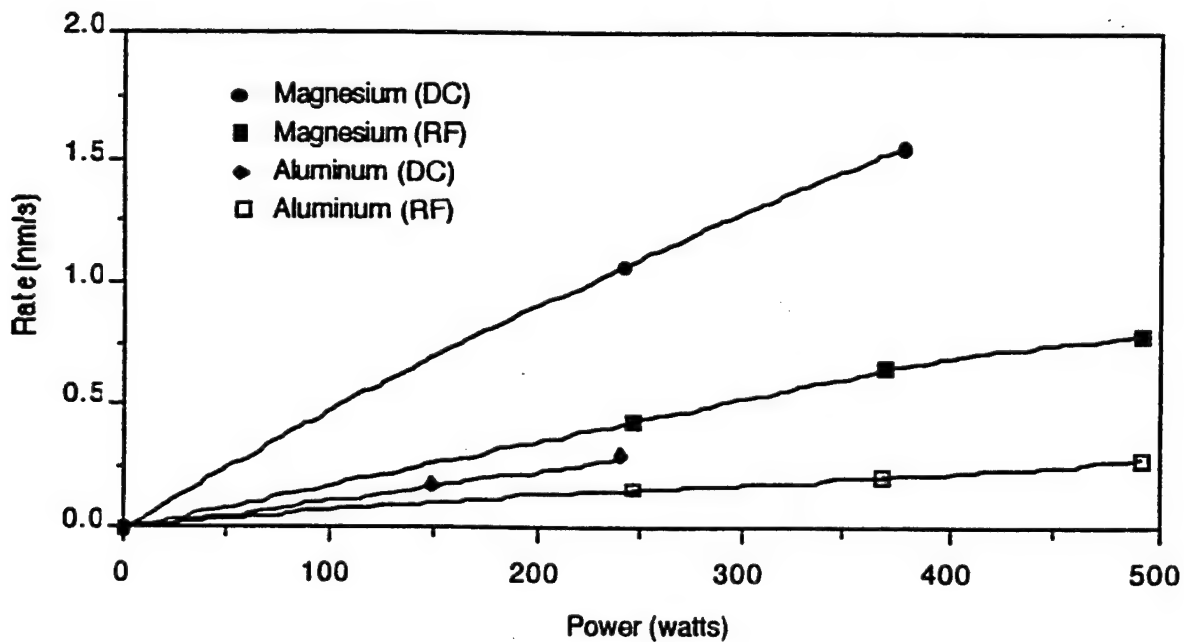

Figure 4-1. *Sputter deposition rates as a function of cathode power settings for transition metal alloying additions.*
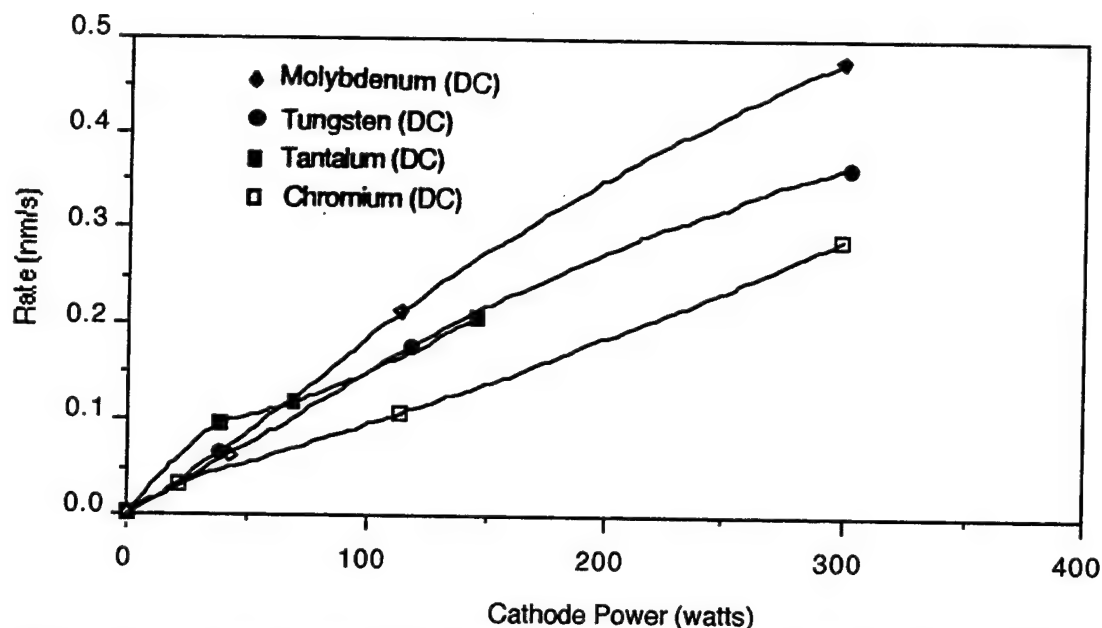
Figure 4-2. **Sputter deposition rates as a function of cathode power settings for transition metal alloying additions.**

4.1.2 Alloy Development

Binary and ternary alloys were deposited onto 100 mm (diameter) silicon wafers using the rates reported above. Composition was predicted using the following relationship:

$$\text{atomic \% solute} = \frac{\dfrac{R_1\rho_1}{MW_1}}{\dfrac{R_1\rho_1}{MW_1} + \dfrac{R_2\rho_2}{MW_2}} \times 100$$

where R is the measured sputtering rate, is density, MW is the molar weight, and the subscripts 1 and 2 refer to the solute and primary binary alloy constituents (Al or Mg), respectively. To obtain solute concentrations between 0.5 and 10 atomic percent, the lowest power settings were used. For example, power settings of 1%, 2%, and 3% were used for DC sputtering of the solute, which corresponded to 7%, 22%, and 38% W, respectively.

Alloys were sputtered for times ranging from 30 to 120 minutes to achieve a desired thickness of no less of 1- 2μm. Visual appearance of each alloy was recorded after sputtering and after heat treating. For the most part, each alloy had a highly reflective metallic appearance indicating low oxide content. An exception was the two gun Mg alloys, which had a cloudy appearance. This cloudiness was attributed to increased surface roughness of these specimens.

4.1.3 Compositional Analysis

Compositions measured by EDS and DCP are listed in Table 4-1 for the Mg-Group Vb & VIb alloys and the Al-Group Vb & VIb alloys. Concentrations reported in this document were based on DCP values when available and all references to concentration, unless otherwise noted, are in atomic percent. An alloy designation such as Al-26W refers to a nonequilibrium Al alloy containing 26 atomic percent atomic percent W.

Alloy	Alloy Designation	Alloy Composition (atomic percent)		
		Predicted	EDS	DCP
Mg-Cr	Mg480.C.Cr10.S.20106.1	1.7Cr	2.4Cr	2.65
	Mg480.C.Cr20.S.20106.1	5.1Cr	7.2Cr	
	Mg480.C.Cr40.S.11215.1	8.5Cr	11.8Cr	
Mg-Mo	Mg480.C.Mo10.S.10906.1	1.5Mo	0.9Mo	
	Mg480.C.Mo20.S.10906.1	4.6Mo	1.8Mo	
	Mg480.C.Mo40.S.10906.1	7.6Mo	2.3Mo	
	Mg2/480.C.Mo10.S.11025.1	0.9Mo	-	
	Mg2/480.C.Mo20.S.11025.1	2.8Mo	1.3Mo	
	Mg2/480.C.Mo40.S.11025.1	4.7Mo	2.4Mo	1.35
Mg-Ta	Mg480.C.Ta10.S.11210.1	2.7Ta	3.0Ta	
	Mg480.C.Ta20.S.11210.1	8.2Ta	7.3Ta	
	Mg480.C.Ta40.S.11210.1	13.3Ta	13.0Ta	
	Mg2/480.C.Ta10.S.11030.1	1.2Ta	1.2Ta	
	Mg2/480.C.Ta20.S.11030.1	3.5Ta	2.9Ta	
	Mg2/480.C.Ta40.S.11030.1	5.9Ta	4.6Ta	1.39
Mg-W	Mg480.C.W10.S.10825.1	1.0W	-	5.31*
	Mg480.C.W20.S.10825.1	4.5W	-	
	Mg480.C.W40.S.10825.1	7.4W	-	11.44†
	Mg480.C.W10.S.11207.1	1.0W	3.2W	
	Mg480.C.W20.S.11207.1	4.5W	8.2W	
	Mg480.C.W40.S.11207.1	7.4W	12.1W	
Mg-Y	Mg480.C.Y40.S.20801.1		8.7Y	
	Mg480.C.Y100.S.21102.1		22.6Y	
	Mg240.C.Y25.S.30914.1		10.1Y	7.5Y
	Mg240.C.Y50.S.30914.1		18.0Y	13.7Y
	Mg240.C.Y75.S.30914.1		28.6Y	20.6Y
	Mg240.C.Y100.S.30914.1		33.8Y	25.4Y
Al-Cr	Al2/480.C.Cr10.S.11004.1	2.4Cr	5.2Cr	
	Al2/480.C.Cr20.S.11004.1	7.3Cr	9.3Cr	
	Al2/480.C.Cr40.S.11004.1	12.0Cr	12.6Cr	11.61
Al-Mo	Al480.C.Mo10.S.10825.1	4.3Mo	-	
	Al480.C.Mo20.S.10825.1	12.3Mo	-	
	Al480.C.Mo40.S.10825.1	19.6Mo	-	25.9
Al-Ta	Al2/480.C.Ta10.S.11005.1	2.8Ta	2.8Ta	
	Al2/480.C.Ta20.S.11005.1	8.2Ta	8.2Ta	
	Al2/480.C.Ta40.S.11005.1	13.4Ta	13.4Ta	8.16
Al-W	Al480.C.W10.S.10825.1	4.1W	21.7	
	Al480.C.W20.S.10825.1	12.1W	33.0	
	Al480.C.W40.S.10825.1	19.0W	40.0	25.57
	Al2/480.C.W10.G.11117.1	2.1W	5.32	
	Al2/480.C.W20.G.11117.1	6.4W	7.64	
	Al2/480.C.W40.G.11117.1	10.5W	10.36	

4.1.4 Alloy Structure (X-ray Diffraction)

Summaries of the x-ray diffraction (XRD) results for the Mg alloys and the Al alloys are listed in Tables 4-2 and 4-3, respectively. For some of these alloys, interpretation of the data was difficult because no phase diagrams exist. Phase diagrams for many of the alloys have been reproduced in Appendix A [Ref 50] for convenience. The results were also complicated by reaction of the alloy with the Si wafer, as well as the preferred orientation that occurs naturally in sputter deposited films.

For the first phase of this task, examination of the data was simplified to a go or no go process. If the only peaks found were Si, Mg or Al, then the alloying element was in solid solution and the alloy was acceptable. If several additional peaks formed after heat treating that could not be related to either Al or Mg, precipitation was assumed to have occurred and a detailed examination of the phases present was not performed. An exception to this process was the Mg alloys where Mg_2Si formed after heat treatment. This reaction would not have occurred if the alloy was deposited onto Gr fibers and, thus, these peaks were identified and removed from further consideration.

Grazing incidence diffraction was also conducted on the Mg-W alloys to compare deposition of the alloys on a glass slide versus a Si wafer to assess whether the film texture varied between substrates and as a function of depth.

Table 4-2. **Summary of XRD Results for the Mg-Base Nonequilibrium Alloys.**

Film Designation	XRD Results (Before HT)		XRD Results (After HT)	
Mg-Mo				
Mg480.C.Mo10.S.10906.1	Si and Mg Peaks, Peak Shift	SS	Mg Peak Intensity Ratio Change, Mg2Si	RS
Mg480.C.Mo20.S.10906.1	Si and Mg Peaks, Peak Shift	SS	Mg Peak Intensity Ratio Change, Mg2Si	RS
Mg480.C.Mo40.S.10906.1	Si and Mg Peaks, Peak Shift	SS	Mg Peak Intensity Ratio Change, Mg2Si	RS
Mg2/480.C.Mo10.S.11025.1	Si and Mg Peaks, Peak Shift	SS	Mg Peak Intensity Ratio Change, Mg2Si	RS
Mg2/480.C.Mo20.S.11025.1	Si and Mg Peaks, Peak Shift	SS	Mg Peak Intensity Ratio Change, Mg2Si	RS
Mg2/480.C.Mo40.S.11025.1	Si and Mg Peaks, Peak Shift	SS	Mg Peak Intensity Ratio Change, Mg2Sii	RS
Mg-W			.	
Mg480.C.W10.S.10825.1	Si and 2 Mg Peaks	SS	Mg Peak Intensity Ratio Change, Mg2Si	RS
Mg480.C.W20.S.10825.1	Single Mg and Si Peaks	SS	Mg Peak Intensity Ratio Change, Mg2Si	RS
Mg480.C.W40.S.10825.1	4 Si and Single Mg Peak	SS	Mg Peak Intensity Ratio Change, Mg2Si	RS
Mg480.C.W10.S.11208.1	Mg, Si and W Peaks	P	Mg Peak Intensity Ratio Change, Mg2Si	RS, P
Mg480.C.W20.S.11208.1	Mg, Si and W Peaks	P	Mg Peak Intensity Ratio Change, Mg2Si	RS, P
Mg480.C.W40.S.11208.1	Mg, Si and W Peaks	P	Mg Peak Intensity Ratio Change, Mg2Si	RS, P
Mg-Ta				
Mg2/480.C.Ta10.S.11030.1	Mg, Si and Ta Peaks	P	Mg, Si, Ta and Mg2Si Peaks	RS, P
Mg2/480.C.Ta20.S.11030.1	Mg, Si and Ta Peaks	P	Mg, Si, Ta and Mg2Si Peaks	RS, P
Mg2/480.C.Ta40.S.11030.1	Mg, Si and Ta Peaks	P	Mg, Si, Ta and Mg2Si Peaks	RS, P
Mg2/480.C.Ta10.S.11210.1	Mg and Si Peaks	SS	Mg Peak Intensity Ratio Change, Mg2Si	RS,SS
Mg2/480.C.Ta20.S.11210.1	Mg and Si Peaks	SS	Mg Peak Intensity Ratio Change, Mg2Si	RS,SS
Mg2/480.C.Ta40.S.11210.1	Mg and Si Peaks	SS	Mg Peak Intensity Ratio Change, Mg2Si	RS,SS

* SS-Solid Solution, A - Amorphous, P - Precipitated, RS - Reacted with Silicon Wafer

Table 4-3. Summary of XRD Results for the Al-Base Nonequilibrium Alloys.

Film Designation	XRD Results (Before HT)		XRD Results (After HT)	
Al-Mo				
Al480.C.Mo10.S.10825.1	Si , Single Amorphous Peak	A	Precipitated Several New Peaks	P
Al480.C.Mo20.S.10825.1	Si , Single Amorphous Peak	A	Amorphous Peak Narrowed	A
Al480.C.Mo40.S.10825.1	Si , Single Amorphous Peak	A	Amorphous Peak Narrowed	A
Al-W				
Al480.C.W10.S.10825.1	Si , Single Amorphous Peak	A	Amorphous Peak Narrowed	A
Al480.C.W20.S.10825.1	Si , Single Amorphous Peak	A	Amorphous Peak Narrowed	A
Al480.C.W40.S.10825.1	Si , Single Amorphous Peak	A	Amorphous Peak Narrowed	A
Al-Cr				
Al2/480.C.Cr10.S.11004.1	Si , Single Amorphous Peak	A	New Peaks, Possibly Cr4Si4Al13	P
Al2/480.C.Cr20.S.11004.1	Si , Single Amorphous Peak	A	New Peaks, Possibly Cr4Si4Al13	P
Al2/480.C.Cr40.S.11004.1	Si , Single Amorphous Peak	A	New Peaks, Possibly Cr4Si4Al13	P
Al-Ta				
Al2/480.C.Ta10.S.11005.1	Si , Single Amorphous Peak	A	New Peaks, Possibly Al3Ta	P
Al2/480.C.Ta20.S.11005.1	Si , Single Amorphous Peak	A	New Peaks, Possibly Al3Ta	P
Al2/480.C.Ta40.S.11005.1	Si , Single Amorphous Peak	A	New Peaks, Possibly Al3Ta	P

* SS-Solid Solution, A - Amorphous, P - Precipitated, RS - Reacted with Silicon Wafer

Mg-Cr & Mg-Y

XRD characterization for these alloys was not conducted after heat treatment. XRD prior to heat treatment revealed no precipitates.

Mg-Mo

In general, the diffraction patterns for all compositions of the Mg-Mo alloys were very similar. In the as-sputtered condition, only the Si and several Mg peaks were found-- indicating a solid solution alloy. There was some evidence of peak shift due to expansion of the Mg lattice by substitutional Mo atoms. After heat treating, Mg_2Si peaks were evident and, in some cases, the relative intensity of the Mg peaks had changed. This was likely a result of shifting of the Mg grain orientation caused by the changing residual stress state of the films during heat treating. No precipitate peaks were found after heat treating, which indicated the Mo was retained in solid solution.

Mg-Ta

The Mg-Ta diffraction patterns were very similar to the Mg-Mo. Before heat treating, only the Si and Mg peaks were found which indicated that the Ta was in solid solution with the Mg. After heat treating, the presence of Mg_2Si indicated that the Mg alloy had reacted with the Si, but no other precipitate peaks were present.

Mg-W

For the one gun Mg-W alloys, only the Mg and Si peaks were present which indicated that the W was in solid solution with the Mg. After heat treating, the only other peak detected was the Mg_2Si peak at 40° -- indicating the film retained its single phase structure. However from the compositional analysis section, it is apparent that the alloy contained a large amount of Al. Therefore, new Mg-W alloy films were sputtered at a later time in the

program. In the as-sputtered condition, XRD patterns for these alloys showed the presence of W. The intensity of the W peak at a diffraction angle of 39° decreased after heat treating because it was next to a strong Mg_2Si peak. Nonetheless, the Mg-W alloys did not appear to be capable of retaining a one phase structure at the temperatures and solute concentrations investigated in this work.

Al-Cr

In the as-sputtered condition, the XRD patterns for the Al-Cr alloys revealed only the Al and Si peaks indicating the Cr was in solid solution with the Al. The Al peaks were slightly shifted to higher angles indicating lattice parameter contraction, consistent with the smaller relative size of the Cr atom. After heat treatment, several new peaks were detected that did not correspond to Al. Preliminary examination indicated the precipitated phase could be either $Al_{17}Cr_9$ or $Cr_4Si_4Al_{13}$. This phase was evident in the Al-5.2Cr, Al-9.3Cr and Al-12.6Cr alloys. Therefore, any corrosion resistance afforded by nonequilibrium alloying of Al with Cr at these concentrations would likely be lost after consolidation of the composite.

Al-Mo

XRD patterns for the as-sputtered Al-Mo alloys contained broad peaks centered at 40° and ~20°, neither of which are exact reflection for Al. These broad, low intensity peaks are usually associated with a very fine grain size or an amorphous structure. The peak at 40° could be a combination of the normal Al peaks at diffraction angles of 38.4° and 44.7°. The shift from either of these angles may be a result of the ultra fine grain size of the sputtered alloys, the lattice parameter shift as a result of W in solid solution in the Al, and/or a lack of properly oriented planes in the highly textured film. After heat treating, several new peaks were present in the Al-4Mo alloy XRD patterns indicating the formation of a precipitate. However, the diffraction patterns for the higher Mo concentration alloys looked very similar before and after heat treating, suggesting the Mo remained in solid solution with the Al.

Al-Ta

As with the Cr alloys, precipitation of a Ta intermetallic compound occurred after heat treatment. Preliminary examination of the diffraction pattern indicated that the precipitated phase could be Al_3Ta or Al_9Ta. From a thermal stability perspective, Al-Ta alloys did not appear attractive.

Al-W

Diffraction patterns for the Al-W alloys were very similar to Al-Mo alloys with the very broad peaks centered at diffraction angles of ~20° and 40°. Again, these peaks were difficult to explain. For the Al-12W and Al-26W alloys, the XRD patterns remained effectively the same before and after heat treatment suggesting that the Al and W were present as a single phase structure (not necessarily a structure consisting of W in solid solution with Al). However for the lower W concentration alloy, Al-4W, several new peaks were present after heat treatment that were not Al related -- indicating that precipitates had formed. It was speculated that with a further decrease in solute concentration precipitation would also occur; however, lower solute concentration Al-W alloys were not examined to confirm this speculation.

4.1.4.1 Thin-Film Orientation Study

Grazing incidence diffraction (GID) was conducted on a Mg-1W alloy deposited on both a Si wafer and a glass substrate during the same deposition run. This was done to determine if the alloy composition or film texture were dependent on the type of substrate.

Figures 4-3, 4-4, and 4-5 show the GID patterns taken at x-ray incidence angles of 1°, 2°, and 5° for the Mg-W alloy on glass and Si. The Mg peaks at diffraction angles of 34.8° and 63.1° are the two major peaks that were detected. At an incident angle of 1°, the highest intensity peak was the Mg peak at diffraction angle of 63.1°. This indicated that the Mg grains were primarily aligned with the (103) plane perpendicular to the surface. Proceeding deeper into the specimen with an x-ray incidence angle of 2°, the intensity of the 63.2° peak decreased while the intensity of the 34.8° peak increased. At an incidence angle of 5°, the 34.8° diffraction angle peak, which corresponds to the (002) plane, had the highest intensity. This data revealed that the crystallographic texturing of the Mg-W alloy changes as the film is deposited.

Since the area of the glass substrate was larger than that of the Si substrate, peak intensity differences were a result of number of counts detected. To determine if the texturing was different for the Mg-W on Si or glass, the ratio of intensity between 63.1° and the 34.8° diffraction angle peaks was calculated for both substrates. This data indicated that the ratio was the same for Si and glass -- indicating that the films' texturing was independent of substrate.
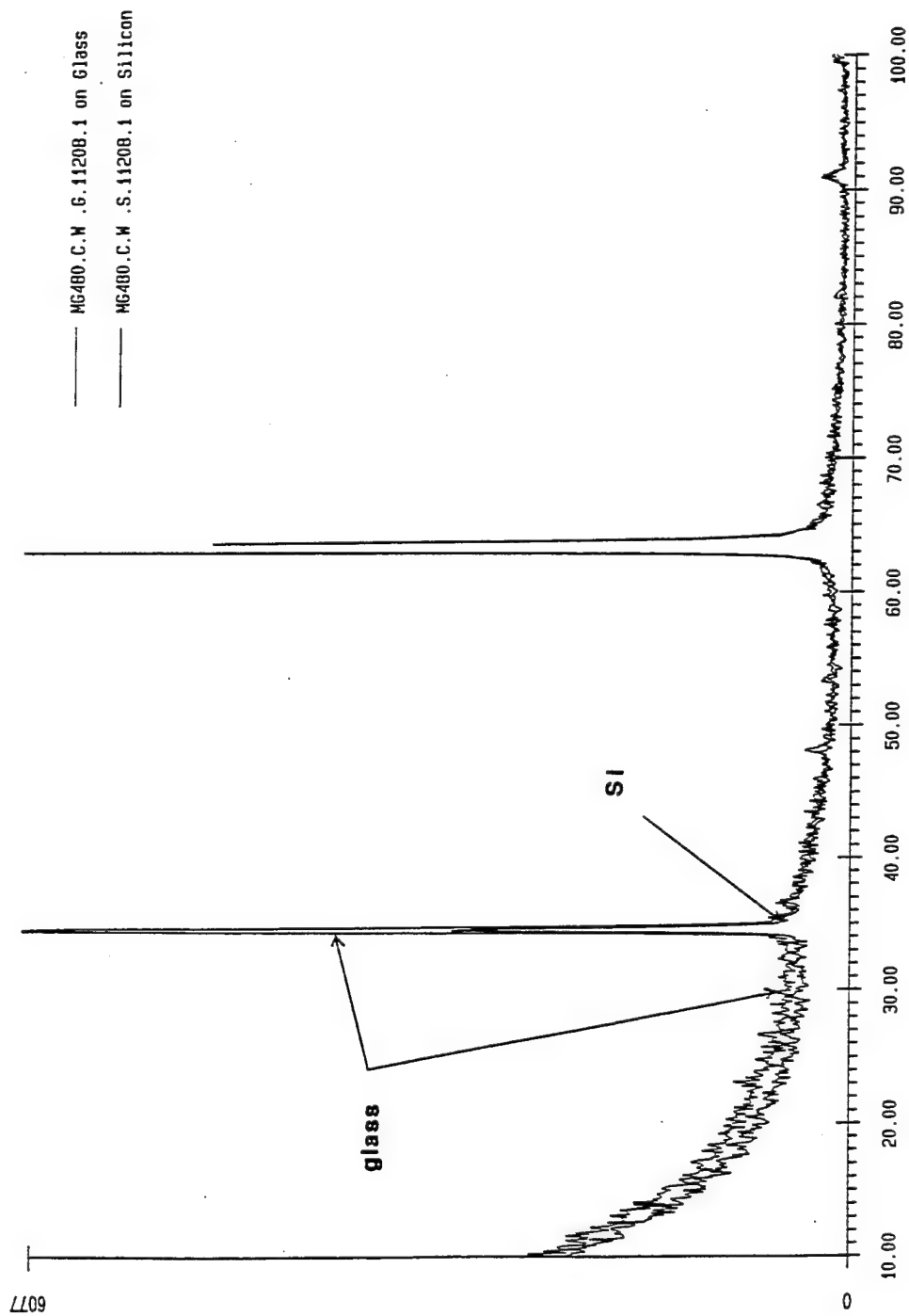
Figure 4-3. *Grazing incidence diffraction at a diffraction angle of 1° for Mg-W deposited on glass and silicon wafer substrates.*

25
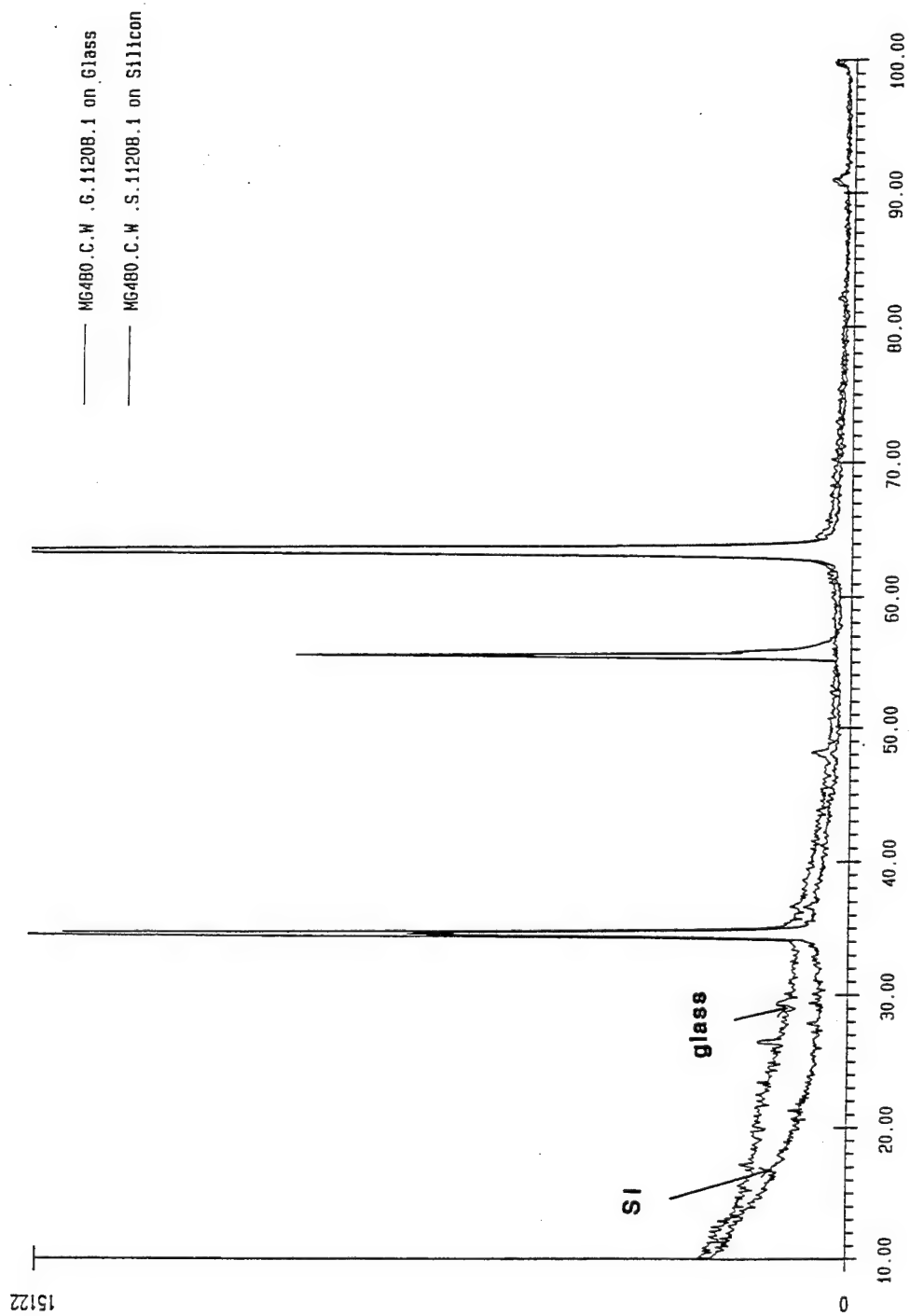
Figure 4-4. *Grazing incidence diffraction at a diffraction angle of 2° for Mg-W deposited on glass and silicon wafer substrates.*

26
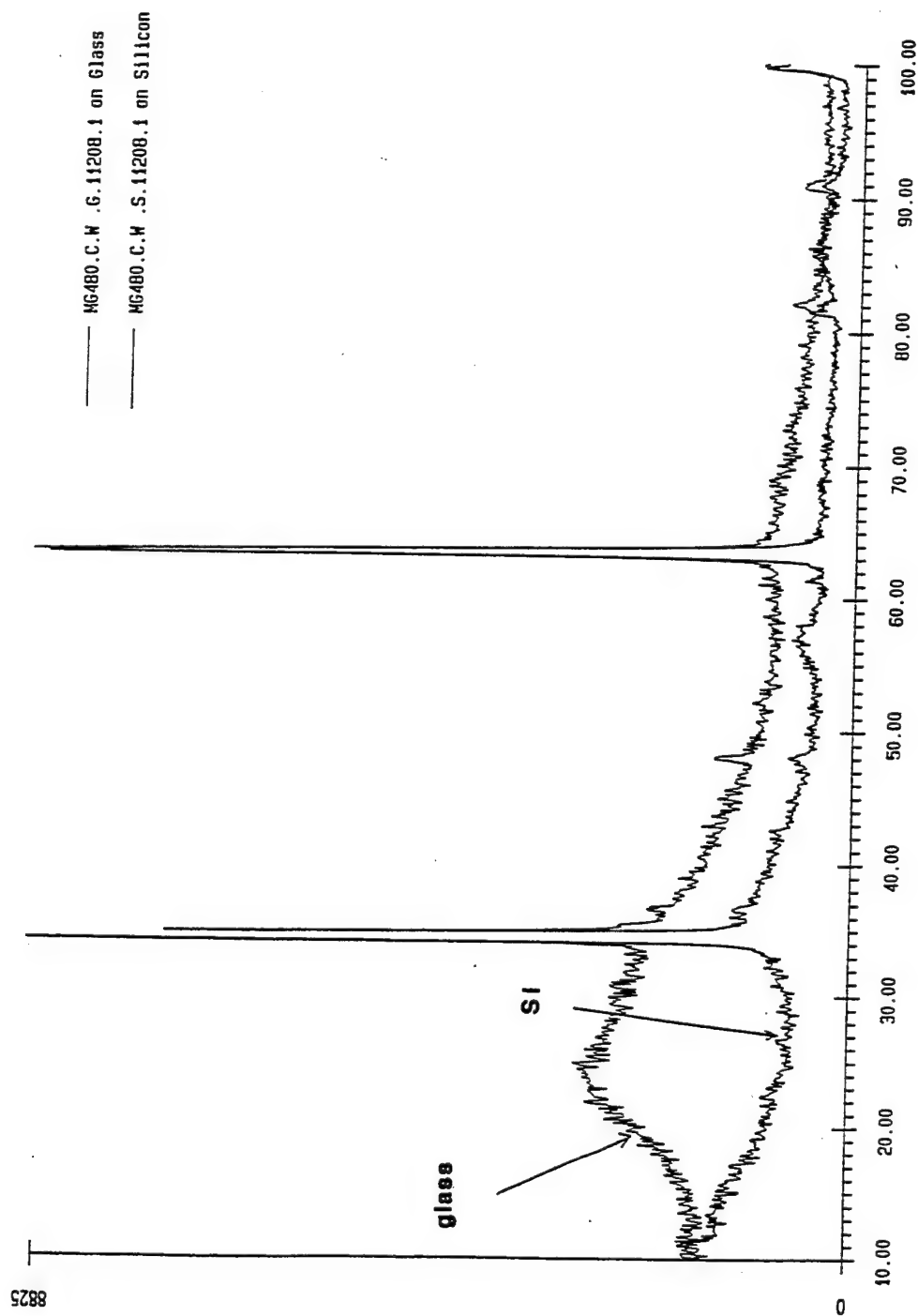
Figure 4-5. *Grazing incidence diffraction at a diffraction angle of 5° for Mg-W deposited on glass and silicon wafer substrates.*

27

4.1.5 Corrosion Behavior

4.1.5.1 Al-Transition Metal Alloys

A comparison of representative polarization curves for each of the low solute concentration alloys is presented in Figure 4-6. This figure reveals that the Al-4%W alloy exhibited the largest passive region extending from -760 to +460 mV$_{SCE}$. The next largest passive region, and the one with the lowest passive current density, was observed for the Al-4%Mo alloy. Similar pitting potentials of approximately -200 mV were observed for both the Al-3%Ta and the Al-2%Cr alloys. Figure 4-7 shows that at the highest solute concentration the pitting potential for the Al-12%Cr was shifted in the positive direction to -5 mV$_{SCE}$; whereas, the pitting potentials for the Al-26%W and the Al-26%Mo alloys were as high as +850 mV$_{SCE}$ and +625 mV$_{SCE}$, respectively. It was interesting to note that passivity was also maintained for these alloys at pH values outside the neutral pH range. Figure 4-8 and 4-9 show the anodic polarization behavior for the highest solute concentration Al-Mo and Al-W alloys in a 0.1 M chloride solution with the initial pH values adjusted to 3, 8, and 10. In both cases, the current density was the highest in the pH 3 solution.

Galvanic diagrams for the Al alloys coupled to P75 graphite are presented in Figures 4-10 through 4-13. These diagrams are based on an area ratio of 1:1 and, for comparison purposes, an anodic polarization curve for pure sputtered Al is also shown. In the case of pure Al coupled to P75 graphite, the cathodic current-limited oxygen reduction curve crosses the anodic curve in the region where pitting is observed and, as a result, relatively high corrosion rates would be expected for the Al as a consequence of galvanic coupling. For each of the aluminum alloys, the cathodic oxygen reduction curve crosses the anodic curve in the passive region resulting in low galvanic corrosion rates. These diagrams share the same limitations as anodic and cathodic polarization data for the evaluation of corrosion behavior since the actual galvanic corrosion rates can be effected by changing surface conditions which may not be predicted from short-term laboratory experiments.

All aluminum alloys were promising from a corrosion standpoint with the largest passive regions and lowest passive current densities exhibited by the Al-W and Al-Mo alloys.
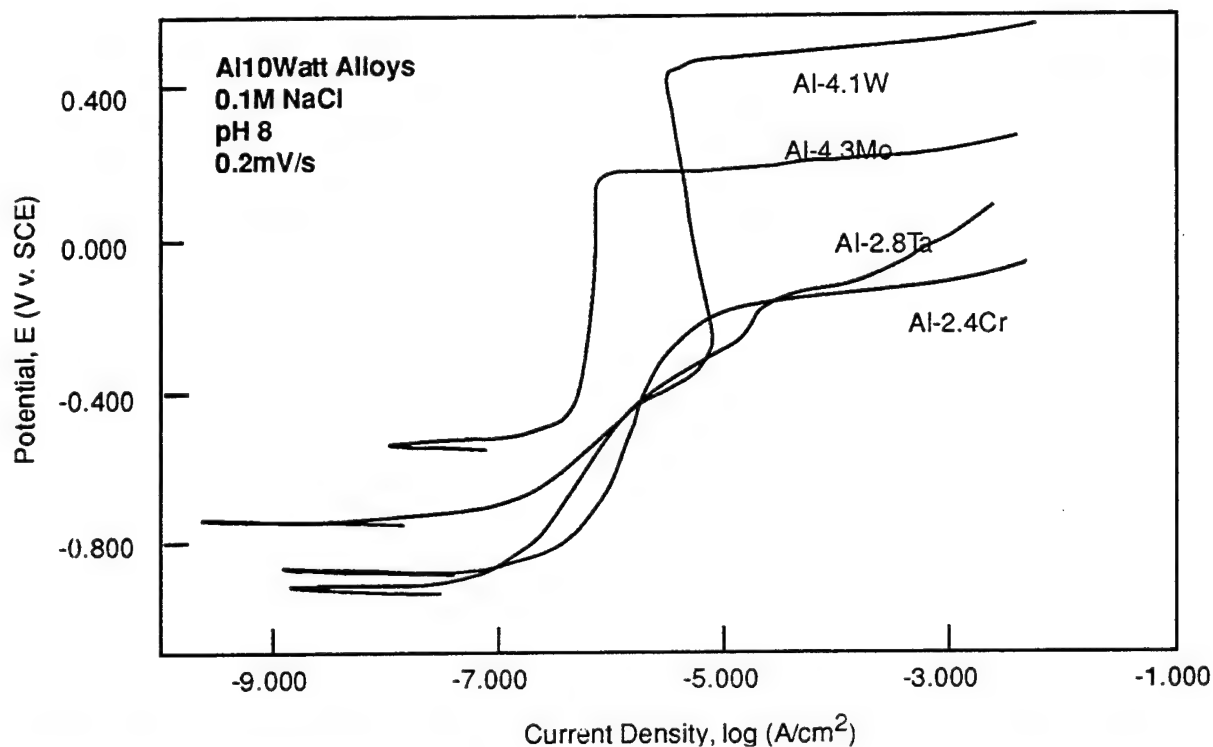
Figure 4-6. *Comparison of the anodic polarization behavior for the lowest solute concentration aluminum nonequilibrium alloys in 0.1M NaCl under quiescent conditions.*
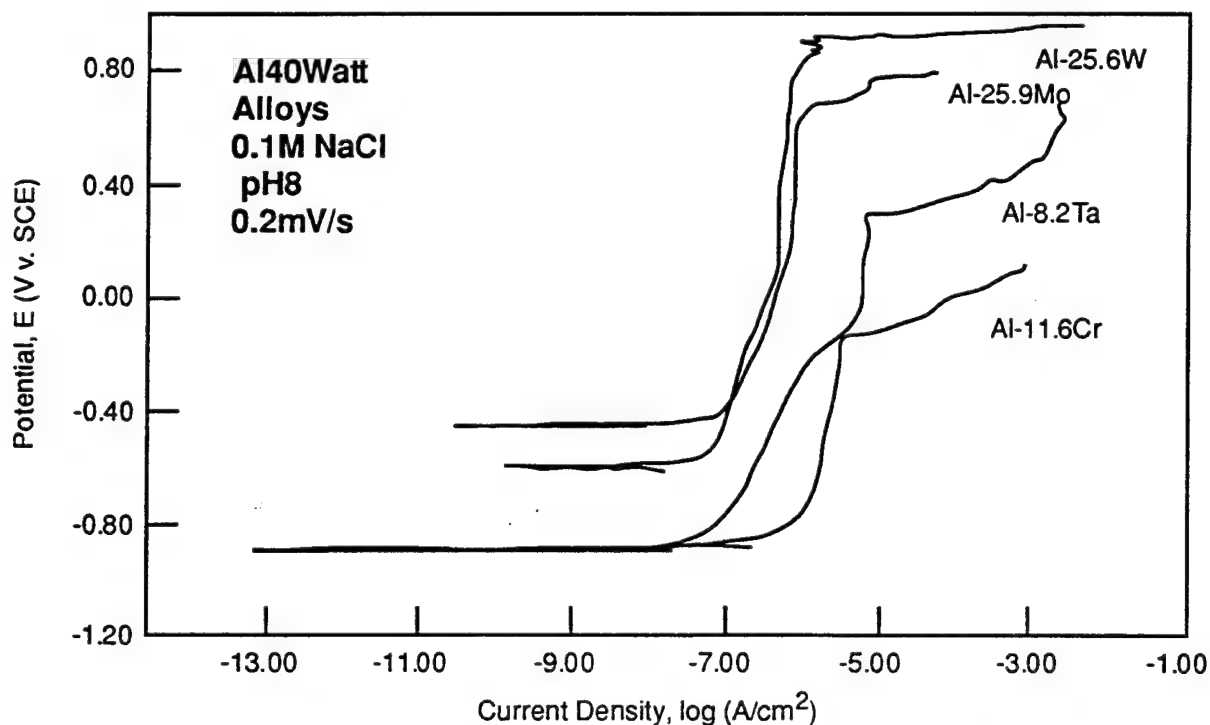

Figure 4-7. *Comparison of the anodic polarization behavior for the highest solute concentration aluminum nonequilibrium alloys in 0.1M NaCl under quiescent conditions.*
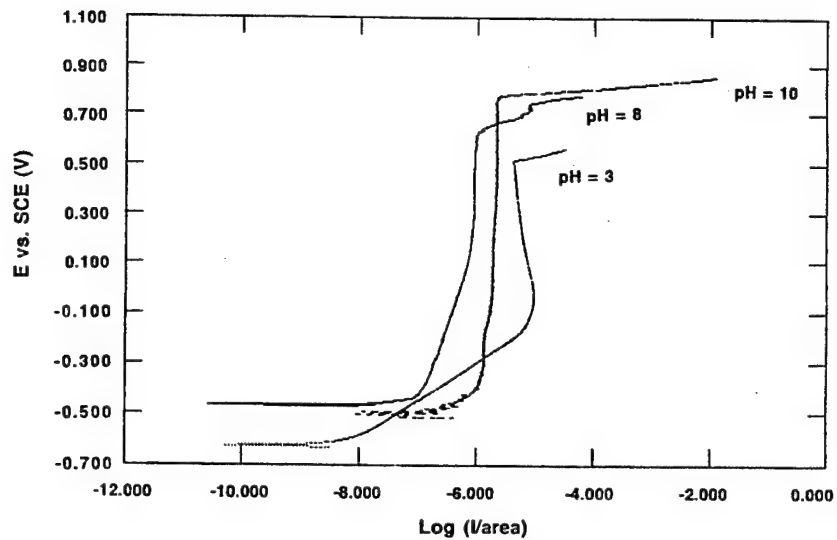
29

Figure 4-8. *Anodic polarization diagrams for the Al-26Mo alloy in a 0.1M NaCl solution with the initial pH values adjusted to values of 3, 8, and 10.*
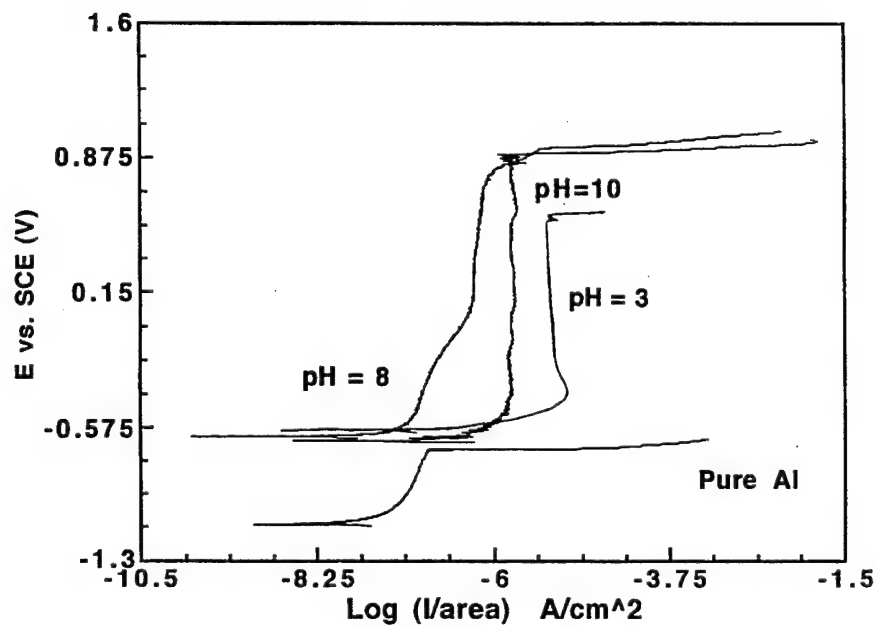
Figure 4-9. *Anodic polarization diagrams for the Al-26W alloy in a 0.1M NaCl solution with the initial pH values adjusted to values of 3, 8, and 10.*

30
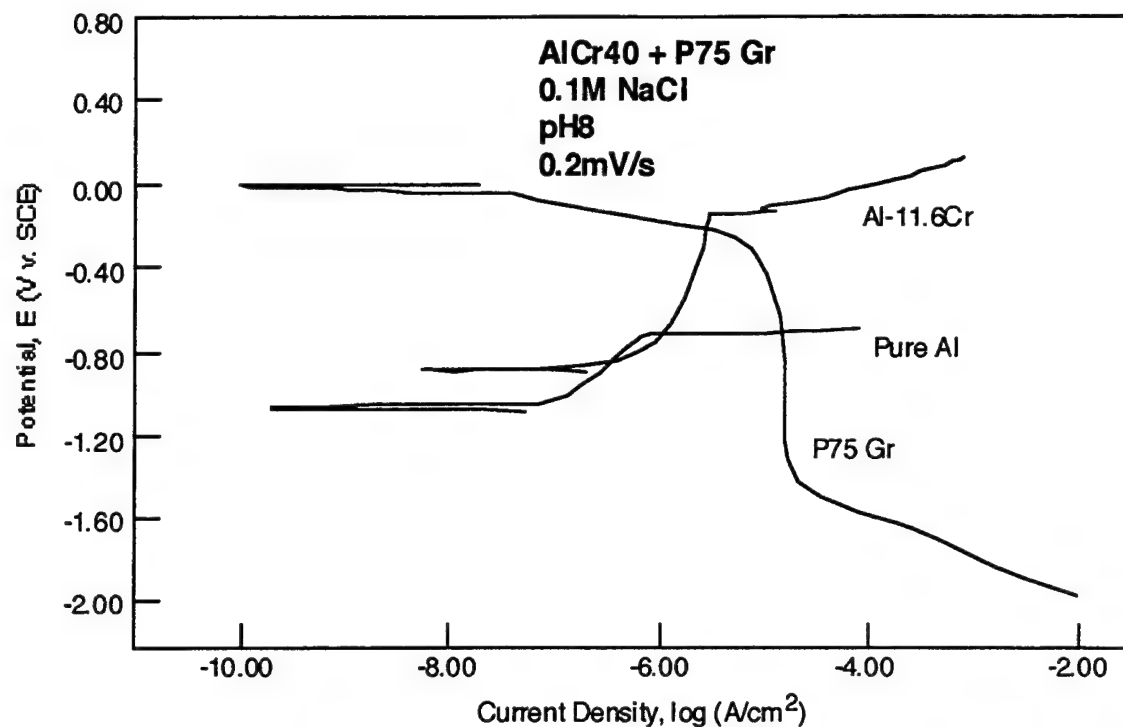
Figure 4-10. *Galvanic diagrams for pure Al and Al-12Cr coupled (individually) to P75 graphite in 0.1M NaCl.*
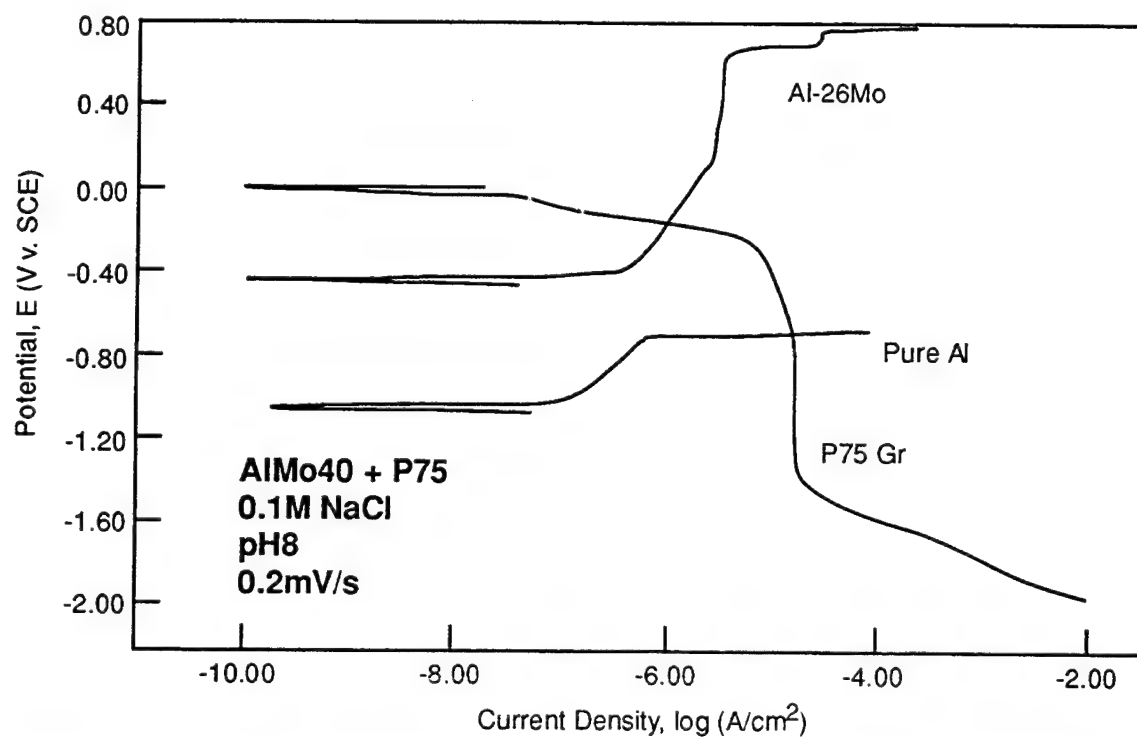
Figure 4-11. *Galvanic diagrams for pure Al and Al-26Mo coupled (individually) to P75 graphite in a 0.1M NaCl.*

31
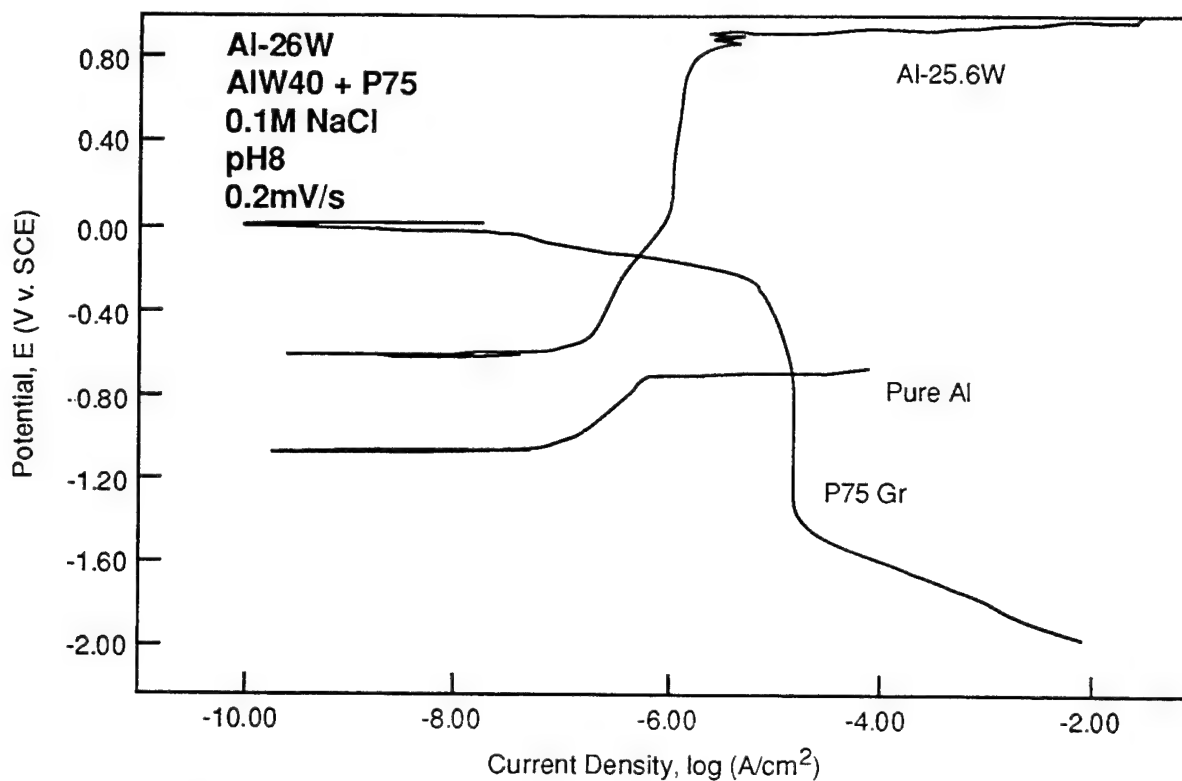
Figure 4-12 *Galvanic diagrams for pure Al and Al-26W coupled (individually) to P75 graphite in 0.1M NaCl.*
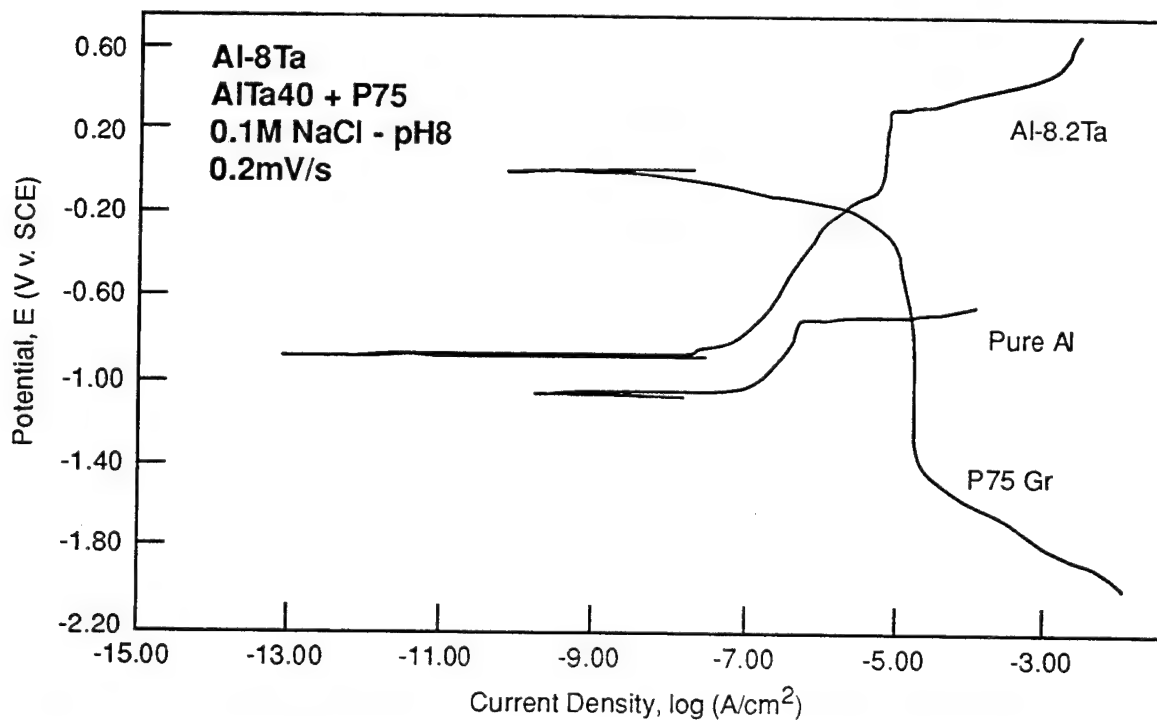
Figure 4-13. *Galvanic diagrams for pure Al and Al-8Ta coupled (individually) to P75 graphite in 0.1M NaCl.*

4.1.5.2 Mg-Transition Metal Alloys

Early in this study, binary Mg alloys with W, Cr, Ta and Mo alloying additions were fabricated. These alloys showed significant improvement over pure Mg, as can be seen in Figure 4-14. This figure shows the anodic polarization behavior of the high solute concentration alloys in a 0.1 M NaCl solution (pH initially adjusted to 8). All alloys showed increased open circuit potentials but no passivity was observed.
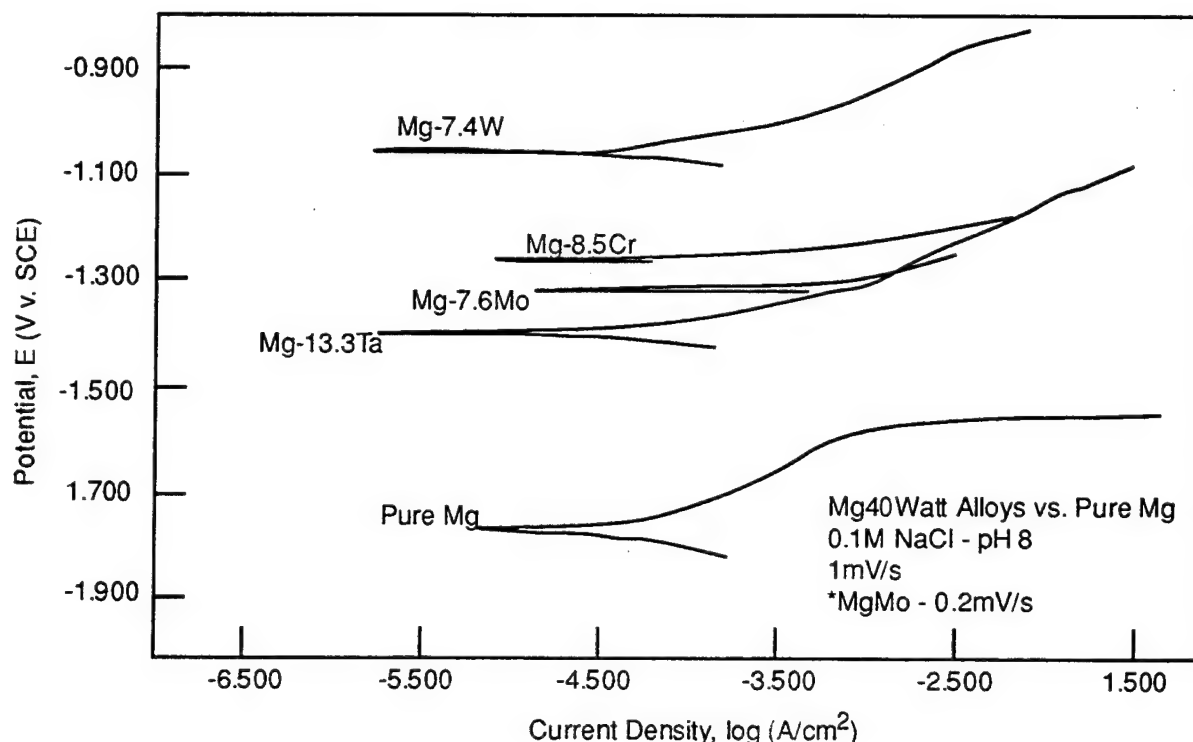
Figure 4-14 *Anodic polarization behavior for the highest concentration Mg Alloys generated at a scan rate of 0.2 mV/s in 0.1 M NaCl.*

The corrosion behavior of the Mg-Y alloys was better than that of the other binary alloys. These alloys (Mg-Y) generally had open circuit potentials comparable to pure Mg but exhibited passive or at least quasi-passive polarization behavior . Figure 4-15 shows the polarization behavior of the nonequilibrium Mg-Y alloys and WE43 in a 0.1 M NaCl solution (pH initially adjusted to 8). From this figure, it can be seen that the E_{oc} values generally increased with increasing solute concentration. It is also apparent that the passive current densities and breakdown potentials tended to decrease with increasing solute concentration. For example, the Mg-26Y alloy (highest yttrium content alloy evaluated) showed no passivity; whereas the Mg-9Y showed an **E** of -1440 mV.

A similar trend of E_{oc} increasing with increasing solute concentration was also noted for the Mg-Y alloys at pH 12. Figure 4-16 shows several of the Mg-Y alloys tested in a 0.1 M NaCl solution that was initially adjusted to a pH of 12. In contrast to the behavior noted in Figure 4-15, the two lowest solute concentration alloys exhibited the lowest E_B values at pH 12. However, the lower concentration alloys (Mg-7Y and Mg-9Y) performed poorly at this pH, exhibiting low breakdown potentials. The discrepancy in corrosion resistance for

33

the low solute concentration alloys at neutral and high pH is believed to be a result of the lower yttrium concentration in the oxide film.
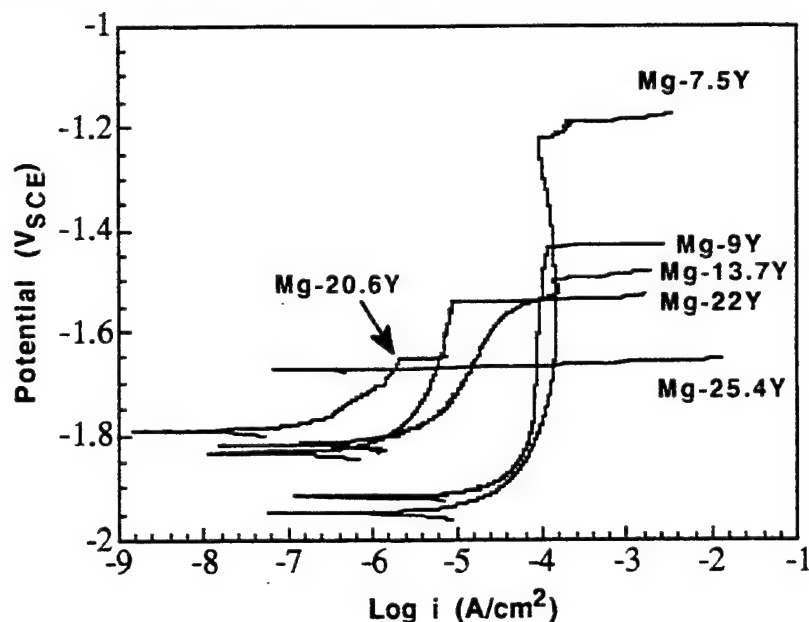

Figure 4-15. *Anodic potentiodynamic polarization behavior of the Mg-Y alloys tested in 0.1 M NaCl (pH=8) and generated at a scan rate of 0.05 mV/s.*
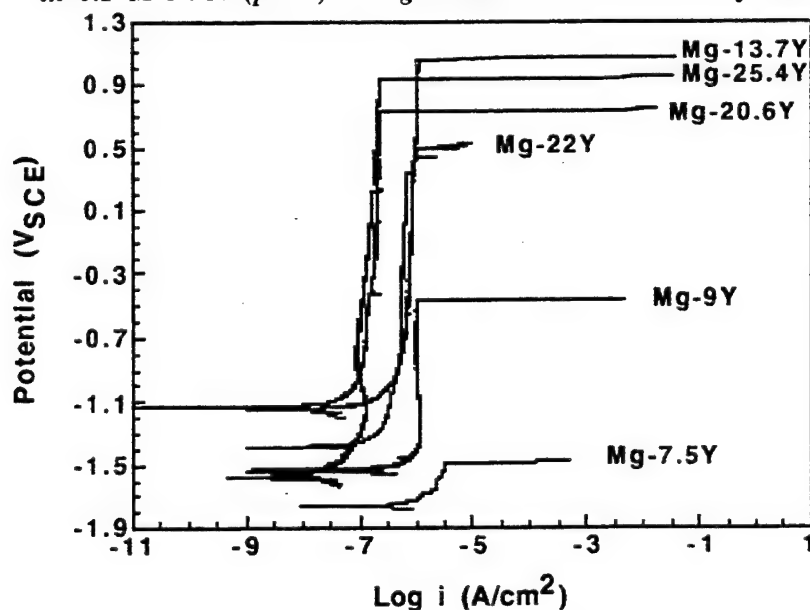

Figure 4-16. *Anodic polarization behavior for the Mg-Y alloys generated in 0.1 M NaCl (pH=12) at a scan rate of 0.05 mV/s.*

For all of the alloys, a large variation in breakdown potential was noted for specimens with the same solute concentration. This variation was especially apparent in the high pH solution because passivity was only seen at the high pH value. These variations in the breakdown potential are believed to be a result defects introduced during sputter deposition or preparation preparation of the electrochemical specimens. Figure 4-17 shows example of pit initiation on a scratch in a Mg-Y alloy. Pit initiation has also been observed on defects in sputtered Al and nonequilibrium Al alloys.
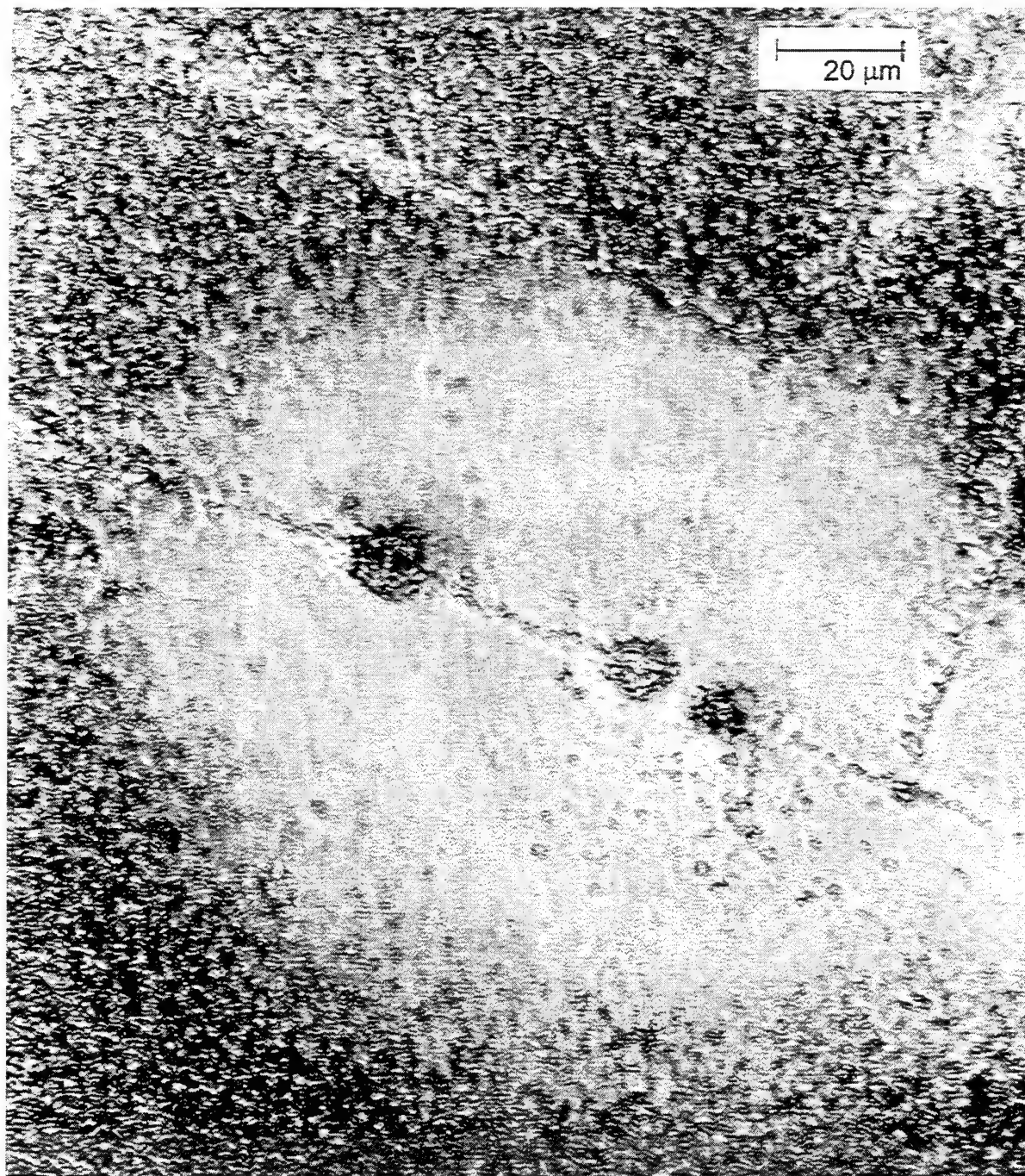
Figure 4-17. Scanning laser micrograph of a Mg-Y alloy showing pit initiation along a scratch in the alloy. (The specimen was anodically polarized in 0.1M NaCl)

Since the goal of this research was to develop nonequilibrium alloys for use in graphite-reinforced composites, galvanic current diagrams were constructed for the Mg-22Y, and Mg-25.4Y alloys coupled to P75 graphite in a 0.1 M NaCl solution (with the pH initially adjusted to 12). This diagram is shown in Figure 4-18 and reveals that the anodic polarization curve intersects the cathodic curve for graphite in the limiting current density region of the cathodic curve. In contrast, the hydrogen evolution region of the cathodic curve for graphite intersects the anodic polarization curve for Mg at high current densities. The galvanic behavior of pure Mg and Mg-7.6 Mo are shown in Figure 4-19. These curves were generated in a 0.1 M NaCl solution with a pH of 8.
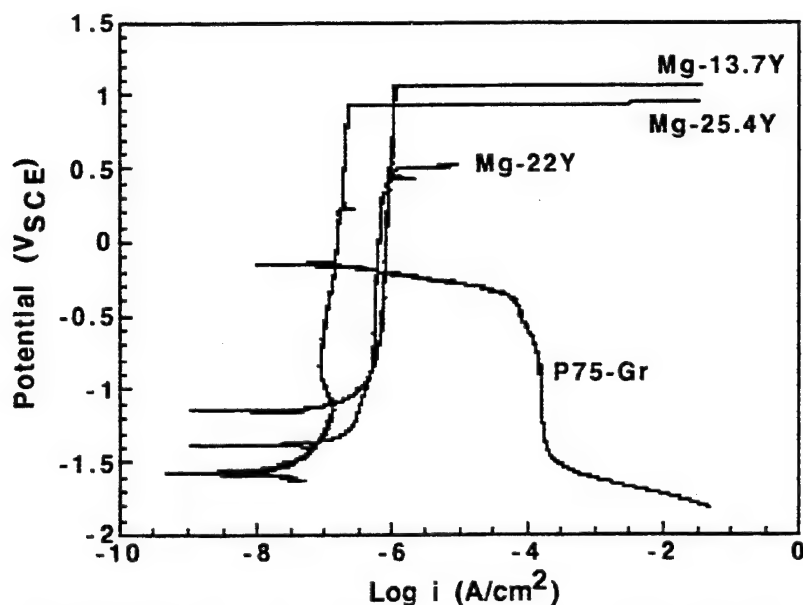
Figure 4-18 *Galvanic diagram for Mg-13.7Y, Mg-22Y, and Mg-25.4Y coupled (individually) to P75-Gr. Curves were generated in 0.1 M NaCl (pH=12) at a scan rate of 0.05 mV/s.*
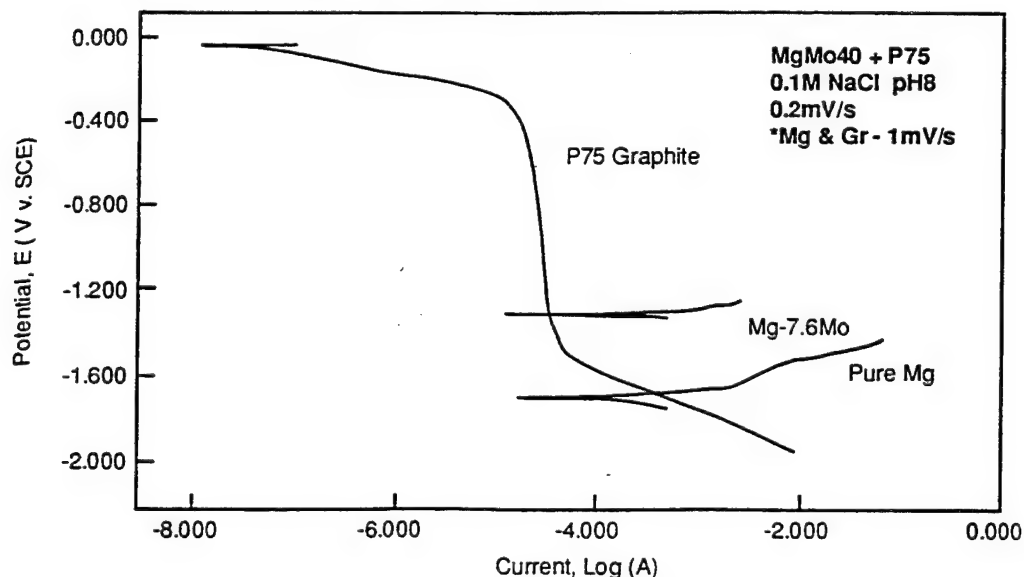

Figure 4-19 *Galvanic diagram for pure Mg and Mg-7.6Mo coupled (individually) to P75 graphite. Curves were generated in 0.1M NaCl.*

4.1.5.3 Inhibitive Treatments

In addition to the composites work, a small investigation into the use of inhibitive treatments as a means for enhancing the corrosion resistance of magnesium was added to the program during the first year. The inhibitors investigated in this segment of the program were chosen based on the earlier work of Mansfeld [51,52] and Shaw et al.[53] on stand-alone Ce-based and Mo-based inhibitive treatments for Al. The specific inhibitors used in the treatments described in this report were cerium chloride, cerium nitrate hexahydrate, cerium fluoride, yttrium nitrate pentahydrate and sodium molybdate. Research on the Mg-Y non-equilibrium alloys, presented in the previous section, led to the investigation of the Y-based treatment.

Variations of the treatments were examined to maximize the effects of treatment time and temperature, as well as pH effects. After some initial experiments, sequential treatments were evaluated and the effects of treatment order were also studied.

The electrochemical technique used to screen the performance of the candidate treatments was anodic potentiodynamic polarization. Once the best candidate was identified in these screening tests, EIS was used to non-destructively evaluate the long-term performance of the treatment and provide information about the resistive and capacitive nature of the protective film. Scribed specimen testing was also conducted to determine the effectiveness of the coating when damaged (scribed). Cathodic scans were performed to verify whether the inhibitor was primarily influencing the anodic reaction, the cathodic reaction, or both reactions.

4.1.5.3.1 Anodic and Cathodic Potentiodynamic Results

Initially, a combination of cerium nitrate, then cerium chloride, then sodium molybdate was applied to improve the corrosion resistance of pure magnesium in chloride containing environments. These tests indicated that the cerium chloride had no beneficial effect. Further research indicated that the other four compounds studied did enhance the resistance of magnesium, with the most beneficial treatment being cerium fluoride. Table 4-4 lists the optimum parameters for each of the treatments studied. Polarization scans for each of these treatments can be seen in Figure 4-20.

Table 4-4.   *Optimum Parameters for the Inhibitive Treatments used on Magnesium.*

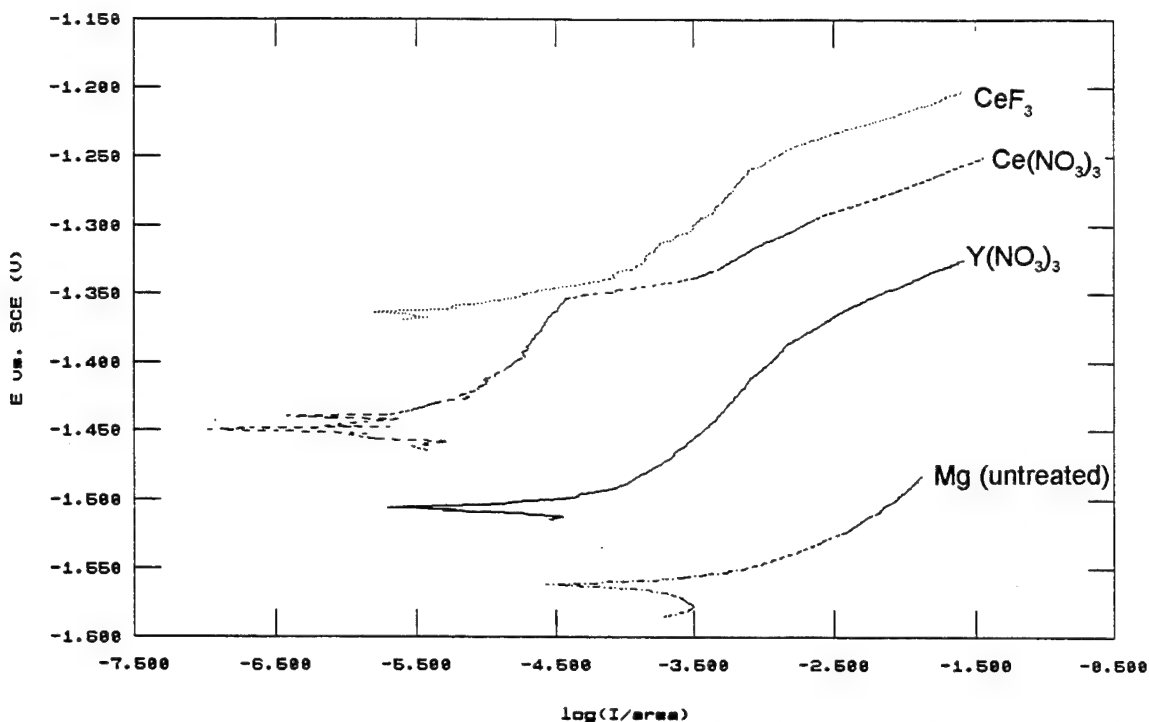| Treatment	Concentration(mM)	Temperature (°C)	pH	Time (h)
$Ce(NO_3)_3$	10	100	10	4
$Y(NO_3)_3$	10	60-70	natural	2
CeF_3	1	60-70	natural	4
Na_2MoO_4	100	room	natural	2

Figure 4-20. Anodic polarization scans for Mg following each of the optimum treatments. Polarization data was generated in 0.1M NaCl at a scan rate of 01 mV/s.

Since the cerium fluoride treatment produced the best results, this exact same treatment was also applied to WE43. The cerium fluoride treatment improved the corrosion resistance of this alloy; however, the improvement was not as significant as that noted on the pure Mg, as can be seen in Figure 4-21. It is important to emphasize that the treated magnesium performed better than either the treated and untreated WE43 (which is one of the most corrosion resistant Mg alloys).
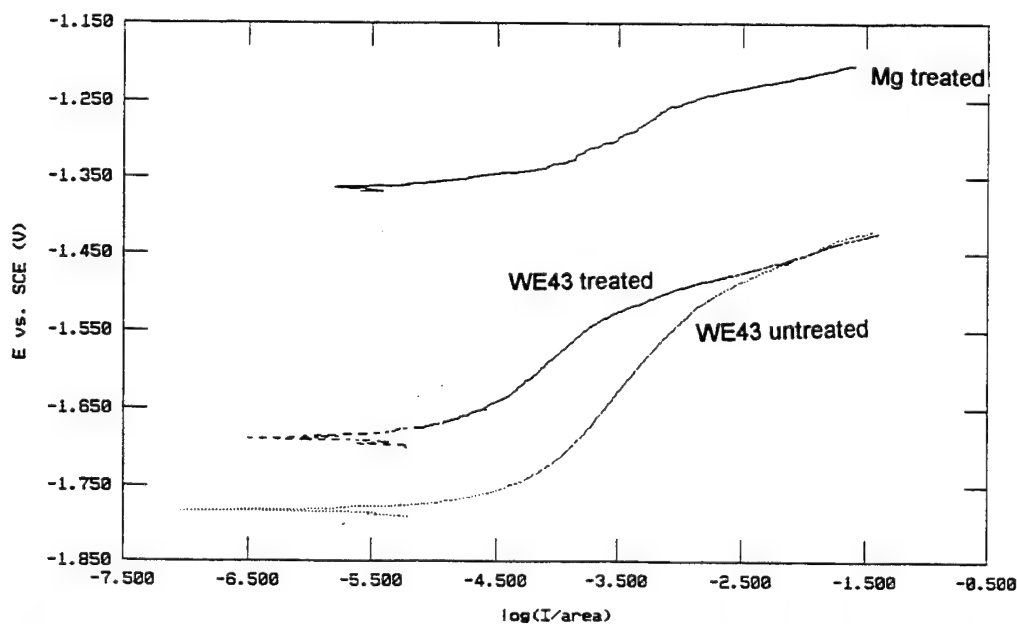
Figure 4-21. Anodic polarization scans for untreated WE43 and pure Mg and WE43 treated with cerium fluoride. Curves were generated in 0.1M NaCl at a scan rate of 0.1 mV/s.

38

Cathodic potentiodynamic polarization scans were generated on Mg specimens with and without the cerium fluoride treatment to verify that the inhibitive treatment had a stronger influence on the anodic reaction than on the cathodic reaction. The results, as seen in Figure 4-22, verified that the inhibitive treatment functioned more as an anodic inhibitor than a cathodic inhibitor.
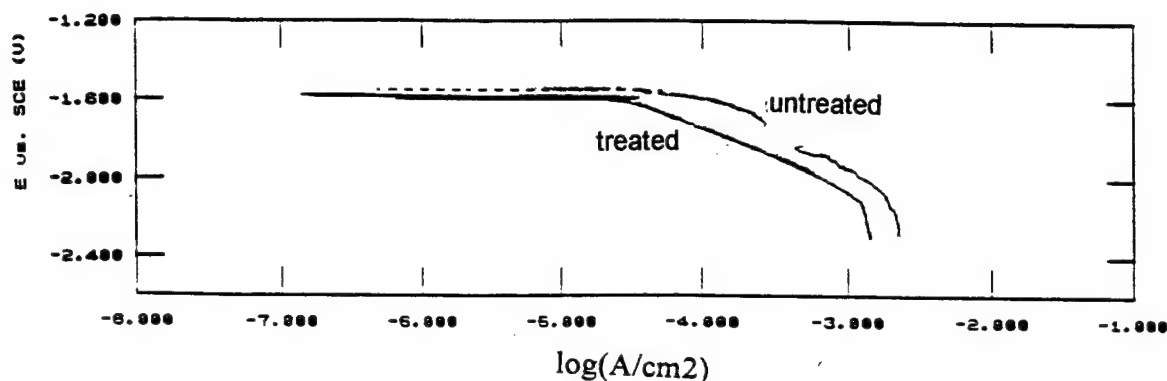

Figure 4-22. Cathodic polarization scans for untreated Mg and pure Mg treated with the optimum treatment. Curves were generated in 0.1M at a scan rate of 0.1mV/s.

4.1.5.3.2 Electrochemical Impedance Spectroscopy Results

The EIS data generated on the Mg treated with the cerium fluoride supported the results obtained in the anodic potentiodynamic experiments and showed that the cerium fluoride treatment did indeed improve the corrosion resistance of pure Mg and WE43. Simple Randles circuit behavior was noted for the pure Mg in the chloride environment ;whereas the cerium fluoride treated magnesium showed a more complicated response containing 2 time constants (Figure 4-23). The EIS spectra for untreated WE43 also showed 2 time constants. These results suggest the formation of a protective film or deposit on the surfaces of the treated pure Mg and the untreated WE43. The film formed on the treated Mg appears to be significantly more protective than the layer that forms naturally on the untreated WE43.
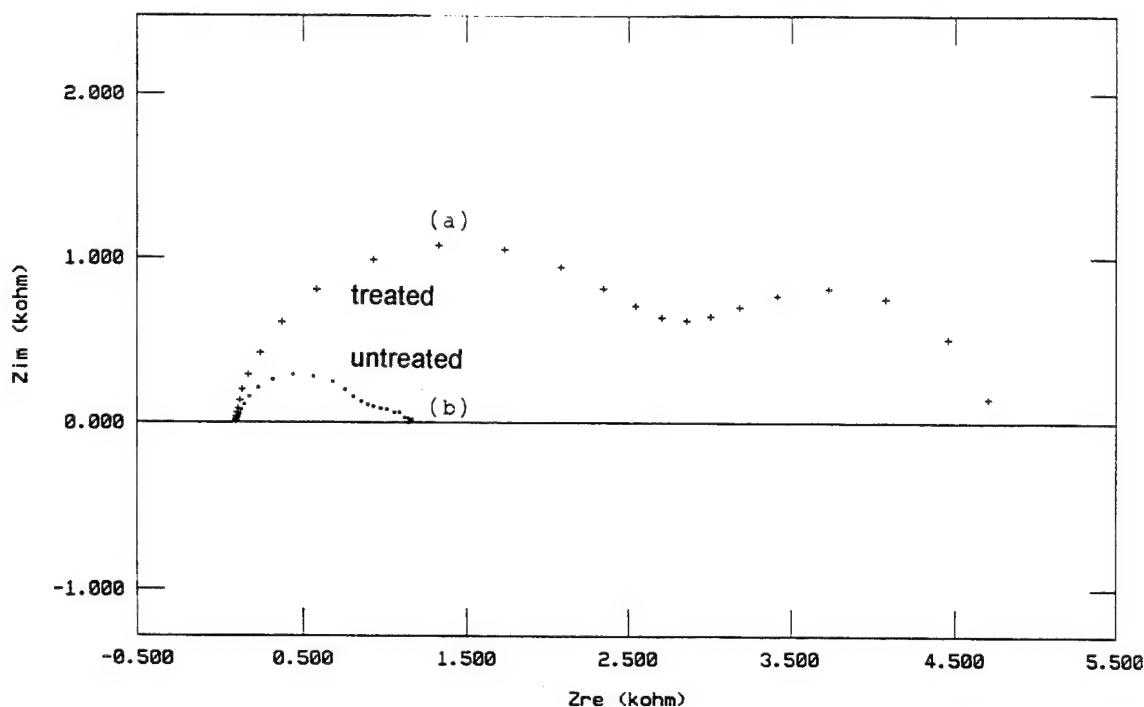
Figure 4-23. Electrochemical impedance spectra for treated and untreated pure Mg in cerium fluoride.

The reactions occurring at the surface of a specimen immersed in a chloride environment can be examined and portrayed by resistive-capacitive electrical circuits. The equivalent circuit model identified for the treated materials in this research is presented in Figure 4-24. A simple Randles circuit is also shown since the behavior for untreated magnesium in a chloride environment can be modeled with this circuit. In this figure R_{sol} represents the resistance of the solution containing the specimen. R_{CT} is the charge transfer resistance; this is also known as R_p, polarization resistance. C_{DL} is the capacitance of the double layer. R_{coat} and C_{coat} are the resistance and capacitance, respectively, of the coating.

EIS spectra were obtained after one hour, one day and one week of exposure to 0.1 M NaCl. For treated magnesium, the results after exposure for one hour were better than those obtained after exposure for one day, as were the results after one day better than the results after one week. The long term results imply that the protective film dissolves with continued exposure to the corrosive environment . Table 4-5 presents the equivalent circuit parameters for these three exposure times. R_{sol}, the solution resistance, is constant, as was expected. R_{coat}, the coating resistance, decreases as the length of exposure increases. This shows that the film is less resistant to corrosion after greater lengths of exposure; the film is degrading with time. C_{coat}, the coating capacitance, which is inversely proportional to coating thickness, increased as the length of exposure time increased, showing that the film thickness was decreasing. R_p, the polarization or charge transfer resistance, is inversely proportional to i_{corr} (current density) and current density is directly proportional to corrosion rate. In this research, R_p decreased over time which in turn means that i_{corr} and hence the corrosion rate, increased with the exposure time.
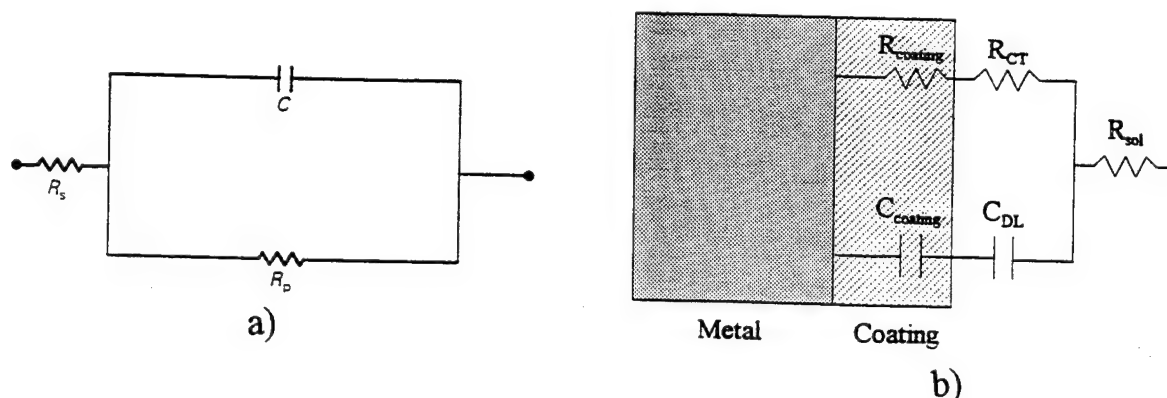
40

Figure 4-24. Equivalent circuit models used in this study for a) untreated and b) untreated Mg.

Table 4-5. Impedance Parameters Obtained From Fitting EIS Spectra With Equivalent Circuit Shown in Figure 4-30.

Parameter	After one hour	After one day	After one week
R_{sol} (ohms)	1.007×10^2	1.071×10^2	9.475×10^1
R_{coat} (ohms)	6.091×10^3	2.156×10^3	5.327×10^2
C_{coat} (mohms)	1.099×10^{-5}	1.429×10^{-5}	2.288×10^{-5}
R_p (ohms)	1.763×10^3	1.709×10^2	1.365×10^2
C_{DL} (mohms)	2.018×10^{-4}	9.225×10^{-3}	3.728×10^{-5}

4.1.5.3.3 Scribed Specimen Testing

Scribed specimen testing was conducted to determine the effectiveness of the deposit when damaged (scratched). After the inhibitive treatment was applied and prior to polarization in a 0.1M chloride solution, panels with the best treatment identified from anodic polarization were scribed with the sharp point of a glass rod. The scribe was made in the shape of an X and cut deep enough into the surface to reach the untreated metal underneath. For pure magnesium, the scratch coating showed some improvement over untreated Mg, but the polarization behavior was not nearly as good as that of the unscratched coating. The scratch treated WE43 showed an improvement over untreated WE43. Both materials showed preferential corrosion along the 'X' mark, as most would predict.

4.2 Phase 2: Alloy Selection for Further Studies

Up to this point, the key factors used to evaluate suitability of the candidate alloys for use in graphite-reinforced composites were corrosion resistance and thermal stability. However for aerospace structures, alloy density and coefficient of thermal expansion (CTE) compatibility with the graphite fibers are also of importance. In order to reduce the number of alloys tested in phase 2 of this investigation, alloy density and CTE compatibility with graphite were given equal merit in choosing alloys for further consideration. A summary of the important attributes of the candidate alloys is presented in this section.

Corrosion Resistance -- All of the binary aluminum alloys and some of the magnesium alloys investigated in the initial stage of this program showed enhanced corrosion resistance when compared to their unalloyed counterparts. In general, as the concentration of the alloying additions in the Al-based alloys increased, the open circuit and breakdown potentials increased. At solute concentrations of 26%, the Al-W and Al-Mo alloys exhibited breakdown potentials as high as +850 mV and +770 mV, respectively.

For the magnesium-based alloys, tantalum and yttrium showed the greatest influence in enhancing corrosion resistance. Unfortunately when these alloys were coupled to graphite in a neural pH solution, the cathodic reaction controlled the corrosion rate and high corrosion rates were observed.

From a corrosion standpoint the aluminum alloys with either tungsten or molybdenum alloying additions showed the best potential for use as corrosion resistant matrices in graphite-reinforced metal matrix composites.

Density -- The density of the alloys can be determined using the following equation:

$$\rho_T = \frac{w_1 + w_2}{V_T}$$

Where ρ_T is the alloy density, w_1 and w_2 are the weight of each element in the alloy and V_T is the total volume. This equation can not be solved directly, but assuming that the solute substitutes for Al or Mg atoms in the lattice without introducing a significant volume change, the alloy density can be rewritten as:

$$\rho_T = \rho_1 x_1 \frac{n_1 a_1^3}{n_1 a_2^3} + (1 - x_1)\rho_2$$

where ρ is the density, c is the atomic percent of the solute in the alloy, n is the number of atoms in the unit cell for the pure element, a is its lattice constant, and 1 and 2 denote the solute and base metal (Mg or Al), respectively, in the alloy. The assumption of a small volume change should only lead to a small error due to the close relative atomic size of the transition metals with Al. The error will be much more significant for the Mg alloys. Solving for density with this relationship was relatively simple and the results are plotted in Figure 4-25. For example, in the case of an alloy containing 20 atomic percent W, the density of the alloy would be approximately 5.8 g/cm^3. Molybdenum, with a density of only 10.28 g/cm^3, would produce an Al-20 atomic percent Mo alloy with a density of 4.1 g/cm^3, and at 10 atomic percent Mo the density would be 3.5 g/cm^3. From a weight standpoint, the Al-Mo alloys would have a significant advantage.
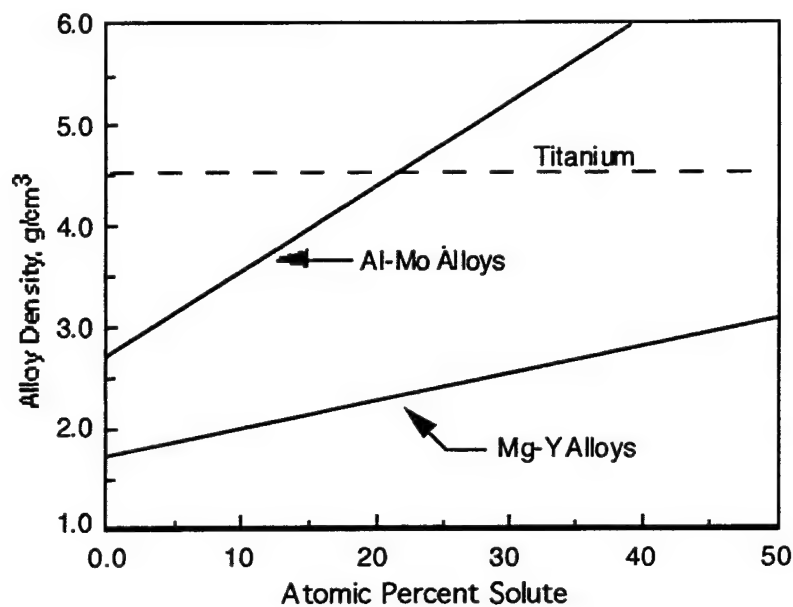
Figure 4-25. Density for Al-Mo and Mg-Y alloys showing maximum solute concentration for the alloy to remain lighter than titanium.

Thermal Stability -- XRD results suggest that the nonequilibrium Al alloys are more stable with higher concentrations of solute in the alloy. This result is surprising and not intuitively obvious, because it would be logical to conclude that a higher concentration of solute would increase the kinetics of precipitation, particularly above $0.5\ T/T_m$, where bulk (volume) diffusion processes begin to become significant. Heat treating at 400°C (~ 0.7 $T/T_{m)}$ would be expected to precipitate the supersaturated solute, and this was found to be true below approximately 10 atomic percent solute. Above this solute concentration, many of the Al alloys, with the exception of the Al-Cr and the Al-Ta alloys, remained stable. From the thermal stability standpoint, the Al-W and Al-Mo alloys showed the best stability at composite consolidation temperatures.

Thermal Expansion -- Large differences in the CTE between the fiber and the matrix will result in the introduction of large residual stresses during cooling. Clearly the effect of residual stress is undesirable, both from a consolidation standpoint and from a long-term durability standpoint. Large residual stresses exceeding the fracture strength of the alloy can result in cracking of the composite. High residual stresses can also promote stress corrosion cracking in aggressive environments and reduce the fatigue life of the metal. Fortunately, the addition of transition metals to Al or Mg reduces the values of their coefficients of thermal expansion, thereby reducing microstrain. The limitation to this approach is that too much transition metal can lead to an alloy with an amorphous structure, which would have a difficult time relieving stresses by yielding. Therefore, final alloy selection must not only be based on the corrosion behavior of the alloy, but also on the processability and fabricability of the alloy.

Alloy Selection -- Based on the reasons cited above, an Al-Mo alloy with a solute concentration of greater than 10 atomic percent (to achieve the corrosion resistance and thermal stability) and less than 25 atomic percent(to maintain the density less than titanium) was chosen for use in phase 3 of the program.

4.3   Phase 3:   Composite Development

After Al-Mo was selected as the most suitable alloy for Gr/Al composites, the Al-Mo system was studied in detail to determine the optimum solute concentration before the alloy was deposited onto graphite fibers. The optimum solute concentration was chosen based on the following factors: extent of enhanced passivity, galvanic compatibility with graphite, corrosion performance after heat treatment at anticipated consolidation temperatures and density of the alloy. Results of this more detailed investigation are presented in this section of the report.

4.3.1   Al-Mo Alloy Development

To obtain Mo solute concentrations between 10 and 25 atomic percent, the Mo was sputtered at low power settings while the Al power was held constant at 485 W (RF mode). For example, while holding the Al power at 485 W (RF), the Mo target was held at 20 W (DC) to achieve an alloy with 12 atomic percent Mo. Similarly, the Al alloy with 20 atomic percent Mo required a cathode power setting of 40 W (DC).

Alloys were sputtered for 60 minutes to achieve an average thickness between 1 and 2 microns. One thicker alloy foil was sputtered for about 100 hours to obtain a final thickness of approximately 0.1 mm (4 to 5 mils). Each alloy exhibited a highly reflective metallic appearance indicating low levels of contamination. Some small inherent defects including scratches, low density areas, and blisters were noted when the alloys were examined under a microscope. After heat treating, most of the alloys retained their specular appearance. In a few cases, after heat treatment the alloy yellowed slightly or turned fluorescent blue. The Al-Mg-Mo alloys heat treated at 500°C exhibited a grainy appearance.

4.3.2   Compositional Analysis

Compositions of the Al-Mo and Al-Mg-Mo alloys produced in this phase of the investigation (measured by semi-quantitative EDS) are listed in Table 4-6 along with the predicted values. Examination of this data revealed good correlation between the predicted composition and the semi-quantitative EDS values. For a few alloys, the Mo concentration was much higher than predicted. For example alloy 6 in the table, which was sputtered using a 20 W (DC) power setting on the Mo target and 480 W (RF) setting on the Al target, had a measured Mo concentration of almost 18 atomic percent; whereas, the predicted Mo concentration was only ~12 atomic percent. This discrepancy was attributed to excessive heating of the magnets in the Al cathode during high power operation. As the magnets overheat, the magnetic strength decreases and plasma confinement on the target is reduced, resulting in a decrease in sputtering rate. The Mo deposition rate was measured after several sputter runs and there was no change. Although the new rate for Al was not measured, the rate of Al was estimated to be 0.20 to 0.22 nm/s (by substituting the measured composition into preceding rate equation given earlier). This represents a reduction of 0.06 to 0.08 nm/s from the rate obtained using new magnets. Alloy 10 in Table 4-6 was fabricated for mechanical property evaluation. This alloy had a thickness of 0.1 mm   (0.004 in.) and a Mo concentration of 14 atomic percent. Since the EDS composition values were thought to be more representative of the actual alloy composition that the calculated values, the EDS compositions were used in this section.

44

Over the course of this research, several alloys were fabricated, corrosion tested, and heat treated for XRD examination. The last five alloys in Table 4-6 (three binary Al-Mo and two ternary Al-Mg-Mo) underwent an extensive evaluation of the effects of heat treating including XRD examination and electrochemical corrosion testing.

Table 4-6.   Predicted and Measured Composition of the Al-Mo Alloys.

| Alloy # | Alloy Designation | Alloy Composition (atomic percent) | |
		Predicted	EDS
1	Al480.C.Mo10.S.10825.1	4.3 Mo	-
2	Al480.C.Mo20.S.10825.1	12.3 Mo	-
3	Al480.C.Mo40.S.10825.1	19.6 Mo	25.6
4	Al480.C.Mo40.S.20126.1	19.6 Mo	19.1 Mo
5	Al480.C.Mo10.S.20709.1	4.3 Mo	10.8 Mo
6	Al480.C.Mo20.S.20709.1	12.3 Mo	17.7 Mo
7	Al480.C.Mo40.S.20709.1	19.6 Mo	23.4 Mo
8	Al480.C.Mg65.C.Mo20.S.20714.1	20.0 Mg, 9.8 Mo	12.1 Mg, 13.4 Mo
9	Al480.C.Mg52.C.Mo20.S.20720.1	14.3 Mg, 10.5 Mo	10.5 Mg, 11.0 Mo
10	Al480.C.Mo20.Cu.20720.1	12.3 Mo	14.0 Mo

4.3.3 X-Ray Diffraction Results for the Al-Mo Alloys

XRD was conducted on both as-sputtered and heat treated Al-Mo alloys to determine whether the Mo (1) was in solid solution in the Al and readily available for enhancing corrosion resistance or (2) had reacted with the Al to form Al_xMo_y intermetallic compounds during the sputtering process. To delineate the onset of precipitation as a function of solute concentration, Al-11Mo, Al-18Mo, Al-23Mo binary alloys and an Al-11Mg-10Mo ternary alloy were sputtered and subjected to a heat treatment matrix of three temperatures (400°C, 500°C and 600°C) for three times (1, 2, and 8 hours). Indexing the peaks in alloys that contained precipitates was difficult because the preferential growth of the sputtered alloys changed peak intensity ratios and some peaks were not present in the XRD spectrum. In addition, by intermixing the Al and Mo on the atomic level via sputtering, the precipitation process was approached from a different starting point than previous investigations of the Al-Mo system by powder metallurgy, melting, or diffusion couples. As a result, phases that were expected from the literature often were not detected. Table 4-7 summarizes the XRD results for the heat treated Al-Mo alloys.

Table 4-7. *Summary of Al-Mo Alloy Structure as a Function of Heat Treatment Time and Temperature.*

Heat Treatment Temperature

	400°C	500°C	600°C
1	Al-11Mo, ppt Al-18Mo, Amorphous Al-23Mo, Amorphous	Al-11Mo, ppt Al-18Mo, ppt Al-23Mo, Amorphous	Al-11Mo, ppt Al-18Mo, ppt Al-23Mo, Amorphous
2	Al-11Mo, ppt Al-18Mo, Amorphous Al-23Mo, Amorphous	Al-11Mo, ppt Al-18Mo, ppt Al-23Mo, Amorphous	Al-11Mo, ppt Al-18Mo, ppt Al-23Mo, Amorphous
8	Al-11Mo, ppt Al-18Mo, Amorphous Al-23Mo, Amorphous	Al-11Mo, ppt Al-18Mo, ppt Al-23Mo, Amorphous	Al-11Mo, ppt Al-18Mo, ppt Al-23Mo, ppt

Heat Treatment Time (h)

Figure 4-26 shows the XRD spectra for the Al-11Mo alloy after heat treatment at 400°C for 1, 2, and 8 hours. The as-deposited Al-11Mo alloy exhibited well defined peaks that correspondedi to Al, which had shifted to slightly higher angles. Although the ratio of peak heights was not consistent with the reported values for polycrystalline Al, indicating the alloy had grown along preferential orientation, this was the only Al-Mo alloy fabricated during this phase of the investigation that was crystalline. A lattice parameter of 0.4004 nm was calculated from the Al (111) peak, which was shifted from the normal angle of 38.4° to 38.94°. This peak shift was consistent with the Mo being in solid solution with the Al.

After heat treating the Al-11Mo alloy at 400°C for 1, 2, and 8 hours, several new peaks formed and the Al peaks disappeared. The predominant phase that formed was $Al_{12}Mo$, but the intensity ratio did not match the reported values, indicating the precipitate phase was preferentially oriented. The majority of the remaining peaks were indexed to Al_5Mo. One peak at 18.85° could not be indexed to any of the Al-Mo intermetallic compounds, the Al or Mo metallic constituents, or possible silicides. As Figure 4-27 shows, similar XRD spectra were observed for the Al-11Mo alloy heat treated at 500°C for 1, 2, and 8 hours.

The as-deposited Al-18Mo alloy exhibited broad amorphous peaks at 21° and 41° [54-58] and there was no apparent change after heat treating between 1 and 8 hours at 400 °C, as Figure 4-28 reveals. However, Figure 4-29 shows that after heat treating at 500°C for just 1 hour, the amorphous peaks disappeared and several new, well-defined peaks formed. After either 1, 2, of 8 hours at 500 °C, the broad 21.5° peak split into three peaks at 20.2°, 21.9°, and 24.9°. These peaks migrated to slightly higher angles as the heat treatment time increased. None of the peaks could be indexed to Al and it appeared that $Al_{12}Mo$, Al_5Mo, and $Mo(Si,Al)_2$ were the dominate phases.

The as-deposited Al-23Mo alloy also exhibited the two broad amorphous peaks at 21.5° and 41.2°. Figure 4-30 shows that no new peaks formed during heat treating at 400°C for 1 and

46

2 hours. However, after heat treating at 400°C for 8 hours, the 21.5° peak began to separate into two broad peaks centered at 21° and 26°. In addition, a shoulder began to form on the 41.2° peak. After heat treating at 500°C for 8 hours, the 21.5° peak separated into four peaks: a well defined peak at 23°, and three broad peaks at 17.5°, 21.2°, and 26° (Figure 4-31). Similarly, several shoulder peaks began to form on the high angle side of 41.2° peak, with the main 41.2° peak becoming much sharper at the apex. Sharpening and formation of the small peaks is likely due to the formation of nano-crystalline Al and intermetallic phases [57]. Figure 4-32 reveals that after heat treating up to 600°C for 2 hours the two main amorphous peaks were found to remain fairly broad although the angle shifted slightly. Precipitation and full loss of the amorphous peaks occurred only after heat treating at 600°C for 8 hours.

The peaks observed after heat treating the Al-23Mo alloy at 600°C for 8 hours were indexed to Al and $Mo(Si,Al)_2$. A lattice parameter of 0.403 nm was calculated. From this lattice parameter, the concentration of Mo in Al was estimated to be approximately 7 atomic percent. This lower-than-expected molybdenum concentration was a result of molybdenum being consumed by the Si substrate to form $Mo(Si,Al)_2$ during the heat treatment.

As expected due to their similar compositions, XRD patterns for the Al-11Mg-10Mo alloy were identical to the patterns for the Al-12Mg-13Mo alloy. Figures 4-33 through 4-36 show the XRD spectra for the Al-11Mg-10Mo and Al-12Mg-13mo alloys. Both ternary alloys were amorphous in the as-deposited condition and precipitation occurred after heat treating at the lowest temperature and shortest time (400°C for one hour). The peaks observed at diffraction angles of 10° and 13° were indexed to MgO_2 and the other (unlabeled) peaks in these spectra were indexed to Mg_2Al.
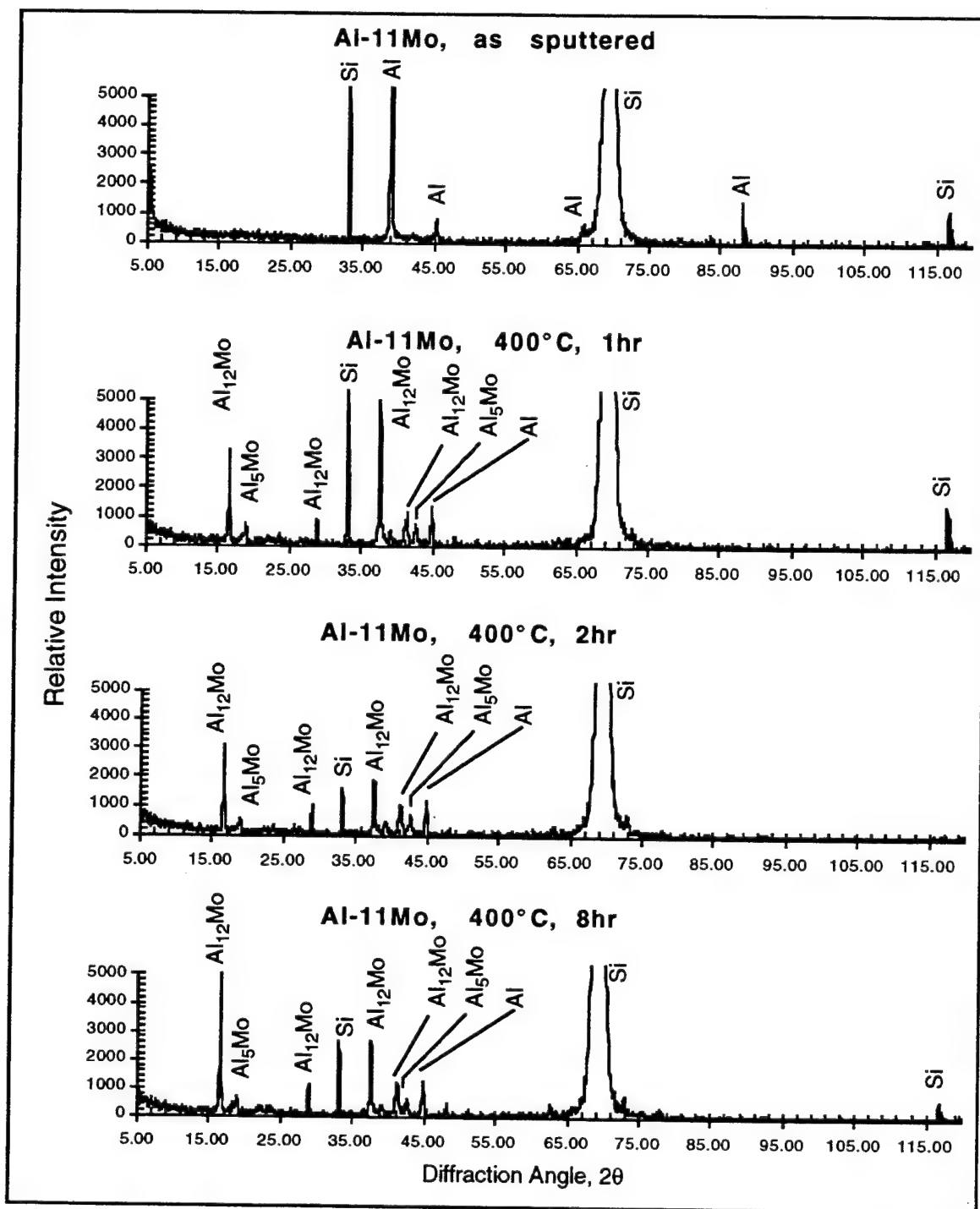
Figure 4-26. X-Ray Diffraction Patterns for Al-11Mo in the As-Sputtered Condition and After Heat Treatments at 400°C for 1, 2, and 8 Hours.
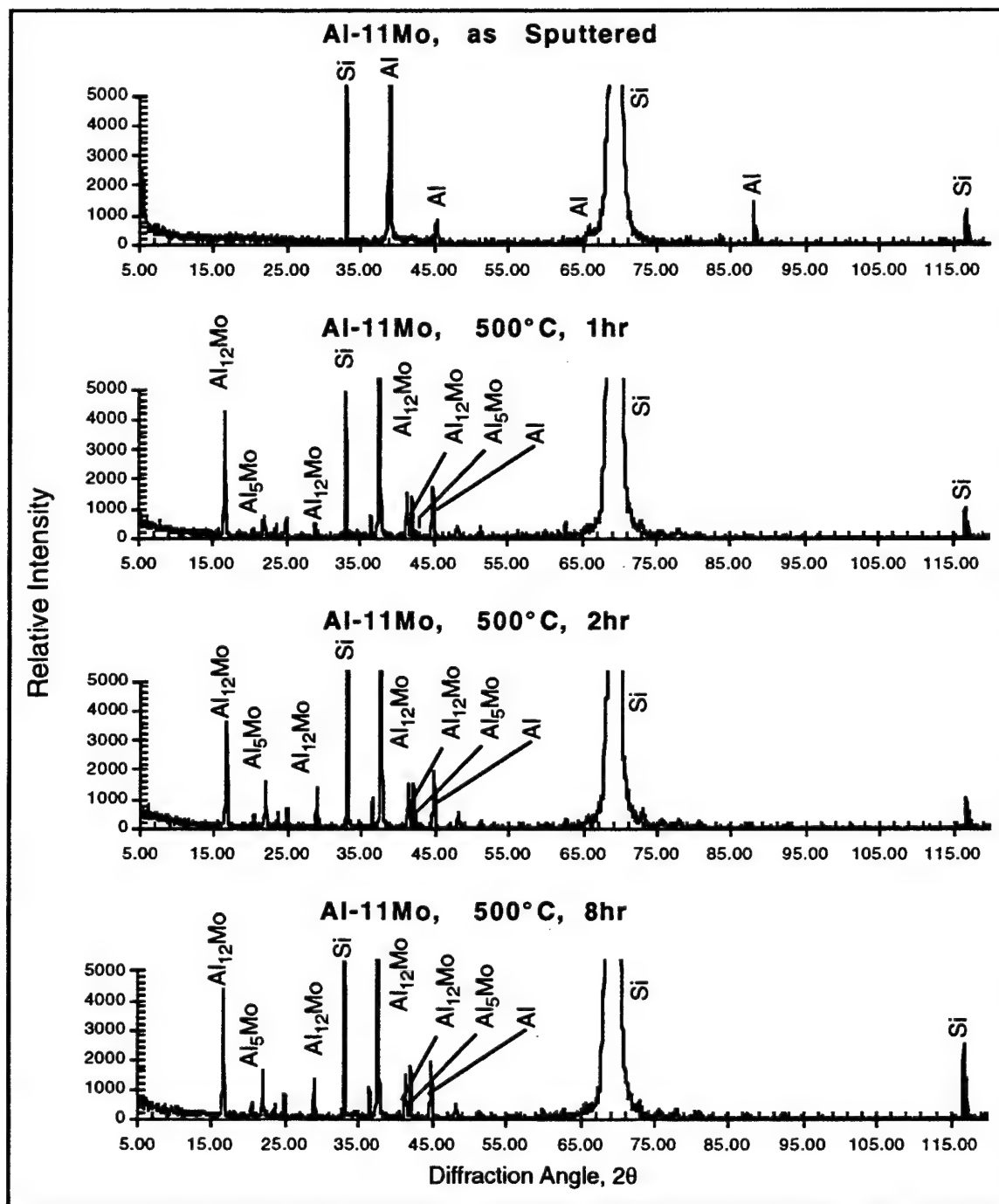
48

Figure 4-27. X-Ray Diffraction Patterns for Al-11Mo in the As-Sputtered Condition and After Heat Treatments at 500°C for 1, 2, and 8 Hours.
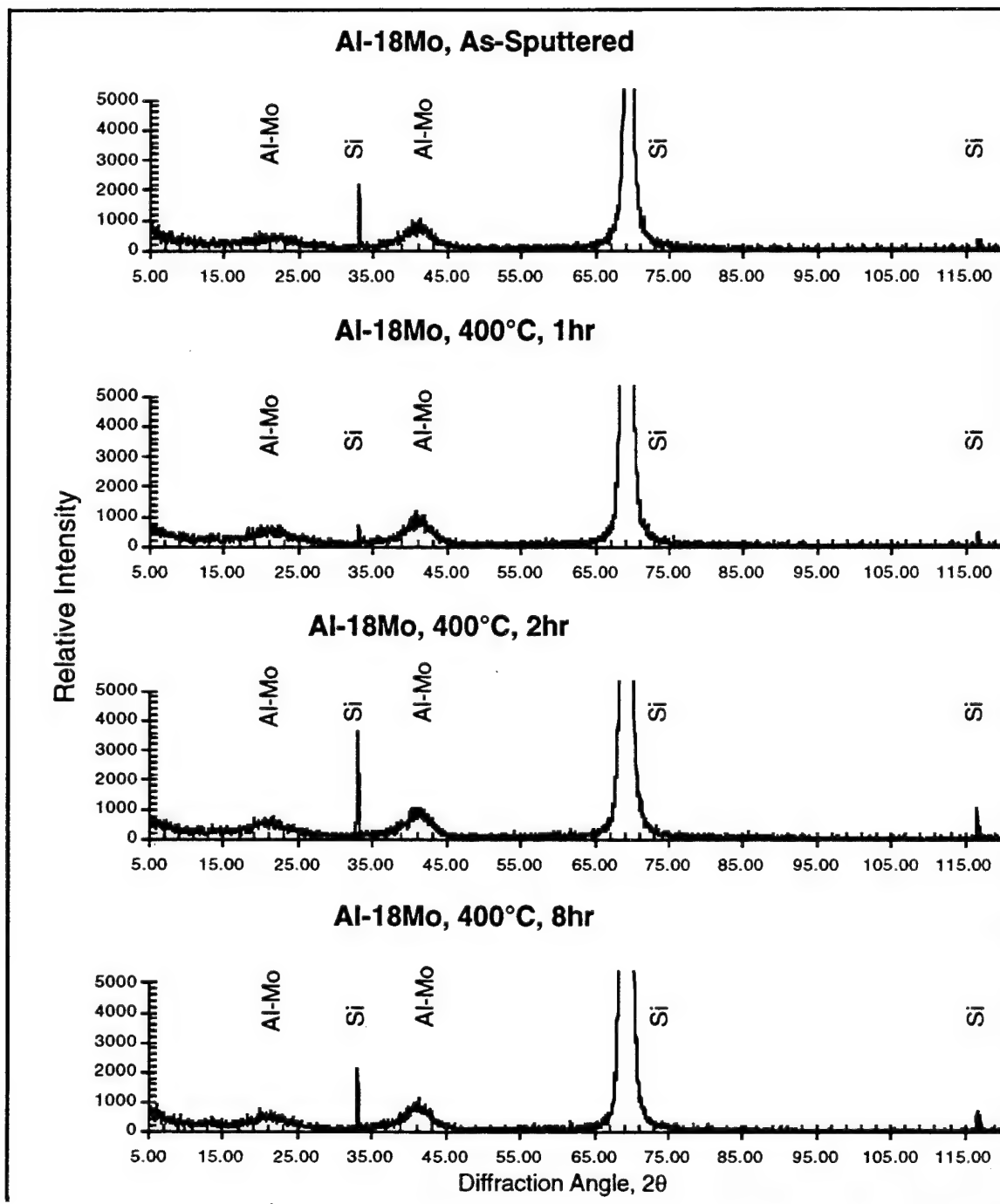
49

Figure 4-28 X-Ray Diffraction Patterns for Al-18Mo in the As-Sputtered Condition and After Heat Treatments at 400°C for 1, 2, and 8 Hours.
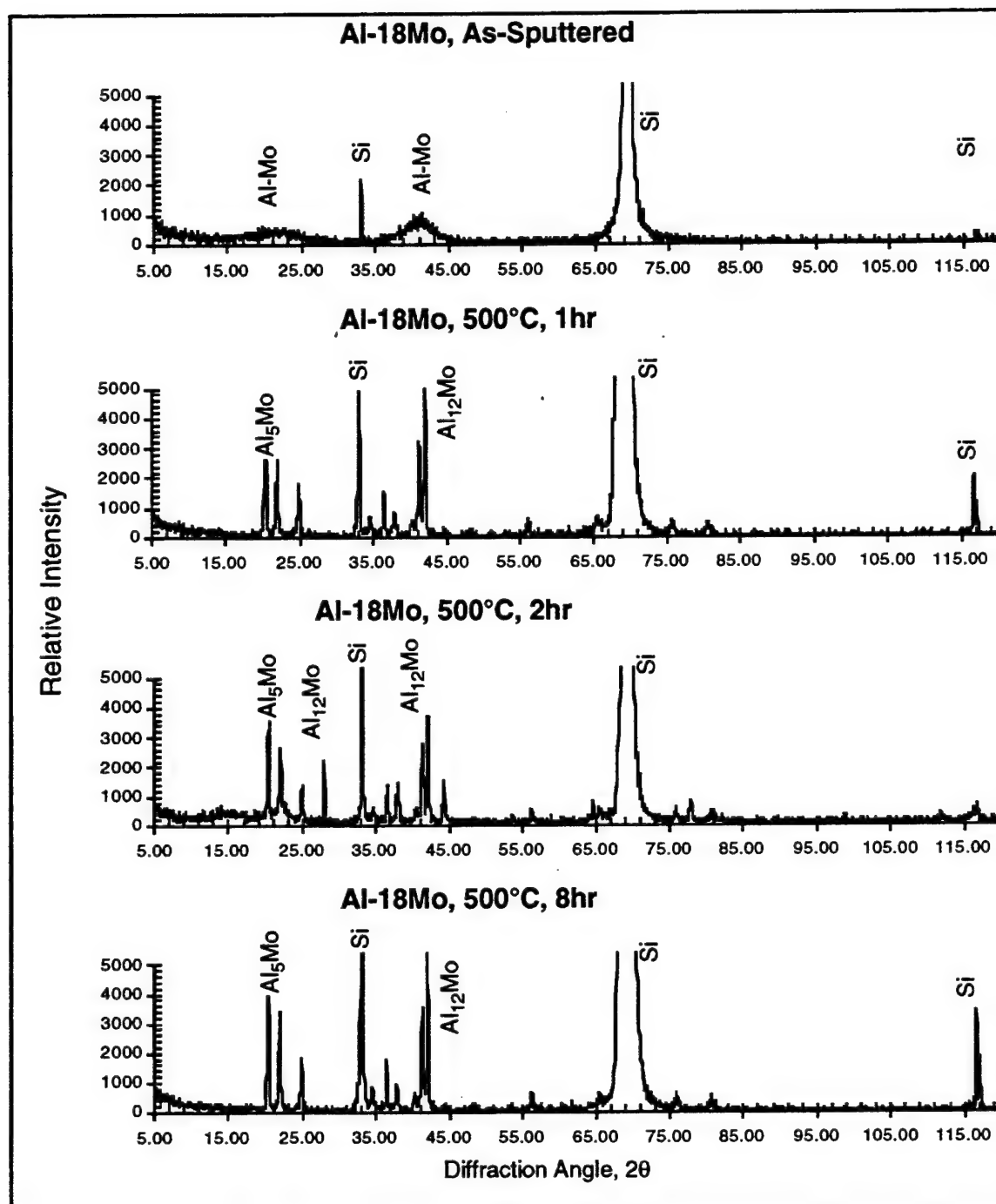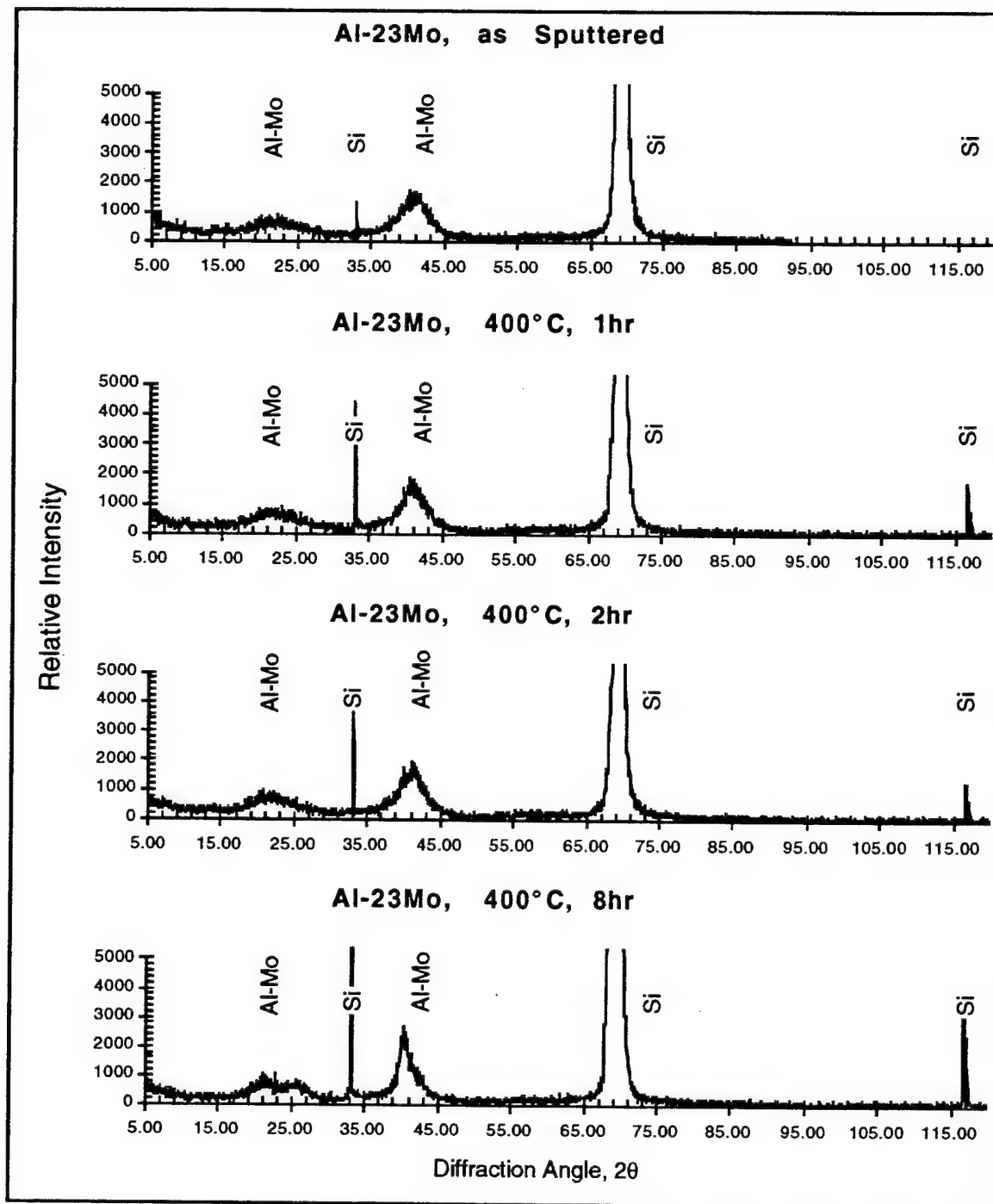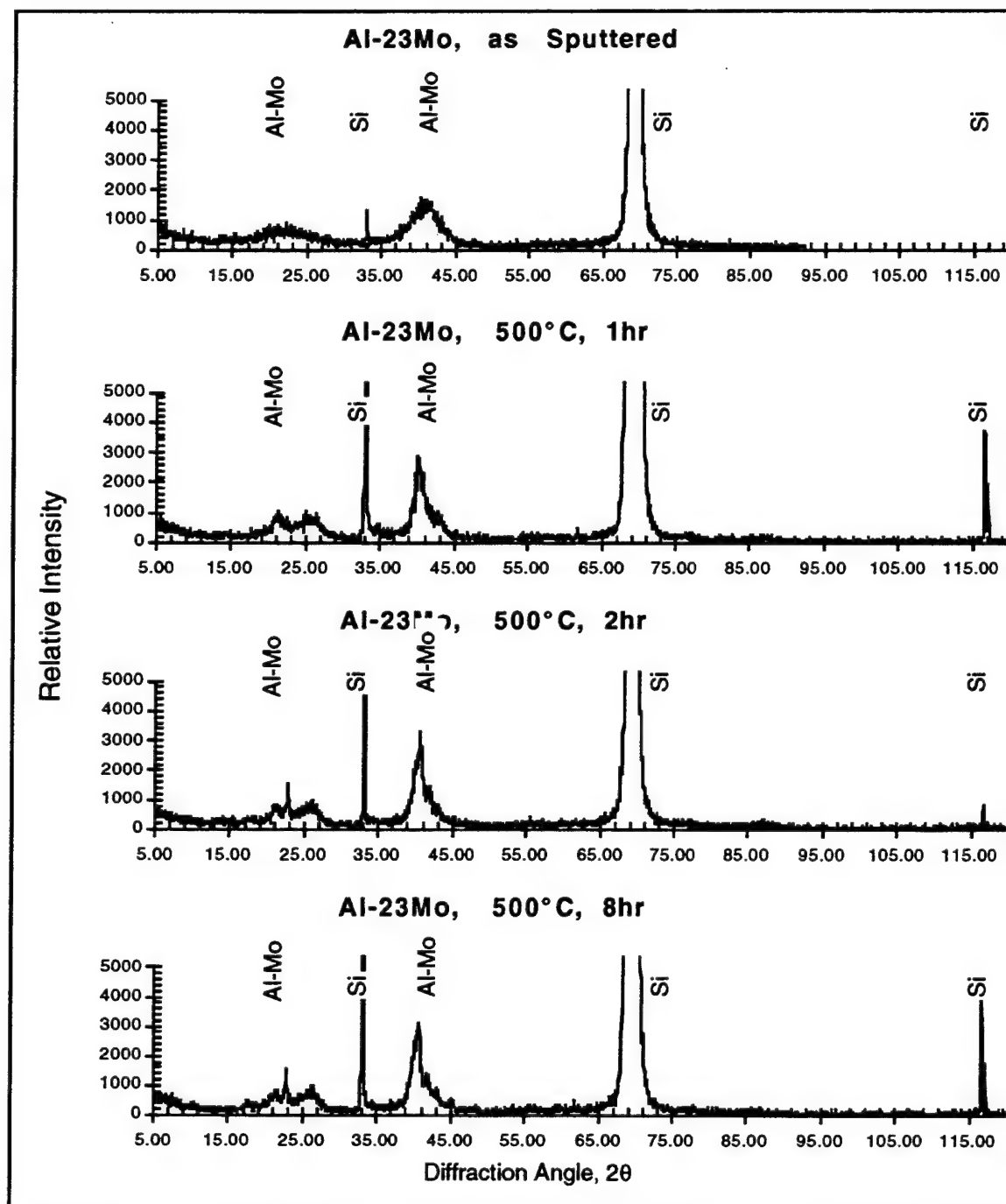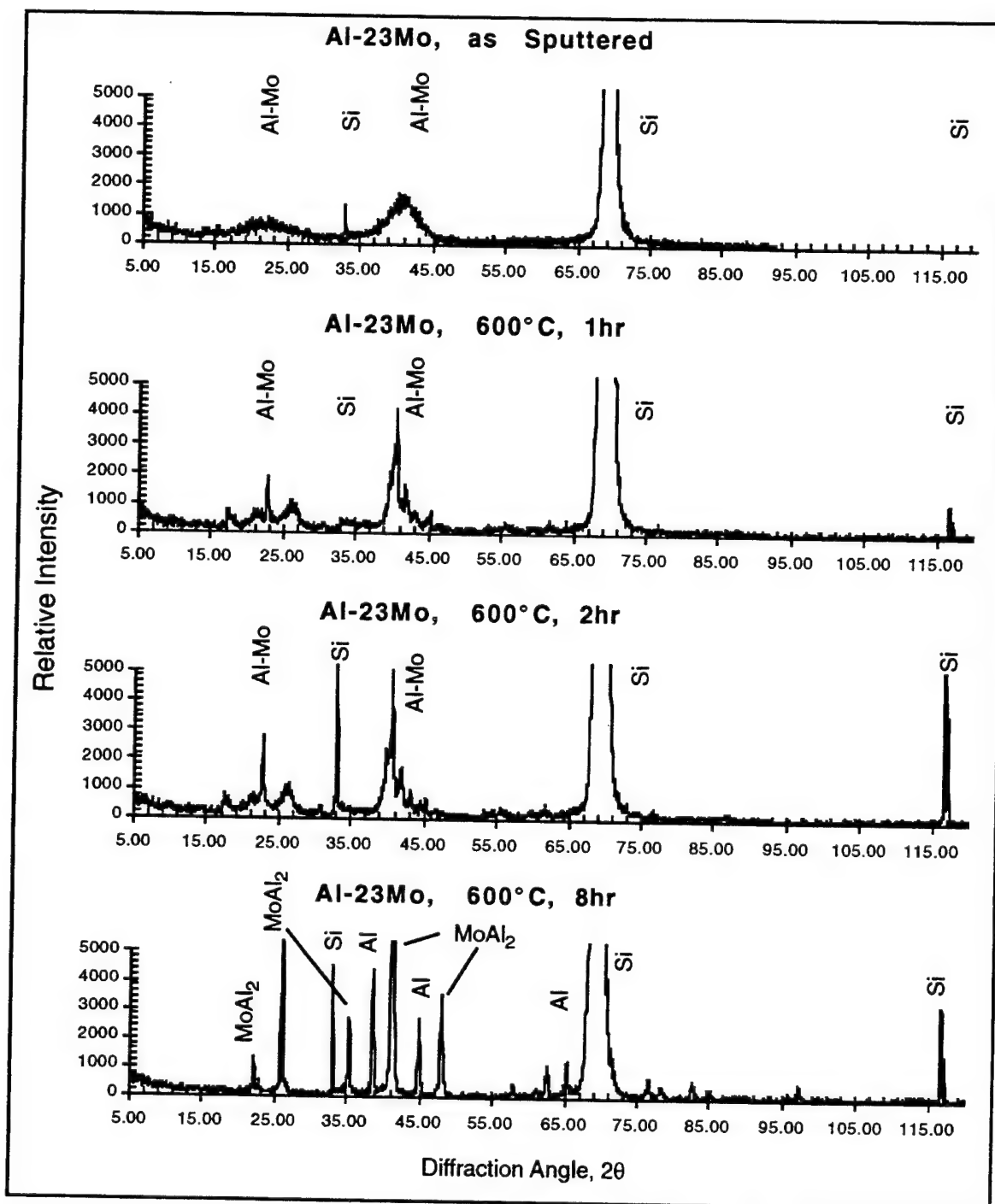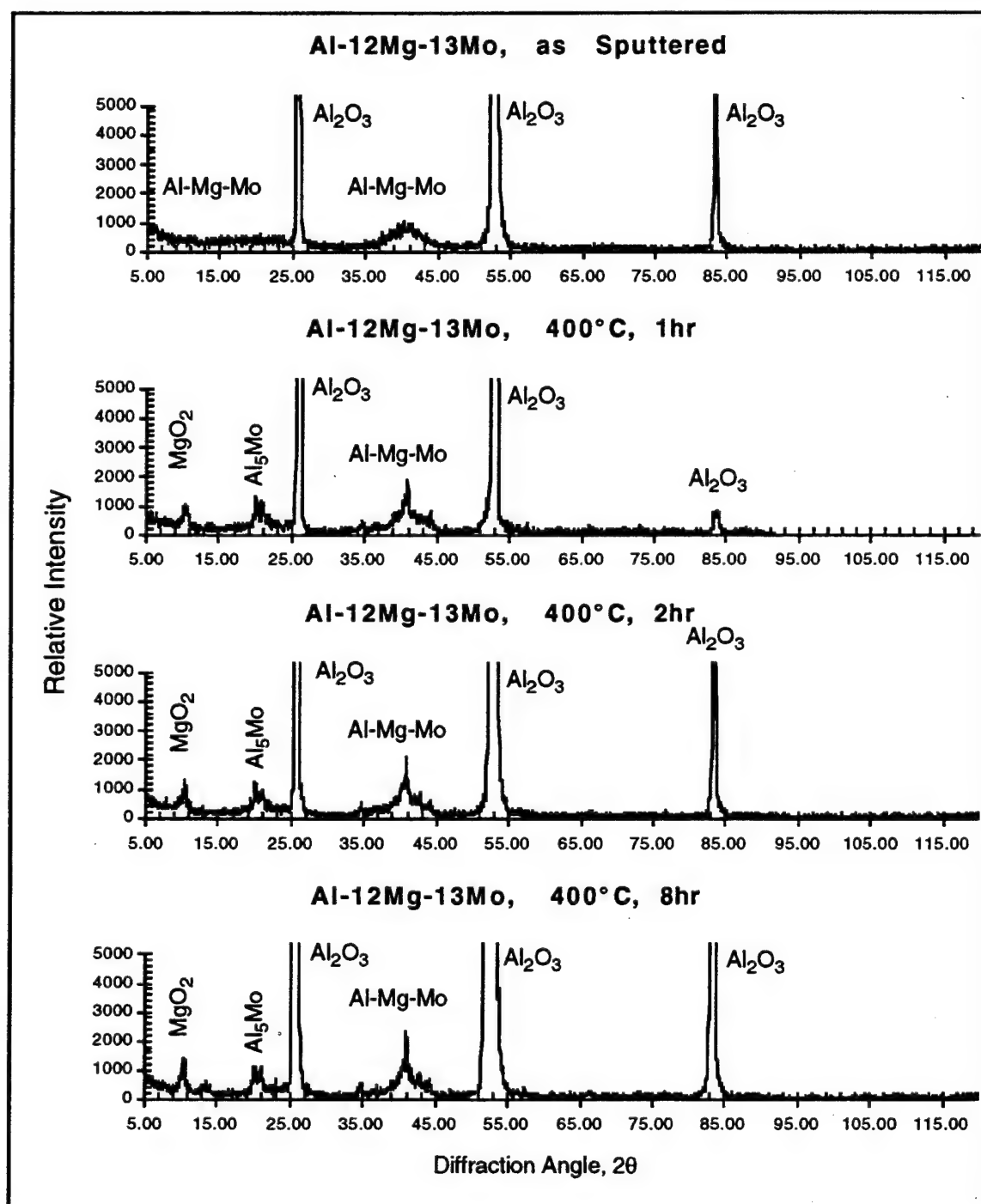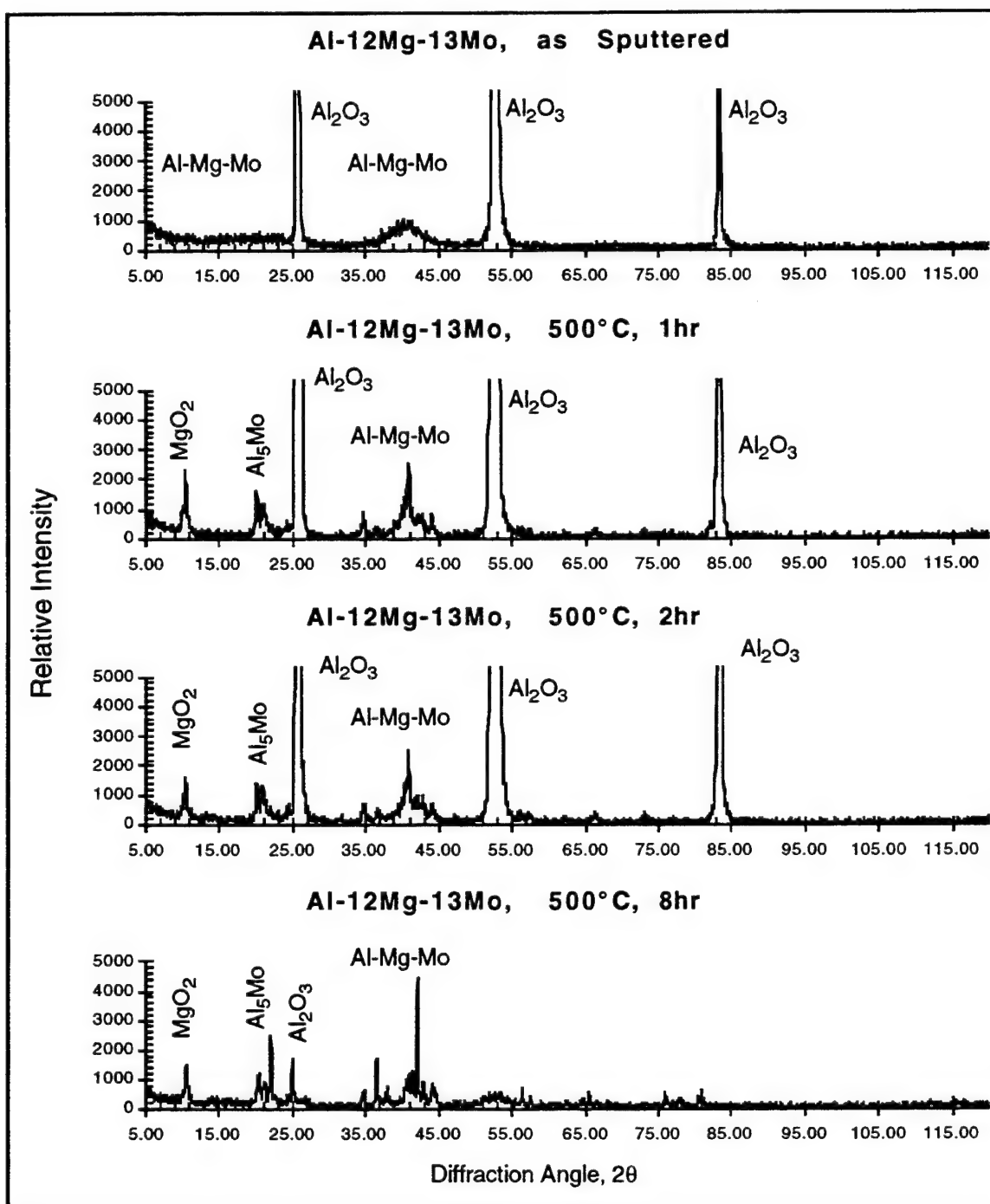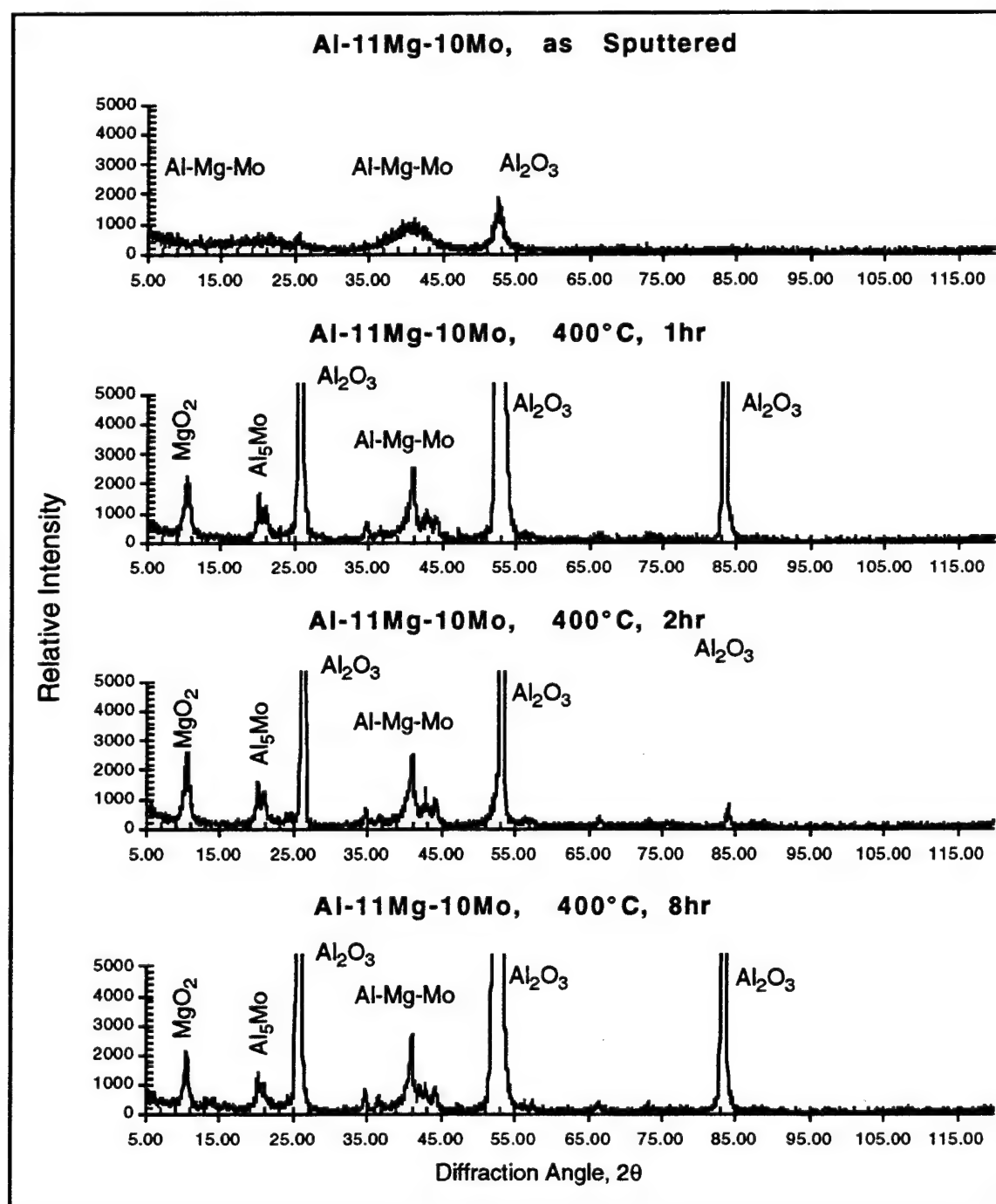
50

Figure 4-29 X-Ray Diffraction Patterns for Al-18Mo in the As-Sputtered Condition and After Heat Treatments at 500°C for 1, 2, and 8 hours.

51

Figure 4-30. X-Ray Diffraction Patterns for Al-23Mo in the As-Sputtered Condition and After Heat Treatments at 400°C for 1, 2, and 8 hours.
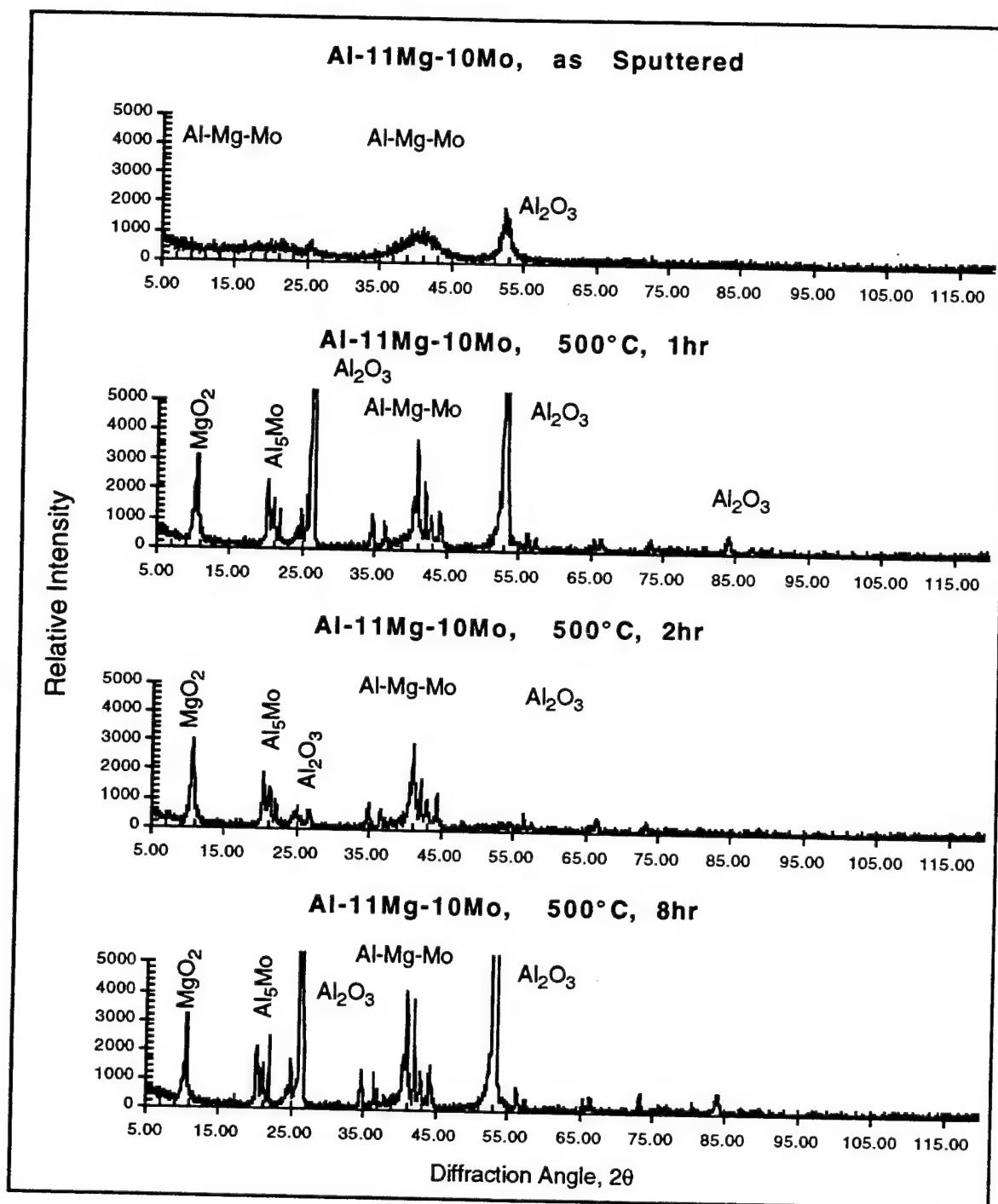
Figure 4-31. X-Ray Diffraction Patterns for Al-23Mo in the As-Sputtered Condition and After Heat Treatments at 500°C for 1, 2, and 8 hours.

53

Figure 4-32. X-Ray Diffraction Patterns for Al-23Mo in the As-Sputtered Condition and After Heat Treatments at 600°C for 1, 2, and 8 hours.

54

Figure 4-33. X-Ray Diffraction Patterns for Al-12Mg-13Mo in the As-Sputtered Condition and After Heat Treatments at 400°C for 1, 2, and 8 hours.

55

Figure 4-34. X-Ray Diffraction Patterns for Al-12Mg-13Mo in the As-Sputtered Condition and After Heat Treatments at 500°C for 1, 2, and 8 Hours.

56

Figure 4-35   *X-Ray Diffraction Patterns for Al-11Mg-10Mo in the As-Sputtered Condition and After Heat Treatments at 400°C for 1, 2, and 8 Hours.*

57

Figure 4-36 X-Ray Diffraction Patterns for Al-11Mg-10Mo in the As-Sputtered Condition and After Heat Treatments at 500°C for 1, 2, and 8 Hours.

4.3.4 Transmission Electron Microscopy

Transmission electron microscopy and selected area diffraction were performed on the as-sputtered Al-18Mo alloy. Figure 4-37 shows a transmission electron micrograph and a selected area diffraction pattern for the 18%Mo alloy. Grain size for this specimen was approximately 0.1 μm. Selected area diffraction showed two rings at lattice spacings of 0.22 nm and 0.156 nm. These d values do not index to aluminum, but the 0.22 nm spacing corresponds to the XRD peak at 41° and the 0.156 nm d value corresponds to the very slight hump at a diffraction angle, 2θ, of 59° in the XRD patterns. The diffuse maxima clearly indicate the alloy is amorphous. The ring that would correspond to the 21° x-ray diffraction peak (d = 0.423 nm) is hidden by the bright transmitted electron beam spot.
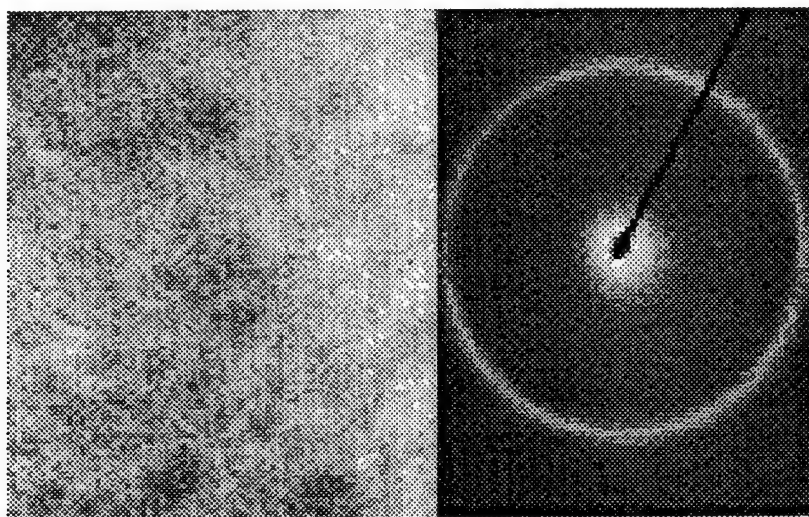

Figure 4-37. *Transmission Electron Micrograph and Selected Area Diffraction Pattern Showing the Amorphous Structure with Short Range Ordering at a d Value of 0.22 nm.*

4.3.5 Corrosion Testing of the Al-Mo Alloys

4.3.5.1 Potentiodynamic Polarization

As-Deposited Alloys -- Table 4-8 and Figure 4-38 summarize the results of the anodic polarization experiments for the binary Al-Mo and ternary Al-Mg-Mo nonequilibrium alloys in the as-sputtered condition. All the as-deposited Al-Mo alloys exhibited extended passive regions and open circuit potentials that were 500 to 600 mV more noble than pure Al. Open circuit potentials for all of the alloys were between -600 to -450 mV with the majority of the measured open circuit potential values ranging from -520 mV to -580 mV. Passive current densities (i_{pass}) for the as-deposited binary Al-Mo and ternary Al-Mg-Mo alloys ranged between 0.1 and 10.0 μA·cm^{-2} and no correlation between solute concentration and i_{pass} was evident. Breakdown potential (E_b) values for most of the as-sputtered alloys in the 0.1M NaCl solution were between 100 and 500 mV as compared to -690 mV for pure

Al. Variations in the passive current density and the breakdown potential were attributed to defects, i.e., scratches, pinholes, etc., in the alloy film. Figure 4-39 shows an in-situ scanning laser microscope image of pit initiation at one such defect on an Al-15Mo alloy.

Additional polarization experiments were conducted on the Al-18 Mo alloy in aerated and quiescent (unstirred solution with no aeration or deaeration) NaCl solutions (near-neutral pH) with Cl⁻ concentrations of 0.1 and 0.55 M. Figure 4-40 shows that the polarization response was not significantly altered by either increasing the Cl⁻ concentration, by solution aeration, or both.

SEM examination and EDS analysis of a newly formed pit on the as-deposited Al-18Mo specimen immediately after polarization to the breakdown potential showed the Mo concentration had risen from 18 to 25 atomic percent in the pit. The increase in Mo in the forming pit indicates that the pitting process involves the preferential dissolution of Al from the alloy, which is consistent with current and previous x-ray photoelectron spectroscopy work conducted on these alloys [8,10].

Heat Treated Alloys -- The polarization response of as-deposited and heat-treated Al-11Mo alloys is presented in Figure 4-41. Although the breakdown potential for the heat treated Al-11Mo alloys decreased from ~420 mV_{SCE} (as-sputtered) to 50 mV_{SCE}, (heat treated), the E_{OC} remained relatively constant at approximately -550 mV_{SCE}. The reduction in E_b was likely the result of precipitates formed during heat treatment creating microgalvanic cells with the surrounding alloy. In contrast to the decrease in E_b, i_{pass} decreased from ~1 μA·cm^{-2} for the as-deposited alloy to ~0.1 μA·cm^{-2} after heat treatment.

Both the open circuit and breakdown potentials for the Al-18Mo alloy were not dramatically affected by heat-treating up to 500°C for 2 hours as Figure 4-42 reveals. Similar to the Al-11Mo alloys, i_{pass} for the heat-treated Al-18Mo specimens was less than that for the as-sputtered alloy, with the exception of the specimen heat-treated at 400°C for 1 hour. No cracks or new defects were found during SEM examination of the heat treated alloys.

Table 4-8. *Alloy Composition and Anodic Polarization Data in 0.1M NaCl (pH 8) for As-Sputtered Binary Al-Mo and Ternary Al-Mg-Mo Nonequilibrium Alloys.*

Alloy Composition (Atomic Percent)	E_{oc} (mV v. SCE)	E_b (mV v. SCE)	i_{pass} ($\mu A \cdot cm^{-2}$)
Al	-1093	-690	0.1
	-1224	-689	0.7
Al-11Mo	-581	220	2.69
	-629	100	23.7
	-681	0.0	46.6
Al-18Mo	-520	461	0.89
	-601	391	3.5
	-555	456	3.63
Al-23Mo	-582	563	45.6
	-582	492	7.6
	-591	496	7.6
Al-26Mo	-440	750	3.0
	-427	700	0.60
	-460	600	0.80
	-495	770	1.90
	-540	760	4.17
Al-12Mg-13Mo	-513	55	1.0
	-573	85	4.5
	-550	39	5.6

61

Figure 4-38. Anodic Polarization Response of Various Al-Mo Alloys, Polarized in Quiescent 0.1M NaCl, pH 8, 25°C.
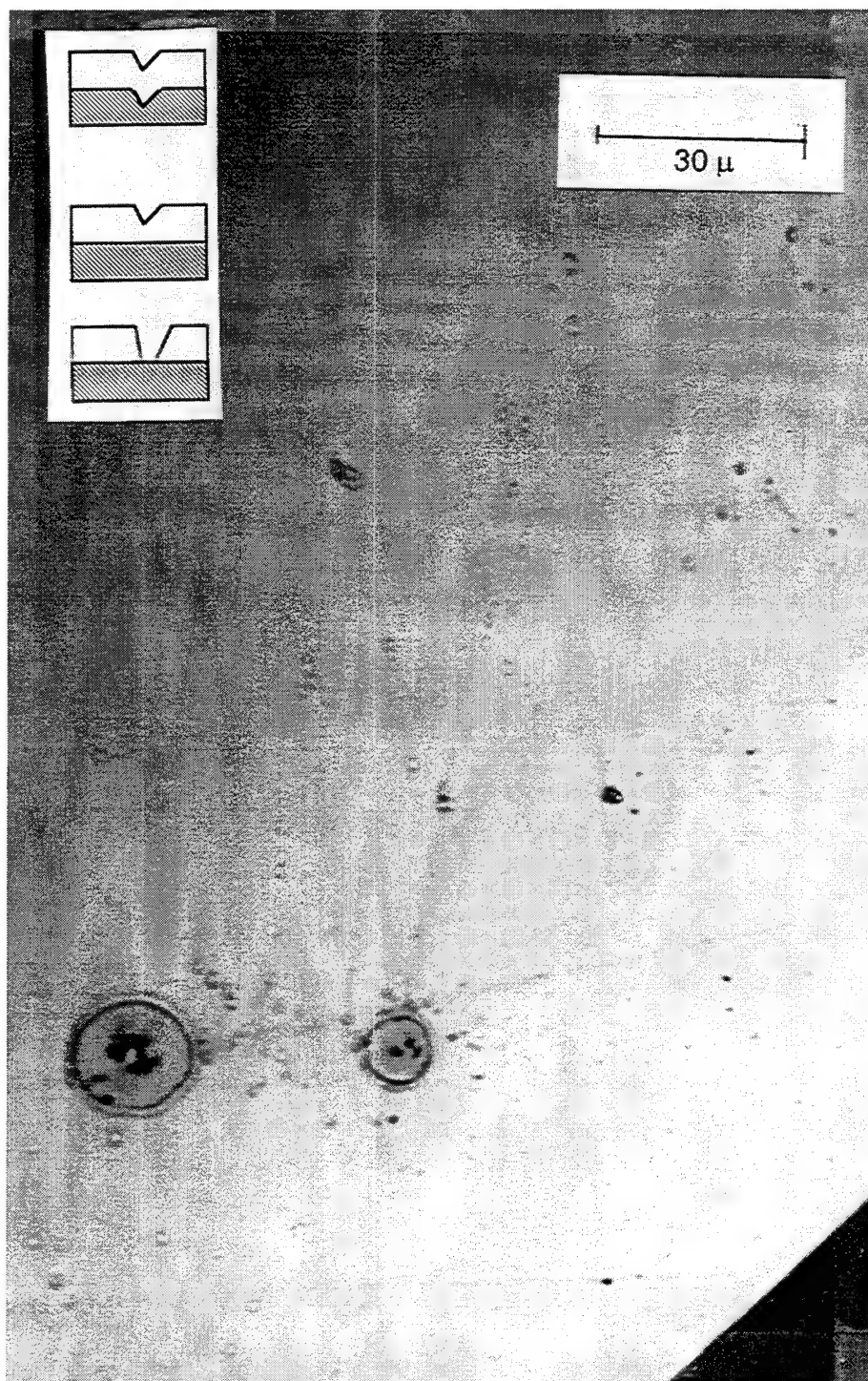
Figure 4-39   *In-situ scanning laser microscope image of an Al-15Mo alloy revealing pit initiation on a defect (a scratch which likely extended to the silicon substrate). The sample was undergoing anodic polarization in 0.1M NaCl when pitting initiated. Inset shows 3 types of defects observed in the thin-film alloys. It is believed that a defect such as the one shown in the bottom of the inset was responsible for pit initiation in this case.*

63
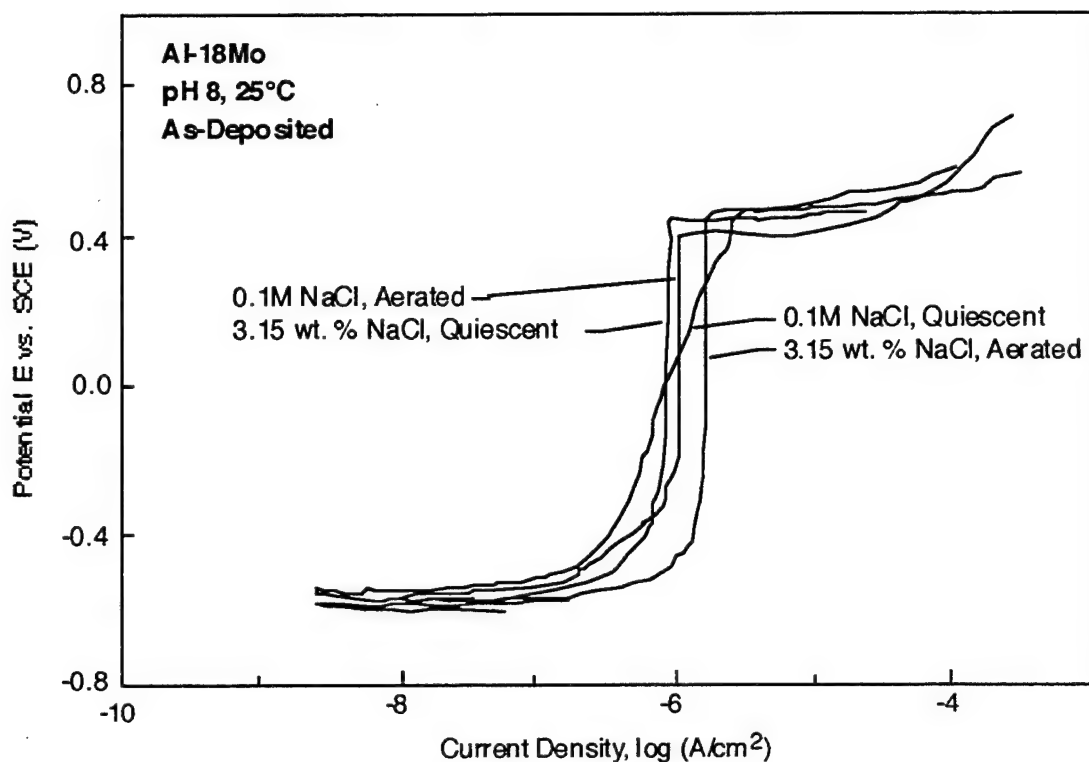
Figure 4-40. Anodic Polarization Response of Al-18 Mo Used for Detailed Heat Treatment Studies, Polarized in Quiescent and Aerated 0.1M and 3.15 wt. % (0.55M) NaCl, pH 8, 25°C.
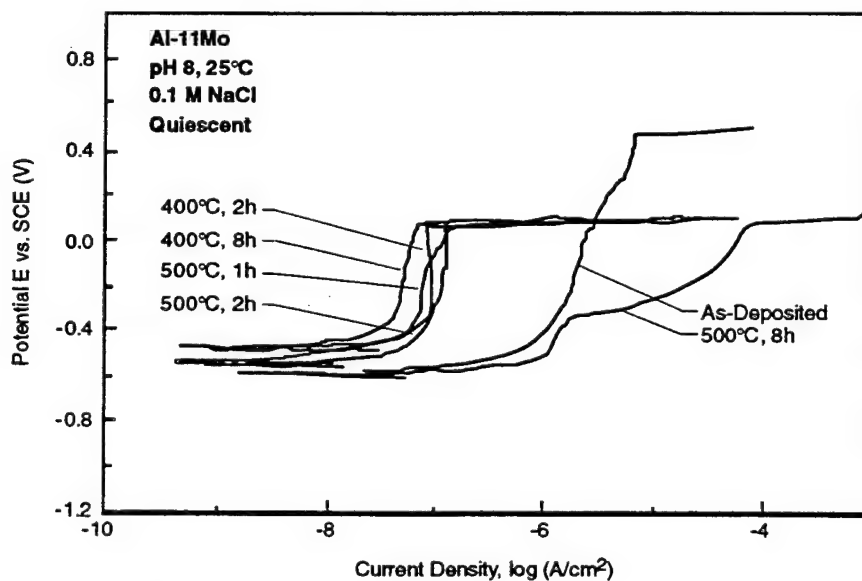

Figure 4-41 Anodic Polarization Response of Al-11Mo Alloy Before and After Heat Treatment at 400¤C for 1, 2, and 8, Polarized in Quiescent 0.1 M NaCl, pH 8, 25¤C.
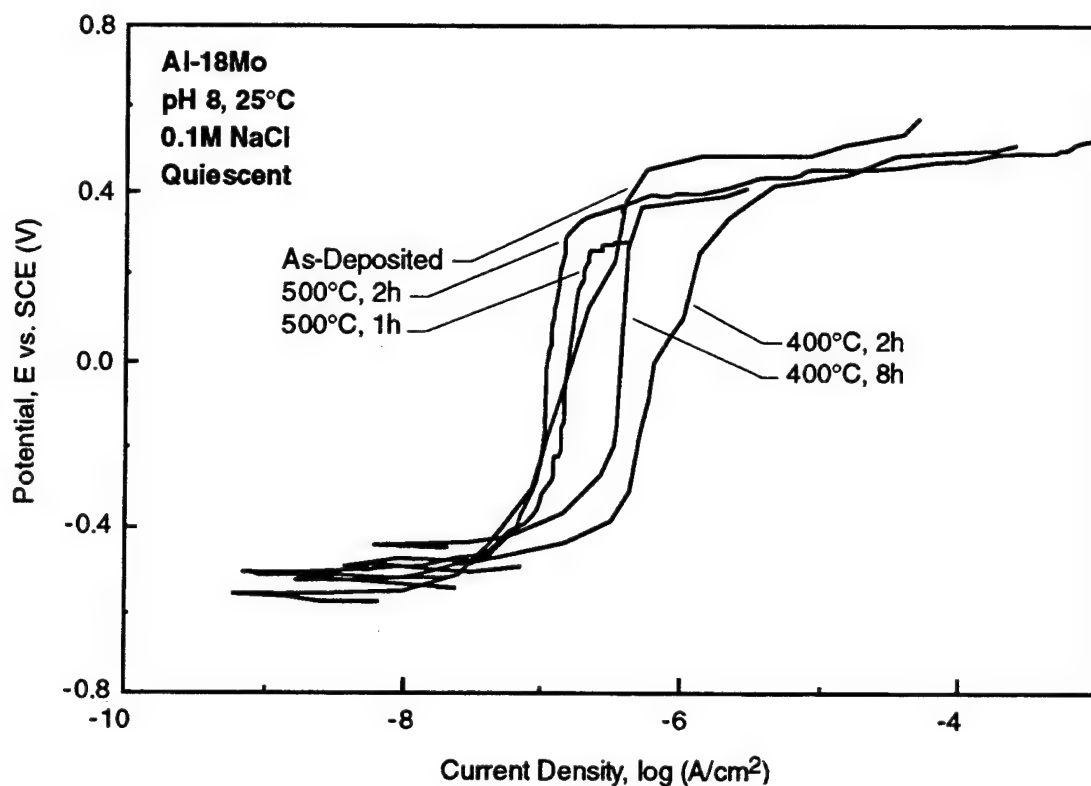
64

Figure 4-42. Anodic Polarization Response of Al-18Mo Alloy Before and After Heat Treatment at 400°C for 2 and 8 h and 500°C for 1 and 2 h, Polarized in Quiescent 0.1 M NaCl, pH 8, 25°C.

65

The Al-12Mg-13Mo alloy exhibited an E_{oc} value of -580 mV and an E_b of 55 mV in the as-deposited condition which was similar to the behavior of the Al-Mo alloys. Figure 4-43 shows that the E_{oc} value of ~ -580 mV was maintained for the Al-12Mg-13Mo alloy after heat-treating at 400°C for 1 h; however, heat-treating the ternary alloy at longer times and higher temperatures resulted in a more active open circuit potential (approximately -800 mV) with no passive response during polarization.
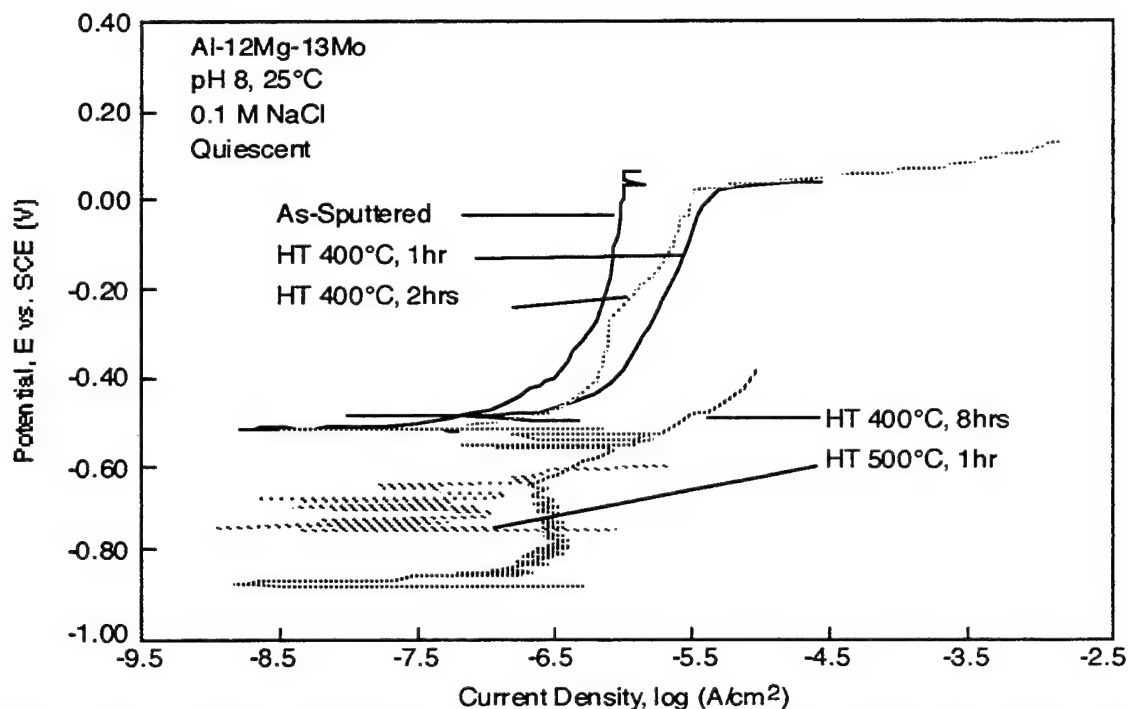

Figure 4-43. *Anodic Polarization Response of Al-12Mg-13Mo Before and After Heat Treatment at 400°C for 1, 2 and 8 h and 500°C for 1 hr, Polarized in Quiescent 0.1M NaCl, pH 8, 25°C.*

4.3.5.2 Galvanic Corrosion Behavior

Galvanic diagrams [48] based on equal metal and graphite areas for pure Al, 6061 Al, and the Al-Mo alloys coupled to P75 Gr fibers are shown in Figure 4-44. This diagram reveals that the galvanic corrosion behavior of pure sputtered and 6061 Al coupled to P75 graphite fibers is cathodically controlled and predicts galvanic current densities on the order of 12 $\mu A \cdot cm^{-2}$. For a cathodically controlled reaction, the cathodic curve shifts to the right (when the diagram is plotted in terms of current rather than current density as is necessary when comparing different areas) as the Gr-to-Al area ratio increases, which accelerates the corrosion rate of the Al matrix. In contrast to the pure Al and the 6061 Al alloy, galvanic corrosion was anodically controlled for the Al-Mo alloys with estimated galvanic current densities of 1 $\mu A \cdot cm^{-2}$ or less. For the anodically controlled galvanic corrosion situation, changing the graphite-to-Al ratio and subsequently shifting the cathodic curve to the right (when the diagram is plotted in terms of current rather than current density) would not significantly change the corrosion rate for the Al-Mo alloys. This result is important because modifying the graphite fiber volume, which is a key design feature of composites to achieve specific thermal or mechanical properties, will not result in dramatic changes in the corrosion response of the Gr/Al-Mo composite.

66

Figures 4-45 and 4-46 show that the galvanic corrosion reaction remained anodically controlled for both the Al-11Mo (Fig. 4-44) and Al-18Mo (Fig. 4-45) alloys after heat treatment. Referring to Table 4-8, although some of the Al-11Mo and Al-18Mo alloys precipitated during heat treatment, they still exhibited passive polarization response and their galvanic diagrams predict that corrosion will be controlled by anodic dissolution of metal. Only after heat treating the Al-11Mo to 500°C for 8 hours did control for the galvanic reaction change from anodic (Al passivation) to cathodic (oxygen reduction on graphite fibers).

To confirm the predictions made using the galvanic diagrams, long-term galvanic current measurements were taken on sputtered Al, Al-11Mo, Al-18Mo, Al-23Mo, and ternary Al-12Mg-13Mo (in the as-deposited condition) individually coupled to P75 Gr fibers. Data from these experiments are presented in Figure 4-47. In these experiments, the galvanic current density values for the alloys are equivalent to the galvanic currents since the anode areas were 1 cm^2. For all the alloys, the galvanic current initially starts off at relatively high values, between 3 and 30 μA·cm^{-2}, but quickly drops to a low steady state value. The Al-18Mo and Al-23Mo reached low measured galvanic current densities of ~0.04 and ~0.08 μA·cm^{-2}, respectively; which were up to three orders of magnitude lower than the galvanic current density values of 30 μA·cm^{-2} measured for pure sputtered Al.

Galvanic current densities for the Al-18 Mo alloys after heat-treatment at 400°C for 2 hours were comparable to the values of ~ 0.08 μA·cm^{-2} noted for the as-deposited alloys. Even after heat-treatment at 500°C for 2 hours, the galvanic current density was an order of magnitude lower than for pure sputtered Al. After galvanic coupling for seven days (605 ks), the pure sputtered Al had completely dissolved from the Si wafer; whereas, the Al-Mo alloys remained intact and highly specular.

The Al-12Mg-13Mo alloy exhibited a galvanic current density of 10 μA·cm^{-2} which was greater than the value noted for the binary Al-Mo alloys, but this value was still 3 times lower than the value observed for pure Al. However, less than 12 hours (40 ks) after immersion in the 0.1 M NaCl solution, the Al-Mg-Mo alloys coupled to P75 Gr fibers exfoliated and completely lifted away from the substrate. Due to the short time in solution for the Al-12Mg-13Mo alloy, data for this alloy was not included in Figure 4-47.
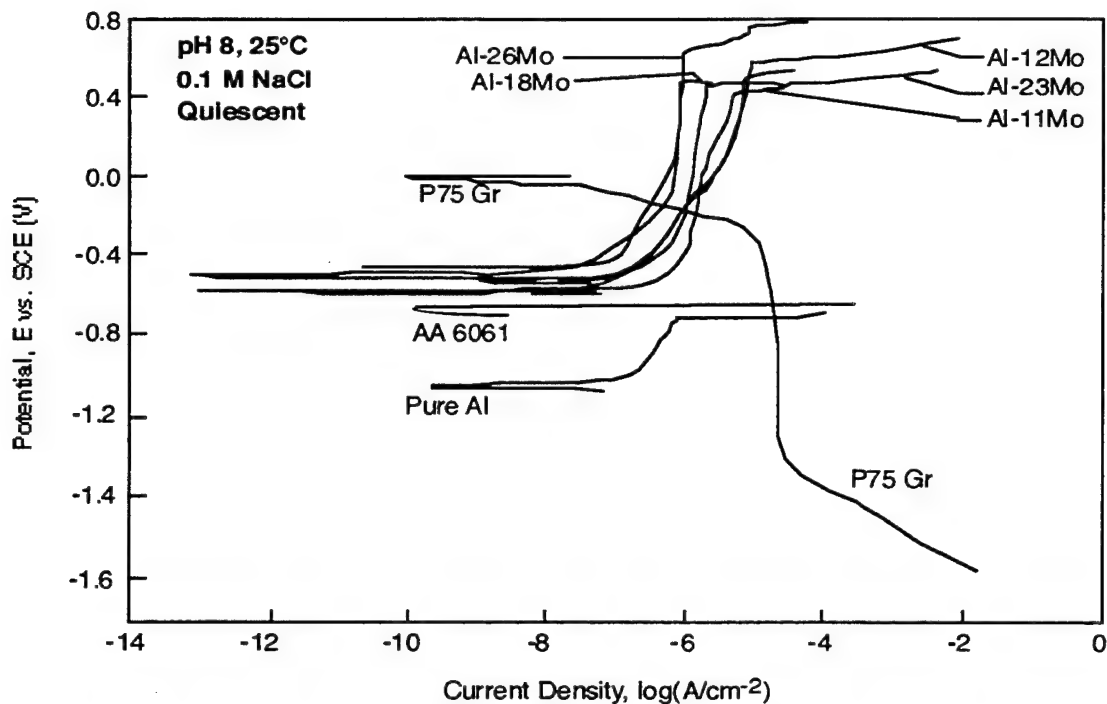
Figure 4-44. *Galvanic Diagram with Anodic Curve of Pure Sputtered Aluminum, Wrought 6061 Al, and Various Sputtered Al-Mo Alloys Combined with the Cathodic Curve for an Equal Area of P75 Graphite Fibers, Tested in Quiescent, 0.1M NaCl, pH 8, 25°C.*
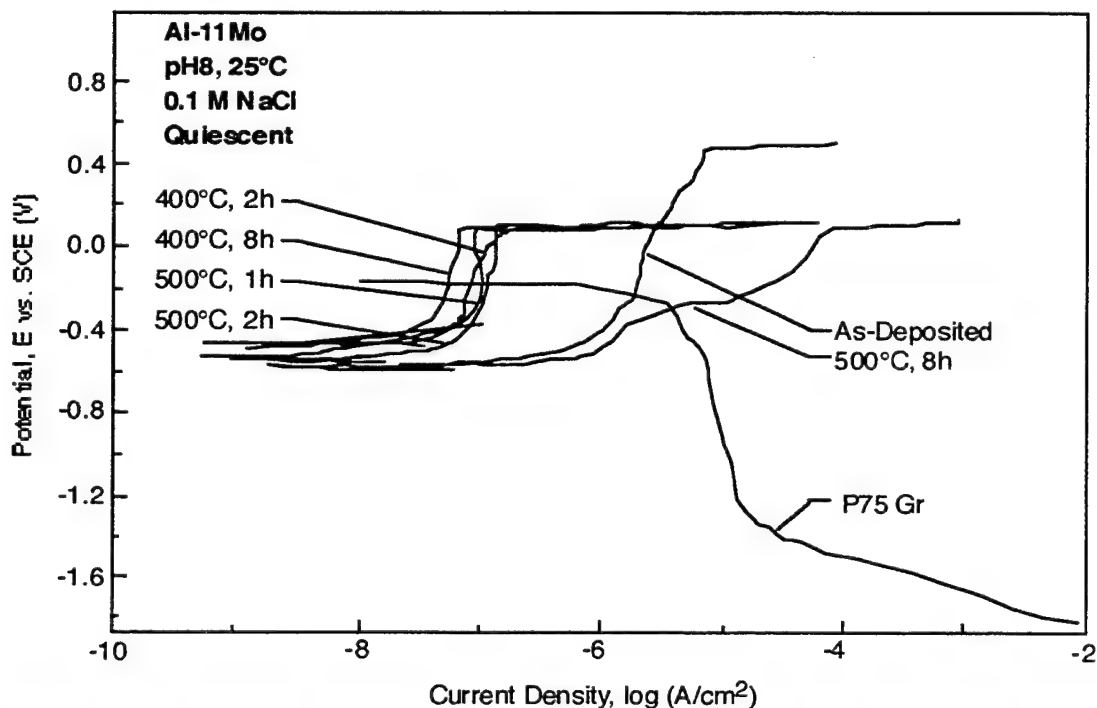

Figure 4-45. *Galvanic Diagram for Al-11Mo Alloy Before and After Heat Treatment at 400° for 2 and 8 h and 500°C for 1, 2, and 8 h With P75 Gr Fibers, Tested in Quiescent 0.1 M NaCl, pH 8, 25°C. (The anode-to-cathode area ratio was equal to one)*
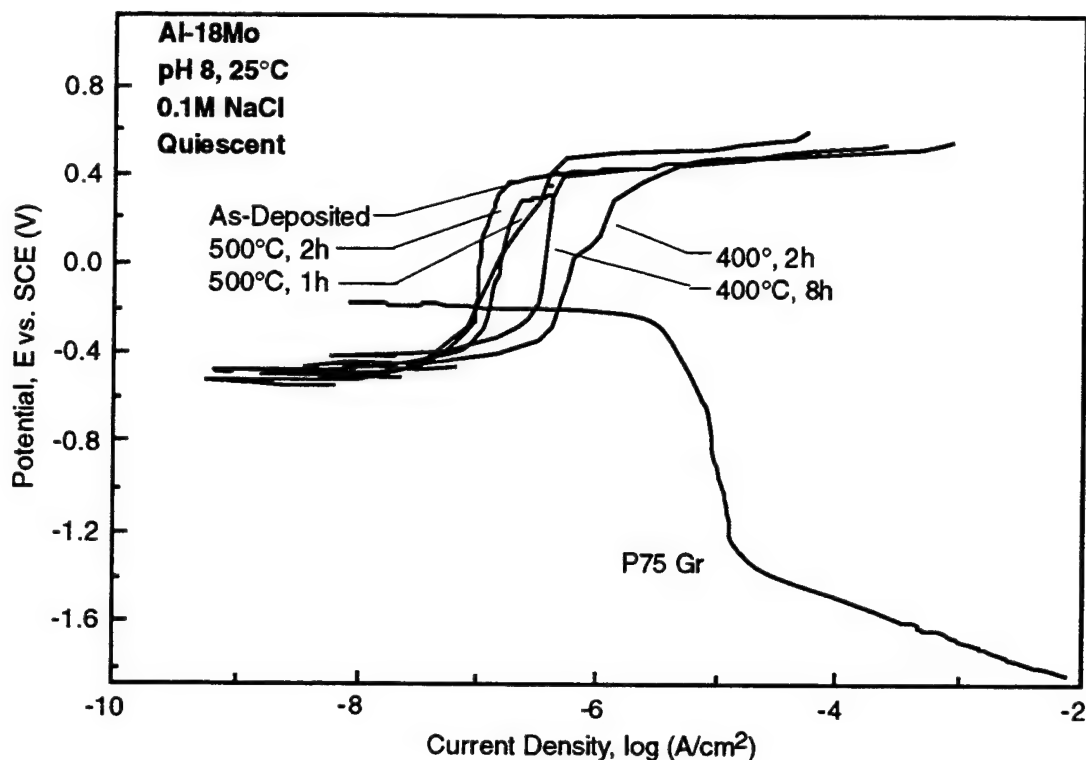
68

Figure 4-46 *Galvanic Diagram for Al-18Mo Alloy Before and After Heat Treatment at 400°C for 2 and 8 h and 500°C for 1 and 2 h With P75 Gr Fibers, Tested in Quiescent 0.1 M NaCl, pH 8, 25°C. (The anode-to-cathode area ratio was equal to one)*
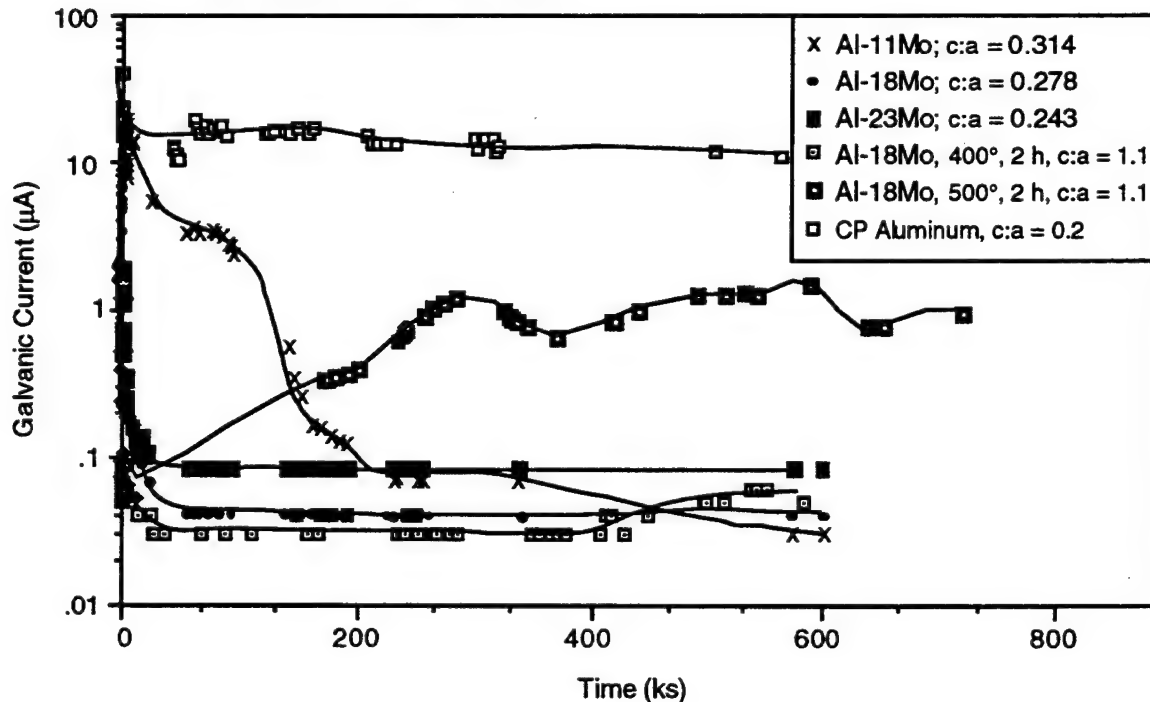

Figure 4-47 *Galvanic Current for Commercially Pure Aluminum and Al-18Mo Alloys (As-Deposited and Heat Treated) Coupled to P75 Graphite Fibers in Quiescent 0.1M NaCl, pH 8, 25°C. (Since the anode area was 1cm² the galvanic current equals the galvanic current density)*

Galvanic corrosion for all of the as-deposited Al-Mo alloys was controlled by the anodic reaction as indicated by the intersection of the passive region of the anodic curve with the oxygen reduction portion of the P75 graphite cathodic curve and the low galvanic corrosion rates observed in the galvanic couple experiments. Galvanic diagrams revealed that galvanic corrosion of the pure Al and the 6061 Al alloy were cathodically controlled and this was confirmed by the relatively high galvanic currents measured in the galvanic couple experiments . For the anodically controlled galvanic corrosion situation, corrosion is limited by passivity of the alloys; whereas, for the cathodically controlled galvanic corrosion situation, corrosion is controlled by the rate of oxygen reduction on the graphite surface. This difference in the rate controlling reaction results in a corrosion rate that is two orders of magnitude lower for the nonequilibrium alloys in comparison to either pure Al or 6061 Al. Since the E_b for the anodic reaction on the Al-Mo alloys are more noble than the E_{oc} for oxygen reduction on the graphite, corrosion of the Al-Mo alloys is expected to be low and stable regardless of the area ratio. Decreasing the anode area (or conversely increasing the cathode area) generally results in lateral displacement of the polarization curves and, as illustrated in Figure 4-48, the corrosion reaction remains anodically controlled. Again, this is beneficial because the composite corrosion behavior will not be adversely affected by increasing the Gr fiber volume.

Even after heat-treatment, the binary Al-Mo alloys exhibited high open circuit potentials of ~-550 mV and breakdown potentials between 100 and 400 mV_{SCE}. As a result, the galvanic diagrams indicate that galvanic corrosion is still anodically controlled and low galvanic corrosion rates (< 1 $\mu A \cdot cm^{-2}$) should be expected.

Hihara evaluated the cathodic polarization behavior of P100 Gr, SiC and, TiB_2 in an aerated 3.15 weight percent (0.55 M) NaCl solution [16]. Figure 4-49 shows that when Hihara's curves are superimposed on the polarization data obtained in this investigation, the cathodic reaction for the P100 graphite fibers (in a solution with a higher chloride concentration) is very similar to the cathodic reaction for the P75 graphite fibers in 0.1M NaCl. The open circuit potentials for both P75 and P100 graphite fibers were approximately 0 mV_{SCE}. Figure 4-49 also reveals that the Al-Mo alloys would be galvanically compatible with other reinforcements, such as silicon carbide (SiC) and with fiber coatings such as titanium diboride (TiB_2), as well. This result is significant because it is the first time that corrosion of graphite reinforced Al-based metal matrix composites has been shown to be controlled by passivity of the matrix alloy rather than by oxygen reduction on the graphite fibers.

4.3.6 · Al-Mo Alloy Mechanical Properties

An understanding of the stress-strain behavior of the Al-Mo alloy was needed in order to evaluate the flow characteristics of the alloy during consolidation. In addition, information concerning the strength of the alloys was needed to evaluate how well the constituent properties were translated to the composite. To provide specimens for mechanical property testing, a thick foil alloy was sputtered through a stainless steel mask onto a 0.38-mm thick copper foil which was 100-mm in diameter. Sputter deposition of the thick alloy film took 92 hours with the aluminum cathode power set at 485 W (RF) and the molybdenum cathode power set at 20 W (DC). This process required that the aluminum target be changed after every 24 to 30 hours of continuous sputtering. During the target change, the alloy/substrate was transferred from the chamber to the load lock and kept under vacuum. After changing the target and pumping the chamber back to a high vacuum (< 5 x 10^{-6} torr), the specimen was transferred back into the chamber and RF etched at 90 W for five

minutes. Following the etch-cleaning step, sputtering was resumed using the same power conditions. After deposition of the alloy, a 500 nm layer of pure molybdenum was deposited onto the alloy surface in order to avoid dissolving the underlying alloy during chemical milling of the copper substrate in a 50 percent nitric acid solution.

Figure 4-50 shows a photograph of the thick film alloy on the copper substrate after the mask was removed. EDS evaluation of the film revealed that it contained 14 atomic percent molybdenum. An optical micrograph of the Al-14Mo alloy cross-section is presented in Figure 4-51. Examination of this micrograph reveals a layered morphology that was created by stopping the sputtering process to change the aluminum target. The total thickness of the free standing foil was ~0.11-mm (0.0045 in.). In addition, the cross-sectional micrograph shows that during the acid etching process the top layer of the alloy pitted.

Hardness--Vickers and Knoop hardness measurements were obtained on a polished cross-section of the thick alloy foil. The average Knoop hardness value from ten hardness tests using a 200 g load was 412 ± 4.8 kg·mm^{-2}. Similarly, Vickers hardness measurements were also made at several different loads from 50 to 700 g, with the average value over five tests of 409 ± 6.5 kg·mm^{-2}. Figures 4-52 and 4-53 show typical diamond indents. A crack formed at the tip of the indentation propagating parallel to the alloy surface on one specimen indented with a 650 g load.

It was difficult to compare this hardness data with other aluminum hardness data because most microhardness data on aluminum has been collected for tests conducted using a 10-mm dia. ball and a 15 kg$_f$ load [59,60]. However, plotting yield strength as a function of hardness of several aluminum alloys showed a linear relationship as shown in Figure 4-54. Linear extrapolation of this data indicates that Al-14Mo alloys with a Vicker's hardness of 409 kg/mm^2 will have a yield strength of 1420 MPa (206 ksi). Therefore, it may be possible that the yield strength of the Al-14Mo alloy is two to three times greater than that of conventional aluminum alloys.
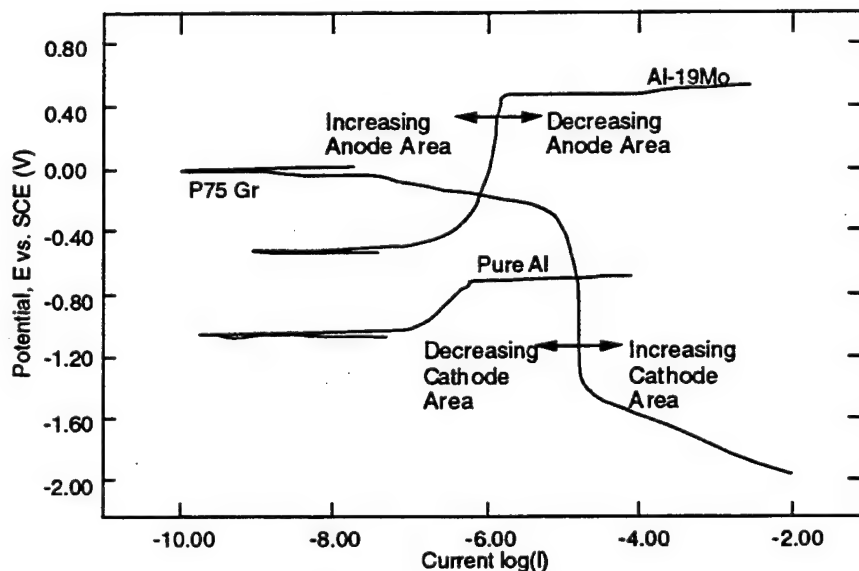

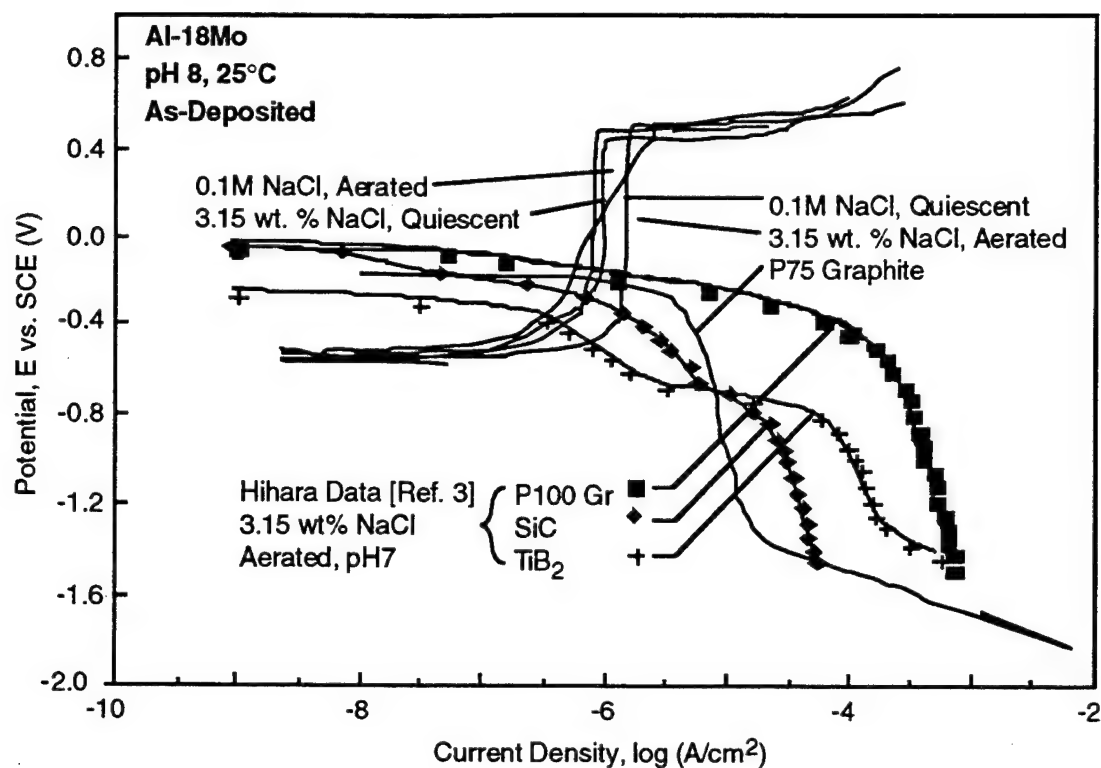*Figure 4-48   Effect of cathode area on galvanic corrosion behavior of MMC composites*

71

Figure 4-49 *Galvanic Diagram Created by Overlaying the Anodic Polarization Data for the Al-18Mo Alloy Tested in Quiescent 0.1M and 0.55 M NaCl on the Cathodic Curves for P75 and P100 graphite, SiC and TiB_2. Cathodic Data for P100 graphite, SiC and TiB_2 taken from Hihara and Latanision [Ref. 16].*
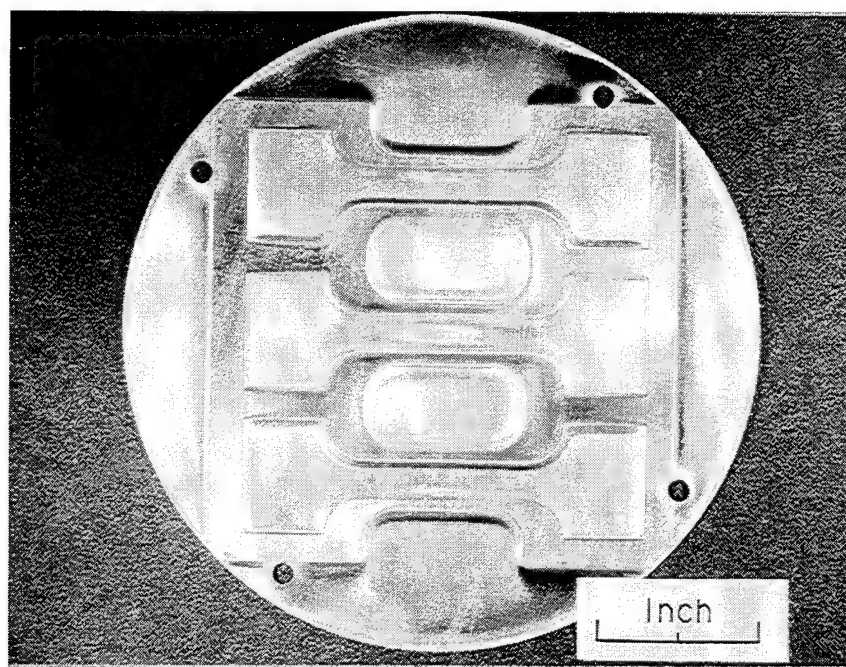

Figure 4-50. *Thick Al-14Mo Film Sputtered onto Masked Copper Substrate to Provide Hardness and Tensile Specimens.*
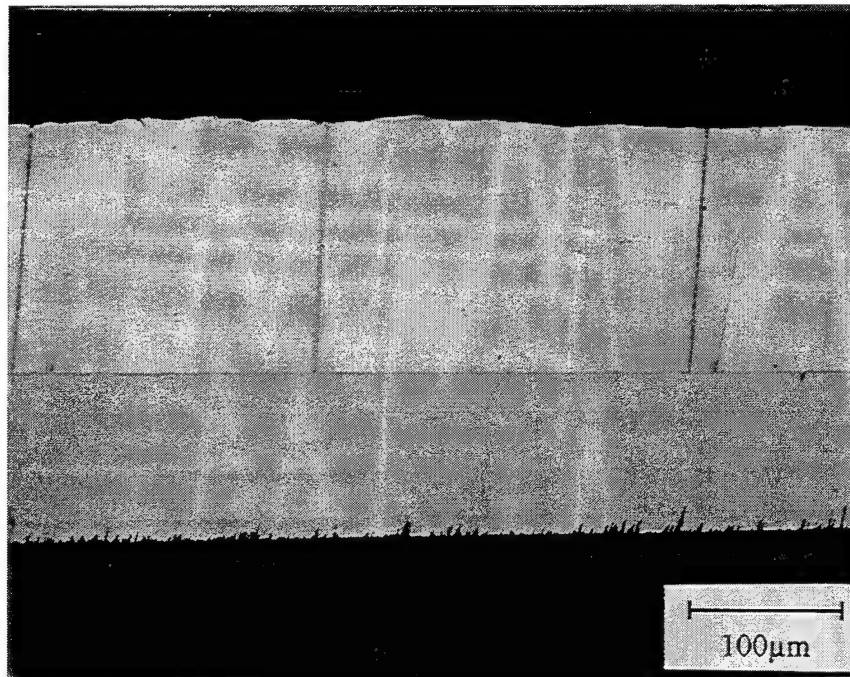
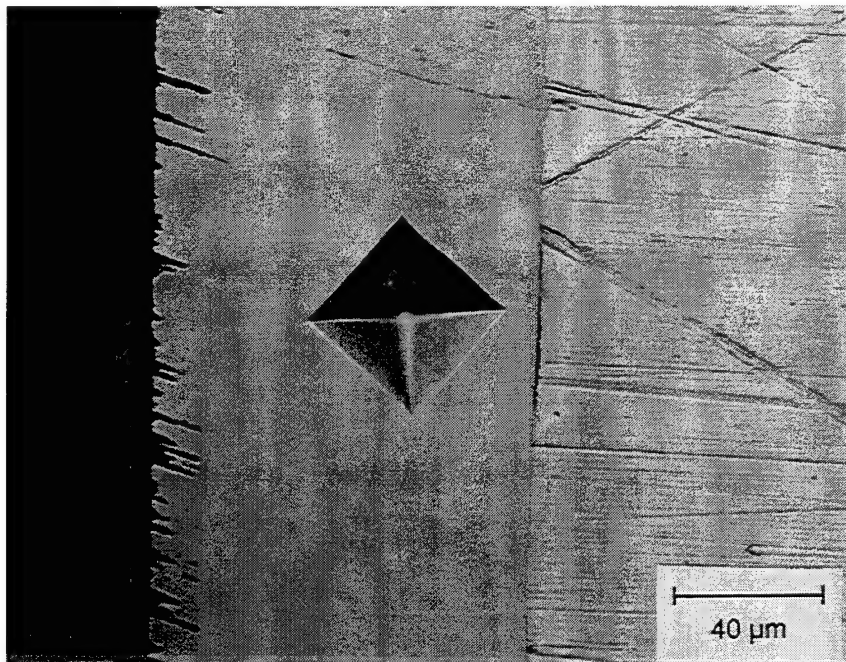Figure 4-51. Metallographic Cross-Section of Thick Al-14Mo Alloy Film Showing Discrete Layers on Copper Backing.

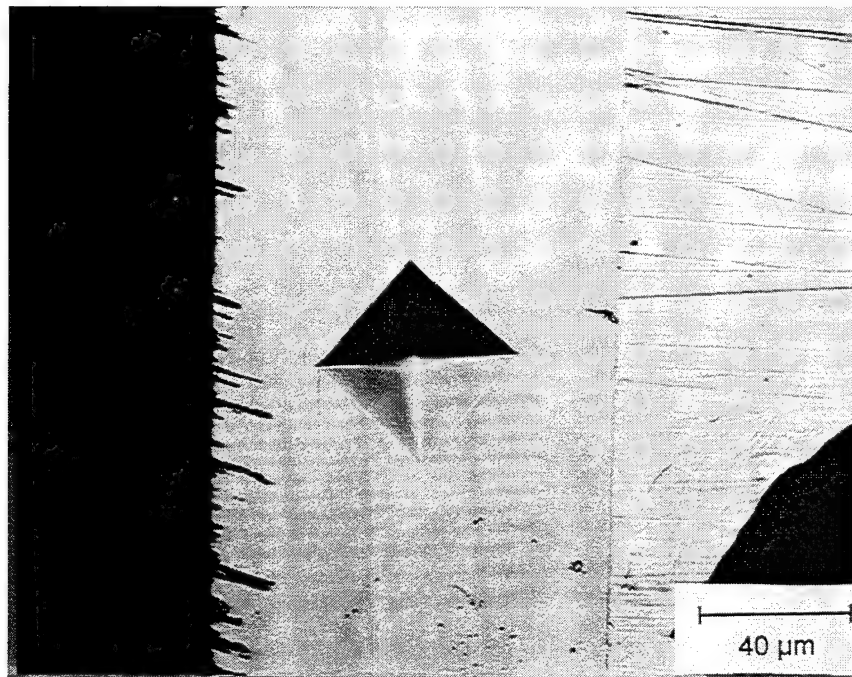Figure 4-52. Vickers Hardness (Diamond Pyramid Indentation) from a 700 g Load.

73

Figure 4-53. *Vickers Hardness (Diamond Pyramid Indentation) from a 650 g Load Showing Cracks Propagating From Diamond Tip Parallel To Substrate Interface.*
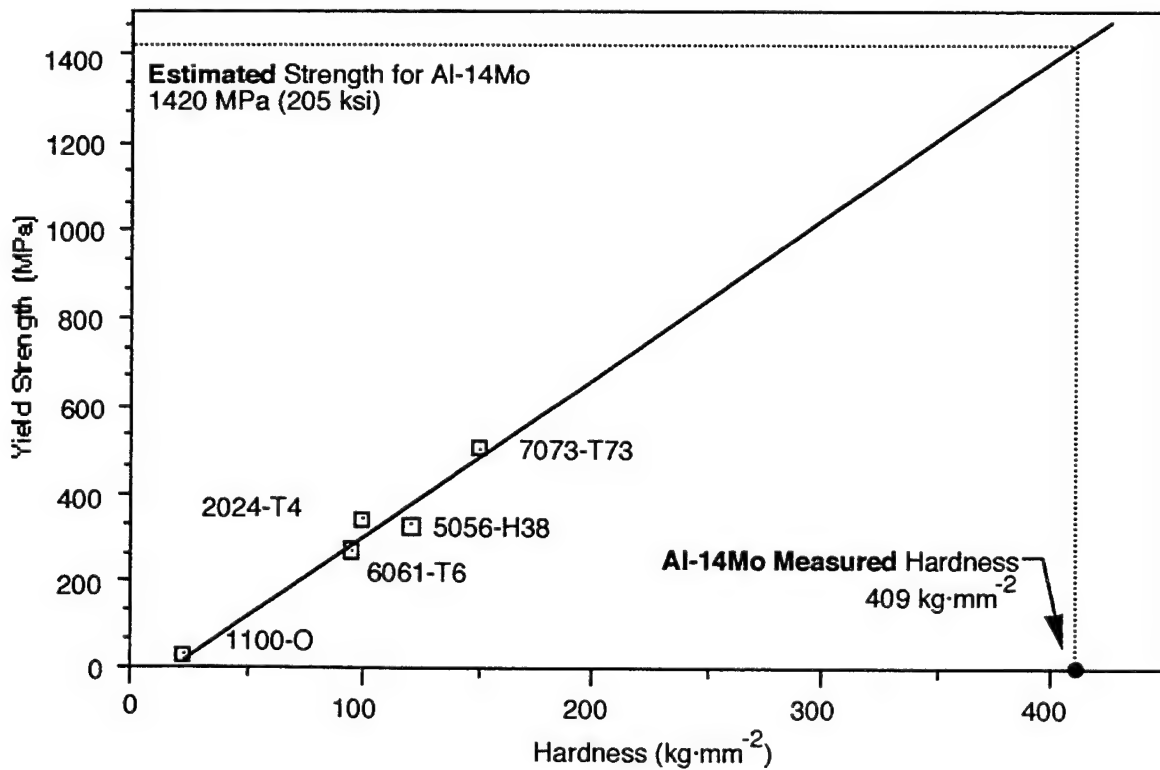

Figure 4-54. *Yield Strength vs. Hardness Plot Showing an Estimated Yield Strength (via linear extrapolation) of 1420 MPa (205 ksi) for the Nonequilibrium Al-14Mo Alloy .*

74

Tensile Properties--Three free-standing tensile dog-bone specimens were fabricated by sputtering the Al-Mo alloy through a stainless steel mask. Load versus deflection curves for each of the alloys were linear, indicating that the specimens had not slipped in the grip ends during testing and that the epoxy was not failing in shear. Measured strength properties represent composite properties of the copper substrate/Al-Mo alloy laminate because the copper was not fully etched from the alloy foil. Therefore, strength of the alloy was calculated using Rule-of-Mixtures [61]:

$$\sigma_L = \sigma_{Al-Mo} \cdot X_{Al-Mo} + \sigma_{Cu} \cdot X_{Cu}$$

where σ is ultimate strength, X is the area fraction of each constituent of the laminate, and L is the laminate. Rearranging to calculate the alloy strength, this equation becomes:

$$\sigma_{Al-Mo} = (\sigma_L - \sigma_{Cu} \cdot X_{Cu})/X_{Al-Mo}$$

Area fractions for the alloy and the laminated structure were measured (using optical microscopy) to be 0.37 for the Al-Mo alloy and 0.63 for the copper. Strength of the copper was established by testing four foils extracted from the same sheet used to make the deposition substrate. The average strength of the copper sheet was 259 ± 25.5 MPa (33.8 ± 3.7 ksi). The measured strength for the alloy/substrate laminate and the calculated alloy strength are presented in Table 4-9.

SEM examination of the tensile specimen fracture surface revealed that the thick foil was made up of columnar grains that extended from the substrate interface to the alloy surface as revealed in Figure 4-49. It appears that when the sputtering process was stopped to change aluminum targets, a new layer was started with the grains growing epitaxially from the underlying grains. The outermost layers of the deposit were porous. Figure 4-56 illustrates the intergranular appearance of the fracture surface. A few fractured columnar fibrils are also apparent in this micrograph. The surfaces on the end of the fractured fibrils were extremely smooth and faceted indicating brittle fracture. However, high magnification examination of the sides of the columnar grain, see Figure 4-57, revealed some submicron dimples, indicating that as the intergranular failure occurred some micro-plastic deformation had taken place.

The tensile strength values for the alloy were considerably lower than what was expected based on the hardness testing. Low tensile strength values are typical for sputtered films because of their textured structure and lower than theoretical density. Testing was conducted transverse to the through-thickness of the columnar grains, which is analogous to transverse testing of a continuous fiber reinforced composite. Due to low strength interfaces between the columnar grains, failure at low stress values occurred. If testing could be conducted parallel to the columnar grains, much higher strength values would be expected.

Table 4-9. *Measured tensile properties of an Al-14Mo thin film alloy (stress was perpendicular to growth direction).*

Specimen	Total Thickness mm (in.)	Ultimate Load kg (lbf)	Laminate Strength MPa (ksi)	Alloy Strength MPa (ksi)
1	0.33 (0.012)	24.9 (54.8)	157 (22.8)	*
2	0.33 (0.012)	32.8 (72.3)	208 (30.1)	164 (23.8)
3	0.33 (0.012)	31.7 (69.9)	201 (29.1)	145 (21.1)

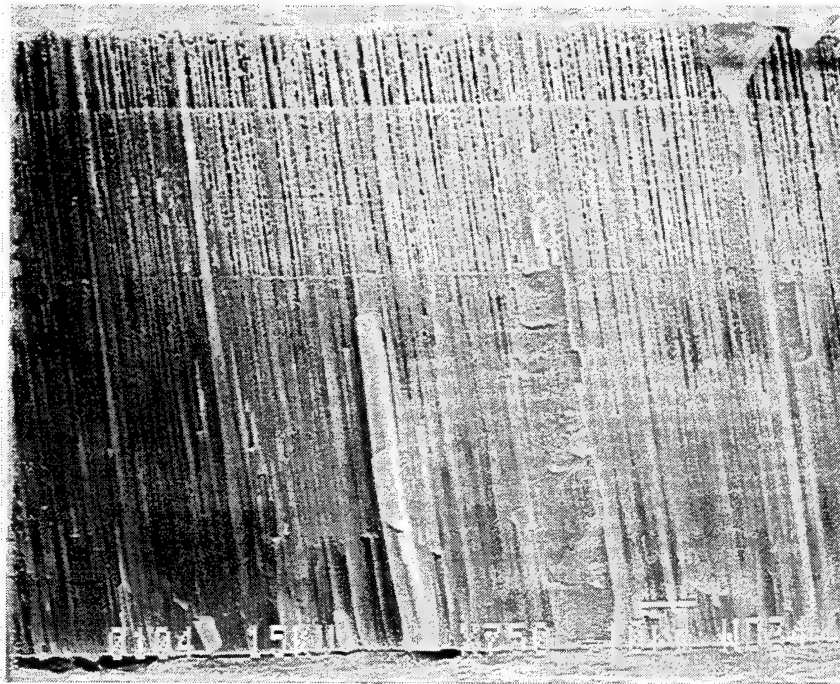* Alloy Contained Through Thickness Defect - Invalid

75

Figure 4-55. SEM fractograph showing columnar morphology of the deposit. Column growth is normal to the substrate.
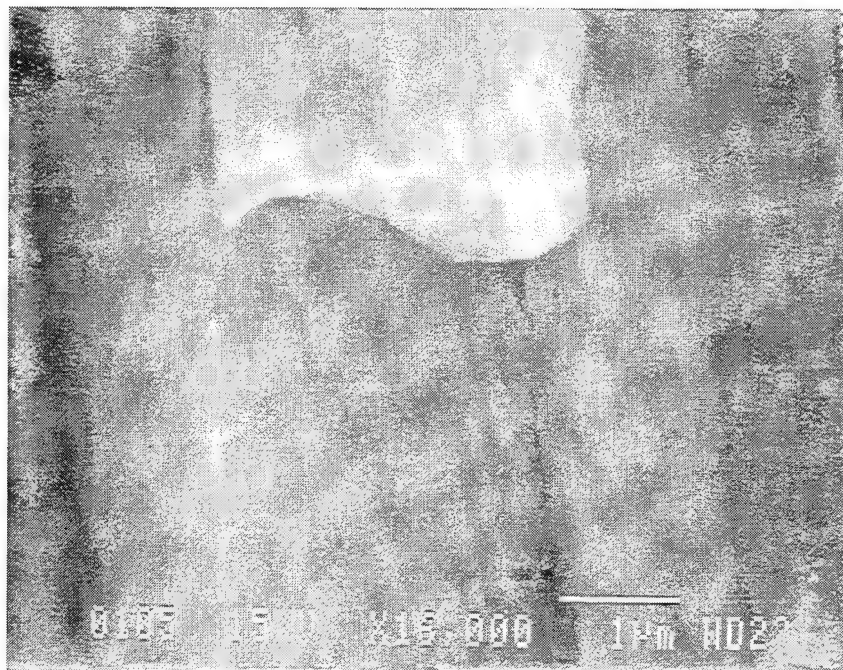

Figure 4-56 SEM Micrograph of the End of a Fractured Column Showing Brittle Fracture.
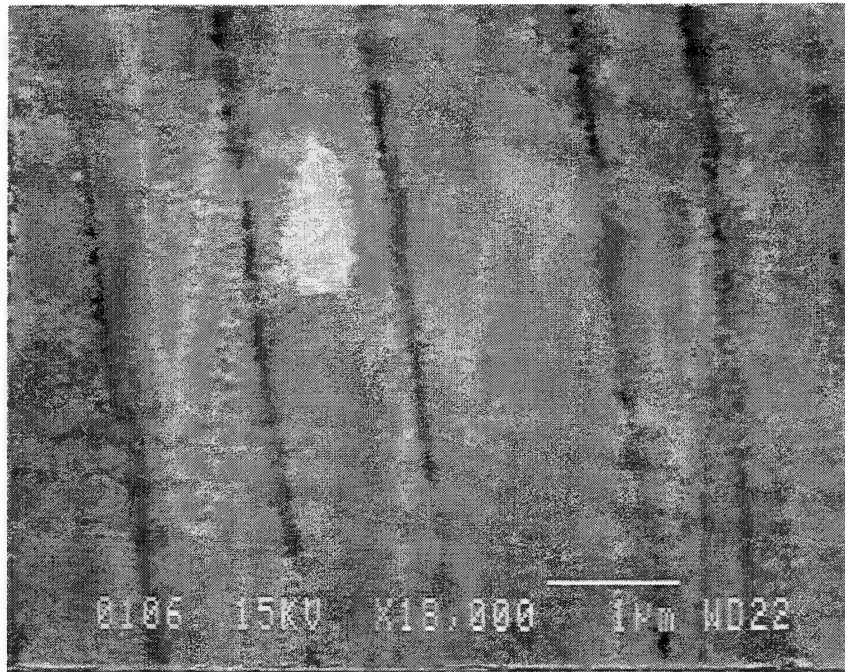
Figure 4-57   Micrograph of the sides of the columns revealing submicron size dimples indicating micro-plasticity.

4.3.7 Thin-Film Alloy Consolidation

An Al-18Mo alloy was used in the hot isostatic press (HIP) studies to establish the parameters needed to consolidate the matrix alloy prior to actual deposition of the alloy on the P75 graphite fibers. The Al-18Mo alloy composition was selected because it exhibited low galvanic current values when coupled to graphite and was the lowest density alloy evaluated that maintained good corrosion behavior after heat-treating to nominal composite consolidation temperatures.

In general, the HIP specimens were prepared by:

• sputtering the alloy on a flexible metallic substrate,

• sectioning the sputtered alloy/substrate into approximately 0.5-inch x 0.5-inch specimens,

• placing two specimens together to create alloy-to-alloy contact,

• vacuum sealing the specimens in a HIP canister, and

• HIPing at prescribed time/temperature/pressure conditions.

After HIPing, the specimens were sectioned, mounted and polished for examination in a scanning electron microscope. The alloy-to-alloy interface was examined to determine if interdiffusion and subsequent bonding had occurred.

Four HIPing experiments were conducted using different substrates and HIP parameters. Details of each of these experiments which were conducted in succession are presented in the next several paragraphs.

Experiment #1 -- A thin (0.010-in) molybdenum foil was used as the alloy substrate for the first HIP experiment. Using the power conditions to obtain an Al-18Mo alloy (Al - 480 W(RF), Mo - 20 W(DC), 7 mtorr Ar overpressure), a 3.75-inch x 3.75-inch Mo foil was coated for 8100 sec for a predicted alloy thickness of approximately 3.0 μm. After sputtering, the Mo foil was sectioned into eight 0.5-inch x 1.0-inch strips and each strip was folded in half in the 1-inch direction to achieve alloy-to-alloy contact.

The specimens were then canned by flattening a 0.5-inch in diameter 304 stainless steel tube that had been welded at one end. The alloy specimens were then placed in the flattened tubes and a vacuum of 5.0 millitorr was applied to the tubes while the opposite end was crimped to create a vacuum seal. The crimped end of the tubes were then welded shut. To ensure that the specimens did not over-heat, the tubes were wrapped in wet cloths during welding.

A total of four specimens were HIPed during the first experiment as listed below:

• 2 Specimens: 400°C. 1 hour, 69 MPa (10 ksi)

• 2 Specimens: 400°C. 4 hour, 69 MPa (10 ksi)

Each canned specimen was placed in a graphite-lined HIP, heated, and allowed to soak at temperature for approximately 15 minutes before the pressure was applied. After HIPing for the prescribed time, temperature, and pressure, the specimen was allowed to cool to

approximately 100°C before the pressure was reduced and the specimen removed from the HIP.

SEM examination of the polished specimen cross-sections showed that the alloy thickness was approximately 4 μm. Alloy adhesion to the Mo substrate was good, but the alloy surfaces that were originally in contact were separated (~20 μm) by a discontinuous product as shown in Figure 4-58. Energy dispersive spectroscopy (EDS) of the region between the alloy foils, shown in Figure 4-59, revealed that the material contained contamination products of Cl, Ti, and S. These contaminants were attributed to capillary wicking of the flux during welding of the HIP cans.

Experiment #2 -- To avoid contamination of the alloy-to-alloy interface in the second experiment, the sputtered alloy/substrate specimens were wrapped in Al foil prior to placement in the HIP can and welding. In addition, a Ni foil was used so that the alloy composition could be measured using EDS without the underlying substrate foil contributing to the Mo peak counts. As before, the power conditions were set to achieve an Al-18Mo alloy (Al - 480 W(RF), Mo - 20 W(DC), 7 mtorr Ar overpressure) while the alloy was sputtered onto a 3.75-inch x 3.75-inch x 0.010-inch Ni foil. After sputtering, the foil was sectioned into 1.0-inch x 0.5-inch specimens which were folded to obtain alloy-to-alloy contact. These specimens were then tightly wrapped in an oil-free Al foil taking precautions not to bend or damage the specimen. For experiment #2, 3003 Al tubing, 0.5-inch in diameter, was used for the HIP can. As before, the tube was flattened and one end welded shut, the specimen placed in the flattened tube, and the opposite end crimped while the tube was pumped to ~50 millitorr.

Table 4-10 shows the HIP parameters for Experiment #2. All the specimens successfully HIPed except for the specimen tested at 500°C for 4 hours which expanded -- indicating that the HIP can was not fully sealed. after HIPing each can was sectioned and the specimen was mounted and polished for SEM examination. Figure 4-60 shows a micrograph of the typical appearance of the specimen cross-sections. This micrograph shows several laminated layers, each of which is the approximate thickness of the original sputtered alloy. Semi-quantitative EDS analysis indicated that each layer contained ~16%Mo. The unusual microstructure seen in the micrograph presented in Figure 4-60 was noted for all of the specimens listed in Table 4-8. These microstructures suggest that the alloy fractured either during canning, HIPing, cool down from the HIP temperature, or during sectioning and polishing. It is most likely that the alloy fractured during cool down from the HIP temperature and flaked and fell out of the cross-section during polishing. In any case, no evidence of consolidation at the alloy-alloy interface was evident. In a few locations, a complex microstructure of intermixed Ni and alloy particles was found as Figure 4-61 reveals. A unique feature of these regions was that the alloy sputtered onto the Ni foil remained intact. This suggests that the Ni substrate and alloy in adjacent regions must have fractured and moved to the surface during polishing.
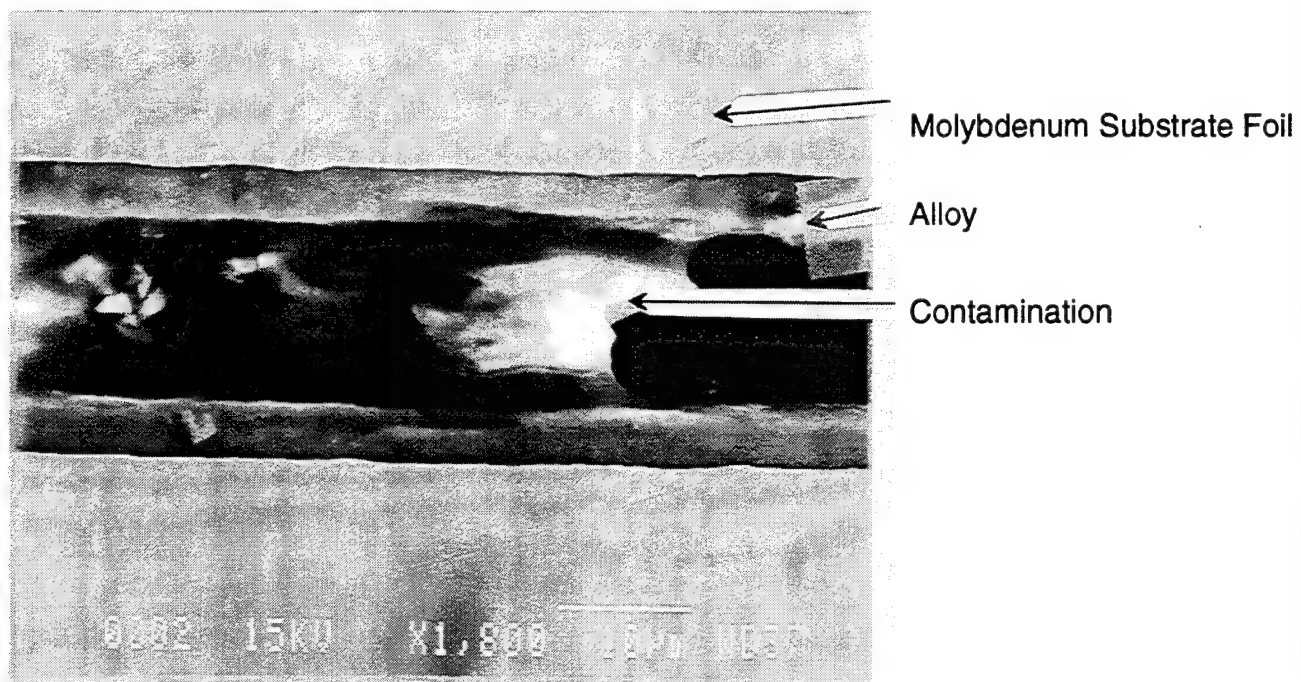
Figure 4-58 SEM of the Al-18Mo alloy after HIPing at 450°C for 1h showing contamination between the alloy foils and lack of consolidation.
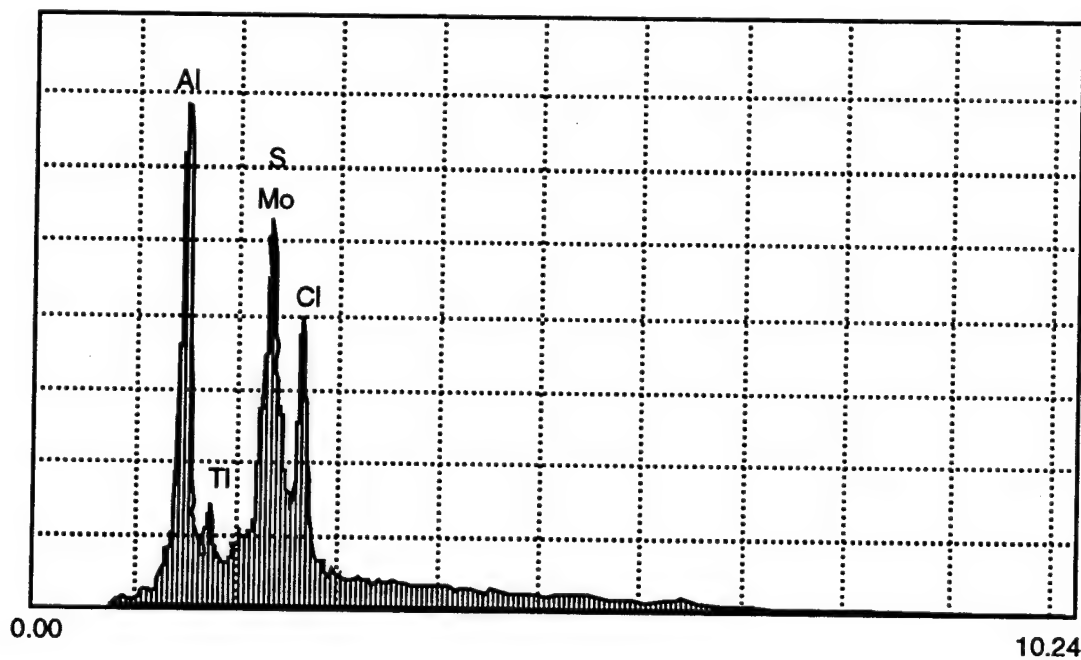
Figure 4-59. EDS Spectra of contaminated region between nn-consolidated Al-18Mo alloy foils after HIPing at 450°C for 4 hours.

81

Table 4-10. HIP Parameters for Experiment #2

Alloy	HIP Parameters			Result
	Temperature, °C	Time, hr	Pressure, ksi	
Al-18Mo*	400	1	25	Passed
	400	4	25	Passed
	450	1	25	Passed
	450	4	25	Passed
	500	1	25	Passed
	500	4	25	Failed†

* Al.480.C.Mo20.Mo.20930.1 → estimated composition based on previous measured results using the same power conditions and pressure.
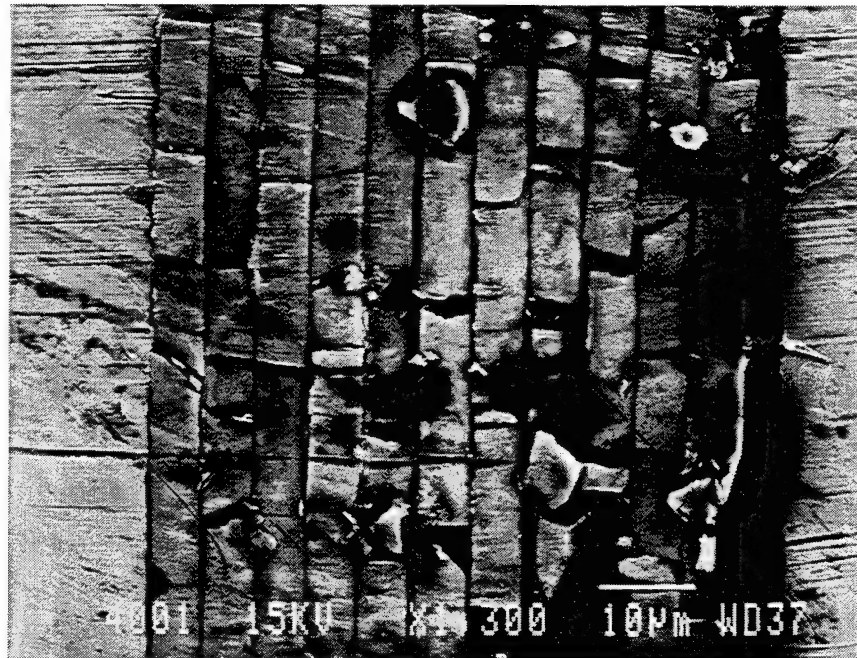

Figure 4-60   Typical microstructure of specimens HIPed during Experiment #2 showing lamellar structure of fractured alloy and the underlying Ni substrate.
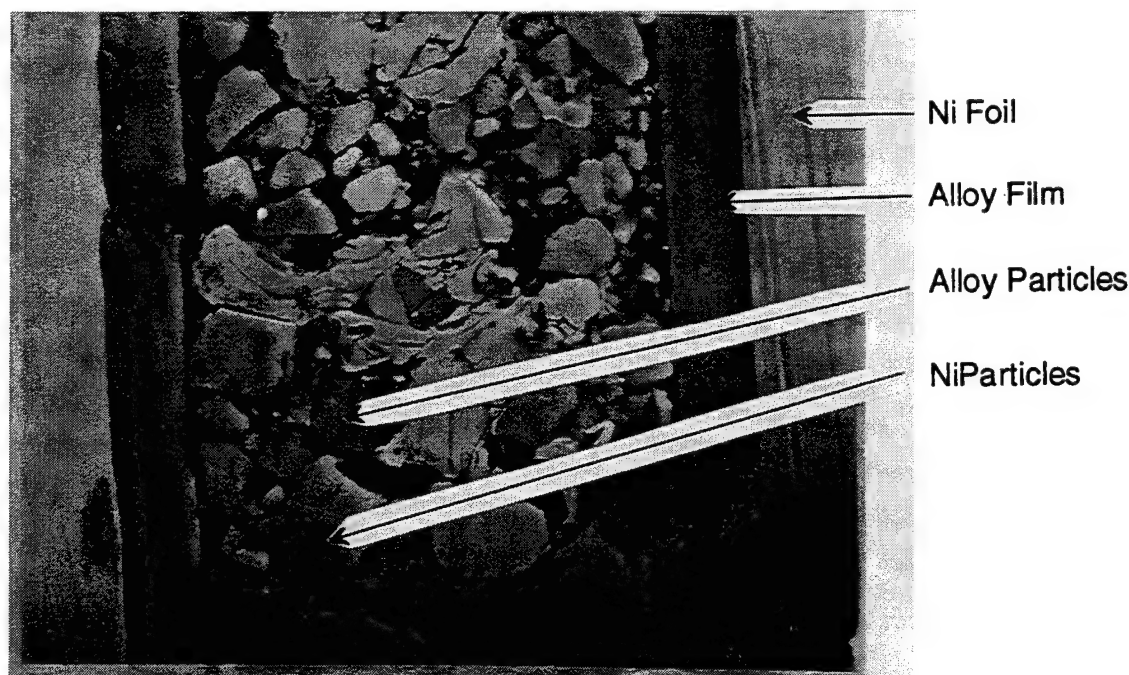
82

Figure 4-67   Region showing intermixture of Ni and Alloy particles suggesting failure of the alloy/Ni substrate during HIPing.

Experiment #3 -- In the previous two HIP experiments, the Al-18Mo alloy film appeared not to consolidate at all. From the previous XRD studies, it was found that the alloy did not precipitate after heat-treatment at 400°C for up to 8 hours. However, lack of precipitation is a good indication that diffusion of constituents within the alloy is extremely sluggish. Therefore, maintaining corrosion resistance by preventing precipitation may have decreased the kinetics of diffusion to the point where consolidation would be impossible in a reasonable period of time. Therefore, in the third experiment, a few new alloy combinations were investigated as listed below.

Specimen #1: Al-11Mo (Precipitated),

Specimen #2: Al-18Mo with an ~1000Å layer of pure Al on the surface,

Specimen #3: A continuously graded alloy ranging in composition from Al-18Mo adjacent to the substrate to pure Al at the surface, and

Specimen #4: A pure Al film in contact with a Al-18Mo film.

In the earlier studies, the Al-11Mo alloy precipitated during heat-treatment but still exhibited enhanced corrosion resistance when compared to pure Al or 6061Al. Precipitation indicates that the kinetics of diffusion may be great enough to get interdiffusion at the alloy-alloy interface. Therefore, the Al-11Mo was selected as the first alloy for this HIP study. The second specimen in this study contained a thin layer of Al over the Al-18Mo alloy (Specimen 2) to create a very thin layer where the local diffusion should approach the self-diffusion coefficient for pure Al. The third specimen evaluated was a graded alloy which was also fabricated to achieve higher localized diffusion at the surface while maintaining a good corrosion behavior underneath. The fourth specimen in this study was a layered film with pure Al on top of the Al-18Mo alloy. This specimen was evaluated to see if the local diffusion kinetics could be improved by bonding across an aluminum-aluminum interface.

83

In experiment #4 the specimens were canned as in experiment #2 and all HIPed at the same time, temperature, and pressure conditions of 4h, 500°C, and 25 ksi, respectively. Similar to the previous experiments, the specimens were placed in the HIP and heated to the 500°C before the pressure was applied.

Specimens 1 and 2 successfully HIPed, but specimens 3 and 4 expanded indicating that the can had not fully sealed. SEM micrographs of representative regions of specimen 1 and 2 are shown in Figure 4-62 and 4-63. Large areas of the tantalum substrate were observed in the region between the substrate foils. It appeared that the substrate yielded and flowed into the region between the two contacting foils. This was especially evident in Figure 4-63 which showed a large globular particle slightly below the polished surface. The entire cross-section of each of these alloys was carefully scanned and no regions of alloy consolidation were found.
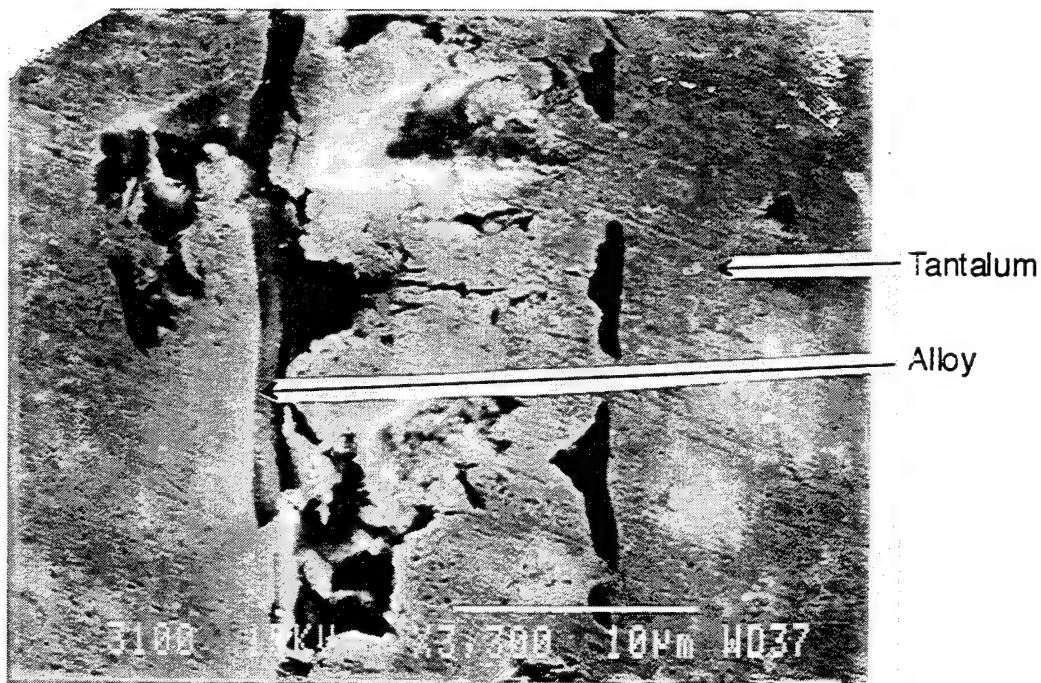

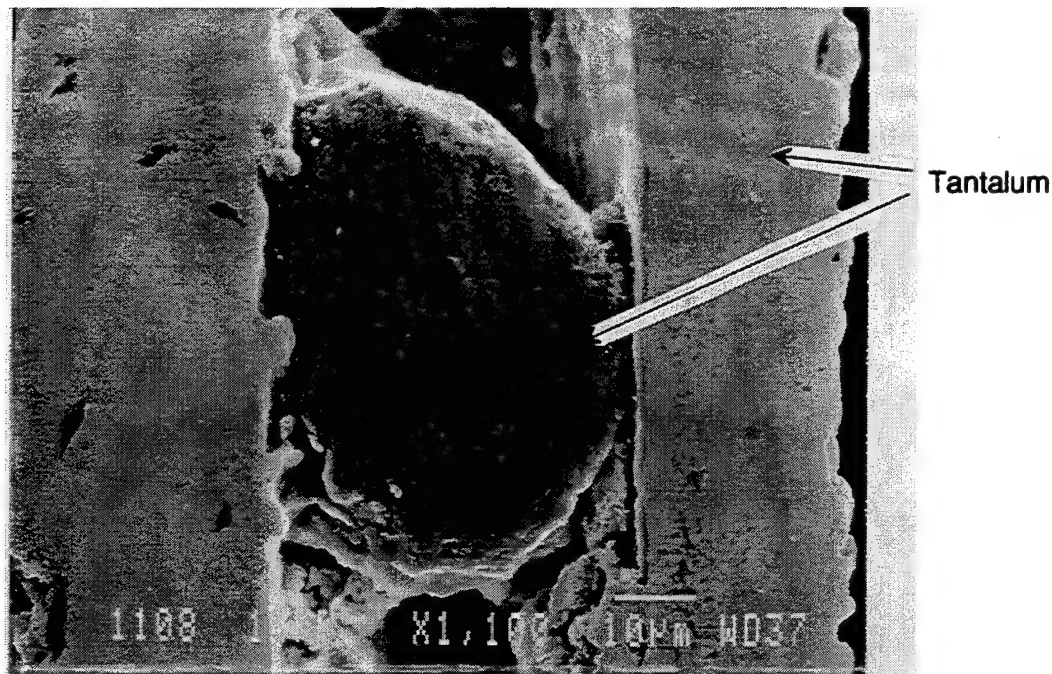*Figure 4-62.* *SEM Micrograph showing Ta Foil extruding out In-between the Substrate Foils.*

Tantalum

Figure 4-63   Large Ta Globule Slightly Below the polished Cross Section Surface.

Experiment #4 -- To alleviate problems associated with the reaction and deformation of the metallic foil substrates, 0.005-inch thick flexible graphite substrates were used in experiment #4. The two alloys listed below were deposited onto the graphite foil:

Specimen 1: Al-11Mo

Specimen #2 Al-18Mo with an ~1000Å layer of pure Al on the surface.

Successful consolidation was achieved for both of these alloys when HIPed at a temperature of 500°C and a pressure of 69 MPa for 240 min. Figure 4-64 shows confirmation of this consolidation for the Al-18Mo alloy. Based on these results, an alloy with a Mo concentration greater than 11% and less than 18% was chosen for deposition onto the graphite fibers.
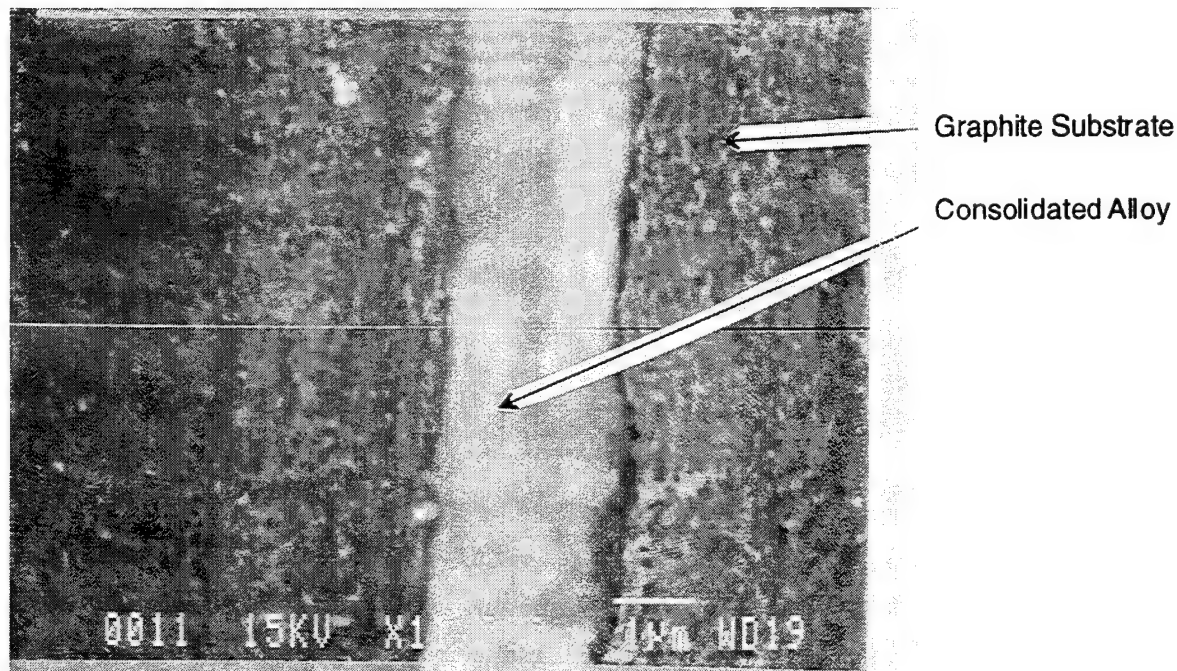

Figure 4-64. HIP specimen made up of two Al-18Mo thin-film alloys in contact with each other after successful consolidation by hot isostatic pressing (HIPing). HIP Parameters: 450°C, 69 MPa, 60 minutes

86

4.3.8   Alloy Deposition on Gr Fibers

4.3.8.1 Deposition and Characterization

Aluminum alloyed with greater than 11% and less than 18% Mo was targeted as the optimum alloy composition because these alloys showed promise for consolidation and retained enhanced corrosion resistance after heat treatment while minimizing the impact of the higher Mo concentrations on alloy density. Several fiber coating trials were conducted on a commercial in-line sputter system, at Cordec Incorporated, designed for rapid deposition of alloys onto graphite fibers. Targets were fabricated by machining slots in high purity (99.99%) Al plates and inserting high purity (99.9%) Mo slugs into the slots. Composition was controlled by modifying the area ratio of Mo and Al. Initially a hollow cathode configuration was investigated, but the alloy coated fibers produced with this system contained residual stresses that caused the fibers to curl. Therefore, an upper and lower planar target arrangement was used to coat the graphite fibers. Results from both the hollow cathode and planar cathode deposition methods are presented in the following section. Amoco P75 and P120, and DuPont E120 graphite fiber tows containing 2000-7 μm diameter fiber filaments were coated in this segment of the investigation. Alloy thickness on the fiber was targeted at 3 μm to achieve a consolidated composite fiber volume of 50 % as shown in Figure 4-65.
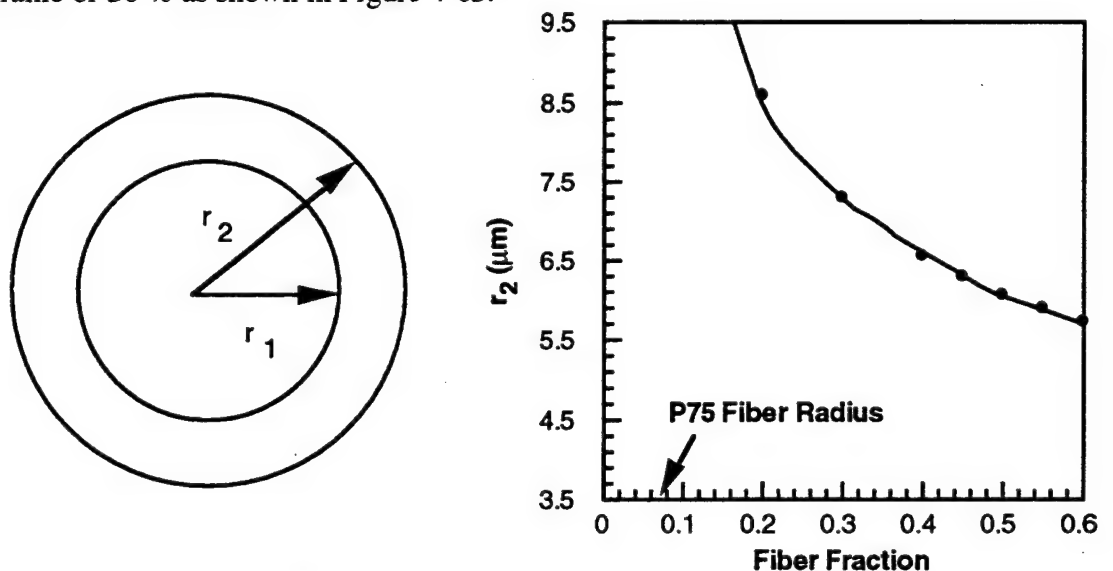

Figure 4-65. Fiber volume as a function of alloy thickness on the graphite fiber.

Hollow Cathode Fiber Coating -- Initially a hollow cathode magnetron configuration was used in which the spread fibers were passed through the center of a cylindrical cathode. Advantages of the hollow cathode arrangement are that the alloy thickness around the fiber is very uniform and the target yield is high (>90%). The hollow cathode was fabricated from a pure aluminum hollow cylinder into which Mo plugs were inserted. Approximately 90 grams (280 linear meters) of fiber were coated in the hollow cathode configuration. Although the fiber coating was fairly uniform, semi-quantitative EDS analysis indicated a Mo concentration of only 3 atomic percent. In addition, the alloy coating was in compression and caused to the fibers to curl when removed from the mandrel. The curling made it very difficult to handle the fibers and, as a result, use of the hollow cathode configuration was discontinued.

87

Planar Cathode Fiber Coating -- In this process, spread fibers were passed between upper and lower 15-inch x 8-inch planar cathodes. The cathode targets were fabricated from pure Al with slots machined across the target into which Mo plugs were inserted. Initially, the Al:Mo ratio was scaled proportional to the area ratio used in the hollow cathode experiment to achieve 15 to 18 atomic percent Mo. This target configuration was used to coat approximately 100 meters of fibers. Although the coating was uniform, semiquantitative EDS compositional analysis indicated the alloy contained approximately 30% Mo. In the next trial run, half of the Mo plugs were removed and an additional 100 meters of fibers were coated. Semi-quantitative EDS analysis of this run indicated a Mo concentration of 17 atomic percent. Once a Mo concentration of 17 atomic percent was achieved, 0.91 kg (2800 meters) of fiber were coated. Figure 4-66 shows a an SEM micrograph of the cross-section of the coated fiber, and Figure 4-67 shows an SEM micrograph of the morphology of the sputter-deposited alloy. The ~2 - 3 μm thick coating exhibited a morphology similar to conventional pure Al and 6061 Al-coated graphite fibers.
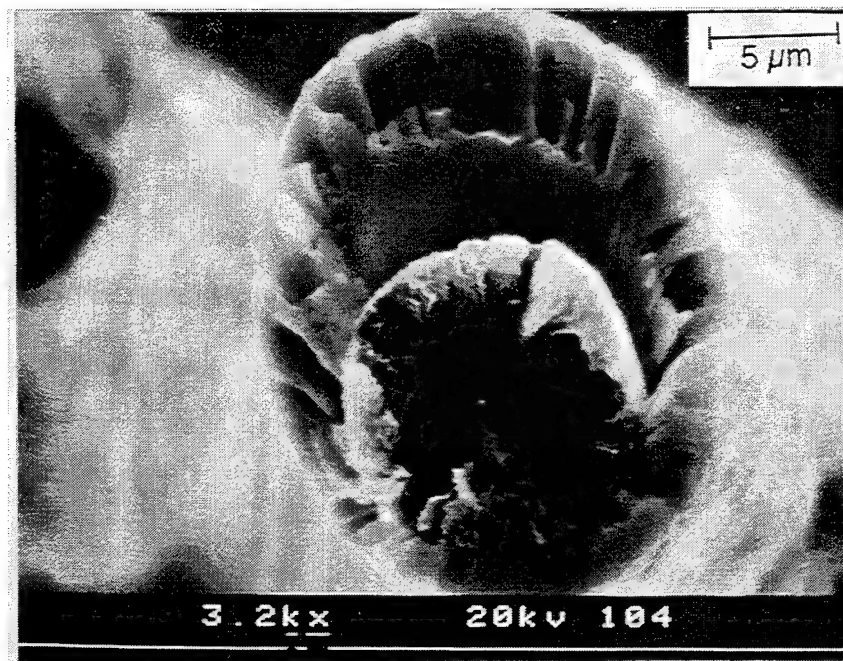

Figure 4-66   Cross-Section of an Al-Mo Alloy Coated Graphite Fiber.
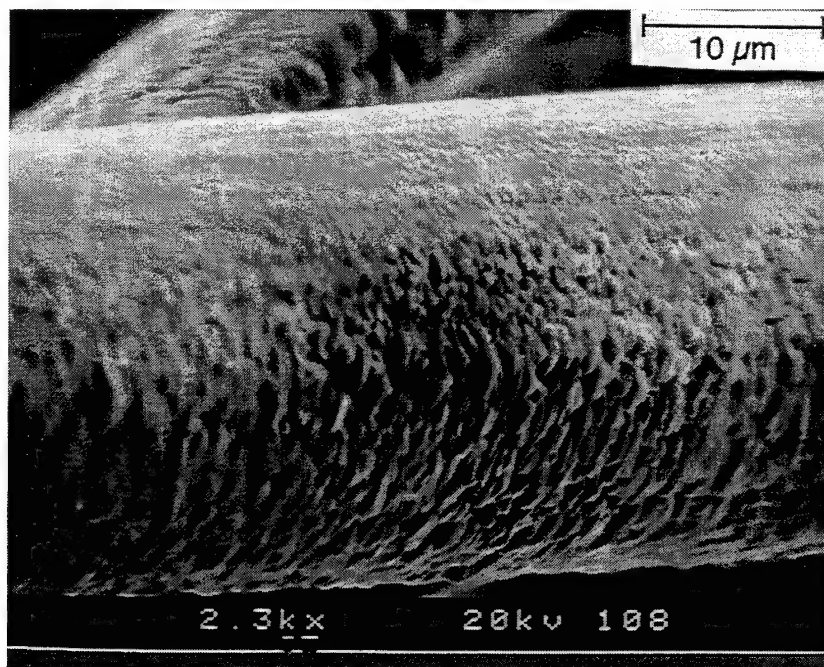
Figure 4-67. SEM micrograph of coated graphite fiber showing surface morphology.

X-ray diffraction of the alloy coated fibers, presented in Figure 4-68, revealed that the alloy contained both some amorphous material as indicated by the broad peak at diffraction angles of 21° and 41° (similar to alloys that were sputtered onto Si wafers) and some crystalline material which was indexed to aluminum shifted to slightly higher diffraction angles. From the diffraction angles, d values were calculated for each peak using Bragg's law [62,63]. Using the space lattice relationship for cubic structures:

$$\frac{1}{d^2} = \frac{h^2 + k^2 + l^2}{a^2}$$

a lattice parameter, a, of 4.010 Å was calculated for the crystalline Al-Mo. Since Mo is in solid solution with the Al, the atomic percent of Mo can be calculated based on the peak shift according to Figure 4-6989. The lattice parameter, a, for pure Al can be calculated using simple geometry and the diameter of the atoms:

$$a^2 + a^2 = (2d)^2$$
$$a = \sqrt{2}d$$

By solid solution substitution of the smaller Mo atom in the Al face-centered-cubic lattice, the lattice parameter can be calculated by the following:

$$a^2 + a^2 = [(1 - X_{Mo})d_{Al} + (X_{Mo})d_{Mo}]^2$$

$$a = \sqrt{2}\,[(1 - X_{Mo})2.86 + (X_{Mo})2.72]$$

where X is the atomic fraction of Mo in solid solution in the face-centered-cubic lattice. Using this relationship, a Mo concentration in the alloy of 17.5 atomic percent Mo alloy was calculated which correlated with the 17 atomic percent Mo measured using semi-quantitative EDS.
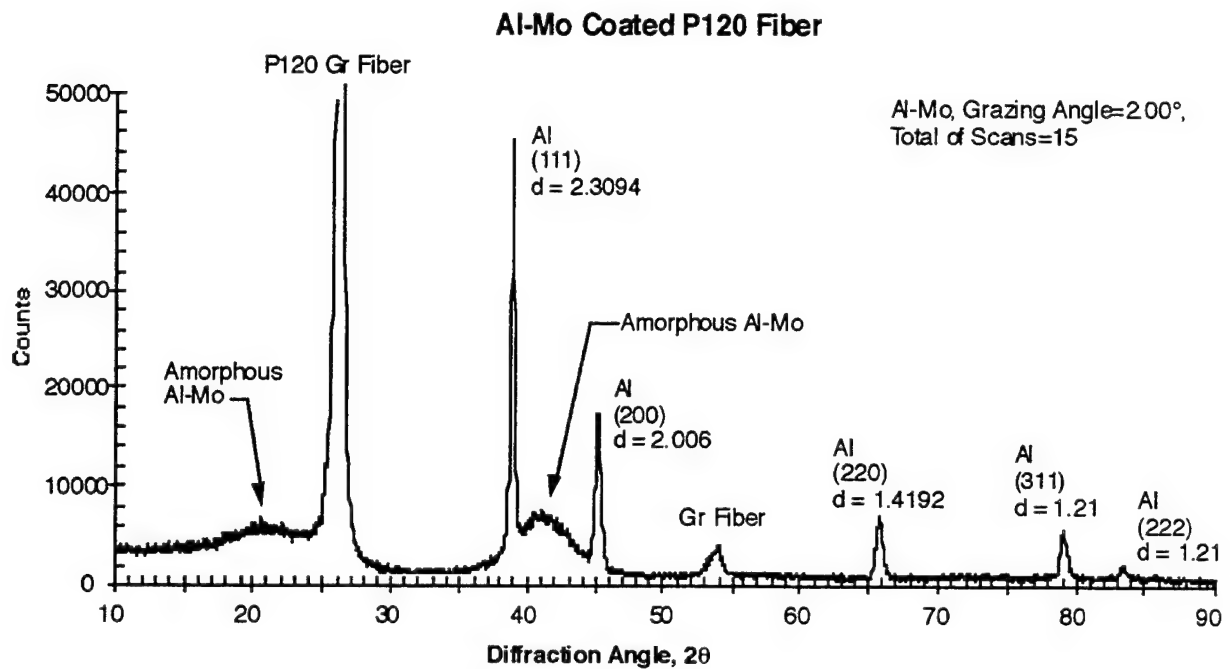

Al-Mo Coated P120 Fiber

Figure 4-68. *X-ray Diffraction Pattern for the Al-17Mo alloy coated P120 Gr Fiber Showing the Presence of both an Amorphous Phase and a Solid Solution Phase of Mo in FCC Al.*
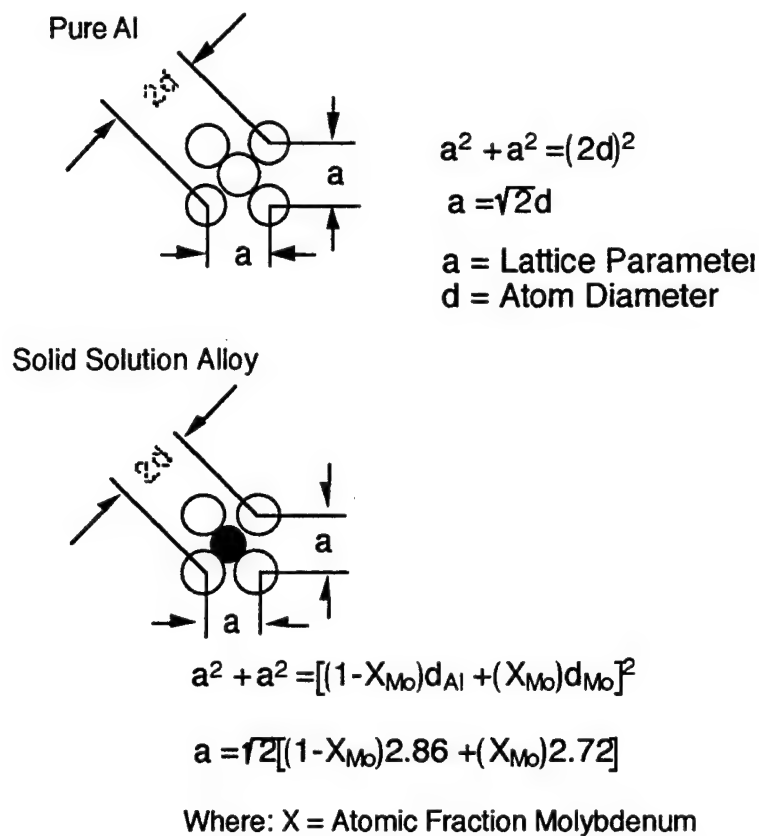
90

Pure Al

$$a^2 + a^2 = (2d)^2$$

$$a = \sqrt{2}d$$

a = Lattice Parameter
d = Atom Diameter

Solid Solution Alloy

$$a^2 + a^2 = [(1-X_{Mo})d_{Al} + (X_{Mo})d_{Mo}]^2$$

$$a = \sqrt{2}[(1-X_{Mo})2.86 + (X_{Mo})2.72]$$

Where: X = Atomic Fraction Molybdenum

Figure 4-69. *Schematic Illustration of the Relationship Between the Lattice Parameter and Atomic Fraction of Solid Solution Mo in Al.*

4.3.8.2 Electrochemical Corrosion Testing--Several attempts to anodically polarize individual fibers in EG&G-type flat cells were made without success. As a result, another electrochemical cell configuration was tried. This cell which also employed a standard three electrode technique for polarizing the specimen is shown in Figure 4-70. In this cell, the coated graphite fiber was placed between 2 buna-N o-rings and electrical contact was made by stacking Cu pennies to a level high enough to support the ends of the graphite fiber without applying any bending stress and using silver paint to couple the graphite fiber to each stack of pennies.

An anodic polarization curve for the coated graphite fiber is shown in Figure 4-70. The passive current density in this curve differs from that of the sputtered Al-15Mo alloy on the Si substrate by approximately one order of magnitude. This difference in passive current density is believed to be a result of error in determining the actual surface area of the coated graphite fiber. Figure 4-67 revealed that the alloy coating was rather rough, making an accurate estimation of the actual surface area difficult. It was estimated that the apparent area used in determining the current density could have been of by a factor of 2 or more, hence explaining the discrepancy. Figure 4-72 is a SEM micrograph of the coated fiber taken after polarization. The dark regions in the lower magnification photo are believed to be the sites where localized degradation of the coating initiated. Despite the fact that the breakdown potential for the individual coated fibers was less than that of the alloys on Si substrates, the coated fibers still showed polarization behavior superior to that of pure Al. In addition, the distinct columnar structure of the alloy coating is expected to densify during consolidation.

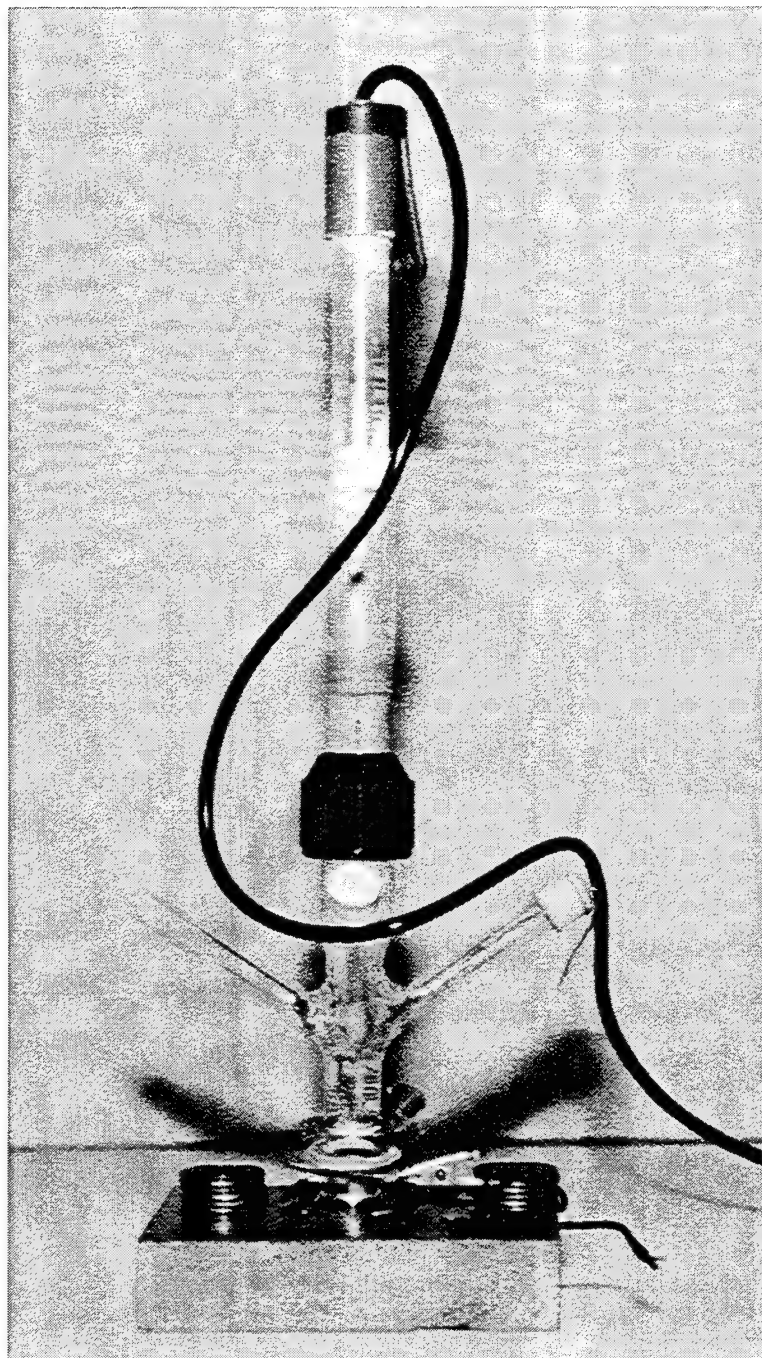*Figure 4-70. Electrochemical cell used for the testing of coated graphite fibers.*
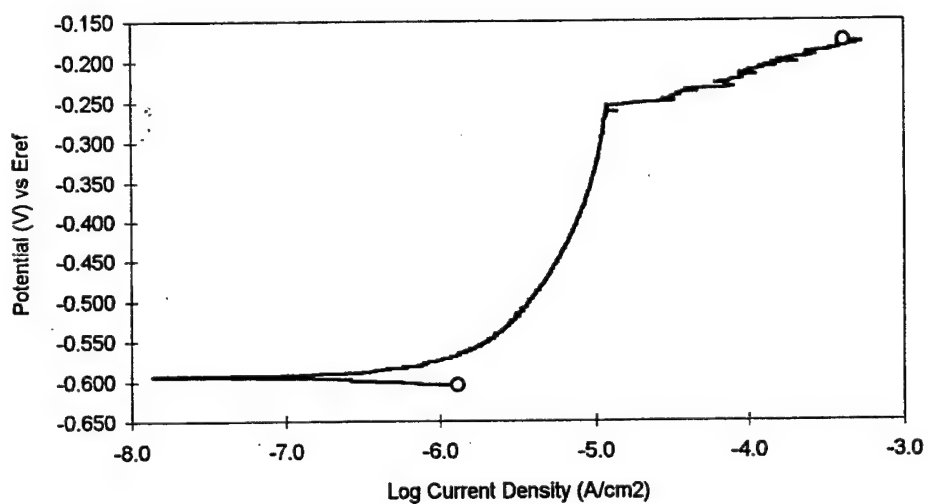
Figure 4-71   Anodic polarization curve for a single coated-graphite fiber   (Al-17Mo   on P120   graphite)   polarized   at   a   scan   rate   of   0.2mV/s   in   0.1M   NaCl.
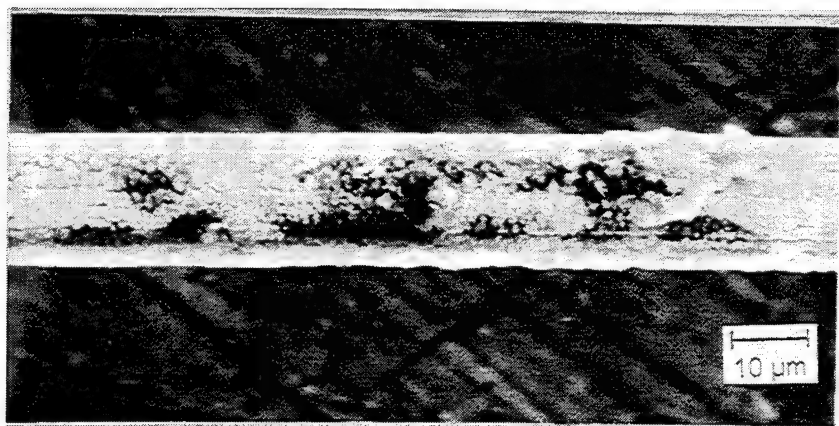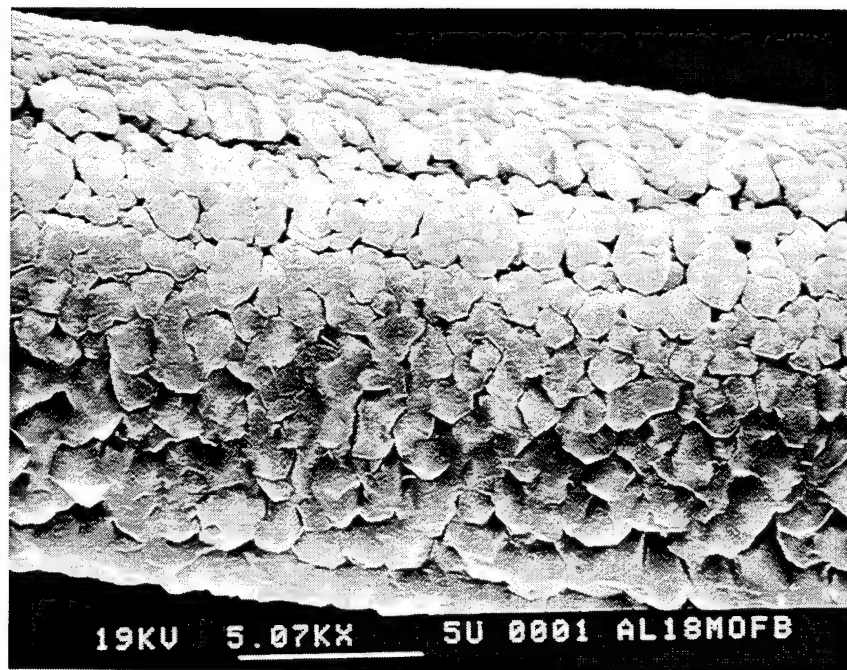
93

Figure 4-72   *SEM micrograph of Al-Mo coated graphite fiber taken before (top) and after (bottom) anodic polarization in 0.1M NaCl.*

94

4.3.9 Consolidation Trials and Testing

Consolidation trials (via hot pressing) were conducted on the Al-17Mo alloy coated fibers at both Martin Marietta and Cordec, Inc. For each consolidation trial, the preforms were created by unidirectional orientation of the coated fibers between Al foils. Preform fabrication and tooling arrangement for the Cordec panels are listed in Cordec proprietary reports. Table 4-11 lists the results of the consolidation study conducted at Cordec and Table 4-12 lists the results of the consolidation study conducted at MMSS. The best consolidation was achieved on the Cordec specimen hot pressed at 550°C at a pressure of 8 ksi for 240 min.

Table 4-11.   *Consolidation Parameters for the Corrosion Resistant Al-Mo/Gr Panels*

Specimen Number	Number of Plies	Panel Size l x w x t	Temperature (°C)	Pressure (ksi)	Time (min.)	Comments
P2-495	72	7x4x.050	500	4	60	Poorly Consolidated
P2-495R	65	7x2.4x0.042	600	2 8	10 30	Trimmed delaminations from P2-495 and re-pressed. Good consolidation with delamination in one corner
P2496	54	7x4x0.035	500	8	240	Some consolidation, retained as pressed.
P2-497	54	7x4x0.027	500	8	60	Vacuum bag not opened because results on P2-495
P2-497R	54	7x4x0.027	600	8	60	Re-press of P2-497. Some cladding adhered to tooling and ripped. Metallography showed some fiber bonding, but several voids evident.
P2-498	60	7x4x0.027	600	3 10	15 30	Partially delaminated during removal from tooling.
P2-499	60	7x4x0.027	550	8	120	Panel stuck to tooling, but did not delaminate.
P2-500	60	7x4x0.027	550	8	120	Increased cladding thickness to 0.005-in.. Completely delaminated.
PR-615	60	7x4x0.027	600	10	60	Tested various schemes for parting the panel from the tooling and decided to change the colloidal graphite release agent.
P2-501	60	6x6x0.033	600	8	120	Used 1100 aluminum coated Celion C12000 fibers to test new release agent. Good consolidation with no cladding delamination.
P2-502	60	6.5x2x0.027	600	8	60	Good consolidation, no sticking, few small voids
P2-503	60	6.5x2x0.027	550	8	120	Good consolidation, no sticking, few small voids
P2-504	60	6.5x4x0.027	550	8	240	Good consolidation, no sticking, few small voids

Table 4-12 Consolidation Parameters for the Composite Panels Produced at MMSS.

Specimen Number	Temperature (C)	Pressure (ksi)	Time (minutes)	Comments
T-1	540	15	120	oxidized surface
T-2	560	20	120	oxidized surface
T-3	560	10	120	oxidized surface
T-4	552	35	120	oxidized surface
T-5	545	35	120	oxidized surface

4.3.9.1 Composite Characterization

Metallographic examination of cross-sections of the best diffusion bonded specimens from Martin Marietta and Cordec was conducted and micrographs of these specimens are presented in Figures 4-73 and 4-74 respectively. Note that the Martin Marietta specimen was produced at a higher pressure. The Martin Marietta specimen contained numerous microstructural voids and severe oxidation of the foil surfaces. In addition to these problems, small cracks were noted in the matrix adjacent to some of the fibers as revealed in the micrographs shown in Figure 4-73 c and d. In Figure 4-73 c it is also possible to see one of the pure Al inter-layers that was added to the composite to aid in bonding. Close examination of the microstructure revealed that the pure Al flowed into areas around the coated fibers. The flow of this pure Al is more clearly evident in the higher magnification optical image shown in Figure 4-75. As Figure 4-74 reveals, the diffusion bonded Cordec specimens exhibited less porosity and surface foils which were mostly intact. The micrograph of the P2-504 specimen presented in Figure 4-74 a shows that in some places the graphite fibers were exposed at the surface. Examination of the surfaces of the Codec composites with an optical microscope, see Figure 4-76, confirmed that the foil surface had indeed been damaged in several locations.

X-ray diffraction of the consolidated composite revealed the presence of precipitates. The presence of precipitates was not surprising since the temperature used for consolidation exceeded the limit determined earlier for precipitation of Al-Mo intermetallic compounds.

Fiber and composite void volumes were measured for the P2-504 specimen using ASTM Standard 3553-76. Table 4-13 lists fiber and void volume and these values appear to correlate to the cross-sectional micrographs. Similar to the HIPing of the alloy film alone, it appears that diffusion kinetic are sluggish for the alloy coated fibers, leading to a need for high consolidation pressures, temperatures, and times.

Table 4-13. *Measured Fiber Volume of Panel P2-504.*

Specimen Number	Fiber Volume (%)	Void Volume (%)
1	51.3	8.6
2	55.5	11.2
3	55.6	10.6
4	53.4	8.7
5	49.8	7.6
Ave	53.1	9.3

4.3.9.2 Composite Tensile Properties

Cordec panel P2-504 was sectioned for tensile property testing. Prior to testing, doublers were attached to the specimen ends to prevent damage and subsequent premature failure of the composite. Biaxial strain gages were bonded to the center of the specimen gage section and the specimens were loaded at 0.05 in/min until failure. Load and change in length were monitored until failure. Table 4-14 lists the properties obtained from these tensile tests.

Table 4-14. *Predicted and Measured Longitudinal Tensile Properties of the Unidirectional Al-Mo/P75Gr Composite Panel.*

Specimen Number	Strain To Failure	Max Load (lb.)	Ultimate Tensile Strength (ksi)	Modulus of Elasticity (Msi)	Predicted Modulus of Elasticity (Msi)	Predicted Ultimate Tensile Strength (ksi)
1	0.03	36	3.9	14.6		
2	0.02	32	3.56	16.3		
3	0.03	46	4.91	15.4		
4	0.02	36	4.02	15.0		
Ave	0.03	38	4.10	15.3	42.5*	135.0*
S. Dev	0.002	6	0.57	0.73		
Coef. of Variation	14.3%	15.11%	13.97%	4.8%		

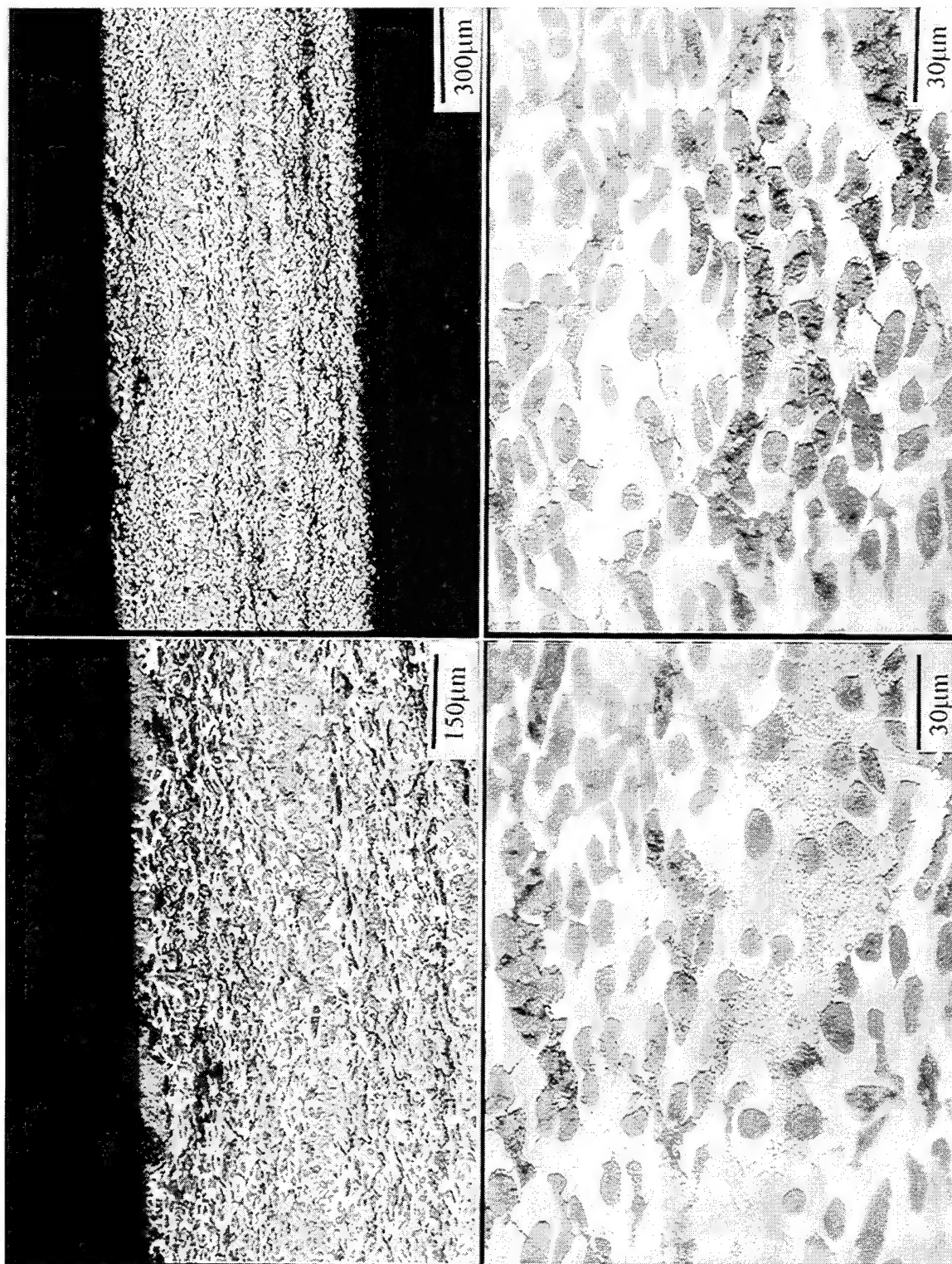* For 50 volume percent P75 graphite fibers

Figure 4-73   Representative microstructures taken from MMSS Al-17Mo/P120 composite . Layers of the coated fibers are sandwiched between layers of commercially pure Al foil.
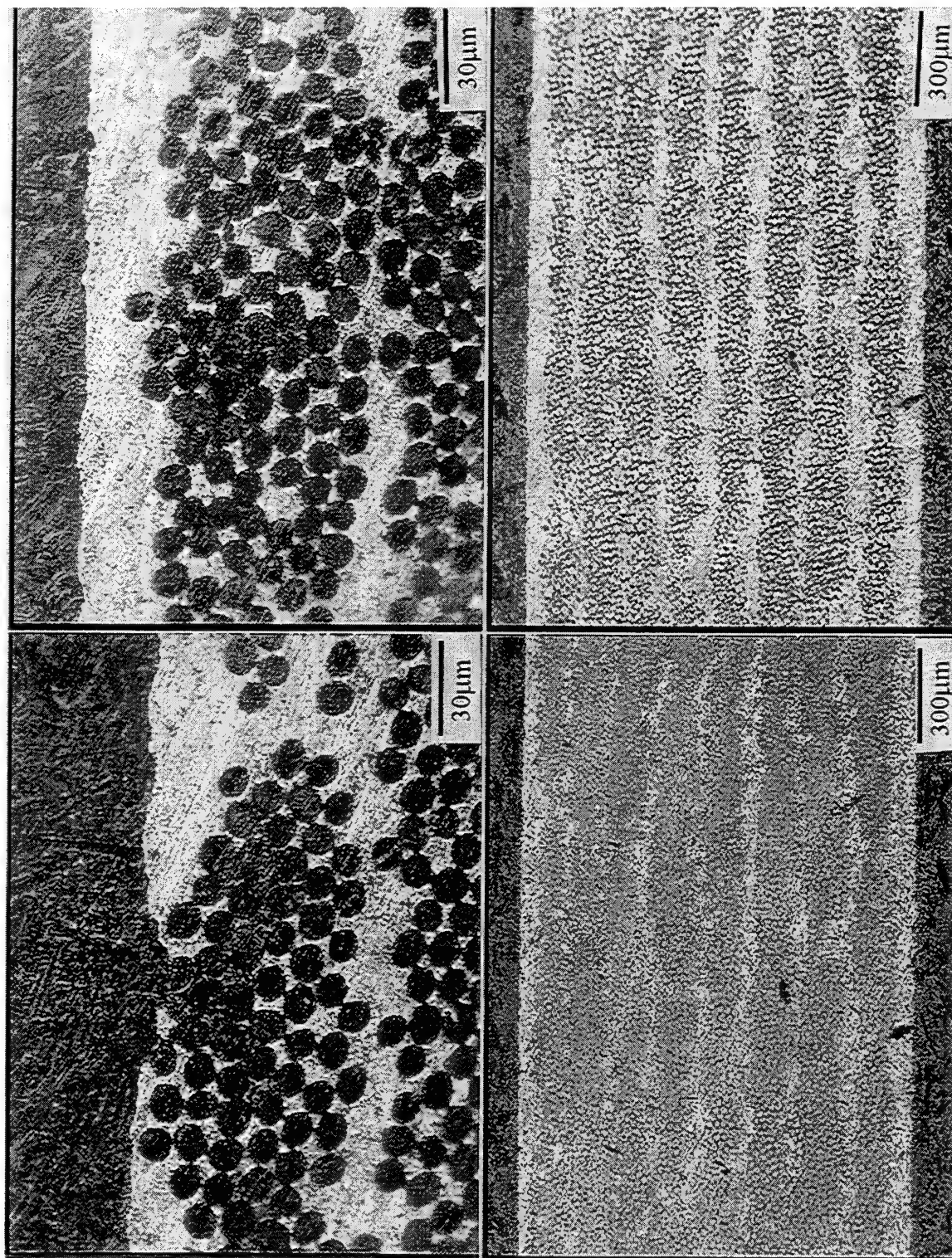
Figure 4-74. *Representative microstructures taken from Composite P2-504 (Cordec) The composite is comprised of Al-17Mo coated P120 Gr fibers sandwiched between 9 layers of commercially pure Al foil.*

Figure 4-75   Optical micrograph of Martin Marietta Al-17Mo/P120 composite
showing flow of the pure Al interlayer into the composite.

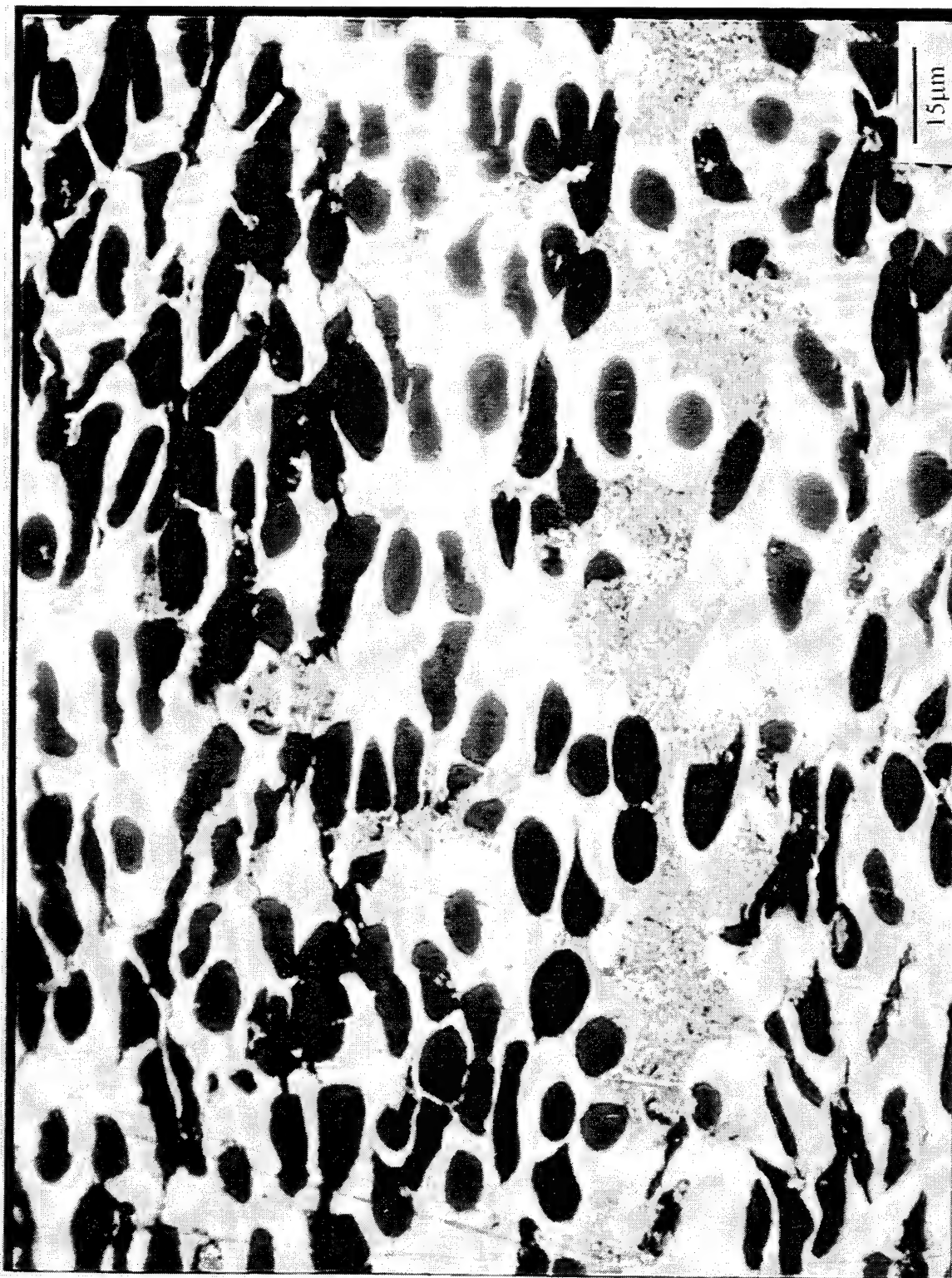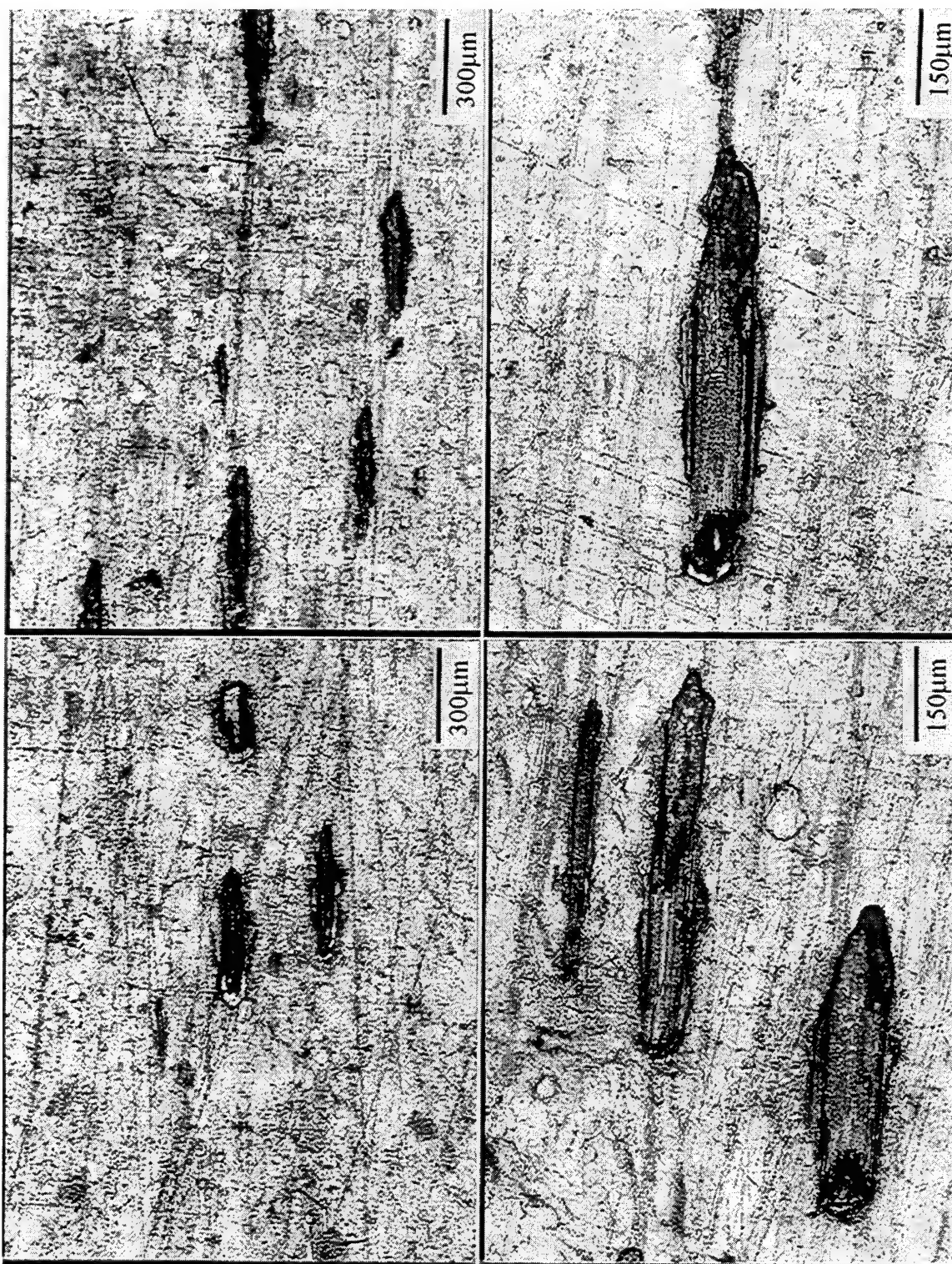Figure 4-76   *Optical micrographs of the surface of best Cordec composite showing tears in the surface foils which exposed graphite fibers.*

4.3.9.3 Corrosion Testing of Composites

Anodic polarization experiments were conducted on the panels that were considered to have consolidated relatively well. None the polarization curves generated for the composite specimens in chloride containing environments showed evidence of passivity. A representative anodic polarization curve for one of the better Cordec specimens is presented in Figure 4-77. The poor anodic polarization performance of the composites was not suprising considering the fact that the exposed surface was pure Al with bare graphite fibers penetrating the surface in several areas. In addition, optical and SEM examination of the polarized specimens revealed that the coated fibers had not really diffusion bonded. Representative optical micrographs taken of the pitted surface of the composite specimen after anodic potentiodynamic polarization are presented in Figure 4-78. Figure 4-79 shows cross-sectional micrographs of the tested composite and reveals that corrosion penetrated the entire composite with the possible exception of the surface foil on the back of the specimen which was not exposed directly to the electrolyte. Figure 4-78 shows an optical image of the composite surface revealing pitting of the surface foil. A better understanding of the mode of degradation for these composites can be gained by looking at SEM micrographs of these pitted regions. Figure 4-80 shows two SEM images of the pitted surface of the Cordec P2-504 specimen after anodic potentiodynamic polarization in 0.1M NaCl. These micrographs clearly reveal that diffusion bonding of the coated fibers was far from complete. In fact, the alloy coating on the fiber surfaces appeared to have undergone little or no change during either diffusion bonding or potentiodynamic polarization.
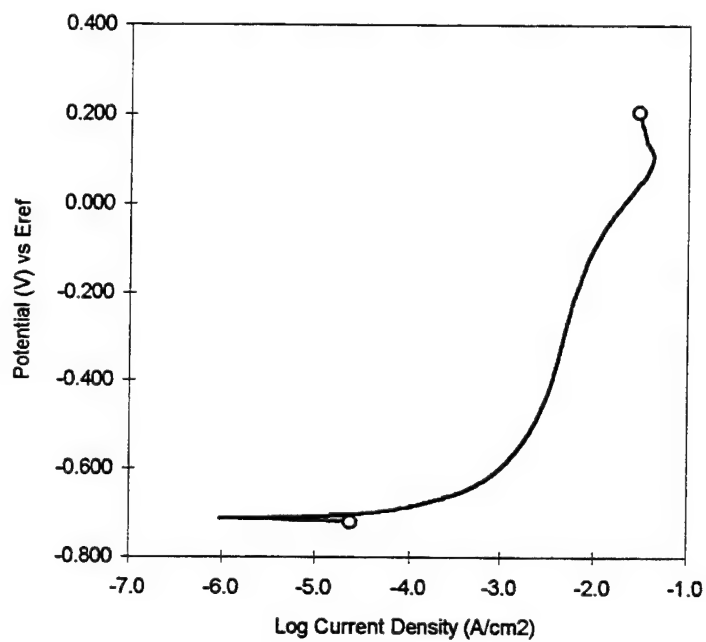
Figure 4-77. Anodic Polarization Results of Cordec Composite #503 in a 0.1M NaCl (Solution was not pH Adjusted).
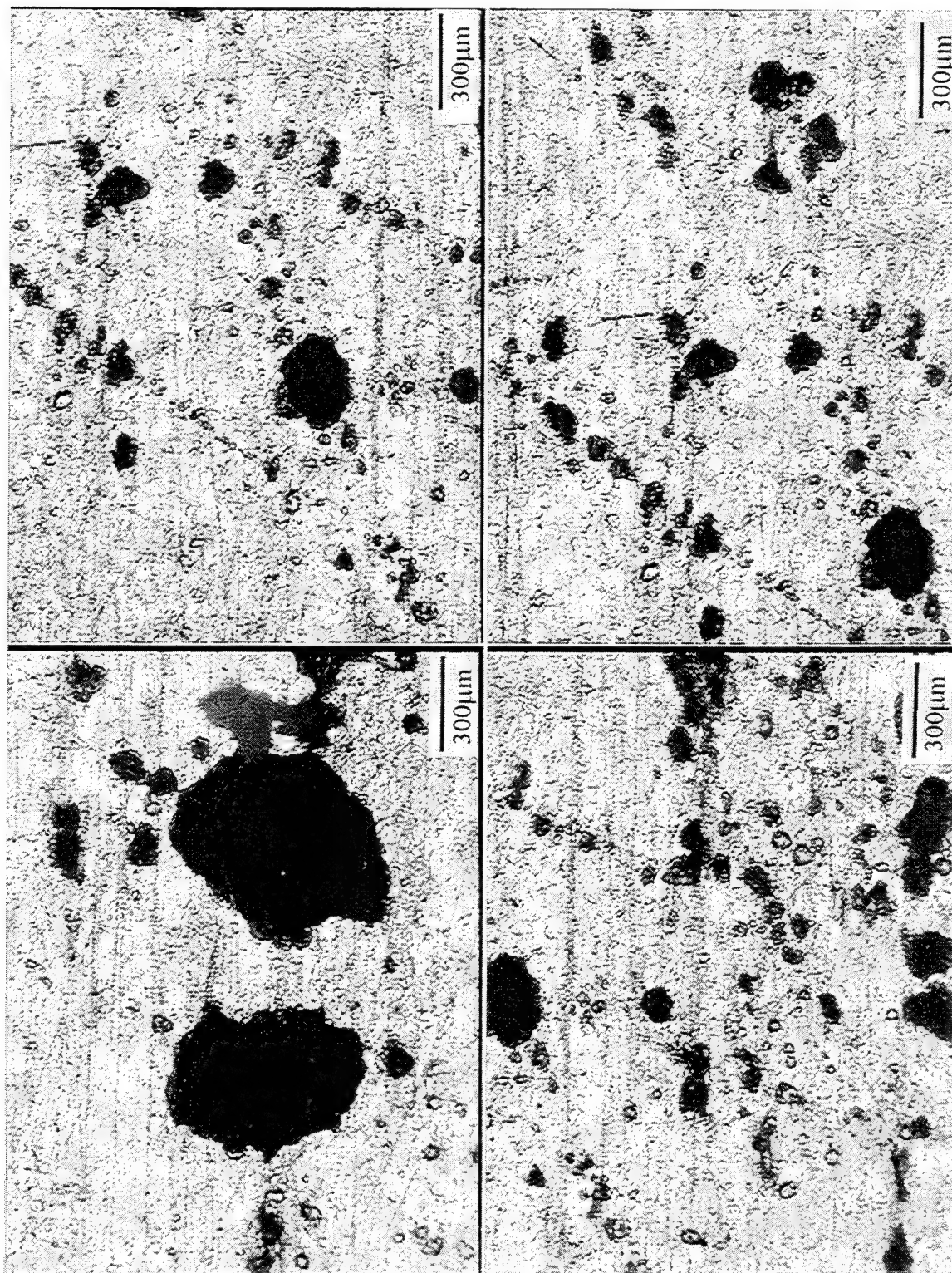
Figure 4-78 *Optical micrographs of the surface of the best Cordec composite after electrochemical testing showing pitting of the surface foils.*

Figure 4-79 Optical micrographs of composite cross-section after electrochemical testing revealing degradation of composite.

Figure 4-80   SEM micrographs of the composites taken after polarization in 0.1M
NaCL Solution with no pH Adjustment.

106

5.0 Summary

This research has clearly revealed that nonequilibrium Al-Mo, Al-W, Al-Ta, Al-Cr alloys exhibit significantly enhanced resistance to pitting and galvanic corrosion when compared to pure Al or any commercial aluminum alloy. For two of the alloys investigated in this program 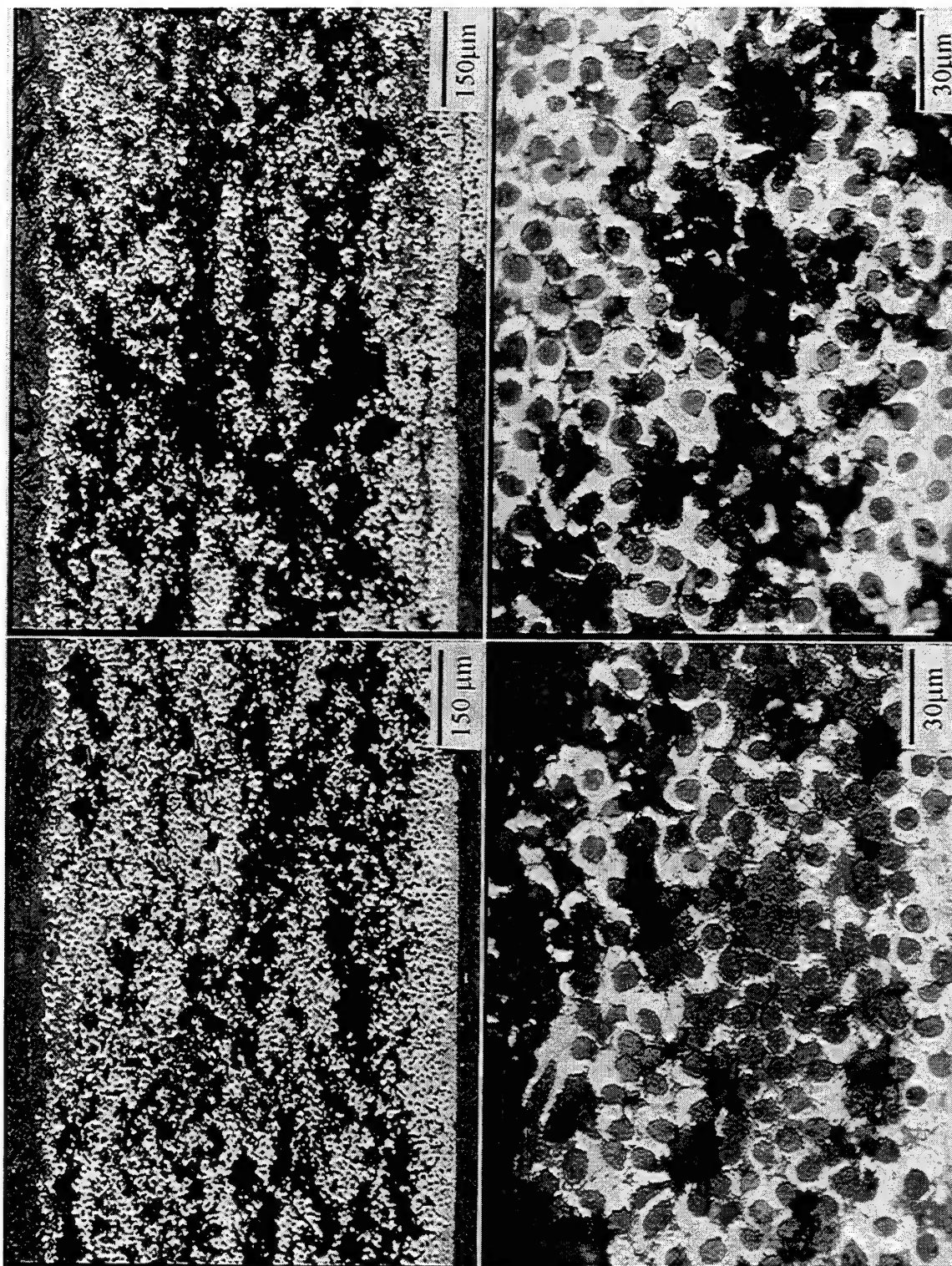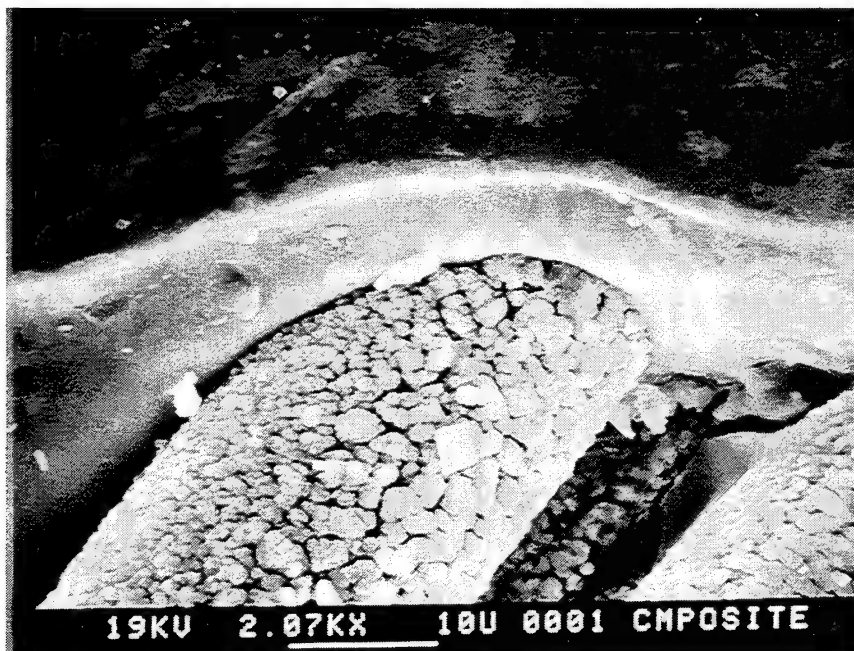(the intermediate solute concentration Al-Mo and Al-W alloys) this significantly enhanced corrosion resistance was maintained at nominal composite consolidation temperatures (400 C). In addition to anodic potentiodynamic polarization testing, the enhanced corrosion resistance of these alloys was confirmed in long-term potentiostatic tests and in long-term galvanic coupling experiments. Precipitation reactions in the intermediate solute concentration Al-Mo and Al-W alloys were retarded because the nanocrystalline/amorphous nature of these sputter deposited alloys.

Commercial deposition of an Al-17Mo alloy on P120 graphite fibers yielded a very columnar deposit which maintained a degree of flexibility similar to that of the uncoated fibers. The breakdown potential for the Al-17Mo coated fiber was several hundred millivolts greater than that of pure Al (or any commercial Al alloy), but it was also several hundred millivolts less than that of the Al-18Mo alloy sputtered on planar substrates at Martin Marietta. This difference in performance between the alloy deposited by Cordec on graphite fibers and the alloy deposited by Martin Marietta on planar substrates was a result the morphology differences between the two deposits. The alloy film produced at Martin Marietta was smooth and dense; whereas, the Cordec deposit was rough and columnar. Rough columnar deposits, such as the one illustrated in Figure 4-72 for the Al-18Mo alloy on the P120 graphite fibers, have been shown to significantly degrade localized corrosion resistance [64]. Fortunately, the morphology of the deposit can be changed by optimizing the sputtering conditions. In this research, optimization of the sputtering process was not conducted because of the limited budget and because it was hoped that hot pressing would densify the alloy.

Consolidation of the alloy via hot pressing proved to be a more difficult task than anticipated. As a result of the relatively high melting temperature of the alloy (715 C), consolidation was far from complete at the temperature and pressure ranges available for hot-pressing. Void concentrations greater than 9 volume %, lack of diffusion bonding of the alloy coated fiber within the composite, and the presence of pure aluminum surface foils and inter-layers results in composite all contributed to the poor corrosion performance of the hot-pressed composite. SEM examination of the composite after anodic polarization testing confirmed that diffusion bonding of the coated fibers was far from complete. In addition, this analysis revealed that little or no degradation of the coated fibers had taken place; instead, corrosion of the composite was confined to the Al surface foils and inter-layers. As a result of the excellent corrosion behavior of the nonequilibrium Al-17Mo matrix alloy under these conditions (despite its less than optimal morphology) , it is believed that corrosion resistant graphite-reinforced composites could be produced with this alloy via hot-isostatic pressing (HIPing). To insure that the enhanced corrosion resistance of the nonequilibrium Al alloy is not compromised by corrosion of the pure Al surface foils or inter-layers these composites should either be HIPed without surface foils or HIPed with vapor deposited Al-17Mo surface foils.

The research conducted on sputter-deposited Mg-based alloys revealed that Y alloying additions showed the most promise for enhancing corrosion resistance in chloride-containing environments. While the Mg-based alloys produced in this research were not optimized to the point where they could be considered as viable matrix alloys for use in graphite-reinforced composites, the alloys do represent a significant step in the development of a corrosion-resistant Mg alloy.

In addition to the work on Mg-based nonequilibrium alloys, an investigation of stand-alone inhibitive treatments for Mg (including Mansfeld's treatment which was found to be effective in enhancing the corrosion resistance of Al and Al-based composites) was also conducted as part of this program. These studies revealed that a simple immersion treatment in cerium fluoride improved the short-term corrosion resistance of Mg immersed in a chloride-containing solution. While electrochemical impedance spectroscopy of Mg with this inhibitive treatment revealed that protection was not maintained with long-term immersion in a sodium chloride environment, the treatment may prove effective in protecting Mg from corrosion under atmospheric conditions.

6.0 Conclusions

1.) Aluminum alloyed with W or Mo at atomic concentrations between 10 and 25 percent showed the best overall corrosion resistance of the alloys investigated in this program. This enhanced corrosion resistance was maintained (or even improved), after heat-treatment at nominal composite consolidation temperatures (400 C).

2.) The most promising alloys for use in MMCs (the Al-Mo and Al-W alloys with intermediate solute concentrations) were amorphous or exhibited minor short range ordering.

3.) Ternary Al-Mg-Mo alloys also showed enhanced corrosion resistance and a lower density than the Al-Mo alloys. Unfortunately, these ternary alloys exhibited much higher galvanic corrosion currents ($\sim 10 \mu A$) and were found to precipitate during heat treating at temperatures as low as 400°C for one hour which resulted in a loss of passivation.

4.) The sputter deposited Al-14 Mo alloy was two to three times harder than conventional aluminum alloys such as 6061-T6 or 7075-T6. Extrapolation of this data suggests that the tensile strength of this material could be in the range of 1,250 to 1,400 MPa. Average measured tensile strength for Al-14Mo of 155 MPa (22.5 ksi) was much lower than expected, which was attributed to pits induced while chemical milling the copper substrate as well as to the textured (columnar) alloy morphology.

5.) Defects and deposit morphology played a critical in the corrosion of sputter-deposited thin-film alloys.

6.) Sputter deposited Mg-Y alloys were significantly more resistant to corrosion in high pH chloride solutions than either pure Mg or WE43.

7.) Of the inhibitive treatments evaluated, including the treatment used by Mansfeld for the protection of Al, a simple immersion treatment in cerium fluoride showed the most promise for enhancing the corrosion resistance of Mg.

7.0 References Cited

1. J.M. Evans and D.M. Braddick, "Corrosion Behavior of Fibre-Reinforced Al Composites," Corrosion Science, 1971, vol. 11, pp. 611-614.

2. D.L. Dull, W.C. Harrigan Jr., and M.F. Amateau, Proceedings of Triservice Corrosion of Military Equipment Conference, F.H. Meyer, ed., Air Force Materials Laboratory Report AFML-TR-75-42, 1975, vol. 1, p. 399.

3. C.R. Crowe, Localized Corrosion Currents from Graphite Aluminum and Welded SiC/Al Metal Matrix Composites, NRL Memorandum report 5415, Naval Research Laboratory, February, 1985.

4. J.H. Payer and P.G. Sullivan, "Corrosion Protection Methods for Graphite Fiber Reinforced Aluminum Alloys," Bicentennial of Materials, Society for the Advancement of Material and Process Engineering, Azusa, CA, 1976 vol. 8, pp. 343-352.

5. D.M. Aylor, and R.M. Kain, "Assessing the Corrosion Resistance of Metal Matrix Composite Materials in Marine Environments," ASTM STP 864 - Recent Advances in Composites in the US and Japan, Vinson and Taya, ed., American Society of Testing and Materials, Philadelphia, PA, 1985, pp. 632-647.

6. P.P. Trzaskoma, "Localized Corrosion of Metal Matrix Composite," Environmental Effects on Advanced Materials, R.H. Jones and R.E. Ricker, ed., The Minerals, Metals, and Materials Society, Warrendale, PA, 1991, pp. 249-266.

7. W.H. Pfeifer, "Hybrid and Select Metal Matrix Composites: A State of the Art Review," W.J. Renton, ed., American Institute of Aeronautics and Astronautics, New York, NY, 1977, pp. 231-252.

8. M.G. Vassilaros, D.A. Davis, G.L. Steckel, and J.P. Gudas, "Marine Corrosion and Fatigue of Graphite Aluminum Composites," Proceeding of the 1980 Tri-Service Corrosion Conference, vol. 2, U.S. Government Publication, 1980.

9. D.M. Aylor, R.J. Ferrara, and R.M. Kain, "Marine Corrosion and Protection For Graphite/Aluminum Metal Matrix Composites," Materials Performance, 1984, vol. 23, pp. 32-39.

10. D.M. Aylor and P.J. Moran, "Effect of Reinforcement on the Pitting Behavior of Aluminum-Base Metal Matrix Composites," Journal of the Electrochemical Society, 1985, vol. 132, pp. 1277-2684.

11.   E.G. Kendall and D.L. Dull, "Salt Water Corrosion Behavior of Aluminum-Graphite Composites," National Technical Information Service, U.S. Department of Commerce, AD-777, p. 160, (1974).

12.   M.A. Buonanno, R.M. Latanision, L.H. Hihara, and J.F. Chiang, "Corrosion of Graphite Aluminum Metal Matrix Composites," Environmental Effects on Advanced Materials, R.H. Jones and R.E. Ricker, ed., The Minerals, Metals, and Materials Society, Warrendale, PA, 1991, pp. 267-282.

13   L.H. Hihara, Corrosion of Aluminum-Matrix Composites, Ph.D. Dissertation, Massachusetts Institute of Technology, (1985).

14.   L.H. Hihara and R.M. Latanision, "Residual Microstructural Chloride in Graphite-Aluminum Metal Matrix Composites," Material Science Engineering A, 1990, vol. 126, pp. 231-234.

15.   L.H. Hihara and R.M. Latanison, "Localized Corrosion Induced in Graphite/Aluminum Metal-Matrix Composites by Residual Microstructural Chloride," Corrosion, 1991, vol. 47, pp. 335-340.

16.   L.H. Hihara and R.M. Latanison, "Galvanic Corrosion of Aluminum-Matrix Composites," Corrosion, 1992, vol. 48, pp. 546-552.

17.   W.C. Harrigan and R.H. Flowers, "Graphite-Metal Composites: Titanium-Boron Vapor Deposit Method of Manufacture," Failure Modes in Composites IV, J.A. Cornie and F.W. Crossman, eds., The Minerals, Metals, and Materials Society, Warrendale, PA, 1977, pp. 319-335.

18.   I.J. Toth, W.D. Brenthall, and G.D. Menke, "A Survey of Aluminum Matrix Composites," Composites: State of the Art, J.W. Weeton and E. Scala, eds., The Minerals, Metals, and Materials Society, Warrendale, PA, 1971, pp. 139-207.

19.   W. Meyerer, D. Kizer, S. Paprocki, "Versatility of Graphite-Aluminum Composites: An Overview," Failure Modes in Composites IV, J.A. Cornie and F.W. Crossman, ed., The Minerals, Metals, and Materials Society, Warrendale, PA, 1977, pp. 319-335.

20.   M.F. Amateau, "Progress in the Development of Graphite-Aluminum Composite Using Liquid Infiltration Technology", Journal of Composite Materials, 1976, vol. 10, pp 279-296.

21.   V.C. Nardone and J.R. Strife, "Advanced Gr/Mg Composite Development," United Technologies Research Center, Interim Report R89-917711-4, East Hartford, CT, July 1989.

22. R.J. Weimer, W.F. Henshaw, T.G. Casswell, B.D. Dickerson, J.P. Hickerson, and S.D. Shelton, Fabrication of Thin-Walled Seamless Tubes from Gr/Mg Precursor Tapes, Cordec Corporation, Lorton, VA, 1992.

23. R.T. Pepper and R.A. Penty, "Mechanical Properties of Aluminum-Graphite Composites Prepared by Liquid Phase Hot Pressing," Journal of Composite Materials, 1974, vol. 8, pp. 29-37.

24. A.A. Baker, C. Shipman, and P.W. Jackson, "The Short-Term Compatibility of Carbon Fibres with Aluminum," Fibre Science and Technology, 1972, vol. 5, pp. 213-218.

25. M. Kh. Shorshorov, T.A. Chernyshova, and L.I. Kobeleva, "Interface Interaction in Aluminum-Carbon System, Progress in Science and Engineering of Composites," ICCM-IV, T. Hayashi, K. Kawata, and S Umekawa, ed., Toyoka, 1982, pp. 1273-1279.

26. R.J. Arsenault and C.S. Pande, "Interfaces in Metal Matrix Composites," Scripta Metallurgica, 1984, vol. 18, pp. 1131-1134.

27. S.J. Baker and W. Bonfield, "Fracture of Aluminum-Coated Carbon Fibres," Journal of Materials Science, 1978, vol. 13, pp. 1329-1334.

28. L. -J. Fu, M. Schmerling, and H.L. Marcus, "Interface Studies of Aluminum Metal Matrix Composites," Composite Materials: Fracture and Fatigue, ASTM Special Publication 907, H.T. Hahn, ed., 1984, pp. 51-72.

29. I.H. Khan, "The Effect of Thermal Exposure on the Mechanical Properties of Aluminum-Graphite Composites," Metallurgical Transactions A, 1976, vol. 7A, pp. 1281-1289.

30. W.C. Harrigan, Jr., "The Effects of Temperature and Pressure on the Interface Chemistry in Graphite-Aluminum Composite System," Metallurgical Transactions A, 1978, vol. 9A.

31. W.C. Moshier, G.D. Davis, J.S. Ahearn, and H.F. Hough, "Influence of Molybdenum on the Pitting Corrosion of Aluminum Films," Journal of the Electrochemical Society, 1986, vol. 133, pp. 1063-1064.

32. W.C. Moshier, G.D. Davis, J.S. Ahearn, and H.F. Hough, "Corrosion Behavior of Aluminum-Molybdenum Alloys in Chloride Solutions," Journal of the Electrochemical Society, 1987, vol. 134, pp. 2677-2684.

33.   W.C. Moshier, G.D. Davis, and G.O. Cote, "Surface Chemistry of Sputter-Deposited Al-Mo and Al-Cr Alloys Polarized in 0.1M KCl," Journal of the Electrochemical Society, 1989, vol. 136, pp. 356-362.

34.   G.D. Davis, W.C. Moshier, G.G. Long, and D.R. Black, "Passive Film Structure of Supersaturated Al-Mo Alloys" Journal of the Electrochemical Soc.iety, 1991, vol. 138, pp. 31943199.

35.   G.S. Frankel, M.A. Russak, C.V. Jahnes, M. Mirzamaani, and V.A. Brusic, "Pitting of Sputtered Aluminum Alloy Thin Films," Journal of the Electrochemical Society, 1989, vol. 136, pp. 1243-1244.

36.   G.D. Davis, W.C. Moshier, T.L. Fritz, and G.O. Cote, "Evolution of the Chemistry of Passive Films of Sputter-Deposited, Supersaturated Al Alloys," Journal of the Electrochemical Society, 1990, vol. 137, pp. 422.

37.   B.A. Shaw, T.L. Fritz, G.D. Davis, and W.C. Moshier, "Influence of Tungsten on the Pitting of Aluminum Films," Journal of the Electrochemical Society, 1990, vol. 137, pp. 1317.

38.   B.A. Shaw, G.D. Davis, T.L. Fritz, B.J. Rees and W.C. Moshier, "The influence of tungsten alloying additions on the passivity of aluminum," Journal of the Electrochemical Society, vol. 138, No. 11, 3288-3295 (1991).

39.   G.D. Davis, B.A. Shaw, B.J. Rees, and M. Ferry, "Mechanisms of passivity of nonequilibrium Al-W alloys," Journal of the Electrochemical Society, vol. 140, 951-959 (1993).

40.   G.D. Davis, B.A. Shaw, B.J. Rees and C.A. Pecile, "Electrochemical behavior and surface chemistry of nonequilibrium Al-Ta alloys: solute-rich interphase model", Surface and Interface Analysis, vol, 22, 609-617 (1995).

41.   P.L. Hagans, "Electrochemical Study of the Passivation and Passive Film Breakdown of Mg70-Zn30 Metallic Glass," Materials Research Society Symposium Proceedings, 1987, 113-120.

42.   J.D. Hanawalt, C.E. Nelson, and J.A. Peloubet, Trans. Am. Inst . of Mining Met. Eng., 147,273-299 (1942).

43.   H.H. Uhlig, Corrosion and Corrosion Control, An Introduction to Corrosion Science and Engineering, John Wiley and Sons, New York, 2nd ed., 1971, 347-350.

44. F. Hehmann, F. Sommer, H. Jones, and R.G.J. Eduvean, "Corrosion inhibition in magnesium-aluminum-based alloys induced by rapid solidification processing," J. Mater. Sci., vol.24, 2369-2379 (1989).

45. R.V. Landan, R.F. Edelman and H. Markus, Trans. ASM, 59, 250 (1966).

46. W. Unsworth and J. King, Metallurgia, 53, 199-200 (May, 1986).

47. J.F. King, G.A. Fowler, and P.Lyon, Light Weight Alloys for Aerospace Applications 11, Edited by E.W. Lee and N.J. Kin, TMS pp 423-38 (1991).

48. D.A. Jones, Principles and Prevention of Corrosion, 1st. ed., Macmillian Publishing Co, New York, NY, 1992, pp. 167-188.

49. M.G. Fontana, "Corrosion Engineering," McGraw-Hill Book Company, New York, 3rd ed., 1986, pp.487-495.

50. ASM Binary Phase Diagrams, American Society of Metals, Metals Park, OH, 1991.

51. F. Mansfeld, V. Wang, and H. Shih, "Developmnt of 'Stainless Aluminum'", Journal of the Electrochemical Society, vol. 138 (December, 1991).

52. F. Mansfeld, V. Wang, and H. Shih, "Steps Towards a Stainless Aluminum", Dept. of Materials Science & Engineering, University of Southern California, 1991.

53. B.A. Shaw, G.D.Davis, T.L. Fritz, K.A. Olver, "A Molybdate Treatment for Enhancing the Passivity of Aluminum in Chloride-Containing Environments", Journal of the Electrochemical Society, vol. 137 (January 1990).

54. Y-T. Cheng and W.L. Johnson, "Disordered Materials: A Survey of Amorphous Solids," Science, 1987, vol. 235, pp. 997-1002.

55. K. Shimizu, G.E. Thompson, G.C. Wood, Y. Kurima, K. Kobayashi, H. Yoshioka, K. Asami, A. Kawashima and K. Hashimoto, "Compositional Non-uniformity in a Sputtered-Deposited Amorphous Al-Ta Alloy, Philosophical Magazine B, 1989, vol. 60, no. 6, pp. 931-935.

56. K. Asami, H. Yoshioka, K. Hashimoto, K. Shimizu and K. Kobayashi, "Superlattice-Like Structure of Sputter-Deposited Amorphous Aluminum-Heavy Element Alloys," Journal of Non-Crystalline Solids, 1989, vol. 110, pp. 258-264.

114

57.   P. Furrer and H. Warlimont, "Crystalline and Amorphous Structures of Rapidly Solidified Al-Cr Alloys," Materials Science and Engineering, 1977, vol. 28, pp. 127-137.

58.   Y. He, S.J. Poon, and G.J. Shiflet, "Synthesis and Properties of Metallic Glasses That Contain Aluminum," Science, 1988, vol. 241, pp. 1640-1642.

59.   Standard Hardness Conversion Tables for Metals, ASTM E140-88, American Society for Testing and Materials, 1988, p. 15.

60.   ASM Metals Reference Book, 2nd ed., American Society for Metals, Metals Park , OH, 1983, pp. 301-02.

61.   G.E. Dieter, Mechanical Metallurgy, McGraw-Hill Book Company, New York, 2nd edition, 1976, pp. 227-232.

62.   B.D. Cullity, Elements of X-Ray Diffraction, 2nd ed., Addison-Wesley Publsihing Co, Reading, MA, 1978, pp.281-292.

63.   A. Gunier, X-Ray Diffraction In Crystals, Imperfect Crystals and Amorphous Bodies, W.H. Freeman and Company, San Francisco, CA, 1963, pp. 121-126.

64.   K.A. Kennedy, The Influence of Film Morphology and Residual Stress on the Corrosion Resistance of Co-Sputter Deposited, Compositionally Graded and Constant Solute Aluminum Thin Films, The Pennsylvania State University (1995).

Appendix A
Phase Equilibrium

In general, the solubility of Group Vb and VIb transition metals in either Al or Mg is extremely limited. In fact, none of these transition metals have been found to have even small solid solubility limits in Mg, except for yttrium. Aluminum, on the other hand will retain small amounts of the Group Vb and VIb transition metals into solid solution. Each of the Al-Group Vb and VIb alloy systems is a peritectic reaction on the Al rich side. Solid solubility limit averages less than 0.5 atomic percent for the Group Vb and VIb metal in Al. A few details of each of the binary systems investigated in this program and their corresponding phase diagrams are presented in the following paragraphs. Although investigators are cited in each section, all data was found in ASM Binary Phase Diagrams, Second Ed. [50]

Mg-Cr -- Although a phase diagram does not exist for Mg-Cr system, Montignie has suggested the formation of $CrMg$, Cr_2Mg_3, $CrMg_3$, and $CrMg_4$. However, these postulated phases have not been experimentally verified and have been questioned because at any given temperature, Cr cannot be in equilibrium with several intermetallic phases.

Mg-Mo -- Investigation by Sauerwald and Climax Molybdenum Company reported that Mo does not alloy with Mg. Therefore, the phase diagram is simply elemental Mg, (Mg), and elemental Mo, (Mo), for all concentrations.

Mg-Ta -- Although a phase diagram does not exist, Gulyae has suggested the Mg-Ta system will have a peritectic reaction at 652°C with an estimated 0.1 to 0.2 atomic percent of Ta in (Mg). However, no data currently exists for this binary system.

Mg-W -- Similar to the previous three magnesium-refractory metal binary systems, no phase diagram exists for the Mg-W binary alloy system. Studies by Kremer and Sauerwald and Busk concluded that Mg does not alloy with W.

Mg-Y -- Figure A-1 shows the binary phase diagram for Mg-Y. The phase diagram was determined by Okamoto in 1991. This diagram indicates a eutectic phase consisting of Mg and e (Mg with 35.9-41.8 wt% Y) at approximately 24 wt% Y.

Al-Cr -- The Al-Cr phase diagram, shown in Figure A-2, is based on experimentation and thermodynamic calculations. On the Al rich side there is a peritectic reaction at 661.45°C with (Al) alloyed with 0.35 atomic percent Cr.

As the Cr concentration increases a two phase field of (Al) and the Al$_7$Cr intermetallic is found. As the concentration of Cr is further increased, a series of intermetallic compounds with increasing Cr:Al ratio can form. Because alloys targeted for this program will contain for 1 to 10 atomic percent Cr, the phase diagram indicates heat treating may result in decomposition of the solid solution to (Al) and Al$_7$Cr.

Al-Mo -- Examining the Al-Mo phase diagram in Figure A-3, the solid solubility of Mo in Al is very low. At 0.077 atomic percent Mo there is a peritectic reaction of liquid and Al$_{12}$Mo to for (Al). For Mo concentrations between 0.07 and 7.9 atomic percent, the equilibrium phases are (Al) and Al$_{12}$Mo; and from 7.9 to 16.8 atomic percent the equilibrium phases are Al$_5$Mo and Al$_{12}$Mo. Early work with rapidly quenched alloys extended the concentration of Mo in (Al) up to 2.7 atomic percent.

Al-Ta -- The Al-Ta phase diagram is shown in Figure A-4. Solid solubility of Ta in (Al) is limited to less than 0.04 atomic percent. Above this concentration, up to 24 atomic percent Ta, there is a two phase region of (Al) and TaAl$_3$.

Al-W -- Similar to all the Al-Group Vb and VIb alloys, The Al-W phase diagram has a peritectic reaction on the Al rich side (Figure A-5). Solubility of W in (Al) is virtually zero. At room temperature, the equilibrium consists of a two phase region for (Al) and g-Al$_{12}$W for compositions between 0 and 8 atomic percent W. From 8 to 17 atomic percent W, the equilibrium phases are Al$_{12}$W and Al$_5$W.
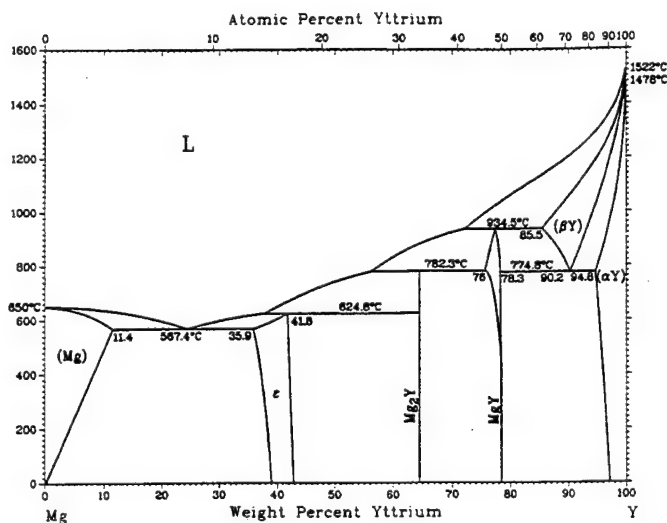

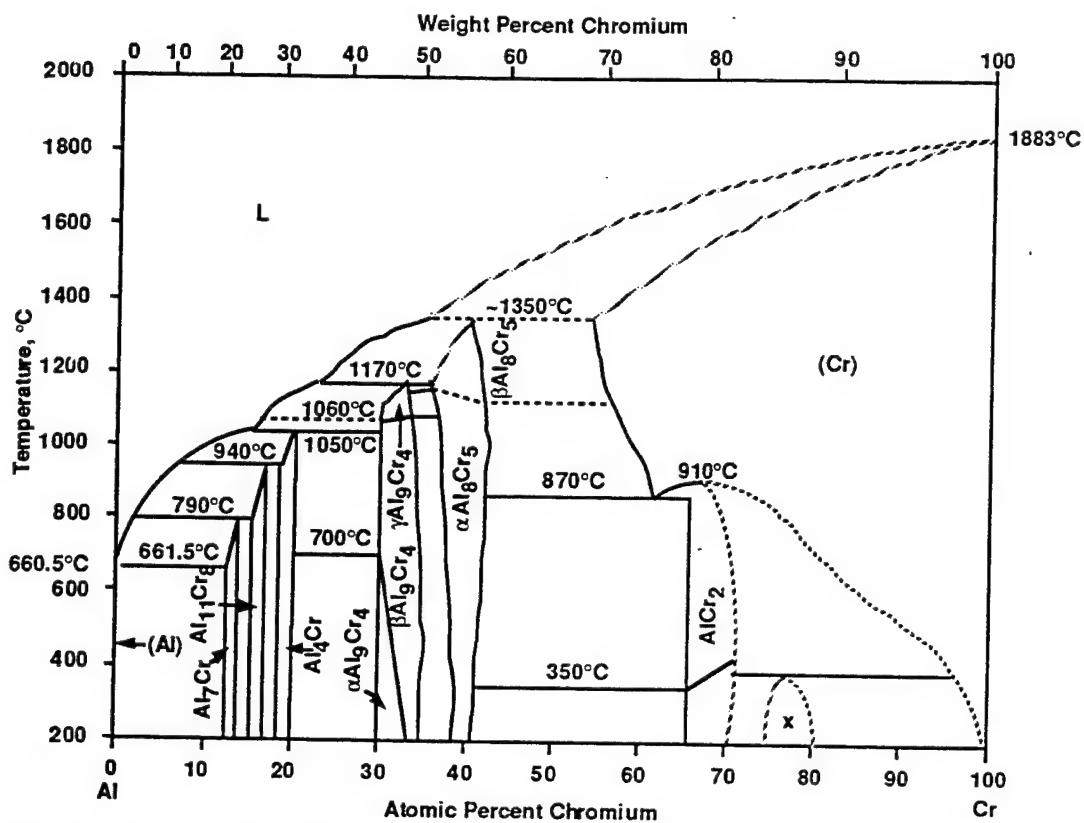***Figure A-1. Equilibrium Phase Diagram for Magnesium-Yttrium.***

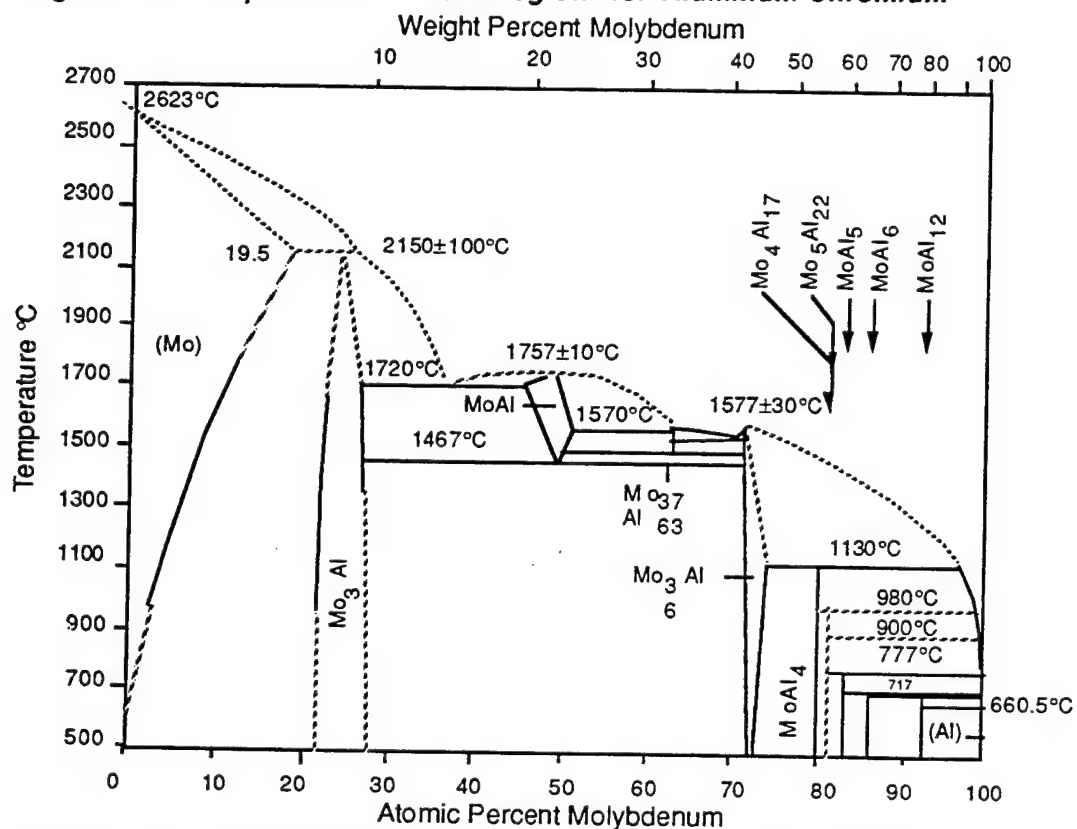Figure A-2. Equilibrium Phase Diagram for Aluminum-Chromium

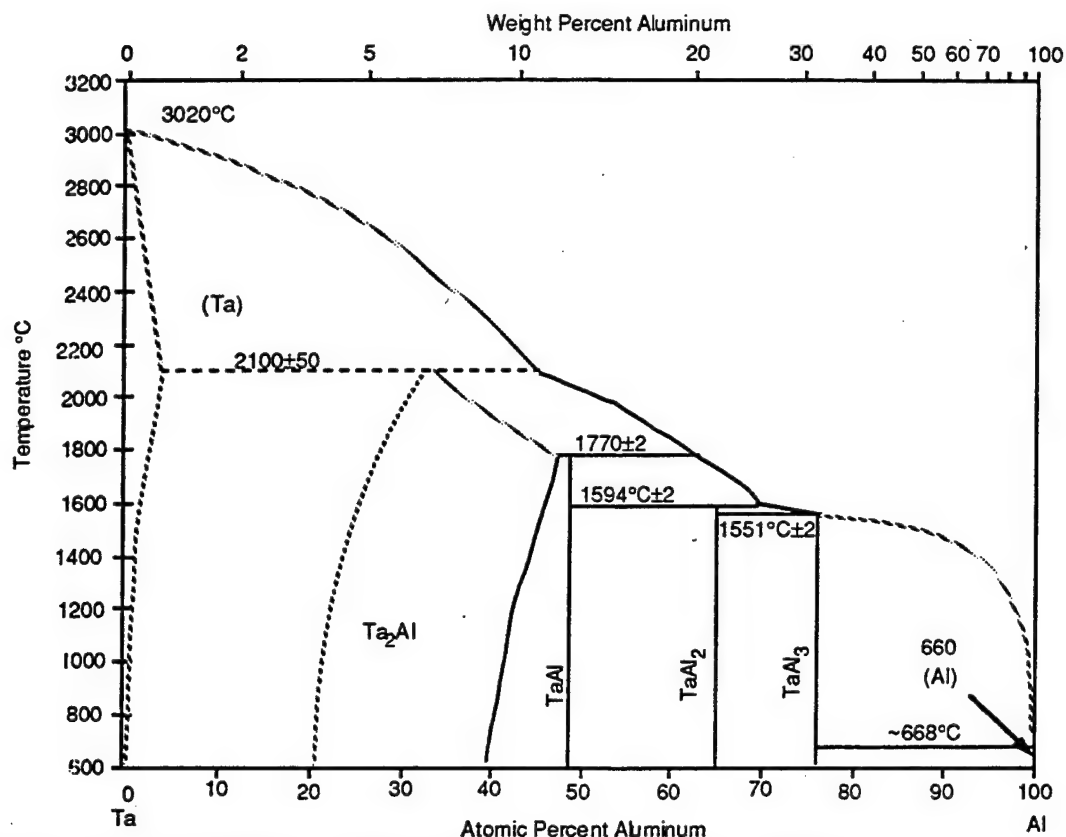Figure A-3. Equilibrium Phase Diagram for Aluminum-Molybdenum.

118
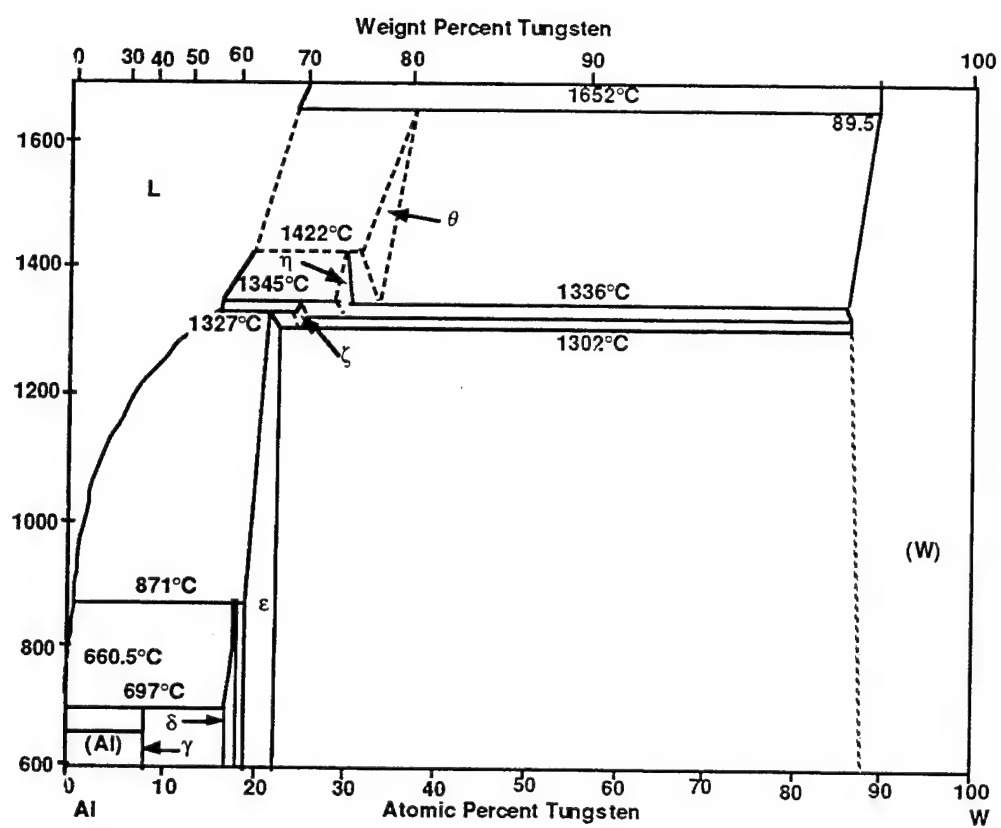
Figure A-4. Equilibrium Phase Diagram for Aluminum-Tantalum.

Figure A-5. Equilibrium Phase Diagram for Aluminum-Tungsten

Nonequilibrium Alloying of Graphite-Reinforced Aluminum Metal Matrix Composites*

T.R. Schrecengost, B.A. Shaw,** R.G. Wendt, and W.C. Moshier****

ABSTRACT

With corrosion behavior superior to pure aluminum (Al), nonequilibrium Al alloys produced by cosputter deposition have great potential for use as matrix metals in graphite (Gr)-reinforced Al composites. These composites offer enhanced properties as a result of their low density matrix and a high modulus reinforcing fiber. Cosputter-deposited Al alloys provide a means to improve corrosion resistance of Al and to remove a conventional processing step that accelerates degradation of the composite once the Gr fibers are exposed. Additions of tungsten (W) and molybdenum (Mo) were found to enhance the localized corrosion resistance of Al. At concentrations of 19 at.% Mo or 26 at.% W breakdown potentials (E_b) increased by 1,115 mV_{SCE} and 1,245 mV_{SCE} over pure Al, respectively. Heat treatment of these alloys at 400°C for 1 h did not result in precipitation of a second phase. The alloys maintained excellent resistance to localized attack. Galvanic current diagrams predicted use of these alloys in composite structures would decrease galvanic corrosion rates by at least 2 orders of magnitude. This enhancement in galvanic corrosion resistance was a result of significant improvements in passivity which occurred with the nonequilibrium addition of Mo or W to Al. Galvanic current measurements confirmed the predicted reduction in galvanic corrosion rates.

KEY WORDS: aluminum, galvanic corrosion, localized corrosion, metal-matrix composites, molybdenum, nonequilibrium alloying, sputtering, tungsten

INTRODUCTION

Graphite (Gr)-fiber reinforced metal matrix composites (MMCs) are under development for a variety of structural aerospace applications. Using aluminum (Al) as the matrix metal reduces the final density of the composite and creates high elastic modulus and excellent strength in the fiber direction. High-modulus, Gr fiber-reinforced composites offer a variety of attractive properties, including high specific modulus, tailorable or zero coefficient of thermal expansion, and high thermal conductivity.

With those properties, structures that are dimensionally stable when subjected to thermal and mechanical loads can be designed and fabricated from MMCs. Unfortunately, Gr-Al MMCs are susceptible to severe corrosion. In marine environments, pitting and extensive galvanic corrosion have been reported for the composites after only a few weeks of exposure.[1-3]

Mechanisms behind the rapid attack of Gr-reinforced composites depend upon the fiber, matrix material, and processing conditions. Pitting,[1,4-5] galvanic corrosion,[3-4,6-7] residual chlorides,[8] and second-phase particles[2,5,9] have been reported to contribute to the corrosion of Gr-Al MMCs. It has been agreed generally that degradation of Gr-Al MMCs initiates at pits in the Al matrix. Residual chlorides and/or carbides produced at the matrix-fiber interface during conventional fabrication have been found to accelerate propagation of attack. Once the Gr fibers were exposed, rapid corrosion of the Al matrix was driven by the cathodic,

oxygen-reduction reaction on the exposed fibers. Final mechanical failure occurred as a result of disbonding or exfoliation of the composite structure.

To improve corrosion resistance of Gr-Al MMCs, researchers have investigated the use of cathodic protection,[8] cathodic inhibitors,[8-9] and barrier coatings.[1-2,4] Cathodic protection was found to be detrimental because it led to formation of hydroxyl ions. Cathodic protection was not recommended because Al is susceptible to corrosion in alkaline environments. Inhibitors such as zinc chloride ($ZnCl_2$) have been shown to form zinc hydroxide ($Zn[OH]_2^3$) precipitates on cathodic sites, reducing the cathodic area and decreasing galvanic corrosion. However, this method has not been practical for use on composites.

Protective coatings such as electroplated[2] or electroless[1,4] nickel (Ni), anodization,[1,4] and organic coatings[2] have been used to extend the time required for localized corrosion to penetrate the composite's outer surface or to seal flaws on the composite's surface. However, coatings are damaged easily and might be detrimental in space systems because they could interfere with dimensional tolerances, increase composite density, or flake off. These actions could interfere with sensitive surfaces on such space hardware as detectors and reflectors. Because these methods, for the most part, only delay pitting and galvanic corrosion, they have been rejected as permanent solutions. A permanent solution to the corrosion of Gr-reinforced MMCs would have to improve the corrosion resistance of the matrix metal and remove corrosion-accelerating species (residual chlorides and carbides) from the matrix-fiber interface.

In the past, nonequilibrium Al alloys containing several at.% tungsten (W), tantalum (Ta), chromium (Cr), or molybdenum (Mo) have been shown to improve the localized corrosion resistance of Al significantly, shifting the breakdown potential (E_b) more than 2 V in some cases.[10-15] Figure 1 compares the polarization behavior for these alloys to E_b of pure Al. The highest corrosion and E_b were noted for the high-solute concentration Al-Mo and Al-W alloys. The mechanisms responsible for the improved passivity of these alloys remain under investigation, but recent results indicated that the oxide film structure and a solute-rich metal-passive film interface play key roles. Previous results have shown that precipitation of a second phase at low and intermediate solute concentrations occurred with heat treatment at 400°C for 1 h. Corrosion performance was degraded.

Thus, use of nonequilibrium alloys as the matrix metal in a Gr-reinforced composite could improve performance significantly if the passivity-enhancing solute remained in solid solution with the Al during fiber consolidation at elevated temperatures. Hot isostatic pressing (HIPing) can be performed as a relatively low-
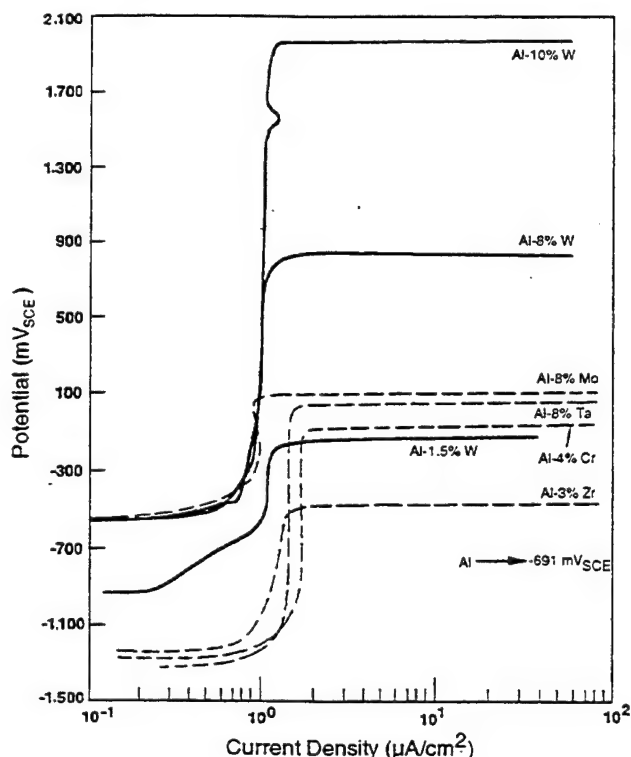

FIGURE 1. Anodic polarization behavior for nonequilibrium Al alloys in aerated 0.1 M KCl compared to spontaneous pitting potential of pure Al (-691 mV_{SCE}) at 0.167 mV/s. (Reprinted with permission, J. Electrochem. Soc. 138 [1991]: p. 3,292).

temperature consolidation process; however, temperatures near 400°C are required. Therefore, the stability of these alloys at 400°C is critical for the ultimate performance of the composite. Direct sputter deposition of these nonequilibrium alloys onto Gr fibers also would circumvent problems associated with residual chlorides and carbides at the matrix-Gr interface that occur with conventional processing and contribute to degradation of the composite structure.

Although pitting-resistant, nonequilibrium alloys can be produced, flaws still may remain in the composite that allow galvanic corrosion.

Several researchers have used polarization data to predict galvanic corrosion rates successfully.[8,16-18] Superimposition of anodic and cathodic polarization behavior to form galvanic current diagrams for estimating galvanic corrosion rates was suggested first by Bennett in 1972.[16] These diagrams are convenient for estimating corrosion rates for galvanic couples when there is an insignificant IR drop between the two members, the contribution of other anodic and cathodic reactions is very small, and the current density (CD) is uniform.[18] Area differences for the coupled metals can be accommodated by multiplying polarization curves by the respective wetted surface areas. Although these diagrams are useful in assessing the galvanic

corrosion behavior of couples, the predictions should be confirmed with direct galvanic current measurements.

The objective of this work was to evaluate effects of heat treatment and galvanic coupling on the corrosion performance of nonequilibrium Al-19 at.% Mo and Al-26 at.% W alloys. Retention of a single-phase structure at composite consolidation temperatures and concomitant undiminished corrosion behavior were important to performance of the composite. Specimens heat-treated at 400°C for 1 h were evaluated by x-ray diffraction (XRD) and anodic polarization for precipitation and subsequent loss of corrosion resistance. Likewise, galvanic compatibility with Gr was important and was evaluated using galvanic current diagrams and galvanic current measurements.[5]

EXPERIMENTAL

Al alloys were produced by radio frequency and direct current magnetron cosputter deposition using a thin film deposition system. The cosputter deposition process has been described in detail elsewhere.[19-20] Two targets (Al and Mo or Al and W) were used to deposit the alloy onto a polished single crystal silicon (Si) wafer (10 cm diam). The substrate stage was rotated at a speed of 30 rpm to produce a uniform solute concentration across the substrate surface at a thickness of 1 μm to 2 μm. Pure Al, an Al-19 at.% Mo alloy, and an Al-26 at.% W alloy, in as-sputtered and heat-treated (except for the pure Al) conditions were produced and characterized by XRD, anodic polarization, and galvanic coupling with Gr.

To evaluate effects of heat treatment on corrosion performance, half of each Al-19 at.% Mo and Al-26 at.% W wafer were heat-treated in the deposition chamber fitted with a hot stage. While the specimens were in the load lock, the stage was heated to 400°C and allowed to stabilize. The specimens were transferred into the chamber and heat-treated for 1 h before removal through load lock and air cooling. The heat treatment was conducted at 100 mTorr (13.33 Pa) in flowing, high-purity argon gas.

Alloys were characterized using XRD, scanning electron microscopy (SEM), energy dispersive spectroscopy (EDS), and optical microscopy (OM). Alloy compositions were determined by EDS in three areas using semiquantitative analysis of the x-ray spectra. XRD was conducted on each film to determine whether the solute elements were in solid solution with the Al after sputtering and after heat treating. Intensity vs diffraction angle (2θ) was measured for each alloy before and after heat treatment and plotted for

comparison of the effect of heat treatment on thermal stability of the alloy. Before and after electrochemical testing, SEM and OM were used to observe surface features such as scratches, defects, pits, and cracks.

Electrochemical specimens were prepared by cleaving the Si wafer into pieces approximately 1 cm by 1 cm. The alloy was attached to a lead wire, and the edges and back of the sample were painted with a marine epoxy so that only the alloy surface was exposed to the electrolyte.

Anodic potentiodynamic polarization curves were generated using a potentiostat interfaced with a personal computer controlled at a scan rate of 0.2 mV/s. A few experiments were conducted at slower scan rates (0.05 mV/s and 0.008 mV/s) to confirm E_b. Experiments were conducted at ambient lab temperature in quiescent 0.1 M sodium chloride (NaCl) solution adjusted to a pH of 8 with sodium hydroxide (NaOH). This pH was chosen because of interest in performance in marine environments. The specimens were allowed to reach a steady state potential prior to polarization, which took approximately 1 h.

Amoco P75[†] Gr fibers (ultimate tensile strength = 2.1 GPa, elasticity = 520 GPa) embedded in polyetheretherketone (PEEK) were used to perform polarization and galvanic couple experiments. Edges of the specimen (approximately 0.21 cm²) were sanded to expose fibers to the electrolyte. Marine epoxy again was used to isolate all but one sanded edge of the specimen. The Gr fibers were polarized cathodically at a scan rate of 0.2 mV/s, and the area was estimated by measuring the tested surface area and multiplying it by the fiber volume fraction (53.8%) as calculated using an image analyzer.

The generated polarization data were superimposed to form galvanic current diagrams that were used to estimate the effects of galvanic coupling on the corrosion rate of the Al and Al alloys. Actual galvanic current measurements were taken for the Gr samples coupled to pure Al, Al-19 at.% Mo, and Al-26 at.% W specimens in as-sputtered and heat-treated conditions. Cathode-to-anode area ratios (c:a) of approximately 0.15 and 0.40 were used to evaluate galvanic compatibility. The higher c:a ratio was chosen to approximate the ratio found in a composite, while the lower value represented a less aggressive ratio. These specimens were tested in 0.1 M NaCl (pH 8) for approximately 1 week. Currents were measured as a function of time using a bank of zero resistance ammeters.

RESULTS AND DISCUSSION

Immediately after removal from the sputtering system and after heat treatment at 400°C for 1 h, surfaces of the Al-19 at.% Mo and Al-26 at.% W alloys

---

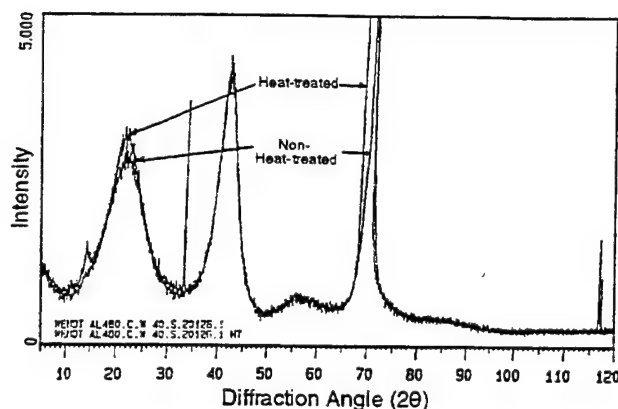† Trade name. Graphite fibers vary between manufacturers.

FIGURE 2. *XRD patterns for Al-26 W before and after heat treatment.*

were examined visually and found to be highly reflective with no cloudiness. This indicated no contaminants in the film. XRD spectra for the Al-26 at.% W alloy is presented in Figure 2. Ignoring the Si peaks at 33°, 70°, and 116°, two very broad peaks were centered at approximately 21° and 41°, which was indicative of an amorphous structure.[21-23] No changes were noted in the diffraction pattern after heat treatment.

The Al-19 at.% Mo XRD pattern was almost identical to the data shown in Figure 2 for the Al-W alloy. Broad peaks were observed at 21° and 41°, and no changes were observed as a result of heat treatment. High-resolution spectra for both alloys are shown in Figure 3. The peak centered at 21° appeared to be an amorphous phase with short range order similar to Al_12Mo and Al_5Mo for the Mo alloy or $Al_{12}W$ and Al_5W for the W alloy. These phases had a number of planes that reflected over these angles.

In a similar fashion, the broad peak centered at 41° may have been more closely associated with the Al, Mo, or W metals. Results indicated the films had no crystalline structure (i.e., no long range order) and that the films actually may have contained the precursors to Al-Mo or Al-W intermetallic compounds.

Subsequent transmission electron microscopy bright-field and selected area diffraction analysis of the alloy films revealed no structure in the films, no diffraction of the beam in tilting, and two large amorphous rings at d values identical to the peaks found at 21° and 41°.

Table 1 presents polarization data for the pure Al, Al-19 at.% Mo, and Al-26 at.% W alloys. Replicate tests were fairly reproducible. The largest variation was 55 mV_{SCE} for the corrosion potential (E_{corr}) and 150 mV_{SCE} for E_b (both for the as-sputtered Al-19 at.% Mo data). With the exception of two experiments, values of the passive current densities were relatively
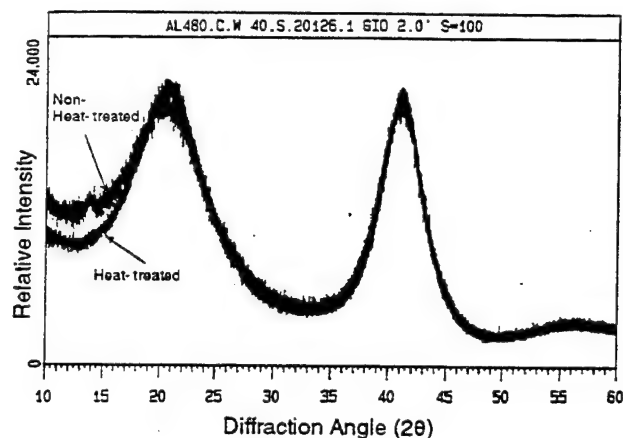
(a)
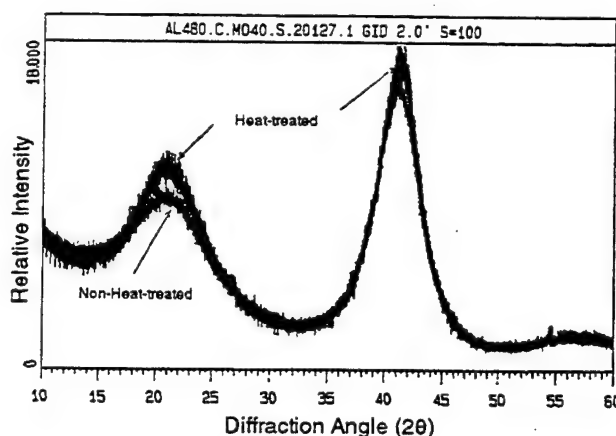
(b)

FIGURE 3. *(a) High resolution x-ray diffraction pattern for the 26 at.% W alloy showing broad amorphous peaks at 21° and 41°. (b) High resolution x-ray diffraction pattern for the 19 at.% Mo alloy showing broad amorphous peaks at 21° and 41°.*

close and similar to that of pure Al. Some variations from specimen to specimen may have been caused by very small defects in the film that resulted from dust particles on the substrate prior to alloy deposition (Figure 4).

Figure 5 shows the anodic polarization behavior for the as-sputtered pure Al, Al-19 at.% Mo, and Al-26 at.% W alloys. As has been reported previously, dramatic improvements in E_b were noted for the nonequilibrium alloys, and both showed more noble E_{corr} than pure Al. The Al-Mo alloy exhibited an average E_{corr} of −515 mV_{SCE} which was 510 mV_{SCE} higher than the pure Al and 215 mV_{SCE} higher than the Al-W. An average E_b of 535 mV_{SCE} was noted for the Al-W that was 1,245 mV_{SCE} higher than the average for pure Al and 140 mV_{SCE} higher than the average for Al-Mo. Similar passive current densities were observed for the

124

TABLE 1
Anodic Polarization Data for Pure Al, Al-19 Mo, and Al-26 W
in 0.1 M NaCl at pH 8

Sample	Scan (mV/s)	E_{corr} (mV$_{SCE}$)	E_b (mV$_{SCE}$)	i_{pass} (μA/cm^2)
Al	0.2	−1,070	−720	0.18
Al	0.2	−980	−700	0.05
Al-19 Mo	0.2	−490	320	1.26
Al-19 Mo	0.2	−545	470	1.26
Al-19 Mo (HT)[A]	0.2	−565	400	9.52
Al-19 Mo (HT)	0.2	—	410	0.50
Al-19 Mo (HT)	0.2	−595	445	1.00
Al-19 Mo (HT)	0.05	−590	440	1.00
Al-19 Mo (HT)	0.008	−560	400	0.60[B]
Al-26 W	0.2	−700	500	4.50[B]
Al-26 W	0.2	−745	550	0.63
Al-26 W	0.2	−740	550	0.63
Al-26 W (HT)	0.2	−775	550	0.63
Al-26 W (HT)	0.2	−775	545	0.63

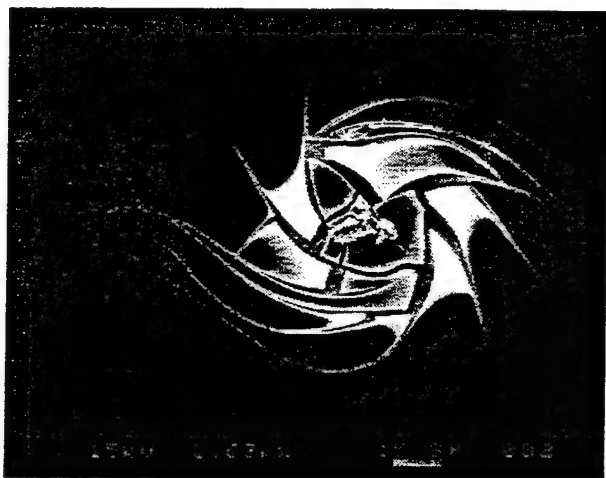[A] HT = heat treated
[B] Average.

FIGURE 4. *SEM micrograph of a breakdown site on an Al-26 W specimens that appeared to have initiated as a result of a dust particle on the Si surface.*

two alloys and for pure Al. These similarities combined with information on the passive film chemistries for Al-W and Al-Mo alloys suggested the modified alloy passive films may have been closer in composition to the film that formed on pure Al than those that formed on pure W or pure Mo.[24]

E_b (Figure 5) for the Al-26 at.% W alloy was significantly lower than E_b for the Al-10 at.% W alloy found earlier by Shaw, et al.,[15] Differences were believed to be related to the conditions under which the alloys were deposited. For the alloys shown in

Figure 1, the sputtering system was located in a class 100 clean room. For the alloys shown in Figure 5, the sputtering system was located in a lab environment. Dust particles on the substrate surface prior to deposition may have affected growth of the film, resulting in lower E_b. E_b reported for the alloys produced in the lab environment still represented a dramatic improvement in corrosion performance over pure Al and were indicative of operating conditions when actual fibers are sputter-coated.

The most encouraging attribute of these alloys was that they retained their enhanced corrosion behavior after heat-treating at 400°C for 1 h (Figures 6 and 7). This performance was attributed to the amorphous structure that was maintained even after heat treatment. Enhanced corrosion resistance at an elevated temperature would be essential for fabrication, because the coated fibers would have to undergo HIP.

These high-concentration Al-Mo and Al-W alloys showed outstanding polarization behavior after heat treatment, which was not observed by Shaw, et al., for the lower solute concentration alloys.[15] The Al-1.5 at.% W and Al-5 at.% W alloys in that research contained precipitates after heat treating for 1 h at 400°C and showed 90 mV$_{SCE}$ to 800 mV$_{SCE}$ decreases in E_b, respectively.

A galvanic current diagram for Gr coupled to pure Al and Al-19 at.% Mo (as-sputtered) is presented in Figure 8. In the case of pure Al, the cathodic, current limited, oxygen reduction reaction for Gr crossed the Al anodic reaction in the pitting region where high galvanic currents were expected.
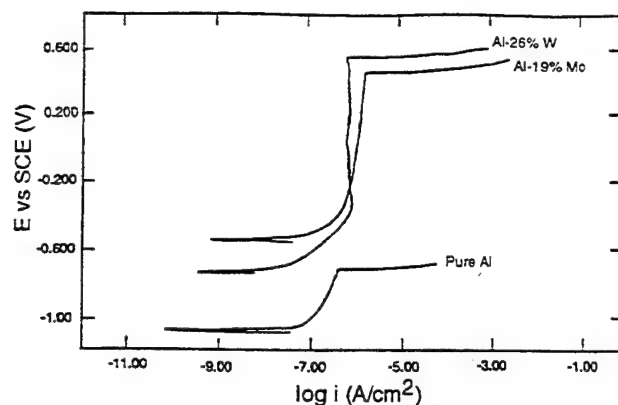
FIGURE 5. *Anodic polarization behavior of Al-19 Mo and Al-26 W in 0.1 M NaCl at pH 8 at 0.2 mV/s compared to pure Al.*
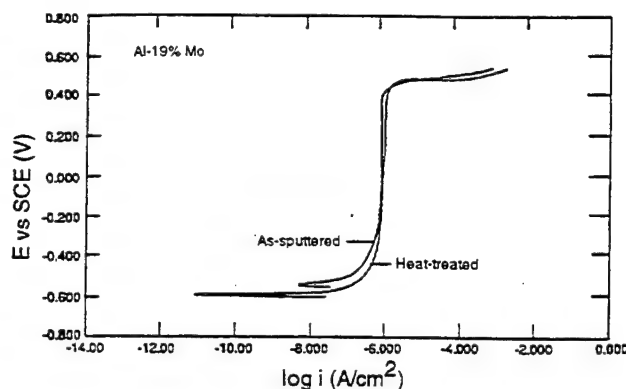

FIGURE 6. *Anodic polarization behavior of Al-19 Mo (as-sputtered vs heat-treated) in 0.1 M NaCl at pH 8 at 0.2 mV/s.*

In the case of the Al-19 at.% Mo, the cathodic, oxygen reduction reaction crossed the alloy's anodic curve in the passive region, where low galvanic corrosion current for the matrix metal was predicted. Considering similar cathode-to-anode area ratios, the pure Al-Gr couple would have had an estimated galvanic corrosion current of 141 μA (141 μA/cm^2), while the predicted galvanic corrosion current of the Al-19 at.% Mo-Gr couple was 0.93 μA.

Therefore, the enhanced passive region for the alloy resulted in a significantly lower galvanic current. The Al-Mo, heat-treated alloy showed similar behavior since the polarization results were identical to those of the as-sputtered sample.

The Al-26 at.% W-Gr galvanic current diagram is shown in Figure 9. The enhanced passivity of the alloy caused the galvanic corrosion current of the couple to decrease from 141 μA for the pure Al-Gr to 0.63 μA for the Al-W-Gr couple. Heat-treated Al-W showed identical behavior due to the similarity of its polarization response to that of the as-sputtered alloys.

Long-term galvanic current measurements were taken to confirm predictions made using galvanic current diagrams. Two alloys from each sample were tested to verify results.

Figure 10 shows the galvanic current vs time data for the as-sputtered pure Al, the as-sputtered and heat-treated Al-19 at.% Mo and the Al-26 at.% W each coupled to Gr in 0.1 M NaCl at pH 8 for 7 days. The pure Al-Gr couple (c:a = 0.11) had an initial galvanic corrosion current of 40 μA that dropped to a value of 10.9 μA (corresponding to a CD of 5.5 μA/cm^2) after 7 days. Visual observations revealed little Al was present on the Si substrate. The other Al-Gr couple had a cathode-to-anode area ratio of 0.13 and exhibited similar behavior.

The cathode-to-anode area ratio for the Al-19 at.% Mo-Gr couple was 0.41. A current of approximately
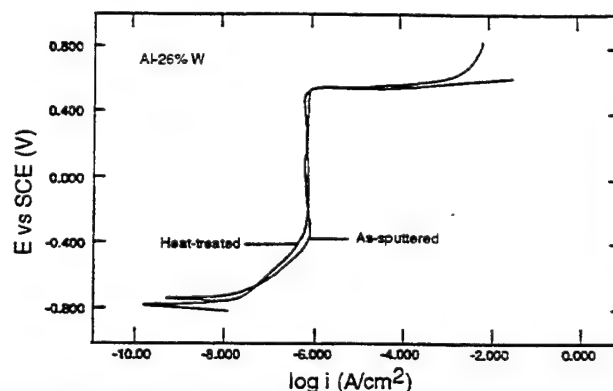

FIGURE 7. *Anodic polarization behavior of Al-26 W (as-sputtered vs heat-treated) in 0.1 M NaCl at pH 8 at 0.2 mV/s.*
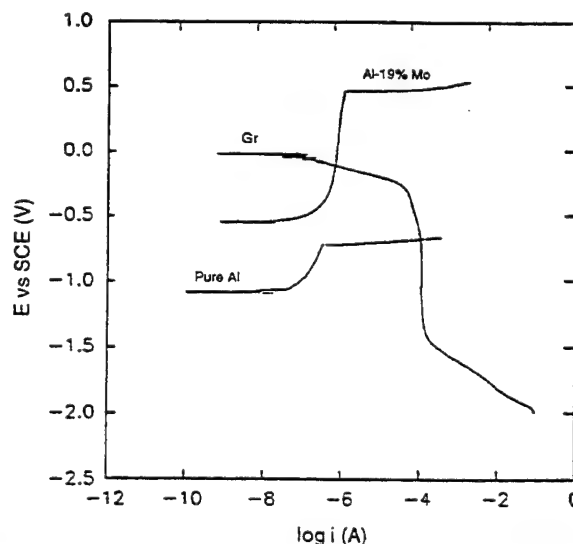

FIGURE 8. *Galvanic current diagram for Gr fiber coupled to pure Al and Al-19 Mo in 0.1 M NaCl at pH 8 at 0.2 mV/s (c:a = 1).*
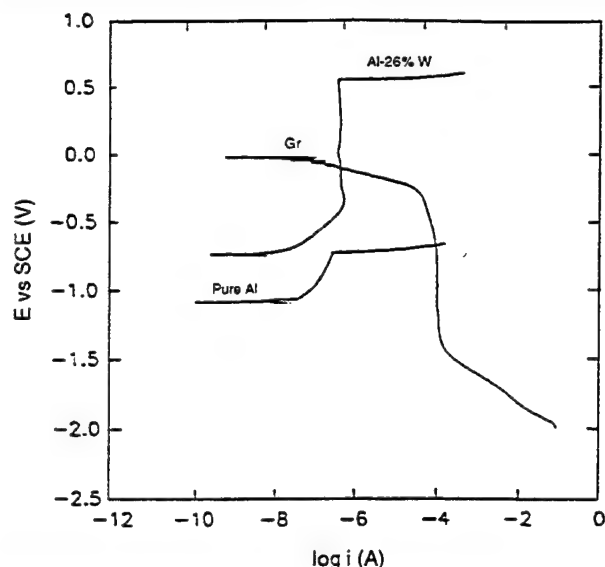
126

FIGURE 9. *Galvanic current diagram for Gr fiber coupled to pure Al and Al-26 W in 0.1 M NaCl at pH 8 at 0.2 mV/s (c:a = 1).*

3 μA was observed initially observed, but decreased to 0.1 μA after 1 h. After 16 h, the current dropped to a steady state value of 0.05 μA (corresponding to a CD of 0.16 μA/cm²) and remained constant for the duration of the experiment. The other Al-Mo-Gr couple (c:a = 0.15) came to a steady state of 0.06 μA (i = 0.09 μA/cm²) for the first 3 days, then increased to approximately 8 μA for the remaining time.

After the experiments, the surfaces of both alloys appeared reflective with no evidence of pitting. SEM of this specimen revealed the coating was still present and in good condition after testing. The increase in current on the second sample was believed to have been caused by a small flaw in the coating or a scratch in the film that initially did not extend to the substrate.

The galvanic current densities after several days of testing were slightly lower than the values predicted by the galvanic current diagram (0.16 μA/cm² vs 0.28 μA/cm²), which showed the diagrams provided a reasonable estimate of the actual galvanic behavior.

The Al-W alloy-Gr couple (c:a = 0.43) had an initial current of 12.4 μA that fell to a value of 0.7 μA (i = 2.1 μA/cm²) for the next 35 h before gradually increasing to a value of 3.2 μA (corresponding to a CD of 9.6 μA/cm²) at the end of the 7-day test. The other galvanic couple for this alloy with a cathode-to-anode area ratio of 0.16 exhibited similar behavior.

After testing, surfaces of both specimens were reflective. No evidence of pitting was observed. Again, it was believed that small flaws or scratches may have led to the increase in current after a few days of exposure.
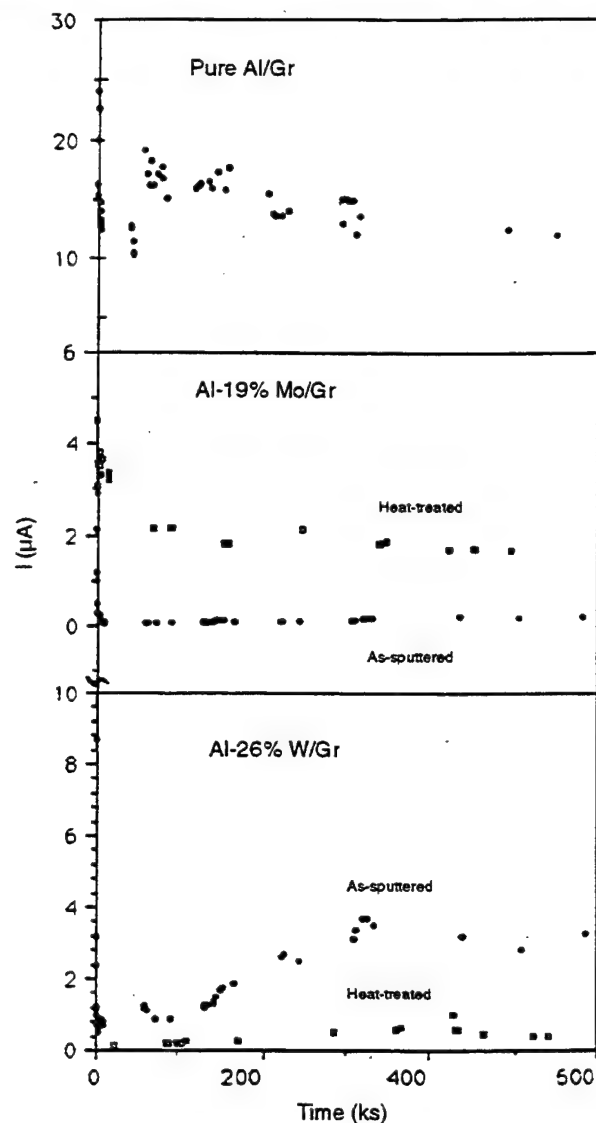

FIGURE 10. *Galvanic current vs time for the as-sputtered pure Al-Gr, the as-sputtered and heat-treated Al-19 Mo-Gr, and Al-26 W-Gr couples in 0.1 M NaCl at pH 8 for 7 days (c:a = 0.11, 0.41, 0.14, 0.14, and 0.43, respectively).*

The heat-treated alloys also had low steady state galvanic corrosion currents. An initial current of 6.1 μA was noted for one of the two Al-19 at.% Mo, heat-treated Gr couples (c:a = 0.14), which dropped to a steady state value of 1.5 μA (1.6 μA/cm²) after approximately 6 days. The second couple with a cathode-to-anode area ratio of 0.18 also showed an initial current of 6.1 μA that fell to a value of 2.4 μA after 45 min and then decreased to 0.16 μA after 50 h. Following this, the current for the second couple increased to 9 μA (i = 12.6 μA/cm²) and occasionally oscillated between anodic and cathodic behavior.

At the end of the test, it was noted that the second specimen contained a small blistered region near the top of the specimen. The remaining 70% of this specimen was intact and in good condition with no pits. After testing, the first specimen was found to be fully intact, optically reflective, and free of pits.

Data for one of the two heat-treated Al-26 at.% W alloy-Gr couples (c:a = 0.43) had an initial current of 16 μA that fell to a steady state value of 0.05 μA (corresponding to a CD of 0.1 μA/cm^2) for the remainder of the experiment. The second heat-treated Al-W alloy-Gr couple with a cathode-to-anode area ratio of 0.16 exhibited an initial current of 1 μA and a steady state value of 0.3 μA (i = 0.33 μA/cm^2). After testing, surfaces of both alloys were reflective. No evidence of pitting was observed.

While the nature of the specimens appeared to make determination of an exact steady state galvanic current difficult in some cases, the important issue of whether performance of a composite could be improved through nonequilibrium alloying was answered easily by the visual appearance of the specimens after testing.

Comparing the appearance of the surfaces of pure Al, the Al-19 at.% Mo alloy, the Al-26 at.% W alloy, and the heat treated Al-26 at.% W alloy after galvanic coupling to Gr for 1 week, the alloy surfaces were optically reflective after testing, while only a small amount of the pure Al film remained after 7 days.

Al-Mo and Al-W alloys containing more than 10 at.% solute were heat-treated at nominal consolidation temperatures and retained their corrosion resistance. XRD results showed no evidence of a change in the diffraction pattern after heat treating.

Below 10 at.% solute, the films could not be heat-treated without the solute reacting to form Al intermetallic phases, which degraded corrosion performance.[20]

CONCLUSIONS

❖ Cosputter-deposited Al-19 at.% Mo and the Al-26 at.% W nonequilibrium alloys showed superior corrosion behavior over pure Al. Heat treatment of these alloys at 400°C for 1 h did not result in the precipitation of a second phase.
❖ Performance of the alloys in polarization experiments and galvanic tests was equivalent to that of as-sputtered alloys. Galvanic current diagrams showed the alloys had much lower galvanic corrosion currents than pure Al as a result of their enhanced passivity.

❖ Long-term galvanic corrosion experiments revealed essentially no degradation for either alloy; whereas, corrosion penetrated the pure Al film, exposing the Si substrate after several days.

ACKNOWLEDGMENTS

REFERENCES

1. M.M. Aylor, R.M. Kain, "Assessing the Corrosion Resistance of Metal Matrix Composite Materials in Marine Environments," ASTM STP 864, Recent Advances in Composites in the US and Japan, Vinson and Taya, eds., (Philadelphia, PA: ASTM, 1985), p. 632.
2. W.H. Pfeifer, "Hybrid and Select Metal Matrix Composites: A State of the Art Review," W.J. Renton, ed., (New York, NY: American Institute of Aeronautics and Astronautics, 1977), p. 231.
3. M.G. Vassilaros, D.A. Davis, G.L. Steckel, J.P. Gudas, "Marine Corrosion and Fatigue of Graphite Aluminum Composites," Proc. 1980 Tri-Service Corrosion Conf., Vol. 2, (Washington, D.C.: US Government Printing Office, 1980), p. 21.
4. D.M. Aylor, R.J. Ferrara, R.M. Kain, MP 23 (1984): p. 32.
5. D.M. Aylor, P.J. Moran, J. Electrochem. Soc. 132 (1985): p. 1,277.
6. D.L. Dull, W.C. Harrigan, Jr., M.F. Amateau, "Final Report - The Effect of Matrix and Fiber Composition on the Mechanical Strength and Corrosion Behavior of Graphite-Aluminum Composites," Aerospace Report ATR-76 (7564)-1, El Segundo, CA (1977).
7. E.G. Kendall, D.L. Dull, "Salt Water Corrosion Behavior of Aluminum-Graphite Composites," National Technical Information Service, U.S. Department of Commerce, AD-777, 160 (1974).
8. L.H. Hihara, "Corrosion of Aluminum-Matrix Composites," (Ph.D. diss., Massachusetts Institute of Technology, Cambridge, MA, 1985).
9. C.R. Crowe, "Localized Corrosion Currents from Graphite-Aluminum and Welded SiC/Al Metal Matrix Composites," NRL Memorandum Report 5415, Naval Research Laboratory, Washington, DC (1985).
10. W.C. Moshier, G.D. Davis, J.S. Ahearn, H.F. Hough, J. Electrochem. Soc. 133 (1986): p. 1,063.
11. W.C. Moshier, G.D. Davis, J.S. Ahearn, H.F. Hough, J. Electrochem. Soc. 134 (1987): p. 2,677.
12. W.C. Moshier, G.D. Davis, G.O. Cote, J. Electrochem. Soc. 136 (1989): p. 356.
13. G.D. Davis, W.C. Moshier, T.L. Fritz, G.O. Cote, J. Electrochem. Soc. 137 (1990): p. 422.
14. B.A. Shaw, T.L. Fritz, G.D. Davis, W.C. Moshier, J. Electrochem. Soc. 137 (1990): p. 1,317.
15. B.A. Shaw, G.D. Davis, T.L. Fritz, B.J. Rees, W.C. Moshier, J. Electrochem. Soc. 138 (1991): p. 3,288.
16. D.C. Bennett, (Master's thesis, University of Connecticut, Storrs, CT, 1972).
17. H.P. Hack, J.R. Scully, Corrosion 42,2 (1986): p. 79.
18. D.A. Jones, Corrosion 40, 4 (1984): p. 181.
19. G.S. Frankel, M.A. Russak, C.V. Jahnes, M. Mirzamaani, V.A. Brusic, J. Electrochem. Soc., 136 (1989): p. 1,243.
20. B.A. Shaw, T.R. Schrecengost, W.C. Moshier, R.G. Wendt, "Inhibiting Corrosion in Gr-Al and Gr-Mg MMCs Using Nonequilibrium Alloying Techniques," Martin Marietta Space Systems Annual Report, ONR-TPSU-MMC-1196-693 (1992).
21. P. Furrer, H. Warlimont, Mater. Sci. E. 28 (1977): p. 127.
22. K. Asami, H. Yoshioka, K. Hashimoto, K. Shimizu, K. Kobayashi, J. Non-Crys. Solids 110 (1989): p. 258.
23. Y. He, S.J. Poon, G.J. Shiflet, Science 241 (1988): p. 1,640.
24. G.D. Davis, B.A. Shaw, B.J. Rees, M. Ferry, J. Electrochem. Soc. 140, 4 (1993): p. 951.

128

Technical Note:
Improving Corrosion Resistance of Magnesium by Nonequilibrium Alloying with Yttrium*

P.L. Miller, B.A. Shaw,* R.G. Wendt, and W.C. Moshier**

ABSTRACT

Significant improvements were achieved in the anodic polarization behavior of magnesium (Mg) by nonequilibrium alloying with 9 at% to 22 at% yttrium (Y). Alloys were fabricated using the nonequilibrium technique of magnetron cosputter deposition. Anodic potentiodynamic polarization experiments were conducted at various scan rates and pH values to assess the corrosion resistance of several MgY alloys. These alloys exhibited significantly enhanced corrosion behavior compared to pure Mg. Differences included higher breakdown potentials and lower passive current densities. X-ray diffraction of each alloy revealed the Y was retained in solid solution.

KEY WORDS: anodic polarization, breakdown potential, corrosion resistance, magnesium, nonequilibrium alloying, pH, x-ray diffraction, yttrium

INTRODUCTION

Previous researchers have reported that alloying additions of yttrium (Y) to magnesium (Mg) enhanced castability and improved its corrosion resistance modestly.[1-3] Unsworth and King documented that an alloy of Mg, Y, and neodymium (Nd) exhibited increased corrosion resistance and better overall castability compared to other Mg alloys.[1] One concern associated with this research was the presence of

precipitates in the Unsworth and King alloy. Second phases increase susceptibility of Mg to galvanic corrosion. Since Mg is extremely electrochemically active, microgalvanic cells could have been established between the Mg and any other phases present. In addition, the formation of precipitates may have tied up the Y, preventing it from contributing to passive film formation.

Krishnamurthy, et al., noted a pseudopassive behavior in rapidly solidified Mg alloys containing 15 wt% to 26 wt% Y.[2] These alloys exhibited a large active nose in the polarization curves prior to formation of the pseudopassive film at relatively high potentials (from 500 mV_{SCE} to more than 1,000 mV_{SCE}). Current densities of a few hundred $\mu A/cm^2$ were observed in the pseudopassive region. Since enhanced passivity was not observed for ingot alloys with the same composition, Krishnamurthy, et al., attributed the improved polarization behavior to the more homogeneous and refined microstructures obtained through rapid solidification of the alloys. While these results showed promise for improving the corrosion resistance of Mg with the addition Y, the large active nose in the polarization curve at the open-circuit potential (E_{oc}) was a significant concern.

Retaining Y in solid solution with Mg is an important step in enhancing the MgY alloy's corrosion behavior. Of the melt spun ribbons tested by Krishnamurthy, the Mg-15 at% Y and Mg-20 at% Y both contained Y-rich precipitates, while the Mg-26 at% Y displayed a "martensitic" type of structure without precipitates.[2] Based on the MgY binary phase

---

diagram, Y alloying additions have a limited solubility (3.75 at%) in Mg.[4]

Magnetron cosputter deposition is a non-equilibrium alloying technique which has been shown to increase the amount of solute that can be maintained in solid solution.[5-18] The objective of this study was to investigate the corrosion behavior of several MgY alloys made by this nonequilibrium alloying technique.

EXPERIMENTAL

MgY alloys were fabricated using magnetron cosputter deposition. Two targets, pure Mg (99.95%) and pure Y (99.95%), were sputtered onto single crystal silicon (Si) substrates, yielding a MgY film ~ 2 μm thick. The substrate was rotated at 30 rpm to ensure uniform solute concentration across the alloy films. Two alloys, Mg-9 at% Y and Mg-22 at% Y, were fabricated for evaluation and testing. Y concentrations in the alloys were estimated using semiquantitative energy dispersive spectroscopy (EDS). Alloys were characterized using x-ray diffraction (XRD), which confirmed that Y solute was retained in solid solution with Mg after the sputtering process.

Specimens for corrosion testing were fabricated by cleaving the alloy-coated Si wafer into 16 pieces, each with an area of ~ 4 cm^2 to 5 cm^2. Individual pieces were then coupled to a potentiostat through a lead wire. Except for the test area, all regions were coated with an adherent marine epoxy to ensure that environmental and electrical isolation were maintained. Anodic potentiodynamic polarization of all alloys was performed using a conventional three-electrode technique on a potentiostat interfaced with a personal computer. All testing was conducted at ambient lab temperature (~ 25°C) in quiescent, 0.1 M sodium chloride (NaCl) solution at pH values of 8, 10, and 12, adjusted using dilute sodium hydroxide (NaOH). All reported potential values were referenced to a saturated calomel reference electrode (SCE). The anodic scans were generated at 0.2 mV/s and 0.05 mV/s. At least two anodic polarization curves were generated for each condition. Prior to anodic polarization, E_{oc} were allowed to stabilize for approximately 30 min. The data were corrected for impedance resistance (IR) drop every 10 s using the current interrupt feature of the potentiostat.

RESULTS AND DISCUSSION

Figure 1 shows anodic polarization curves for Mg, Mg-9 at% Y, Mg-22 at% Y, and Y, generated at a scan rate of 0.2 mV/s in 0.1 M NaCl at pH = 8. Polarization curves for Mg were generated using wrought Mg (99.95%), while sputtered films were used for the Y
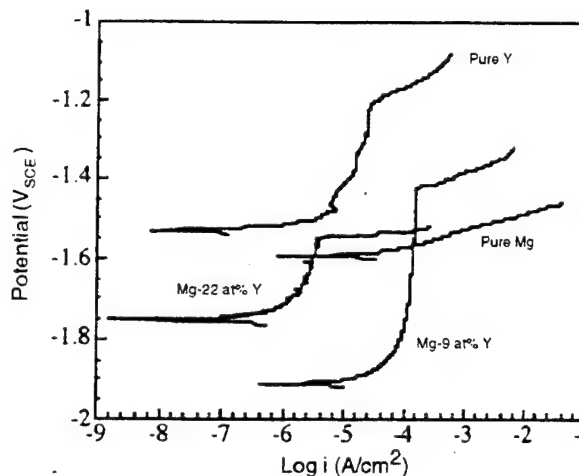

FIGURE 1. *Anodic potentiodynamic polarization curves for Mg, Mg-9 at% Y, Mg-22 at% Y, and Y, generated at a scan rate of 0.2 mV/s in 0.1 M NaCl, pH 8, 25° C.*

and MgY alloys. Sputtered Mg was not used because of its extremely rapid degradation in atmosphere and in solution. The only notable difference between wrought and sputtered Mg was E_{oc}, which for wrought Mg ranged from −1,560 mV$_{SCE}$ to −1,590 mV$_{SCE}$. E_{oc} values for sputtered Mg were 120 mV$_{SCE}$ to 140 mV$_{SCE}$ more electrochemically active than those of wrought Mg. More active E_{oc} values for the sputtered Mg were believed to result from impurities going into solid solution with the Mg and from finer grain sizes incurred during the deposition process. At pH = 8, the Mg-22 at% Y maintained a lower passive current density (i_{pass}), whereas the Mg-9 at% alloy displayed the higher breakdown potential (E_b). Values for i_{pass} ranged from 0.7 A/cm^2 to 4.9 A/cm^2 for Mg-22 at% Y. Values for Mg-9 at% Y were between 40 μA/cm^2 and 128 μA/cm^2. E_b values for Mg-9 at% Y ranged from −1,398 mV$_{SCE}$ to −1,460 mV$_{SCE}$, whereas E_b values for Mg-22 at% Y were between −1,543 mV$_{SCE}$ and −1,597 mV$_{SCE}$. E_{oc} for both alloys decreased with the addition of Y to Mg. Lower E_{oc} values for the MgY alloys compared to pure Mg probably resulted from differences in Tafel behavior and exchange current density (i_o). Mg exhibited an i_o value (10^{-6} A/cm^2 to 10^{-9} A/cm^2) greater than that of Y (10^{-9} A/cm^2 to 10^{-12} A/cm^2).[19]

Experimental data revealed i_o values of 10^{-6} A/cm^2 to 10^{-7} A/cm^2 for Mg and 10^{-9} A/cm^2 for Y. The data were consistent with results reported by West.[19] Therefore, a lower E_{oc} value was obtained by alloying Mg with Y. These trends also applied to anodic polarization curves generated at the scan rate of 0.05 mV/s. The slower scan rate curves were generated to ensure that decreasing the scan rate did not affect E_b significantly.
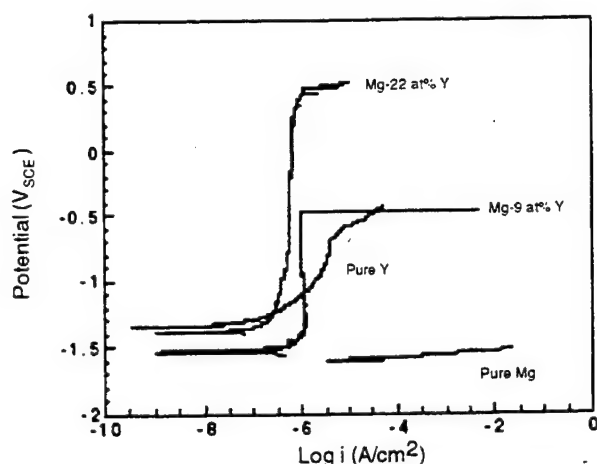
948

FIGURE 2. *Anodic potentiodynamic polarization curves for Mg, Mg-9 at% Y, Mg-22 at% Y, and Y generated at a scan rate of 0.05 mV/s in 0.1 M NaCl, pH 12, 25°C.*

FIGURE 3. *Scanning laser microscope photo of an uncleaved, untested MgY alloy showing disparities on the surface (950x).*

Based on thermodynamic behavior alone, Mg might be expected to have better corrosion resistance at pH values above ~ 11.6.[20] Increasing the solution pH from 8 to 10 yielded little change in the anodic polarization behavior of the MgY alloys. The only notable difference was an increase in E_b (approximately 100 mV_{SCE}) for the Mg-22 at% Y alloy. Compared to that of pure Mg, anodic polarization curves for MgY alloys generated at pH values of 8 and 10 exhibited increased corrosion resistance. Changing solution pH from 10 to 12 resulted in significant changes in the polarization behavior of the MgY alloys.

Figure 2 shows anodic polarization curves for pure Mg, Mg-9 at% Y, Mg-22 at% Y, and pure Y generated at a scan rate of 0.05 mV/s in 0.1 M NaCl, pH = 12. Values of i_{pass} for the Mg-22 at% Y alloys were slightly lower (0.5 $\mu A/cm^2$) than those of the Mg-9 at% Y alloys (1.3 $\mu A/cm^2$). E_{oc} values were more electro-chemically noble in the pH 12 solution, compared to values observed at pH 8 and 10. Values of E_b for both alloys tested at pH 12 varied from -465 mV_{SCE} to -972 mV_{SCE} for Mg-9 at% Y and $+340$ mV_{SCE} to -92 mV_{SCE} for the Mg-22 at% Y alloy. The wide range of E_b values was believed to be a result of film defects, such as the one shown in Figure 3, created during the sputtering and handling processes.[5] Another possibility for the varied E_b values was that the 0.05 mV/s scan rate used for the anodic potentiodynamic curves was not slow enough to allow electrolyte-film surface reactions to reach steady state. In contrast to the anodic polarization curves generated at a pH of 8, E_b at a pH of 12 for the alloy containing higher concentrations of Y was consistently greater than that of Mg-9 at% Y.
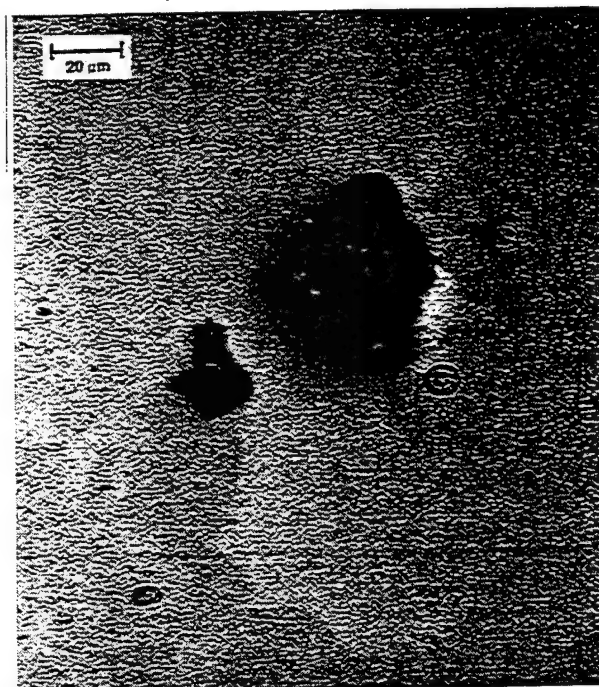
Krishnamurthy, et al., conducted anodic potentiodynamic polarization experiments with Mg-Y (approximately 5 at% to 9 at%) in 0.01 M NaCl (pH not mentioned) and found that ribbons and splats exhibited a pseudopassive behavior at high potentials (> 250 mV_{SCE}), which led to lower current densities of 300 $\mu A/cm^2$ to 400 $\mu A/cm^2$.[2] Comparing those pseudopassive current densities to those obtained in the present work, much lower passive current densities were observed for the sputterdeposited alloys tested in a higher (0.1 M) concentration NaCl solution.

Pseudopassive behavior of Krishnamurthy's alloys at such high overpotentials may be unrealistic in most practical applications. At low to moderate overpotentials, the sputterdeposited MgY alloys exhibited significantly lower current densities compared to the splat-quenched alloys. The enhanced corrosion resistance obtained for the sputter-deposited alloys likely resulted from the absence of second phases, which freed more Y solute to be used for passivity enhancement of the alloy.

CONCLUSIONS

❖ Addition of Y to Mg significantly altered its polarization behavior. Differences included increased E_b and lower i_{pass} values compared to pure Mg.

❖ Both MgY alloys exhibited greater corrosion resistance than pure Mg when tested in 0.1 M NaCl solution at pH =12. These results were a dramatic improvement in both E_b and i_{pass} for Mg alloys. Values for E_b were quite varied at the high pH for both scan rates. Even with the wide variability in E_b noted for the low-solute-concentration alloy, this polarization behavior represented a significant improvement over pure Mg and other Mg alloys.

ACKNOWLEDGMENTS

REFERENCES

1. W. Unsworth, J. King, Metallurgia 53 (1986): p. 199.
2. S. Krishnamurthy, M. Khobaib, E. Robertson, F.H. Froes, Mater. Sci. E. 99 (1988): p. 507.
3. A. Joshi, R.E. Lewis, Advances in Magnesium Alloys and Composites, H. Paris, W.C. Hunt, eds., 89 (Warrendale, PA: TMS,1988).
4. T.B. Massalski, ed., Binary Alloy Phase Diagrams, 2nd ed., Vol. 3 (Metals Park, OH: ASM International, 1990), p. 2,568.
5. T.R. Schrecengost, B.A. Shaw, R.G. Wendt, W.C. Moshier, Corrosion 43 (1993): p. 842.
6. R.G. Wendt, "Development of Corrosion Resistant Aluminum Alloys for Graphite Fiber Composites" (Master's thesis, Colorado School of Mines,1992).
7. W.C. Moshier, G.D. Davis, J.S. Ahearn, H.F. Hough, J. Electrochem. Soc. 133 (1986): p. 1,063.
8. W.C. Moshier, G.D. Davis, J.S. Ahearn, H.F. Hough, J. Electrochem. Soc. 134 (1987): p. 2,677.
9. W.C. Moshier, G.D. Davis, G.O. Cote, J. Electrochem. Soc. 136 (1989): p. 356.
10. G.D. Davis, W.C. Moshier, T.L. Fritz, G.O. Cote, J. Electrochem. Soc. 137 (1990): p. 422.
11. B.A. Shaw, T.L. Fritz, G.D. Davis, W.C. Moshier, J. Electrochem. Soc. 137 (1990): p. 1,317.
12. G.D. Davis, W.C. Moshier, G.G. Long, D.R. Black, J. Electrochem. Soc. 138 (1991): p. 3,194.
13. B.A. Shaw, G.D. Davis, T.L. Fritz, B.J. Rees, W.C. Moshier, J. Electrochem. Soc. 138 (1991): p. 3,288.
14. B.A. Shaw, G.D. Davis, T.L. Fritz, B.J. Rees, W.C. Moshier, in Critical Factors in Localized Corrosion, G.S. Frankel, R.C. Newman. eds., PV 92-9, (Pennington, NJ: The Electrochemical Society Softbound Proceedings Series, 1992), p. 323.
15. G.S. Frankel, M.A. Russak, C.V. Jahnes, M. Mirzamaani, V.A. Brusic, J. Electrochem. Soc. 136 (1989): p. 1,243.
16. H. Yoshioka. H. Habazake, A. Kawashima, K. Asami, K. Hashimoto, Corros. Sci. 32 (1991): p. 313.
17. H. Yoshioka, A. Kawashima, K. Asami, K. Hashimoto, in Corrosion Electrochemistry and Catalysis of Metallic Glasses, R.B. Diegle, K. Hashimoto. eds., PV 88-1 (Pennington, NJ: The Electrochemical Society Softbound Proceedings Series, 1988), p. 242.
18. Z. Szklarska-Smialowska. in Critical Factors in Localized Corrosion, G.S. Frankel, R.C. Newman. eds., PV 92-9, (Pennington, NJ: The Electrochemical Society Softbound Proceedings Series, 1992), p. 311.
19. J.M. West, Electrodeposition and Corrosion Processes (London, U.K.: Van Nostrand Reinhold, 1965), p. 50.
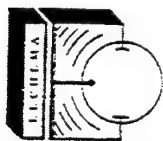20. M. Pourbaix, Atlas of Electrochemical Equilibria in Aqueous Solutions (Houston, TX: NACE, 1974), p. 141.
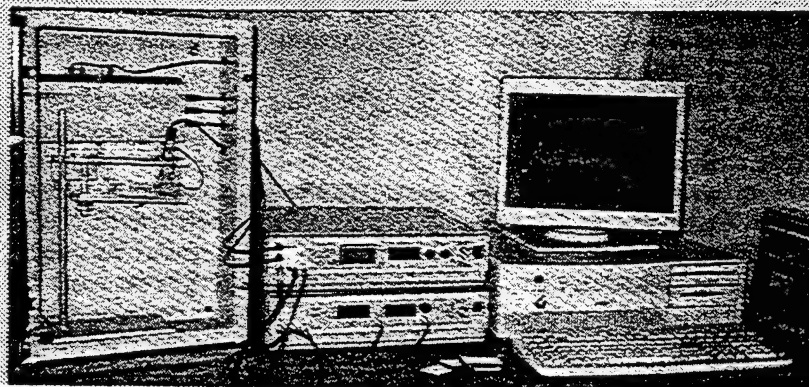
Corrosion-Resistant Aluminum Matrix for Graphite-Aluminum Composites*

R.G. Wendt, W.C. Moshier,* B. Shaw,** P. Miller,*** and D.L. Olson****

ABSTRACT

Graphite-aluminum (Gr-Al) metal matrix composites (MMC) possess several attractive mechanical and thermal properties, but use of these materials has been limited, partly because they are extremely susceptible to corrosion. Corrosion-resistant Al alloys that contained nonequilibrium concentrations of molybdenum (Mo) were developed as the matrix for Gr-Al composites using co-sputter deposition. Corrosion testing included potentiodynamic polarization and galvanic coupling of as-sputtered (AS) and heat-treated (HT) alloys. Polarization behavior of the AS and HT alloys measured in sodium chloride (NaCl) solutions was improved greatly over that of pure Al and traditional Gr-Al matrix alloys such as type 6061 Al (UNS A96061). Galvanic current density values for as-deposited and HT Al-18% Mo and Al-23% Mo alloys coupled to equal areas of pitch-based graphite from Amoco P75† Gr fibers were found to be up to 3 orders of magnitude lower than for pure sputtered Al-to-Gr couples. Galvanic diagrams for the Al-Mo alloys indicated corrosion was controlled by the anodic reaction irrespective of the cathode-to-anode area ratio.

KEY WORDS: alloying, aluminum, composites, galvanic coupling, graphite, metal matrix composites, molybdenum, potentiodynamic polarization

INTRODUCTION

High-modulus graphite-aluminum (Gr-Al) metal matrix composites (MMC) offer high specific modulus and ultimate tensile strength (E/ρ and UTS/ρ, respectively), high thermal conductivity (K), and a coefficient of thermal expansion (α) that can be designed to be 0 μm/m/°C by selecting the appropriate Gr fiber type, volume, and lay-up. These properties are ideal for designing mechanically (E/ρ) and thermally (α/K) stable structures. However, Gr-Al is very susceptible to corrosion, which has limited its application in aircraft, spacecraft, and marine structures severely.

Gr-Al composites have been shown to corrode 80 times faster than monolithic Al alloys in an aerated 3.15 wt% sodium chloride (NaCl) solution at room temperature.[1] One key factor in the rapid corrosion of Gr-Al composites has been the residual microstructural chlorides introduced during the liquid metal infiltration (LMI) process used to fabricate precursor Gr-Al wires.[1-4] Corrosion of Gr-Al composites has initiated by pitting of the Al facesheet foils at a rate commensurate with Al alloys. Once the Al facesheet foils are penetrated, corrosion is accelerated by residual microstructural chlorides within the composite and by exposure of the Gr fibers, creating a galvanic couple.

Several techniques have been investigated to improve the corrosion resistance of Gr-Al, including coatings, cathodic protection, and cathodic inhibitors.[1,5] These methods have provided various

Galvanic corrosion response of the Al-Mo and Al-Mg-Mo alloys was estimated using galvanic diagrams constructed from the polarization data.[12] In these diagrams, the anodic data for the Al-Mo alloys and pure sputtered Al were superimposed on the cathodic curve for the Gr fiber. Assuming the potential drop due to solution resistance between the metal and Gr fibers was insignificant, there were no contributions from reverse reactions, and current distribution between the metal and graphite was uniform. The intersection of the anodic and cathodic curves was used to estimate the current in the galvanic couple.

To confirm the galvanic diagram predictions, galvanic currents were measured by coupling the AS or HT alloy specimens to the Gr fibers. The Gr fibers were prepared for testing by embedding them into a nonconductive epoxy and electrically connecting them to a external lead. Area fractions of the exposed Gr fibers were measured using an image analyzer. Nominal cathode-to-anode area ratios ranged from 0.2:1 to 1.1:1. The alloy specimen and the Gr-epoxy composite were coupled electrically and immersed in 0.1 M NaCl solution (pH = 8). Galvanic current was monitored as a function of time using a potentiostat-zero resistance ammeter (ZRA).

RESULTS

Alloy Fabrication and Heat Treatment

Compositions and anodic polarization results of the AS Al-Mo and Al-Mg-Mo alloys are listed in Table 1. All AS alloys had a highly reflective metallic appearance, which indicated low levels of contaminants. After heat treating, most of the alloys retained their highly reflective appearance.

XRD revealed that all the AS alloys were amorphous (Figure 1). Table 2 summarizes XRD results for the alloys that were heat treated at 400°C, 500°C, and 600°C for 1 h, 2 h, and 8 h to determine the effect of composite consolidation on the alloy structure. As Mo concentration in the Al alloy increased, its propensity to form precipitates during heat treatment decreased. For example, Al-11% Mo precipitated at the shortest time (1 h) and lowest temperature (400°C), whereas Al-23% Mo remained amorphous after heat treatment at 600°C for 2 h. This result was unexpected because the thermo-dynamic driving force for precipitation increased as Mo concentration increased. Lack of precipitation indicated the kinetics for precipitation in these alloys was very sluggish. The Al-Mg-Mo alloys also were amorphous in the AS condition but were found to react at all heat treatment times and temperatures, forming precipitates as well as oxides as a result of the reaction of Mg with the sapphire substrate.

TABLE 1

Composition and Anodic Polarization Data for AS Binary Al-Mo and Ternary Al-Mg-Mo Nonequilibrium Alloys in 0.1 M NaCl (pH 8)

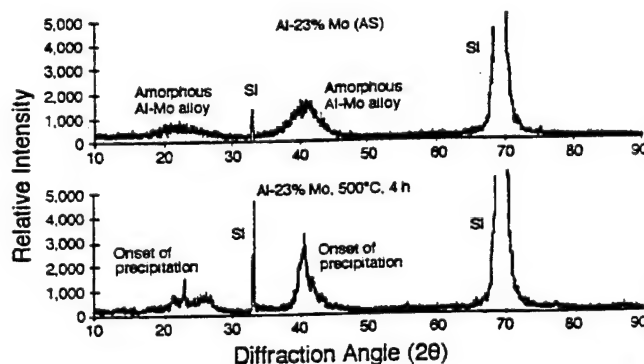| Composition (at%)	E_{oc} (mV$_{SCE}$)	E_b (mV$_{SCE}$)	I_{pass} (µA/cm²)
Al	−1,093	−690	0.1
	−1,224	−689	0.7
Al-11% Mo	−581	220	2.69
	−629	100	23.7
	−681	0.0	46.6
Al-18% Mo	−520	461	0.89
	−601	391	3.5
	−555	456	3.63
Al-23% Mo	−582	563	45.6
	−582	492	7.6
	−591	496	7.6
Al-26% Mo	−440	750	3.0
	−427	700	0.60
	−460	600	0.80
	−495	770	1.90
	−540	760	4.17
Al-12% Mg-13% Mo	−513	55	1.0
	−573	85	4.5
	−550	39	5.6

FIGURE 1. *XRD of Al-23% Mo alloy in AS condition and after heat treatment. The AS alloy was amorphous and was just beginning to precipitate after heat treatment at 500°C for 2 h.*

Polarization Testing

As-Deposited Alloys — Table 1 and Figure 2 summarize results of the anodic polarization experiments for the binary Al-Mo and ternary Al-Mg-Mo nonequilibrium alloys in the AS condition. All the as-deposited Al-Mo alloys exhibited an extended passive region and an E_{oc} 500 mV to 600 mV more noble than pure Al. E_{oc} values for all the alloys were

134

levels of improved corrosion resistance but only have delayed pitting and subsequent galvanic interaction between the Al matrix and Gr fiber. None of these techniques has addressed the true problem, which is poor corrosion resistance of the Al matrix in chloride (Cl⁻) environments, especially when the metal is coupled galvanically to Gr fibers.

An alternate method for preparing Gr-Al composites is to deposit the Al matrix directly onto individual Gr fibers by physical vapor deposition (PVD).[6] The flexible alloy-coated fibers are arranged in the desired orientations and consolidated by diffusion bonding. The versatility of the PVD process allows virtually any matrix alloy to be deposited onto Gr fibers. Advantages of the PVD process over the LMI process include: (a) elimination of fiber-matrix reactions because the composites can be consolidated well below the melting point of Al where the kinetics for aluminum carbide formation are sluggish, (b) minimization of thermal strain hysteresis because of the high strength of the sputtered alloy matrix and the smaller thermal excursion required for diffusion bonding compared to melting, (c) development of near-net shape processing capability, and (d) elimination of residual microstructural chlorides.

Several Al-molybdenum (Mo) alloys have been fabricated using sputtering, which is similar to the PVD process used for Gr-Al composites.[7-11] These Al-Mo alloys were tested electrochemically and were shown to exhibit improved corrosion resistance over typical Al alloys.

In the present work, additional Al-Mo compositions were investigated to determine the feasibility of using these alloys as the matrix for Gr-Al composites. Alloys were fabricated and tested to assess whether the improvement in corrosion behavior was maintained after heat treating at typical composite consolidation temperatures. In addition, galvanic corrosion experiments were conducted to determine electrochemical stability of Al-Mo by coupling the nonequilibrium alloys to Amoco P75[†] Gr fibers embedded in a nonconductive epoxy. Throughout this work, the increased density that resulted from the addition of refractory metals to Al was taken into consideration. Mo additions to Al were studied, as was the impact of adding magnesium (Mg) as a low-density ternary element to assess whether highly noble breakdown potentials (E_b) could be achieved and maintained after heat treatment.

EXPERIMENTAL PROCEDURE

Binary Al-Mo and ternary Al-Mg-Mo alloys were fabricated by co-sputtering from pure-element targets

onto either 100-mm-diam silicon (Si) wafers in the case of the binary alloys or single-crystal sapphire : the Al-Mg-Mo alloy. Sapphire was used for the ternary alloy to eliminate formation of magnesium disilicide ($MgSi_2$) at low temperatures and short heat treatment times. However, sapphire also was found to react with Mg to form spinels and oxides during heat treating. Hence, it was difficult to identify an in substrate for the ternary alloy study.

Substrate temperature was not controlled durin sputtering and reached a maximum of ≈ 100°C during a 1-h deposition that resulted in an alloy film ~ 1 μm thick. Alloy composition was controlled by holding the Al cathode power constant at 485 W at 13.56 MHz radio frequency (RF) while the power to the Mo and Mg cathodes was varied between 10 W and 100 W direct current (DC). High-purity argon (10 ppb oxygen [O_2]) working gas was introduced a flow rate of 200 standard cm³/min (SCCM), and pressure was held constant at 7 mtorr (0.90 Pa) by adjusting the conductance of the system. The sputtering heads were spaced ≈ 100 mm from the substrate and were focused at 60° from the substra normal. By rotating the substrate at 30 rpm, alloy composition uniformity could be maintained to within a few atomic percent of solute across the substrate.

Composition of the sputtered alloys was measured using energy dispersive spectroscopy (EDS) using a scanning electron microscope (SEM) Compositions of several specimens also were measured by inductively coupled plasma (ICP) for comparison.

X-ray diffraction (XRD) was conducted using a 12-kW rotating anode diffractometer with a monochromatic copper (Cu-K$_a$) x-ray source. Both as-sputtered (AS) and heat-treated (HT) Al-Mo alloy were analyzed to determine whether the Mo was in solid solution with the Al and readily available for incorporation into the passive film or whether precipitation had occurred, resulting in the formatior of Al_xMo_y intermetallic compounds.

Anodic polarization tests were conducted at ambient pressure and temperature in a quiescent (nonstirred with no purge gas [i.e., neither aerated nor deaerated but in open air]) 0.1 M NaCl solution with the pH adjusted to 8 using reagent-grade sodium hydroxide (NaOH). Alloys that exhibited enhanced corrosion behavior were prepared for additional polarization tests where the concentratior of Cl⁻ in solution was varied (either 0.1 M or 0.55 M NaCl) and the solution was aerated. Using a potentiostat-galvanostat, specimens were allowed t reach a stable open-circuit potential (E_{oc}) and were polarized in the anodic direction starting at a potenti 10 mV$_{SCE}$ cathodic to E_{oc} at a rate of 0.2 mV/s until breakdown occurred.

TABLE 2
Summary of Al-Mo Alloy Structure as a Function of Heat Treatment Time and Temperature

| Heat Treatment Time (h)	Heat Treatment Temperature		
	400°C	500°C	600°C
1	Al-11% Mo, ppt[A]	Al-11% Mo, ppt	Al-11% Mo, ppt
	Al-18% Mo, Amorphous	Al-18% Mo, ppt	Al-18% Mo, ppt
	Al-23% Mo, Amorphous	Al-23% Mo, Amorphous	Al-23% Mo, Amorphous
2	Al-11% Mo, ppt	Al-11% Mo, ppt	Al-11% Mo, ppt
	Al-18% Mo, Amorphous	Al-18% Mo, ppt	Al-18% Mo, ppt
	Al-23% Mo, Amorphous	Al-23% Mo, Amorphous	Al-23% Mo, Amorphous
8	Al-11% Mo, ppt	Al-11% Mo, ppt	Al-11% Mo, ppt
	Al-18% Mo, Amorphous	Al-18% Mo, ppt	Al-18% Mo, ppt
	Al-23% Mo, Amorphous	Al-23% Mo, Amorphous	Al-23% Mo, ppt

[A] ppt = fully precipitated.
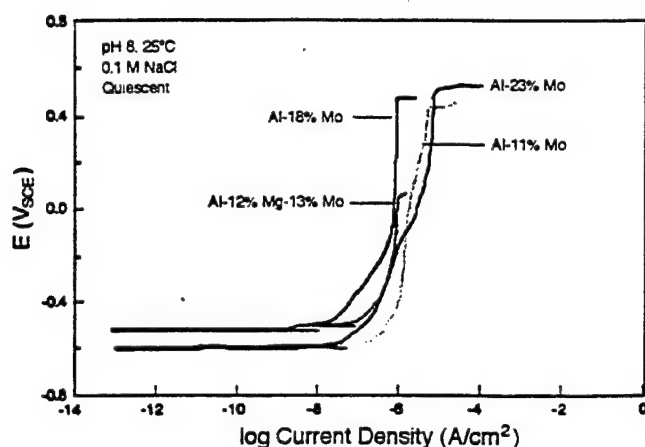
FIGURE 2. *Anodic polarization response of various Al-Mo alloys, polarized in quiescent 0.1 M NaCl at pH 8, 25°C.*

measured between −600 mV$_{SCE}$ and −450 mV$_{SCE}$. The majority of measured E$_{oc}$ values ranged from −520 mV$_{SCE}$ to −580 mV$_{SCE}$. There was no apparent trend in E$_{oc}$ as a function of solute concentration for the Al-Mo alloys tested, in agreement with previous work on Al-Mo alloys.[7-8,10] Passive current densities (i$_{pass}$) for the as-deposited binary Al-Mo and ternary Al-Mg-Mo alloys ranged between 0.1 μA/cm² and 10.0 μA/cm², but as in the case of E$_{oc}$, no correlation between solute concentration and i$_{pass}$ was evident. Variations in i$_{pass}$ were attributed to general defects (i.e., scratches, pinholes, etc., in the alloy film). E$_b$ values for most of the AS alloys were between 100 mV$_{SCE}$ and 500 mV$_{SCE}$ compared to −690 mV$_{SCE}$ for pure Al.

Additional polarization experiments were conducted on the Al-18% Mo alloy in aerated and quiescent NaCl solutions (pH 8) with Cl⁻ concen-

trations of 0.1 M and 0.55 M. Figure 3 shows the polarization response was not altered significantly by increasing [Cl⁻], by aerating the solution, or both.

SEM examination and EDS analysis of a newly formed pit on the as-deposited Al-18% Mo specimen immediately after polarization to E$_b$ showed [Mo] increased from 18 at% to 25 at% in the pit. The increase in Mo in the forming pit indicated the pitting process involved the preferential dissolution of Al from the alloy, which was consistent with x-ray photoelectron spectroscopy work conducted during earlier studies.[8,10]

HT Alloys — The polarization response of as-deposited and HT Al-11% Mo alloys is shown in Figure 4. Although E$_b$ for the HT Al-11% Mo alloys decreased from ~ 420 mV$_{SCE}$ (AS) to 50 mV$_{SCE}$ (HT), E$_{oc}$ remained relatively constant at ~ −550 mV$_{SCE}$. E$_b$ likely was reduced as the result of precipitates formed during heat treatment that created microgalvanic cells with the surrounding alloy. Conversely, i$_{pass}$ decreased from ~ 1 μA/cm² for the as-deposited alloy to ~ 0.1 μA/cm² after heat treatment.

Neither E$_{oc}$ nor E$_b$ for the Al-18% Mo alloy was affected dramatically by heat treating to 500°C for 2 h (Figure 5). Similar to the Al-11% Mo alloys, i$_{pass}$ for the HT Al-18% Mo specimens was less than that for the AS alloy, with the exception of the specimen heat treated at 400°C for 1 h. No cracks or defects that might contribute to lower E$_b$ values were found during SEM examination of the HT alloys.

The Al-12% Mg-13% Mo alloy exhibited an E$_{oc}$ value of −580 mV$_{SCE}$ and E$_b$ of 55 mV$_{SCE}$ in the as-deposited condition, which was similar to values for the Al-Mo alloys (Figure 6). The E$_{oc}$ value was maintained after heat treating at 400°C for 1 h; however, heat treating the ternary alloy at longer times and higher temperatures resulted in a more
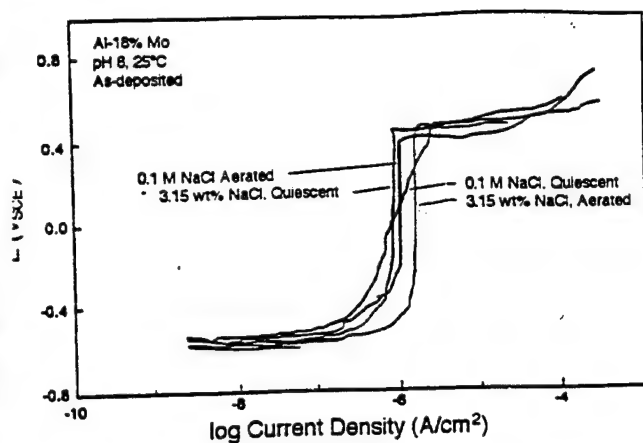
FIGURE 3. *Anodic polarization response of Al-18% Mo used for detailed heat treatment studies, polarized in quiescent and aerated 0.1 M and 3.15 wt% (0.55 M) NaCl at pH 8, 25°C.*
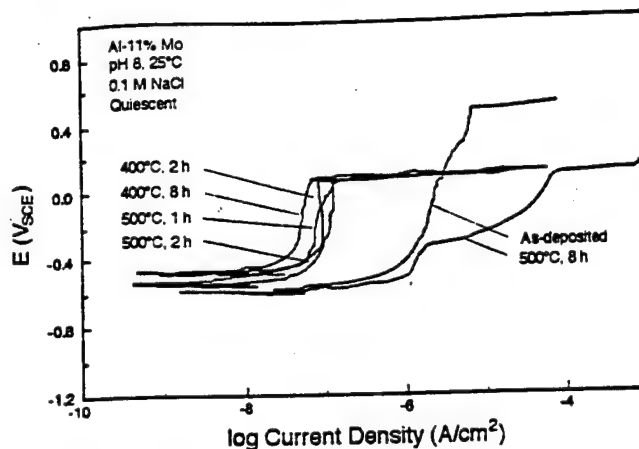

FIGURE 4. *Anodic polarization response of Al-11% Mo alloy before and after heat treatment at 400°C for 1 h and 2 h and at 500°C for 1 h, 2 h, and 8 h, polarized in quiescent 0.1 M NaCl at pH 8, 25°C.*

active E_{oc} (~ –800 mV$_{SCE}$) with no passive response during polarization.

Galvanic Corrosion Behavior

Galvanic diagrams based on equal metal-Gr areas for pure Al, type 6061 Al (UNS A96061),[1] and the Al-Mo alloys coupled to the Gr fibers are shown in Figure 7.[12] This diagram estimates that the galvanic corrosion of pure sputtered and type 6061 Al coupled to the Gr fibers was controlled cathodically, with a high current density value of 12.5 µA/cm². For a cathodically controlled reaction, the cathodic curve shifted to a higher current density as the Gr-to-Al area ratio increased, which accelerated the corrosion rate of the Al matrix. Unlike the case for pure Al, galvanic corrosion was controlled anodically for the Al-Mo alloys, with an estimated galvanic current density of 1 µA/cm². For anodically controlled corrosion, changing the Gr-to-Al ratio and subse- quently shifting the cathodic curve to higher current density values (or anodic curve to lower current density) did not change the corrosion rate for the Al-Mo alloys significantly. This result was important because modifying the Gr fiber volume, which is a key design feature of composites to achieve specific thermal or mechanical properties, did not result in dramatic changes in the corrosion response of the Gr-Al-Mo composite.

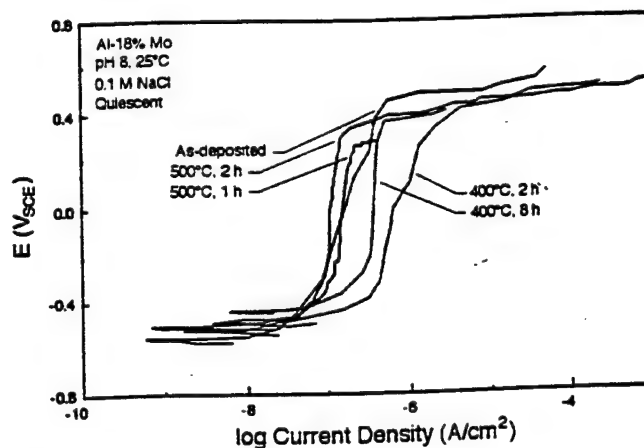The galvanic corrosion reaction remained anodically controlled for both the Al-11% Mo

FIGURE 5. *Anodic polarization response of Al-18% Mo alloy before and after heat treatment at 400°C for 2 h and 8 h and at 500°C for 1 h and 2 h, polarized in quiescent 0.1 M NaCl at pH 8, 25°C.*

(Figure 8) and Al-18% Mo (Figure 9) alloys after heat treatment. Although some of the Al-11% Mo and Al-18% Mo alloys precipitated during heat treatment (Table 2), they still exhibited a passive polarization response and the galvanic diagrams predicted corrosion would be controlled by anodic dissolution of metal. Only after heat treating the Al-11% Mo to 500°C for 8 h was control for the galvanic reaction changed from anodic (Al passivation) to cathodic (O$_2$ reduction on Gr fibers).

To confirm predictions made using the galvanic diagrams, long-term galvanic current tests were

___

[1] UNS numbers are listed in *Metals and Alloys in the Unified Numbering System*, published by the Society of Automotive Engineers (SAE) and cosponsored by ASTM.
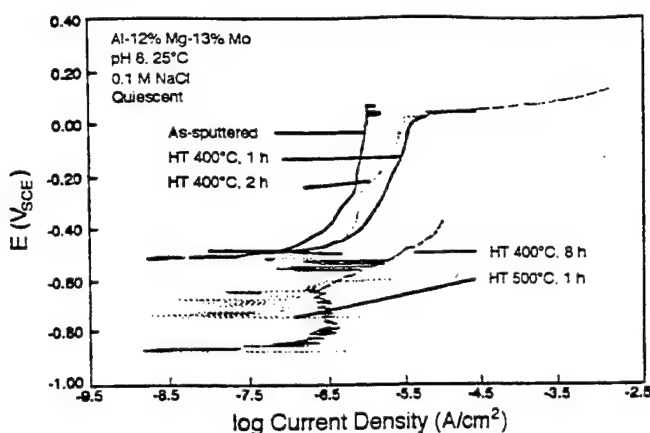
823

137

FIGURE 6. *Anodic polarization response of Al-12% Mg-13% Mo before and after heat treatment at 400°C for 1 h, 2 h, and 8 h and at 500°C for 1 h, polarized in quiescent 0.1 M NaCl at pH 8, 25°C.*
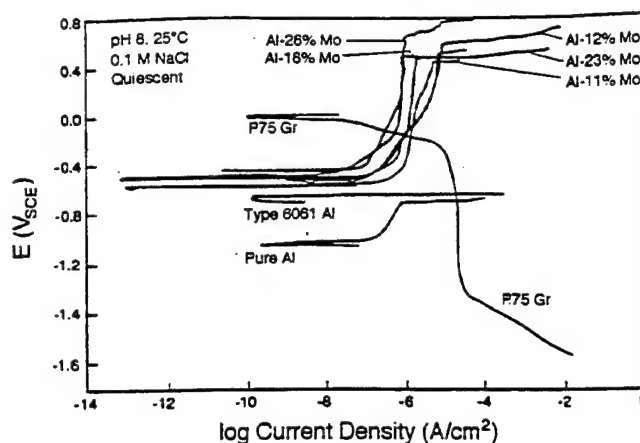

FIGURE 7. *Galvanic diagram showing the anodic curve of pure sputtered Al, wrought type 6061 Al, and various sputtered Al-Mo alloys combined with the cathodic curve for and equal area of P75 Gr fibers, tested in quiescent 0.1 M NaCl at pH 8, 25°C.*
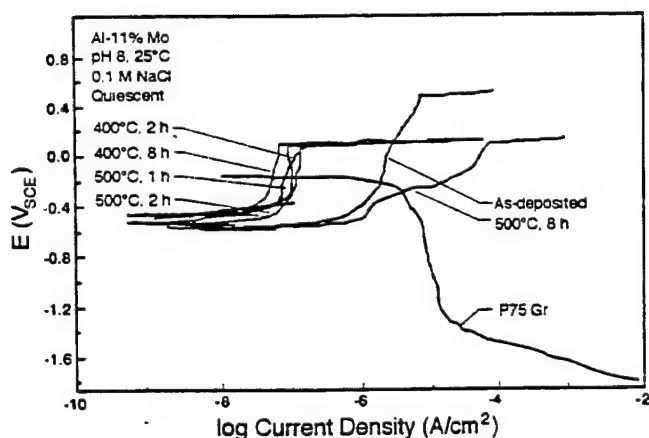

FIGURE 8. *Galvanic diagram for equal areas of P75 Gr fibers and of Al-11% Mo alloy before and after heat treatment at 400°C for 2 h and 8 h and at 500°C for 1 h, 2 h, and 8 h with P75 Gr fibers, tested in quiescent 0.1 M NaCl at pH 8, 25°C.*

conducted on sputtered Al, Al-11% Mo, Al-18% Mo, Al-23% Mo, and ternary Al-12% Mg-13% Mo in the as-deposited condition by coupling the alloy to the Gr fibers (Figure 10). Galvanic current values were equivalent to current densities since the anode areas were 1 cm². For all the alloys, the galvanic current initially started at relatively high values (between 3 µA/cm² and 30 µA/cm²), but dropped quickly to a low steady-state value. The Al-18% Mo and Al-23% Mo reached low measured galvanic current densities of ~ 0.04 µA/cm² and ~ 0.08 µA/cm², respectively. These values were up to 3 orders of magnitude lower

than the galvanic current density values of 30 µA/cm² measured for pure sputtered Al. Current density values of the Al-18% Mo after heat treatment at 400°C for 2 h were comparable to the AS value of 0.08 µA/cm². Even after heat treatment at 500°C for 2 h, the galvanic current density was 1 order of magnitude lower than for pure sputtered Al. After galvanic testing for 7 days (605 ks) the pure sputtered Al had dissolved completely from the Si wafer. The Al-Mo alloys remained intact and highly specular.

The Al-12% Mg-13% Mo alloy exhibited a galvanic current value of 10 µA/cm², which was greater than that of the binary Al-Mo alloys but still 3 times lower than for pure Al. However, in less than 12 h (40 ks) after immersion in the 0.1 M NaCl solution (pH = 8), the Al-Mg-Mo alloys coupled to the Gr fibers had exfoliated and lifted completely away from the sapphire wafer. Because of the short time in solution for the Al-12% Mg-13% Mo alloy, data for this alloy was not included in Figure 10.

DISCUSSION

XRD examination indicated the Al-Mo alloys containing > 11 at% Mo were amorphous even though the substrate was allowed to heat to ≈ 100°C during the sputtering process. The broad peak at 21° was attributed to short-range ordering associated with the Al_xMo_y intermetallic compounds, which have high intensity peaks at these low angles. Similarly, the broad peak at 41° was indexed to amorphous Al and was indicative of what has been found for other
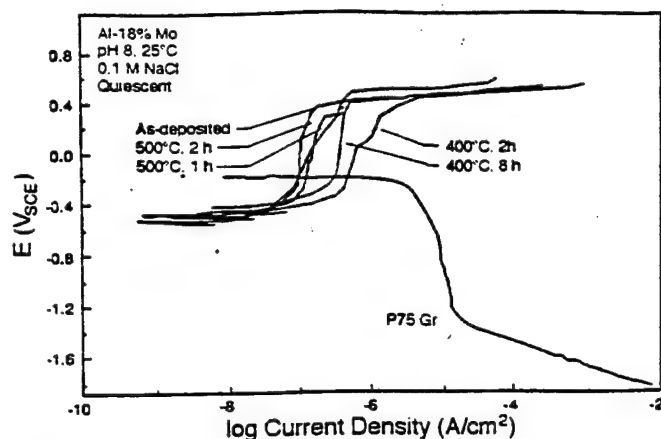
138

FIGURE 9. *Galvanic diagram for equal areas of P75 Gr fibers and of Al-18% Mo alloy before and after heat treatment at 400°C for 2 h and 8 h and at 500°C for 1 h and 2 h, tested in quiescent 0.1 M NaCl at pH 8, 25°C.*

FIGURE 10. *Galvanic current for commercially pure (CP) Al and Al-Mo alloys (as-deposited and HT) coupled to P75 Gr fibers in quiescent 0.1 M NaCl at pH 8, 25°C.*

FIGURE 11. *Anodic polarization response of Al-18% Mo tested in quiescent 0.1 M and 0.55 M NaCl at pH 8, 25°C superimposed with P75 cathodic curve and cathodic data for P100, SiC, and TiB$_2$ from Hihara and Latanision.[3]*

sputtered and rapidly solidified Al alloys.[13-15] XRD indicated Mo had not precipitated to form Al$_x$Mo$_y$ intermetallic compounds and thus was available for incorporation into the passive film. Alloys that did not form precipitates during heat treatment exhibited E$_{oc}$ and E$_b$ values very similar to the as-deposited alloys; E$_{oc}$ remained similar to that of the as-deposited alloys, but E$_b$ was more electrochemically active for heat treatments which produced precipitates. For the Al-18% Mo alloy, a noble E$_b$ of ≈ 400 mV$_{SCE}$ was observed after heat treatment to 500°C for 2 h even though XRD indicated secondary phases had precipitated.

Galvanic corrosion for all the as-deposited Al-Mo alloys was controlled by the anodic reaction as indicated by the intersection of the passive region of the anodic curve with the O$_2$ reduction portion of the Gr cathodic curve. The galvanic diagrams showed galvanic corrosion of pure Al and type 6061 Al alloy was controlled cathodically, whereas galvanic corrosion of the nonequilibrium alloys was controlled anodically.

For cathodic-controlled corrosion, dissolution of the alloy occurred at a high rate corresponding to the rate of the reduction reaction. The result was that the nonequilibrium alloys corroded at a rate ~ 2 orders of magnitude lower than pure Al or conventional Al alloys when coupled galvanically to Gr fibers. Because E$_b$ for the anodic reaction was more noble than E$_{oc}$ for the cathodic reaction, Al-Mo alloys coupled to Gr fibers were expected to be stable regardless of the area ratios.

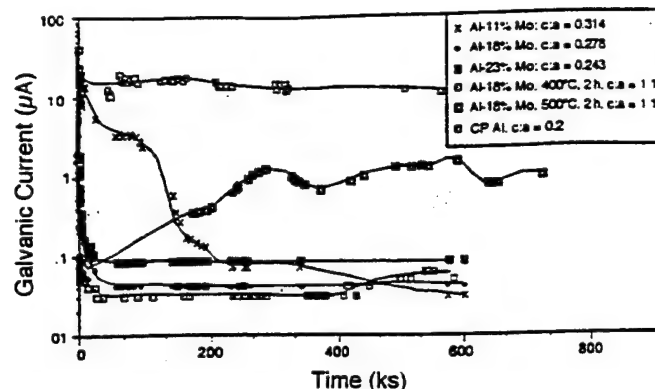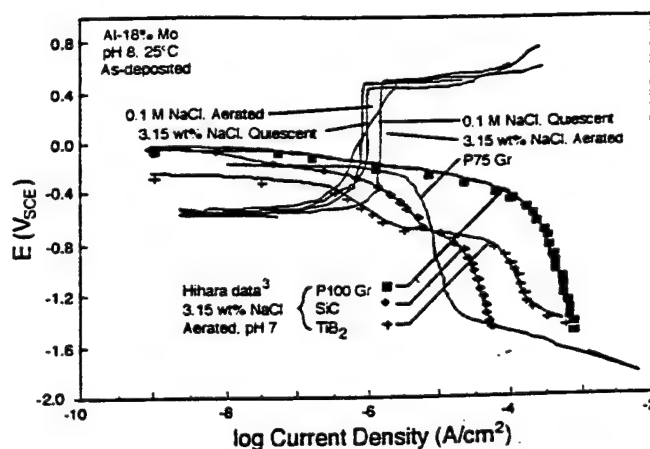Decreasing the anode area (or conversely increasing the cathode area) generally resulted in

lateral displacement of the polarization curves, and the corrosion reaction remained anodically controlled. This was beneficial because the composite corrosion behavior was not affected adversely by increasing the Gr fiber volume.

Even after heat treatment, the binary Al-Mo alloys exhibited high E$_{oc}$ of –550 mV$_{SCE}$ and E$_b$ values between 100 mV$_{SCE}$ and 400 mV$_{SCE}$. As a result, the galvanic diagrams indicated the couple was controlled anodically, and the current density was >1 μA/cm^2.

Hihara and Latanision measured the cathodic reaction of P100† Gr, SiC, and, titanium diboride (TiB$_2$) in an aerated 3.15 wt% (0.55 M) NaCl solution.[3] Superimposition of these results onto the

139

galvanic diagrams presented in this work showed the cathodic reaction on the P100 Gr fibers in a higher Cl$^-$ concentration solution was very similar to the cathodic reaction of the P75 Gr fiber in 0.1 M NaCl of pH 8 (Figure 11). E_{oc} for P75 and P100 Gr fibers were ≈ 0 mV$_{SCE}$.

Figure 11 shows that the Al-Mo alloys also would be stable galvanically with higher modulus Gr fibers such as P100, as well as other reinforcements such as SiC, and with fiber coatings such as TiB$_2$. This result is significant because it is the first time corrosion of Gr-reinforced composites has been shown to be controlled by the alloy matrix, rather than driven by the Gr fibers.

CONCLUSIONS

❖ Nonequilibrium Al-Mo alloys fabricated by magnetron sputtering were shown to be promising matrix alloys for Gr-Al composites. Al with 18 at% Mo to 23 at% Mo could be heat treated to 400°C for 8 h without detectable precipitation or change in corrosion behavior. The Al-23% Mo alloy could be heat treated to 600°C for 2 h without degrading corrosion performance. Al-18% Mo heat treated at 400°C for 8 h exhibited E_{oc} of −556 mV$_{SCE}$, E_b of 335 mV$_{SCE}$, and i_{pass} of ~ 0.4 μA/cm^2 in 0.1 M NaCl solution of pH 8.

These values were very similar to the AS Al-18% Mo alloys and were a significant improvement over pure Al and type 6061 Al alloy, which are typical matrix materials for Gr-Al composites.

Galvanic current densities measured for the Al-18% Mo alloy and the Al-23% Mo alloy of ~ 0.04 μA/cm^2 to ~ 0.08 μA/cm^2 were 3 orders of magnitude < the 30 μA/cm^2 measured for pure Al in the 0.1 M NaCl, pH 8 solution when coupled to the Gr fibers. Galvanic diagrams of the anodic response of the alloy superimposed with the cathodic curve for the Gr fibers predicted the galvanic corrosion rate to be controlled by the rate of the anodic reaction. The Al-Mo alloys were predicted to be stable electro-chemically when coupled to Gr fibers regardless of the area ratios (in a 0.1 M NaCl electrolyte).

Galvanic current density values for the Al-18% Mo alloy heat treated at 400°C for 2 h were similar to the AS alloy but increased after 2 h of treatment at 500°C.

❖ The ternary Al-12% Mg-13% Mo alloy exhibited improved polarization behavior with respect to pure

Al and type 6061 Al alloy and had a lower density than the Al-Mo alloys. Unfortunately, the ternary alloys exhibited much higher galvanic current density values (~ 10 μA/cm^2) and were found to precipitate during heat treatment for the shortest time (1 h) and lowest temperature (400°C), which resulted in a loss of passivation.

❖ The polarization and galvanic data indicated Al alloyed with between 10 at% Mo and 26 at% Mo provided a matrix that could be processed and consolidated at high temperatures and still retain its inherent corrosion resistance when coupled to the Gr fibers in the composite. Therefore, the optimum alloy composition studied was the Al-18% Mo alloy because it was the lowest-density alloy that could be coupled to Gr fibers after heat treatment and retain its passive behavior without increasing its galvanic corrosion.

ACKNOWLEDGMENTS

REFERENCES

1. L.H. Hihara, "Corrosion of Aluminum-Matrix Composites" (Ph.D. diss., Massachusetts Institute of Technology, 1985).
2. L.H. Hihara, R.M. Latanision, Corrosion 47 (1991): p. 335-340.
3. L.H. Hihara, R.M. Latanision, Corrosion 48 (1992): p. 546-552.
4. W.C. Harrigan, R.H. Flowers, "Graphite-Metal Composites: Titanium-Boron Vapor Deposit Method of Manufacture," in Failure Modes in Composites IV, eds., J.A. Cornie, F.W. Crossman (Warrendale, PA: The Minerals, Metals, and Materials Society, 1977), p. 319-335.
5. J.H. Payer, P.G. Sullivan, "Corrosion Protection Methods for Graphite Fiber-Reinforced Aluminum Alloys, in Bicentennial of Materials, Proc. 8th Natural SAMPE Technical Conference, Seattle WA, Oct. 12-14, 1976 (Azusa, CA: Society for the Advancement of Material and Process Engineering, 1976), p. 343-352.
6. V.C. Nardone, J.R. Strife, "Advanced Gr-Mg Composite Development," United Technologies Research Center, Interim Report R89-917711-4, East Hartford, CT, July 1989.
7. W.C. Moshier, G.D. Davis, J.S. Ahearn, H.F. Hough, J. Electrochem. Soc. 133 (1986): p. 1,063-1,064.
8. W.C. Moshier, G.D. Davis, J.S. Ahearn, H.F. Hough, J. Electrochem. Soc. 134 (1987): p. 2,677-2,684.
9. G.S. Frankel, M.A. Russak, C.V. Jahnes, M. Mirzamaani, V.A. Brusic, J. Electrochem. Soc. 136 (1989): p. 1,243-1,244.
10. G.D. Davis, W.C. Moshier, T.L. Fritz, G.O. Cote, J. Electrochem. Soc. 137 (1990): p. 422.
11. T.R. Schrecengost, B.A. Shaw, R.G. Wendt, W.C. Moshier, Corrosion 43 (1993): p. 842.
12. D.A. Jones, Principles and Prevention of Corrosion, 1st ed. (New York, NY: Macmillian Publishing Co., 1992), p. 176-188.
13. P. Furrer, H. Warlimont, Mater. Sci. Eng. 28 (1977): p. 127-137.
14. K. Asami, H. Yoshioka, K. Hashimoto, K. Shimizu, K. Kobayashi, J. Noncrystalline Solids 110 (1989): p. 258-264.
15. Y. He, S.J. Poon, G.J. Shiflet, Science 241 (1988): p. 1,640-1,642.

Assessing the Corrosion Resistance of Nonequilibrium Mg-Y Alloys

P.L. Miller and B.A. Shaw
The Pennsylvania State University
Department of Engineering Science and Mechanics
University Park, PA 16802

R.G. Wendt and W.C. Moshier
Martin Marietta Astronautics Group
Denver, CO 80201

ABSTRACT

Magnesium-yttrium alloys containing concentrations of 7 to 26 atomic percent solute were fabricated using magnetron co-sputter deposition. X-ray diffraction revealed that no second phases were present in any of the alloys and that all except two of the alloys (Mg-7Y and Mg-14Y) were nanocrystalline and/or amorphous. Anodic potentiodynamic polarization performed in 0.1 M NaCl at both near-neutral and high pH values showed improved anodic polarization behavior for most of the alloys when compared to either pure Mg or one of the most corrosion resistant commercial Mg alloys (WE43). In the high pH solution, it was not uncommon for the E_b values of the Mg-Y alloys to be 2000 mV higher than the values noted for WE43. Long-term galvanic and potentiostatic testing were performed on selected alloys to verify anodic polarization behavior. Potentiostatic testing was also performed in a pH 12 buffer solution, and when defects did not affect corrosion behavior, low current density values were obtained, with one specimen exhibiting a current density of 0.9 $\mu A/cm^2$ at a potential in excess of +300 mV_{SCE}. X-ray photoelectron spectroscopy conducted on Mg-22%Y revealed that, once the alloy was immersed in solution, yttrium was significantly enriched in the passive film, and it is this presence of oxidized Y in the passive film that is believed to be responsble for the exceptional corrosion resistance of these alloys.

INTRODUCTION

The factor that limits the utilization of magnesium in many engineering systems is its poor corrosion resistance. This poor corrosion resistance is typically the result of galvanic interactions with alloying additions, impurities, or other metals (or conductors) and is not surprising in light of magnesium's position in the galvanic series[1]. In fact, corrosion rates of 5 - 100 $mg/cm^2 \cdot day$ (410 - 8300 mpy) have been observed for pure Mg (99.9%pure) in a 3% NaCl solution.[2] These high corrosion rates have been attributed to the presence of Fe, Ni, and Cu impurities in the magnesium.[2,3] However, corrosion rates of 12 mpy have been observed when the purity level of the Mg is increased to 99.994%. [2]

Recently, rapid solidification processing (RS) has been investigated as a means for increasing strength and enhancing the corrosion resistance of Mg and Mg alloys. [4-17] Das et. al.[10] developed RS techniques (jet casting and planar flow casting) capable of producing magnesium alloys with significantly enhanced mechanical properties and corrosion resistance (UTS values of up to approximately 517 MPa (75 ksi) and corrosion rates as low as 12 mpy). Improvements in mechanical properties and corrosion resistance for these alloys have been attributed to the formation of a homogeneous distribution of fine dispersoids within the alloy. Makar et al.[13] investigated the use of conventional alloying additions, such as Li, Al, Zn, and Ca, and RS (melt spinning) as a means for enhancing the corrosion resistance of Mg. Their results revealed that the corrosion rate of melt spun Mg ribbons could be lowered from 52 mpy to 12 mpy with the addition of 43 wt.% Al. This research showed that other alloying elements such as Li, Si and Zn caused varying increases in the corrosion rate. In addition, they observed that the RS Mg-Al alloys experienced relatively uniform attack and repassivaed faster and more completely than their as-cast counterparts, suggesting greater chemical or microstructural homogeneity for the RS Mg-Al alloys. They speculated that increased homogeneity retards pit nucleation, thereby retarding the development of local environments that impair repassivation. Increasing the Al content from 1 to 9 at.% improved the repassivation rate of their alloys, indicating that Al enhances passive film repair.

Yttrium and neodymium have also been reported to enhance the the corrosion resistance of conventional and RS Mg alloys.[8,16,18,19] Krishnamurthy et al.[8] compared the corrosion resistance of alloys prepared by chill block melt spinning and splatting techniques to those for ingot alloys of the same composition. The RS alloys were reported to exhibit significantly finer and more uniform microstructures than the ingots. Anodic potentiodynamic polarization data (generated in areated 0.01 M NaCl) for RS Mg-3.6 to 20 wt.% Nd and Mg-15 to 26 wt.% Y alloys showed a pseudopassivation effect at high potentials (>250 mV) which led to lower current densities of 100 to 1000 $\mu A/cm^2$ (one to two orders of magnitude less than the ingots which did not exhibit this pseudopassive behavior). The pseudopassivation effect for the RS alloys was thought to occur because of Nd or Y enrichment at the surface, leading to modification of the passive film.

Another fabrication method which can be used to produce nonequilibrium alloys with significantly enhanced corrosion resistance is magnetron sputter deposition. Many references to the exceptional corrosion resistance of sputter-deposited nonequilibrium Al alloys have been presented in the literature in the past.[20-33] Unlike more common rapid solidification processes, sputtering is vapor phase deposition process that circumvents the liquid-solid transition and, as a result, can be used to dramatically increase solute solubility. For example, in the Al-Mo system in which molybdenum (Mo) has virtually no solubility in Al, Mo can be retained in solid solution in amounts of at least 25 atomic percent (at. %).[20] The absence of second phases, even after several years of room temperature storage, aids in enhancing the corrosion resistance of these alloys. Nanocrystalline or amorphous alloys are also easily produced with this

deposition method. The corrosion resistance of magnetron sputter-deposited Fe-based alloys has also been investigated, but little work[34,35] has been done to explore the feasibility of using this deposition method to enhance the corrosion resistance of Mg.

In this reseach, several nonequilibrium Mg alloys were fabricated by magnetron co-sputter deposition and screened for their corrosion resistance. Alloys such as Mg-W, Mg-Ta, Mg-Mo, Mg-Al-Mo, and Mg-Mo-W with various compositions were evaluated. At low to moderate solute concentrations, none of these alloying additions passivated Mg in neutral pH chloride solutions. Based on the promising results of Krishnamurthy and a commercial Mg-Y-Nd alloy (WE43), sputter-deposited Y-containing Mg alloys were evaluated. This paper documents the results of a corrosion investigation conducted on several sputter-deposited Mg-Y alloys. The objective of this research was to determine if Mg-Y alloys with significantly enhanced corrosion resistance (when compared to WE43) in chloride-containing environments could be developed using magnetron co-sputter deposition. Of specific interest with regard to these alloys, are their resistance to uniform, localized, and galvanic corrosion.

EXPERIMENTAL

Mg-Y alloys were fabricated by magnetron co-sputter deposition using co-focussed cathodes. Alloys were sputtered from two targets, Mg (99.9 %) and Y (99.9 %), onto single crystal silicon wafers, yielding Mg-Y alloy films approximately 1 to 2 μm thick. Substrate temperature was not controlled during sputtering and reached a maximum temperature of approximately 100 °C during a 1 hour deposition. The sputtering rate was 1 - 2 μm/hr. Pressure in the chamber was held constant at 7.0 mtorr during sputtering by introducing purified (< 10 ppb O_2) Ar gas at a flow rate of 200 standard cubic centimeters per minute (sccm) and adjusting the conductance of the system. Compositions of different Mg-Y alloys were controlled by holding the Mg cathode between 240 and 480 Watts (W) RF, while the power for the Y cathode was varied between 25 and 100 W DC. Uniform alloy composition on each Si wafer was maintained by spacing the cathode heads approximately 100 mm (4 in) from the substrate, focused 60° from the substrate normal and rotating the substrate at 30 rpm during deposition.

Compositions of the sputtered alloys were determined using energy dispersive spectroscopy (EDS) and direct current plasma (DCP). EDS employed a semi-quantitative computer program that analyzed the x-ray spectra to determine alloy composition through comparison of acquired peaks to a library of references stored on disk. DCP involved dissolving the Mg-Y alloy in a 20 vol. % HCl solution and analyzing the solution chemistry.

Prior to electrochemical testing, x-ray diffraction (XRD) was conducted using a Rigaku Rotoflex 12 kW rotating anode diffractometer containing a monochromatic Cu-K$_\alpha$ x-ray source. Intensity versus diffraction angle (2θ) was

measured to determine whether the yttrium solute was maintained in solid solution with Mg.

Alloy surface morphology was characterized using optical microscopy, scanning electron microscopy (SEM), and confocal scanning laser microscopy (SLM). Optical microscopy and SLM were used prior to electrochemical testing to observe surface defects such as scratches and cracks incorporated during sputtering and handling (i.e., cleaving of the alloy-coated Si wafer) of the alloy. SEM was also used prior to polarization so that EDS could be employed for semi-quantitative compositional analysis. All three microscopy techniques were used following electrochemical testing so that the morphology of the breakdown regions could be evaluated.

X-ray photoelectron spectroscopy (XPS) was conducted on one of the alloys prior to and immediately following electrochemical testing. Analysis was conducted on the following specimens: as-received, E_{corr} in 0.1 M NaCl at pH 8 and 12, and E_{corr} plus 400 mV in 0.1 M NaCl at pH 12. XPS was conducted so that information on the passive oxide or hydroxide film could be obtained.

Polarization specimens were prepared by cleaving the alloy-coated Si wafer into pieces with areas of approximately 4 to 5 cm^2. Individual specimens were then coupled to a potentiostat through a lead wire and all regions, except the test area, were coated with an adherent marine epoxy to ensure that environmental and electrical isolation were maintained.

Anodic polarization was conducted using a potentiostat coupled to a personal computer. Polarization curves were generated at scan rates of 0.2 mV/sec and 0.05 mV/sec in 0.1 M NaCl. Solution pH was initially adjusted to either 8, or 12 using NaOH. While it is realized that the pH of such solutions will not be stable with time, especially at a pH of 8, this approach allowed the behavior of the alloy to be investigated without the influence of buffers which can be incorporated in the passive films of the alloys and significantly affect alloy performance. For the solutions initially adjusted to a pH of 12, the pH fell to a value of 11.8 after 18 hours. For solutions initially adjusted to a pH of 8, the pH fell to 7.8 after 20 minutes, 7.5 after 60 minutes and 7.3 after 120 minutes. These solutions will be refered to as near neutral pH (8 to 6.8) and high pH (12 to 11.8) in this paper. A buffered solution, which is described in the final paragraph of this section, was used for the long-term potentiostatic tests. A conventional three electrode technique was employed for the electrochemical tests and consisted of a SCE, graphite counter electrodes, and sample electrode. The corrosion potential (E_{corr}) was allowed to stabilize in the test solution for approximately 30 minutes prior to each anodic polarization. A minimum of two tests were conducted for each condition to confirm the validity of results. Unless specifically noted, all potentials reported in this paper are referenced to the SCE.

Cathodic polarization of graphite fibers (chosen because of their noble position in the galvanic series and possible future applications of Mg-Y alloys as the matrix material in graphite-reinforced MMCs) was conducted so that galvanic

diagrams could be generated. Electrochemical response of the graphite fibers was measured by testing a composite consisting of 62.5 vol. % P75 Gr fibers embedded in an epoxy adhesive with a tradename of ERXL 1962. Prior to testing, the edges of the specimens (with an approximate graphite area of 0.74 cm^2) were sanded to reveal the fibers and to make an electrical connection. The specimen and holder were electrically isolated by embedding the composite in an epoxide resin. The graphite was cathodically polarized at a scan rate equivalent to the anodic scans, and the area of the graphite fibers was estimated by measuring the tested surface area and multiplying it by the fiber area fraction of the exposed surface (55 %) calculated with an image analyzer.

By superimposing the cathodic curve of the graphite onto the anodic curve of the pure Mg or Mg alloys, the galvanic corrosion current can be estimated from the intersection of the two curves providing there is an insignificant IR drop, the contribution of other contributing reactions is small, and the current density is uniform.[36] The galvanic current diagrams in this paper are for equal areas of 1 cm^2; therefore, the current is equal to the current density.

Galvanic current measurements were taken to confirm galvanic current diagram predictions. Prior to initiation of each experiment, E_{corr} was allowed to stabilize for approximately 1 hour. In these experiments, Mg-Y alloys were coupled to graphite fibers in 0.1 M Cl^- having initial pH values of either 8, 12, or buffered 12 for a period of 7 days or until the alloy had corroded away. The currents were recorded as a function of time using banks of potentiostats/zero resistance ammeters (ZRAs) interfaced to a personal computer using data acquisition software. Data were recorded a minimum of every ten minutes with each data point being averaged for a period of at least ten seconds.

Long term potentiostatic tests were conducted on one of the Mg-Y alloys in a 0.1 M Cl^- solution buffered to pH 12. The buffer solution[37] was prepared by mixing 500 ml of 0.05 M $Na_2HPO_4 \cdot 7H_2O$ and 269 ml of 0.1 M NaOH adding 5.845 g of NaCl, and diluting to 1 L with deionized water. Tests were conducted using banks of potentiostats/ZRAs interfaced to a personal computer using data acquisition software. The potentiostats were adjusted to the desired potentials and the current values were measured through the ZRAs.

RESULTS AND DISCUSSION

X-ray diffraction was conducted on the sputtered Mg-Y alloys to determine whether the yttrium was in solid solution with the Mg or in the form of Mg_xY_y precipitates. As mentioned earlier, microgalvanic cells significantly increase the corrosion of Mg and Mg alloys and should, therefore, be avoided in the development of a corrosion resistant Mg alloy. In general, it is also beneficial for the Y to be retained in solid solution, rather than tied up in a precipitate, so that it will be available for passivity enhancement.

Figure 1 shows XRD patterns for several Mg-Y alloys. The two lower solute composition alloys have very sharp peaks, indicating a crystalline structure;

whereas, the alloys with higher solute concentrations have very broad peaks, denoting a nanocrystalline and/or amorphous structure. The primary peak present in the crystalline alloys at approximately 34° was indexed to the (002) plane of Mg. The sharp peak observed at 55.5° is the Si wafer. These patterns do not correlate to the relative peak intensities of polycrystalline Mg, indicating that the sputter-deposited film has a preferential orientation on the Si wafer. The broad peaks observed for the higher concentration alloys were centered at 33.6° and 33.3° for Mg-20Y and Mg-26Y, respectively.

An overlay of the (002) Mg peaks for several Mg-Y alloys is presented in Figure 2. Note that a decreasing 2θ value is observed when increasing the solute content of the Mg-Y alloy. For pure Mg, the d value for the (002) plane is 2.606 Å, yielding a 2θ value of 34.38° using Bragg's law.[38] All observed 2θ values for the Mg-Y alloys are less than this value. Peak shifts were calculated for the two crystalline peaks assuming that the Y solute is placed into the lattice substitutionally and that a hexagonal-close-packed (hcp) structure was maintained. Table 1 shows the results of these calculations. The predicted peak shifts are greater than those observed from the data. Possible explanations for these differences are misalignment of the x-ray system, variations in solute composition, phase separation, or, most probably, film elastic stress.

A total of 83 anodic potentiodynamic polarization experiments were performed on bulk Mg, sputtered Mg, bulk WE43, sputtered Y, and sputtered Mg-Y alloys. Sputtered Mg was not generally used because the thin film alloys (1 - 2 μm) were completely consumed by corrosion shortly after being exposed to the chloride solution. In addition, significant degradation of the surface of the pure Mg occurs during room temperature storage in the lab. This degradation alone made the use of the pure Mg thin-films unacceptable after several weeks of storage. The only notable difference in polarization behavior observed between bulk and sputtered Mg was E_{corr}, which was 120 to 140 mV more noble for bulk Mg, ranging from -1560 to -1590 mV. This shift in E_{corr} may be the result of impurities being in solid solution with the Mg in the sputtered alloys and being present as a descrete phases in the bulk alloys.

Anodic polarization scans for the Mg-Y alloys and WE43 generated in a near-neutral pH solution at a scan rate of 0.2 mV/s are shown in Figure 3. In general, E_{corr} increased and i_{pass} and E_b decreased with increasing solute concentration. For example, average i_{pass} and E_b values were 127 μA/cm^2 and -1440 mV for Mg-7%Y, 25 μA/cm^2 and -1490 mV for Mg-14%Y, and no passive region was observed for Mg-26Y. Anodic polarization plots generated at a scan rate of 0.05 mV/s in the neutral pH solution also behaved in this manner. The slower scan rate curves were generated to ensure that decreasing the scan rate did not significantly reduce the breakdown potentials. For both scan rates, the low solute concentration alloys exhibited passive regions over the largest potential ranges (approximately 580mV for the Mg-7% alloy and 330mv for the Mg14%Y alloy) while the high Y-content alloys displayed limited (160 mV for the Mg-22%Y alloy) or, in the case of the Mg-26%Y, no passivity. With the

146

exception of the Mg-26%Y alloy, corrosion initiated in a localized manner in the form of pits on the alloy surfaces.

For all of the Mg-Y alloys, an increase in E_{corr} was evident when increasing the pH to the range of 11.6 to 12. In virtually all cases, a significant increase in E_b occurred at high pH. Finally, lower i_{pass} values were observed at the higher pH. Figure 4 shows anodic polarization behavior exhibited by the Mg-Y alloys and WE43 generated at a scan rate of 0.05 mV/s in 0.1 M NaCl adjusted to pH 12 (the pH was initially adjusted to 12 with NaOH). E_{corr} values varied for the different solute concentrations, tending to increase with increasing Y content. These same trends in E_{corr} were noted for the anodic curves generated at the faster 0.2 mV/s scan rate. Passive current densities exhibited by Mg-14%Y, Mg-20%Y, Mg-22%Y, and Mg-26%Y at both scan rates were quite low (less than 2 $\mu A/cm^2$). Slightly higher values were observed for the Mg-7%Y and Mg-9%Y alloys, ranging from 1 to 10 $\mu A/cm^2$. At both scan rates, Mg-14%Y and Mg-26%Y exhibited the highest breakdown potentials, breaking down as high as 1115 mV for Mg-14%Y and 1260 mV for Mg-26%Y for the slowest scan rate data. These breakdown potentials are at least 2500 mV higher than the E_b observed for WE 43. The lowest E_b values observed at the high pH value were for the Mg-7%Y and Mg-9%Y alloys. Lower breakdown potentials and higher passive current densities measured for the lower solute composition alloys at the high pH are likely due to the smaller concentrations of Y in these alloys. Degradation of all of the sputter-deposited Mg-Y alloys, with the exception of the Mg-26%Y alloy, initiated in the form of pitting.

Breakdown potentials observed for the Mg-Y alloys at the high pH were quite varied (averaging 475 mV between duplicate tests of the same alloy under the same conditions). These differences in E_b are believed to be a result of defects incorporated into the alloy during the sputtering and handling process. Such defects include inherent defects, dust, or other particles on the Si substrate during sputtering along with scratches and marks incurred during handling (e.g. cleaving) of the alloy.[38,40] Examples of some of these defects are presented in Figures 5 and 6. Figure 5 shows a good region of the alloy on the right hand part of the micrograph with pinhole type defects which contain even larger marks within the pinholes on the left. Figure 6 is an example of some of the scratches observed on the alloy surface prior to cleaving of the alloy. (These scratches are mostly likely the result of translation of polishing scratches present on the Si substrate up through the deposit.) Breakdown has been observed to initiate at these defects, as shown in Figure 7 . In this figure, 3 pits are observed on a scratch in a Mg-9%Y alloy - similar results have been observed for sputter deposited Al as illustrated in Figure 8. Despite these variations in E_b, the lowest E_b values for the Mg-Y alloys are still significantly higher than the E_b values obtained on the most corrosion resistant commercial Mg alloys. For example, the lowest E_b measured on a Mg-14 %Y alloy was 1825 mV higher than the E_b measured for WE 43.

The significance of the improved anodic polarization behavior of the sputter-deposited alloys becomes quite evident when the alloys are coupled to other materials such as steel or graphite. By overlaying the Mg-Y anodic polarization

curve with the cathodic polarization curve for P75 graphite, it is possible to estimate coupled current densities. (Graphite was chosen because of its position at the noble end of the galvanic series in seawater and because of its use as a reinforcement material in metal matrix composites.) If the anodic curve of the Mg-Y alloy and the cathodic curve of the graphite cross in the passive regime of the Mg-Y alloy, then the reaction is anodically controlled. Under anodic control, low i_{pass} values for the anodic polarization curve determine the coupled current density. Large passive regions enable anodic control to be attained. None of the Mg-Y alloys coupled to graphite in the near-neutral pH solution were anodically controlled. However, decreased i_{galv} values were observed for all except the two high solute composition alloys when compared to that of pure Mg. These decreased coupled current densities are a result of the passivity exhibited by these alloys. All of the Mg-Y alloys tested in the high pH solution had i_{galv} values much lower than those for either pure Mg or WE43. As is seen in Figure 9, galvanic corrosion of several of the sputtered Mg-Y alloys is anodically controlled when the alloys are coupled to P75-Gr. This anodic control, results in galvanic corrosion rates 2 to 3 orders of magnitude lower for the sputtered Mg-Y alloys when compared to WE 43. Those alloys which were not anodically controlled (Mg-9%Y and Mg-7%Y) were in the limiting current region of the oxygen reduction reaction of the P75-Gr cathodic curve. While the coupling of Mg and Mg alloys to graphite in an electrolyte may appear to be an unlikely situation because of their divergent positions in the emf and galvanic series, this coupling does serve to illustrate the dramatic enhancements in passivity and galvanic compatibility that are achievable with the nonequilibrium addition of Y to Mg.

Long-term galvanic tests were also conducted by coupling the Mg-Y alloys to P75 graphite in 0.1 M NaCl solution at near-neutral and high pH values. In these intial tests, cathode to anode area ratios of 2.3 : 1 to 0.93 : 1 were used and the solutions were not buffered. In the near-neutral pH solution, corrosion of the Mg-Y alloys occurred immediately upon immersion of the coupled materials in the electrolyte. Couples in the high pH solution lasted from one to eight hours. The relatively rapid degradation of the Mg-Y alloys in the high pH solution was attributed to the aggressiveness of the test. In addition to a drop in pH of the solution with time, a relatively large cathodic area was used which may have contributed to the rapid degradation. Several additional tests were conducted on the Mg-14%Y and Mg-26%Y alloys in 0.1 M Cl⁻ solution buffered to pH 12 with a very small graphite area of 0.02 cm² (simulating a coated graphite fiber with a small region of the graphite exposed). Several of these tests exhibited promising results having currents of less than 1 μA (current densities of 0.8 - 1.2 μA/cm²). WE43 coupled to graphite under similar conditions pitted immediately upon immersion of the coupled materials in the electrolyte -- exhibiting an initial galvanic current density of 42 μA/cm² which rose to 1400 μA/cm² after 1 hour. Figures 10 and 11 show results for long-term galvanic tests conducted in 0.1 M Cl⁻ (buffered to a pH of 12) on Mg-14%Y and Mg-26%Y, respectively. The Mg-14%Y alloy (Figure 10) represents the best data obtained thus far, lasting for 136.5 hrs coupled to graphite. Figure 11 depicts results from two galvanic tests conducted on the Mg-26%Y alloy. These

tests resulted in the alloy lasting for 12 and 23.4 hrs before breakdown occurred.

Long-term potentiostatic tests were conducted on twelve Mg-14%Y specimens. Four of the specimens began corroding immediately upon immersion in the 0.1 M NaCl. These specimens were believed to have some form of major defect within the alloy that caused exposure of the underlying semiconducting Si substrate to the electrolyte. Four of the remaining 8 specimens began corroding immediately upon application of the potential. In these cases, the substrate was probably not exposed initially -- instead it became exposed as a result of corrosion of thin, weak, or porous regions of the deposit. The remaining four potentiostatic tests resulted in low current densities (< 1 $\mu A/cm^2$) being obtained. For three of the cases, -1100, -900, and -700 mV, the alloys lasted 3 to 5 days at the applied potentials before localized breakdown occurred. For the other case, a potential of -248 mV was applied for approximately 20.5 hrs. The potential was then increased to: -98 mV for 3.4 hrs, +2 mV for 1.5 hrs, +103 mV for 1.5 hrs, +202 mV for 17.3 hrs, and finally +313 mV until breakdown. Figure 12 is a current versus time plot for this experiment. This specimen was resistant to corrosion (having current densities less than 1 $\mu A/cm^2$) until a potential of +313 mV was applied. Approximately 1.5 hrs after increasing the potential to +313 mV, the specimen broke down. It is believed that this test is indicative of the good corrosion behavior which can be obtained when there are no significant defects in the alloy or passive film.

In all tests, with the possible exception of anodic polarization of the Mg-26%Y alloy at near-neutral pH, corrosion of the sputter deposited Mg-Y alloys initiated via localized corrosion in the form of pitting. Once pitting initiated, corrosion of the thin-film alloys proceeded rapidly, consuming the entire 1 to 2 micron thick specimen within approximately one minute. This rapid consumption of the alloys indicates that some form of passive film must be present prior to breakdown, otherwise, rapid degradation of the alloy would occur immediately upon immersion in a chloride solution. Further, this rapid propagation of attack reveals that pit initiation is the rate-controlling step in the corrosion of these alloys.

XPS was conducted on one of the alloys (Mg-22%Y) before and after polarization in the high pH chloride solution and revealed that the Y in the passive film was present in several oxidation states. Deconvolution of some of this data will require further experimentation, but information concerning the total concenratations of elemental and oxidized Y and Mg were obtained and provide insight into the protection mechanism. A plot showing elemental, oxide, and total Mg/Y ratios (representing the integrated intensities (i.e., areas) for the respective characteristic photoelectron peaks) for the alloy is shown in Figure 13. The Mg/Y (total) ratio indicated a greater amount of Mg only in the "as-received" material. Once the Mg-22%Y alloy was placed in 0.1 M NaCl solution, this ratio dropped dramatically, indicating a large increase in Y in both elemental and oxide forms. For the elemental Mg/Y ratio, a less dramatic effect was observed in going from "as-received" to pH 12 at E_{corr} and a greater change was noted in going from "as-received" to pH 8 at E_{corr}. When analyzing

the data for the elemental Mg/Y ratios at a potential 400 mV anodic to E_{corr}, no elemental Mg was found. The dramatic decreases in Mg total, oxide, and elemental could indicate several things. First, upon immersion, the Mg could have gone into solution, creating a Y-enriched layer at the surface of the alloy. Second, the oxide layer may have grown sufficiently enough so that the XPS did not detect the elemental Mg. Finally, significant Y-enrichment in the passive film could have occurred.

This research clearly reveals that dramatic enhancements in the passive behavior of Mg can be achieved in high pH solutions by nonequilibrium alloying of Mg with Y. Potentiodynamic, potentiostatic and galvanic couple experiments confirm the outstanding corrosion resistance of these alloys in comparison to pure Mg or WE 43 at high pH. Surface analysis of one of the alloys before and after polariation points to yttrium enrichment as the likely reason for passivity enhancement. At neutral pH values where the oxide on Mg is not stable, two alloys (Mg 22%Y and Mg-14%Y) showed modest improvements in passivity over the commercially available WE 43 alloy. At high pH where $Mg(OH)_2$ is stable, the Y addition to the passive film extended the region over which the passive film was stable by more than 2500 mV and improved the protective nature of the oxide film by lowering the passive current density 1 to 2 orders of magnitude. Finally, rapid propagation of pitting in these sputter-deposited alloys reveals that pit initiation is the rate controlling step in the degradation of these alloys.

SUMMARY AND CONCLUSIONS

Several Mg-Y alloys made by magnetron co-sputter deposition exhibit enhanced corrosion resistance in 0.1 M Cl⁻ solutions when compared to both pure Mg and a commercially available, corrosion resistant WE43 alloy. At near-neutral pH values, modest improvements in anodic polarization behavior are observed for the 14, 20 and 22 %Y alloys, while at high pH, significant increases in corrosion resistance for all but the lowest solute concentration alloys are seen.

The presence of defects (both inherent and resulting from the cleaving process) in sputter deposited nonequilibrium Mg alloys significantly affects corrosion performance. The influence of these defects was most noticable at high pH. Breakdown at low potentials was probably due to defects being present on the surface or within the alloy, while breakdown at very noble potentials was attributed to failure of the passive oxide film. Once pitting occurred, corrosion of the entire alloy occurred extremely fast.

XPS revealed that, once immersed in chloride solution, yttrium became enhanced both in oxide and elemental forms in the Mg-22Y alloy. The yttrium-enhanced oxide film is believed to be a major contributor to the significantly enhanced corrosion resistance observed at the the high pH values.

A complete mechanism for the corrosion of sputter-deposited Mg-Y alloys has not yet been developed, but the following components have become clear:

1) corrosion of sputter deposited nonequilibrium Mg-Y alloys occurs in a localized (pitting) mode.

2) once pitting occurs, corrosion of the alloys occurs very rapidly (pit initiation is the rate controlling step).

3) yttrium is enriched in the passive film upon immersion in a chloride solution.

151

REFERENCES

1. H.P. Hack, <u>Metals Handbook</u>, **13**, Corrosion, 9th ed., ASM, Metals Park, OH, p. 234 (1987).

2. G. L. Makar, M.S. Thesis, Johns Hopkins University (July 1988).

3. J. D. Hanawalt, C. E. Nelson, and J. A. Peloubet, *Trans. Am. Inst., mining Met. Eng.*, **147**, 273 - 99 (1942).

4. J. E. Hillis, <u>Light Metal Age</u>, pp. 25 - 29 (June 1983).

5. E. D. Gibson and D. N. Carlson, *Trans ASM*, **52**, 1084 (1960).

6. D. Mizer and J. B. Clark, *Trans TMS-AIME*, **221**, 607 (1961).

7. R. V. London, R. E. Edelman, and H. Markus, *Trans ASM*, **59**, 250 (1966).

8. D. L. Albright, <u>Advances in Magnesium Alloys and Composites,</u> Ed. by H. Paris and W. H. Hunt, Published by The Minerals, Metals, and Materials Society, pp. 57 - 75 (1988).

9. W. Unsworth and J. King, *Metallurgia*, **53**, pp. 199 - 200 (May 1986).

10. J. F. King, G. A. Fowler, and P. Lyon, <u>Light Weight Alloys for Aerospace Application II</u>, Edited by E. W. Lee and N. J. Kin, The Minerals, Metals, and Materials Society, pp. 423 - 438 (1991).

11. A. Joshi and R. E. Lewis, <u>Advances in Mg Alloys and Composites</u>, The Minerals, Metals, and Materials Society, 89 (1988).

12. S. K. Das and C. F. Chang, <u>Rapidly Solidified Crystalline Alloys</u>, The Metallurgical Society, Proceedings of a TMS-AIME Northeast Regional Meeting, 137 (1985).

13. G. L. Makar and J. Kruger, *J. Electrochem. Soc.*, **137** (2), 414 (1990).

14. S. Krishnamurthy, M. Khobaib, E. Robertson, and F. H. Froes, *Mater.Sci. E.*, **99**, 507 (1988).

15. G. L. Makar, J. Kruger, and A. Joshi, <u>Advances in Magnesium Alloys and Composites,</u> Ed. by H. Paris and W. H. Hunt, 105 (1988).

16. S. K. Das, C. F. Chang, and D. Raybould, International Magnesium Association Proceedings, 43rd World Magnesium Conference, June 15 - 18, 1 (1986).

17.   K. J. Clark, International Magnesium Association Proceedings, 43rd World Magnesium Conference June 15 - 18, 26 (1986).

18.   S. Krishnamurthy, E. Robertson, and F. H. Froes, Advances in Magnesium Alloys and Composites, Ed. by H. Paris and W. H. Hunt, 77 (1988).

19.   F. Hehmann, F. Sommer, H. Jones, and R. G. J. Edyvean, *J. of Mat. Sci.*, **24**, 2369 (1989).

20.   F. Hehmann, and H. Jones, Magnesium Technology, Proceedings of London Conference, 83, November (1986).

21.   G. L. Makar, J. Kruger, and K. Sieradzki, *J. Electrochem. Soc.*, **139** (1), 47 (1992).

22.   D. S. Ahmed, R. G. J. Edyvean, C. M. Sellars, and H. Jones, *Materials Science and Technology*, **6**, 469, May (1990).

23.   C. F. Chang, S. K. Das, D. Raybould, R. L. Bye, and E. V. Limoncelli, Light Metal Age, 23 (1989).

24.   R. G. Wendt, M. S. Thesis, Colorado School of Mines (1992).

25   W. C. Moshier, G. D. Davis, J. S. Ahearn, and H. F. Hough, *J. Electrochem. Soc.*, **133**, 1063 (1986).

26.   W. C. Moshier, G. D. Davis, J. S. Ahearn, and H. F. Hough, *J. Electrochem. Soc.*, **134**, 2677 (1987).

27.   W. C. Moshier, G. D. Davis, and G. O. Cote, *J. Electrochem. Soc.*, **136**, 356 (1989).

28.   G. D. Davis, W. C.Moshier, T. L. Fritz, and G. O. Cote, *J. Electrochem. Soc.*, **137**, 422 (1990).

29.   B. A. Shaw, T. L. Fritz, G. D. Davis, and W. C. Moshier, *J. Electrochem. Soc.*, **137**, 1317 (1990).

30.   G. D. Davis, W. C. Moshier, G. G. Long, and D. R. Black, *J. Electrochem, Soc.*, **138**, 3194 (1991).

31.   B. A. Shaw, G. D. Davis, T. L. Fritz, B. J. Rees, and W. C. Moshier, *J. Electrochem. Soc.*, **138**, 3288 (1991).

32.   B. A. Shaw, G. D. Davis, T. L. Fritz, B. J. Rees, and W. C. Moshier, in *Critical Factors in Localized Corrosion*, G. S. Frankel and R. C. Newman, Editors, PV 92 - 9, p. 323, The Electrochemical Society Softbound Proceedings Series, Pennington, NJ (1992).

33.   G. S. Frankel, M. A. Russak, C. V. Jahnes, M. Mirzamaani, and V. A. Brusic, *J. Electrochem. Soc.*, **136**, 1243 (1989).

34.   H. Yoshioka, H. Habazake, A. Kawashima, K. Asami, and K. Hashimoto, *Corrosion Science*, **32**, 313 (1991).

35.   H. Yoshioka, A. Kawashima, K. Asami, and K. Hashimoto, in *Corrosion Electrochemistry, and Catalysis of Metallic Glasses*, R. B. Diegle and K. Hashimoto, Editors, PV 88-1, p. 242, The Electrochemical Society Softbound Proceedings Series, Pennington, NJ (1988).

36.   Z. Szklarska-Smialowska, in *Critical Factors in Localized Corrosion*, G. S. Frankel and R. C. Newman, Editors, PV 92 - 9, p. 311, The Electrochemical Society Softbound Proceedings Series, Pennington, NJ (1992).

37.   T. R. Schrecengost, B. A. Shaw, R. G. Wendt, and W. C. Moshier, *Corrosion.*, **49** (10), 842 (1993).

38.   T.R. Schrecengost, M.S. Thesis, The Pennsylvania State University (1992).

39.   P.L. Miller, B.A. Shaw, R.G. Wendt, and W.C. Moshier, *Corrosion*, **49** (12), 947 (1993).

40.   D. A. Jones, Principles and Prevention of Corrosion, Macmillan Publishing Co., New York, 167 (1992).

41.   B.D. Cullity, <u>Elements of X-ray Diffraction</u>, 2nd Edition, Addison-Wesley Publishing Co., Philippines, pp. 87, 501, 507, 509 (1978).

42.   M. Pourbaix, Atlas of Electrochemical Equilibria in Aqueous Solutions, NACE, pp. 10, 141 (1974).
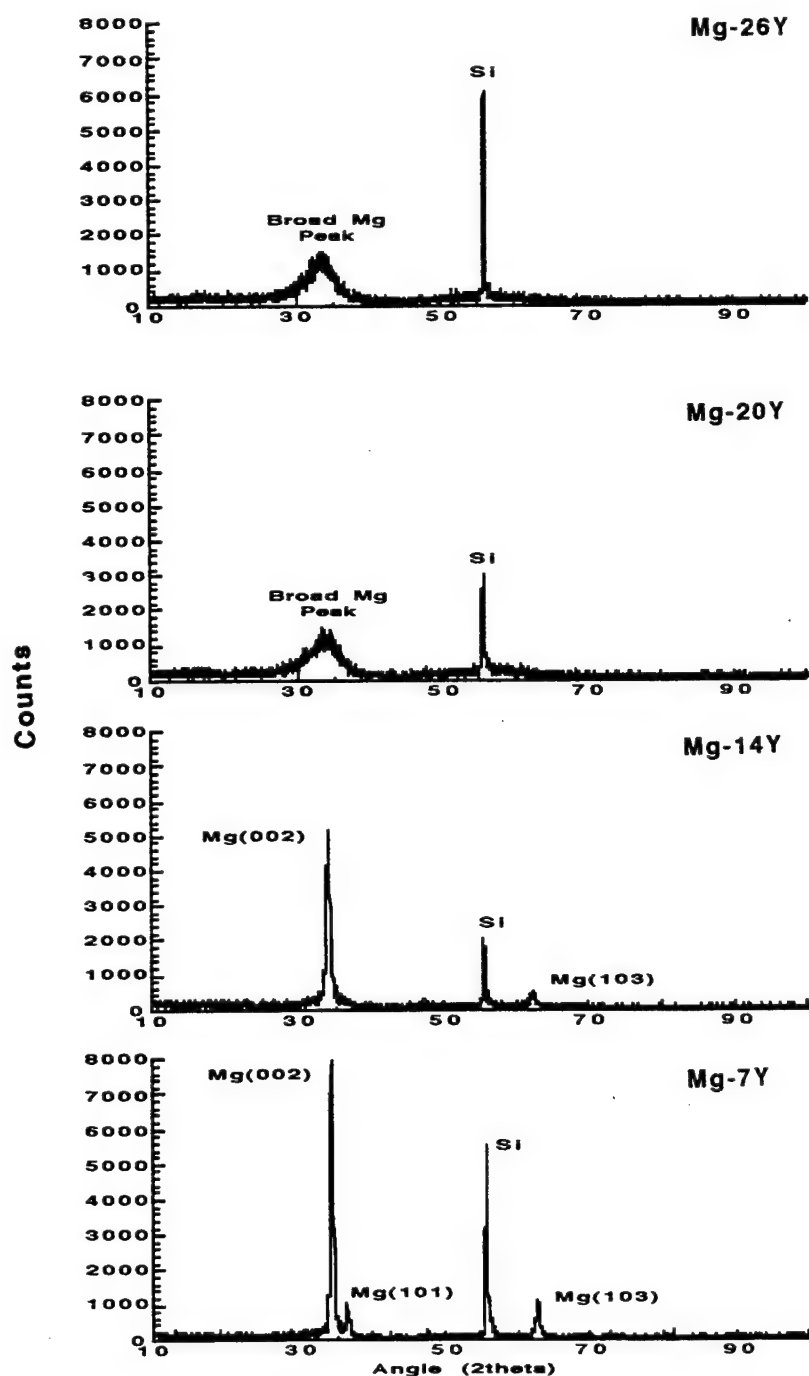
Figure 1. XRD patterns for four of the Mg-Y alloys. Solute
concentration decreases moving down the Figure.
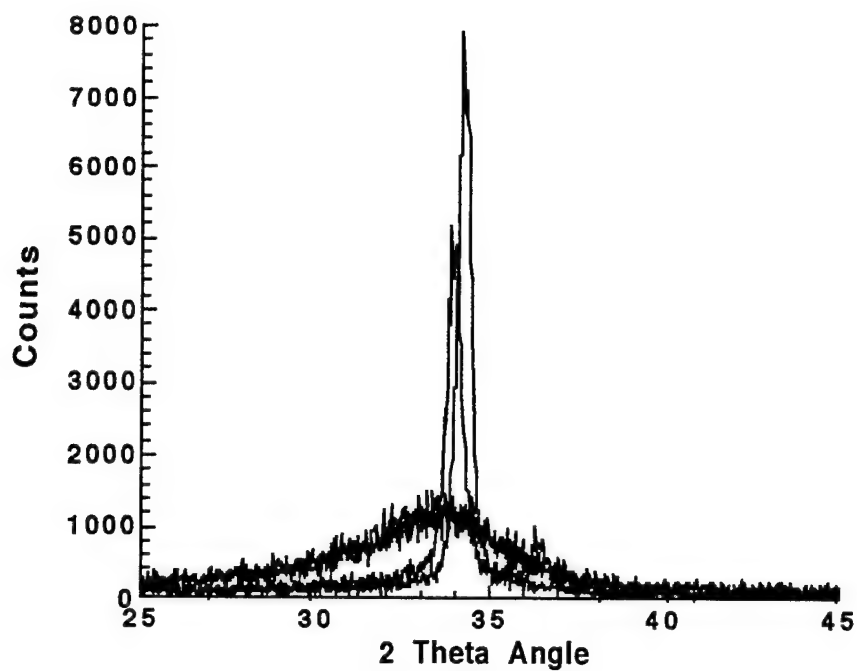
Figure 2. Close-up of the (002) Mg peaks.

Table 1. Predicted and Measured Peak Shifts for the Crystalline Mg-Y Alloys.

Alloy At. %	a, calculated (Å)	c, calculated (Å)	d, predicted (Å)	2θ, predicted (degrees)	2θ, measured (degrees)
Mg-7Y	1.622	5.298	2.649	33.8	34.1
Mg-14Y	1.637	5.345	2.673	33.5	33.9
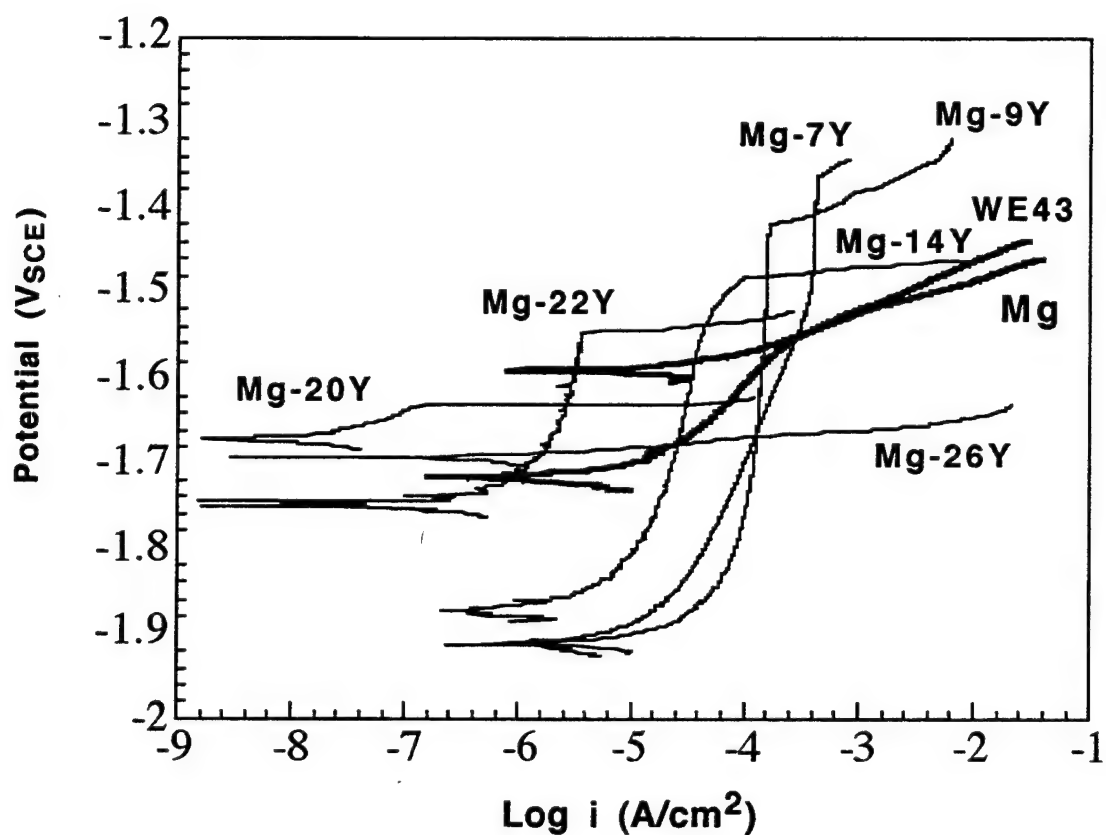
Figure 3. Anodic potentiodynamic polarization behavior of the Mg-Y alloys compared to WE43 and pure Mg. Tests were conducted in 0.1 M NaCl (initially adjusted to a pH of 8) at a scan rate of 0.2 mV/s.
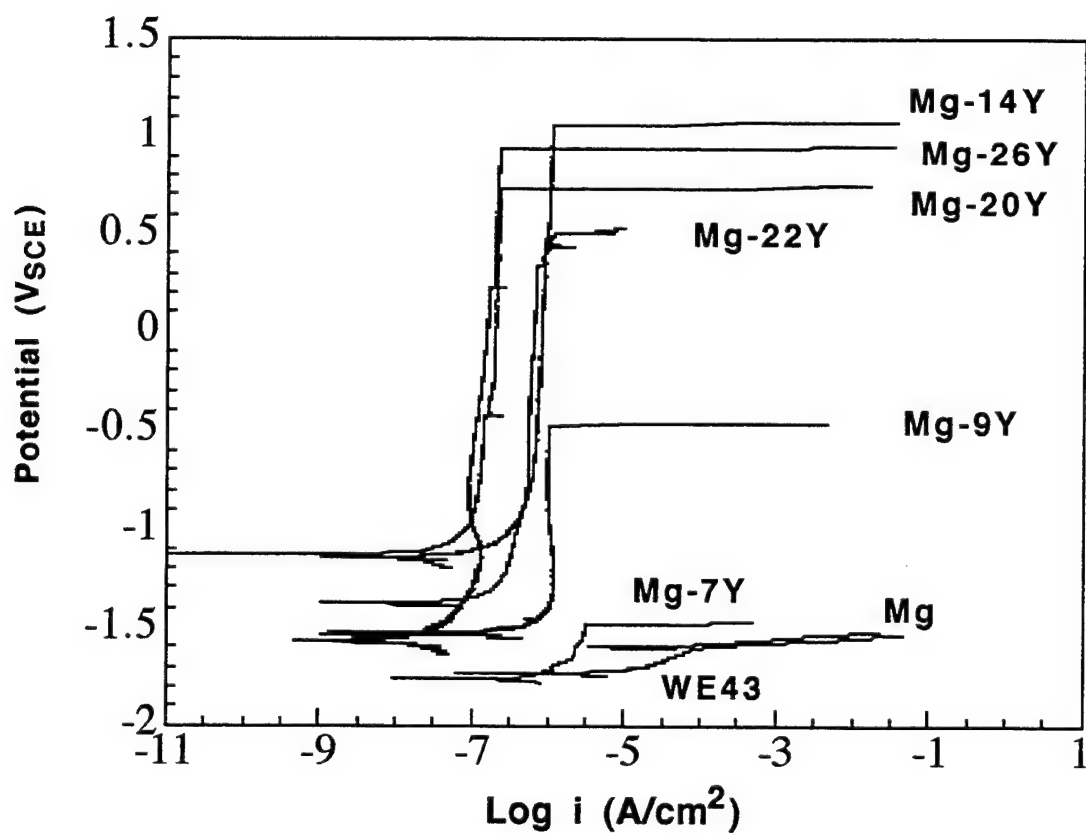
Figure 4. Anodic potentiodynamic polarization behavior for the Mg-Y alloys compared to WE43 and pure Mg generated in 0.1 M NaCl (initially adjusted to a pH of 12) at a scan rate of 0.05 mV/s.
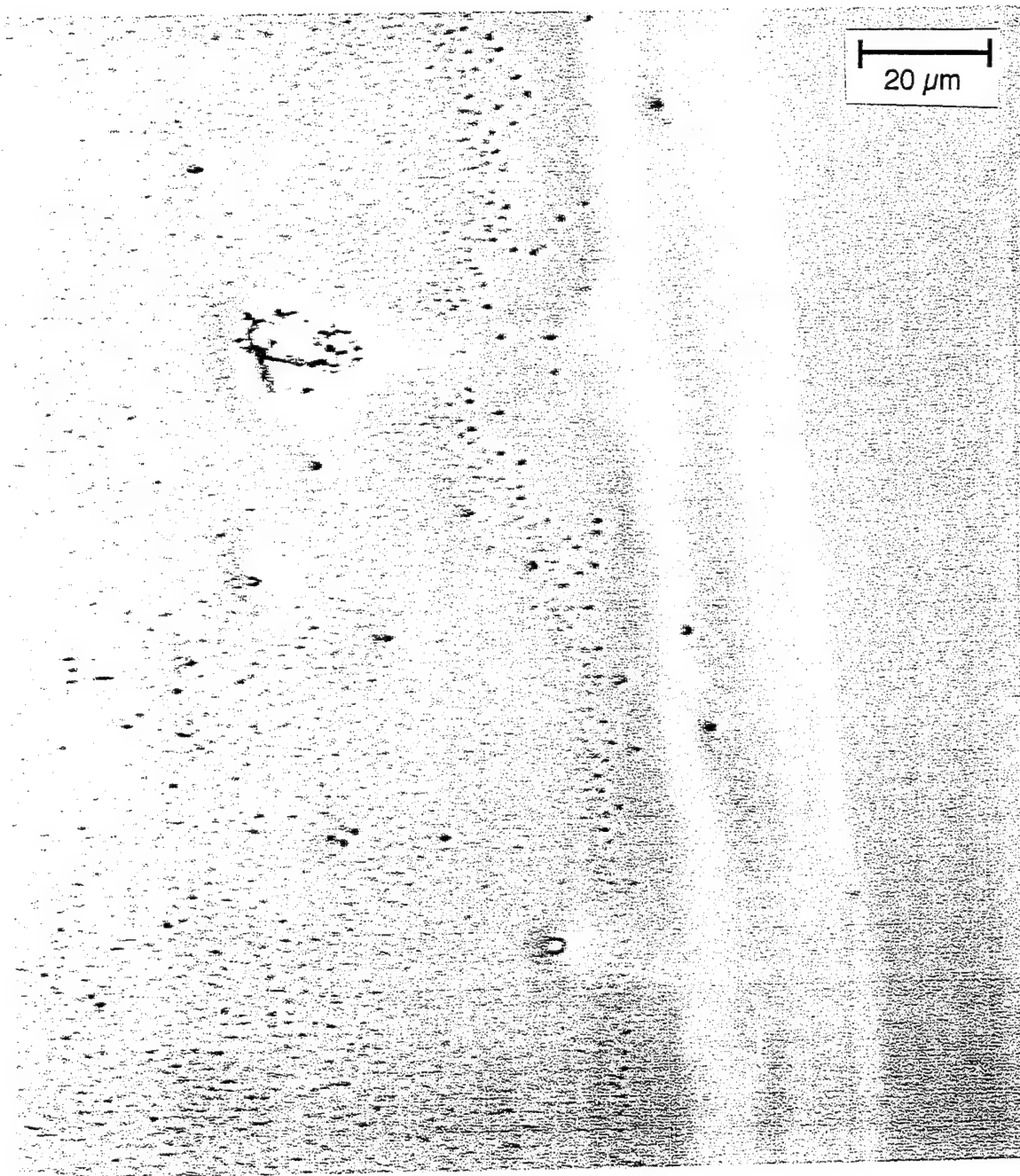
Figure 5. SLM micrograph showing defects on the surface of an uncleaved, untested Mg-Y alloy.
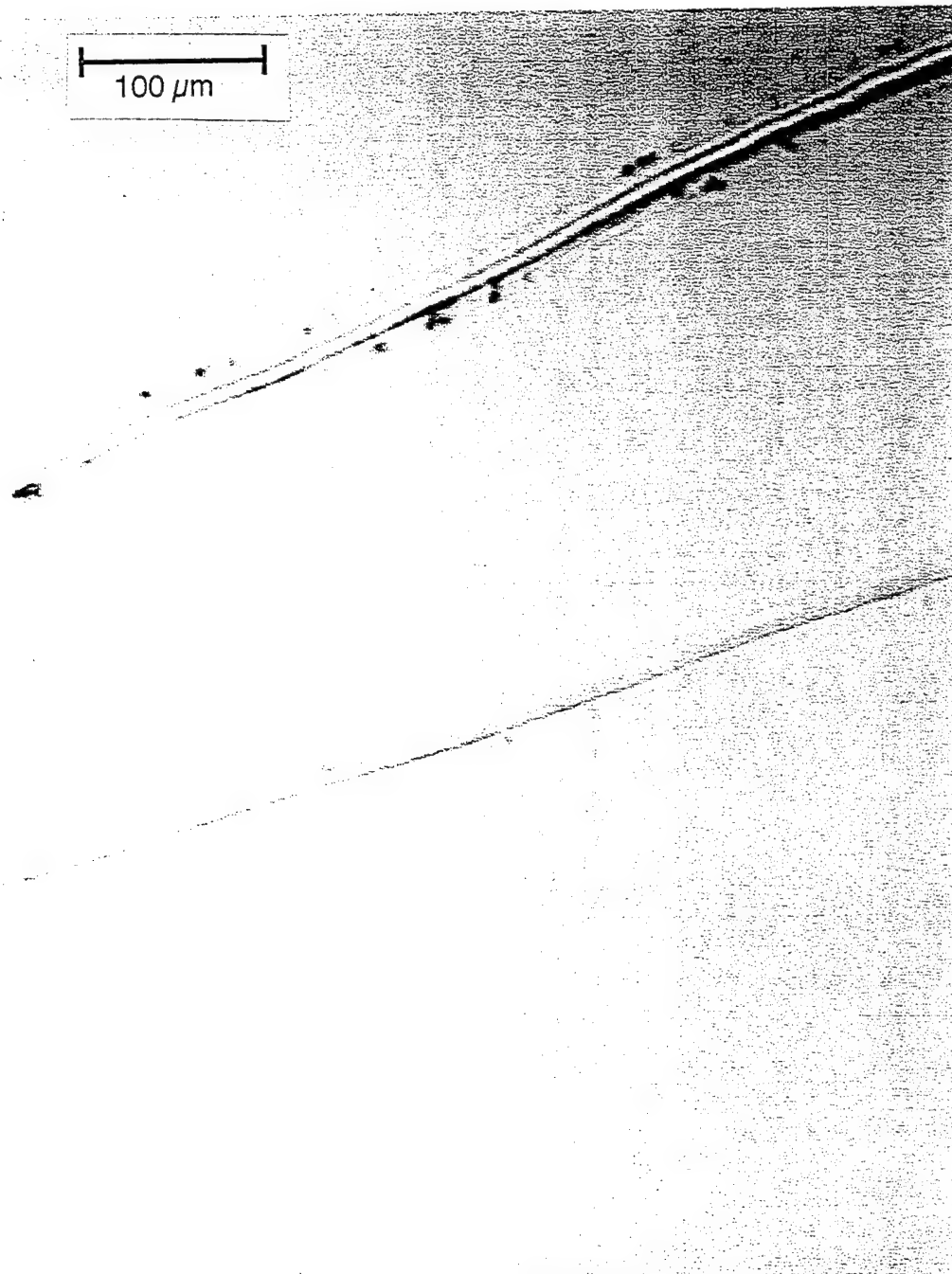
Figure 6.   SLM micrograph showing two scratches on the surface of an uncleaved, untested Mg-Y alloy.
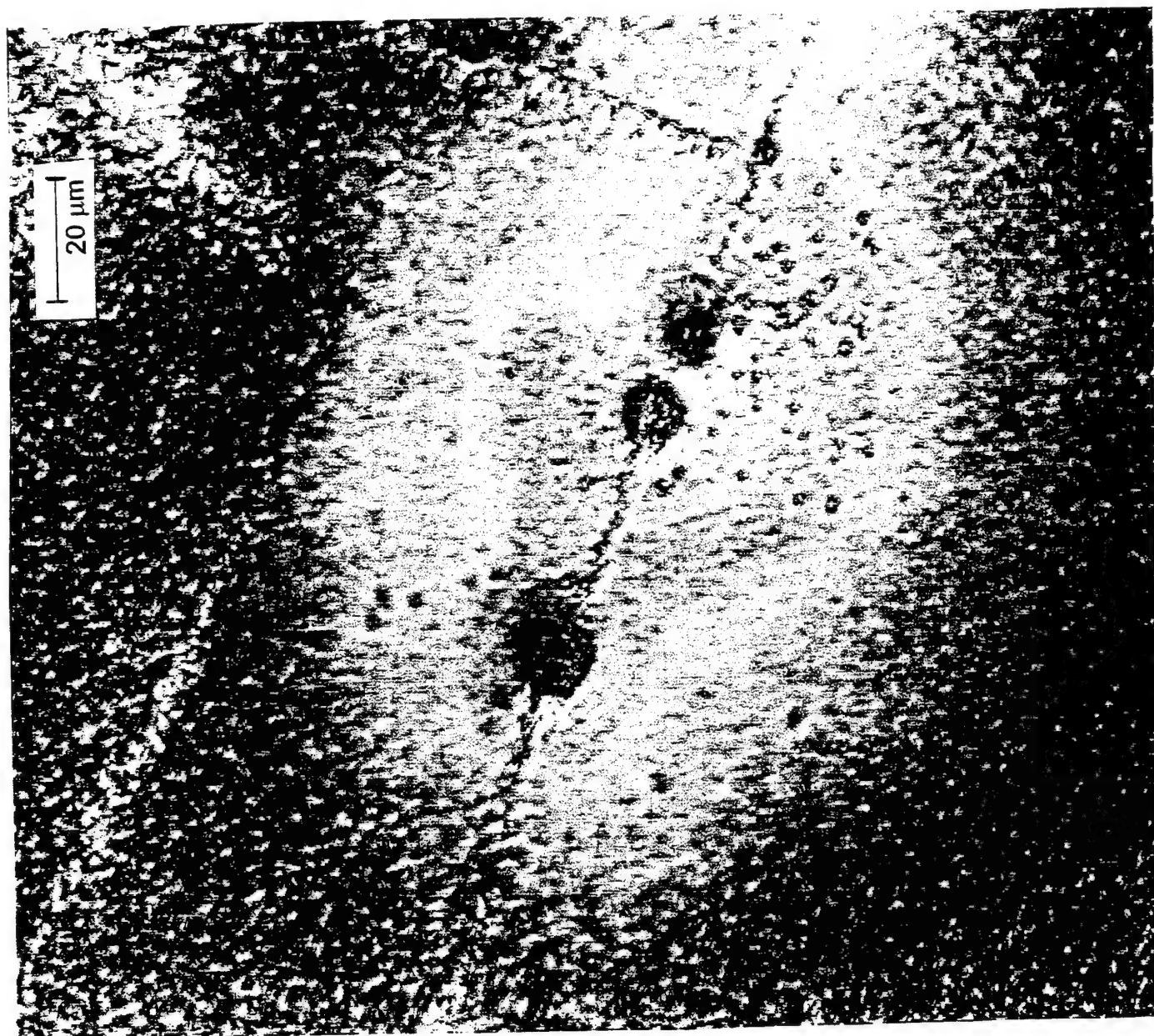
Figure 7. Scanning laser micrograph showing inherent defects along a scratch in a thin film alloy before polarization.
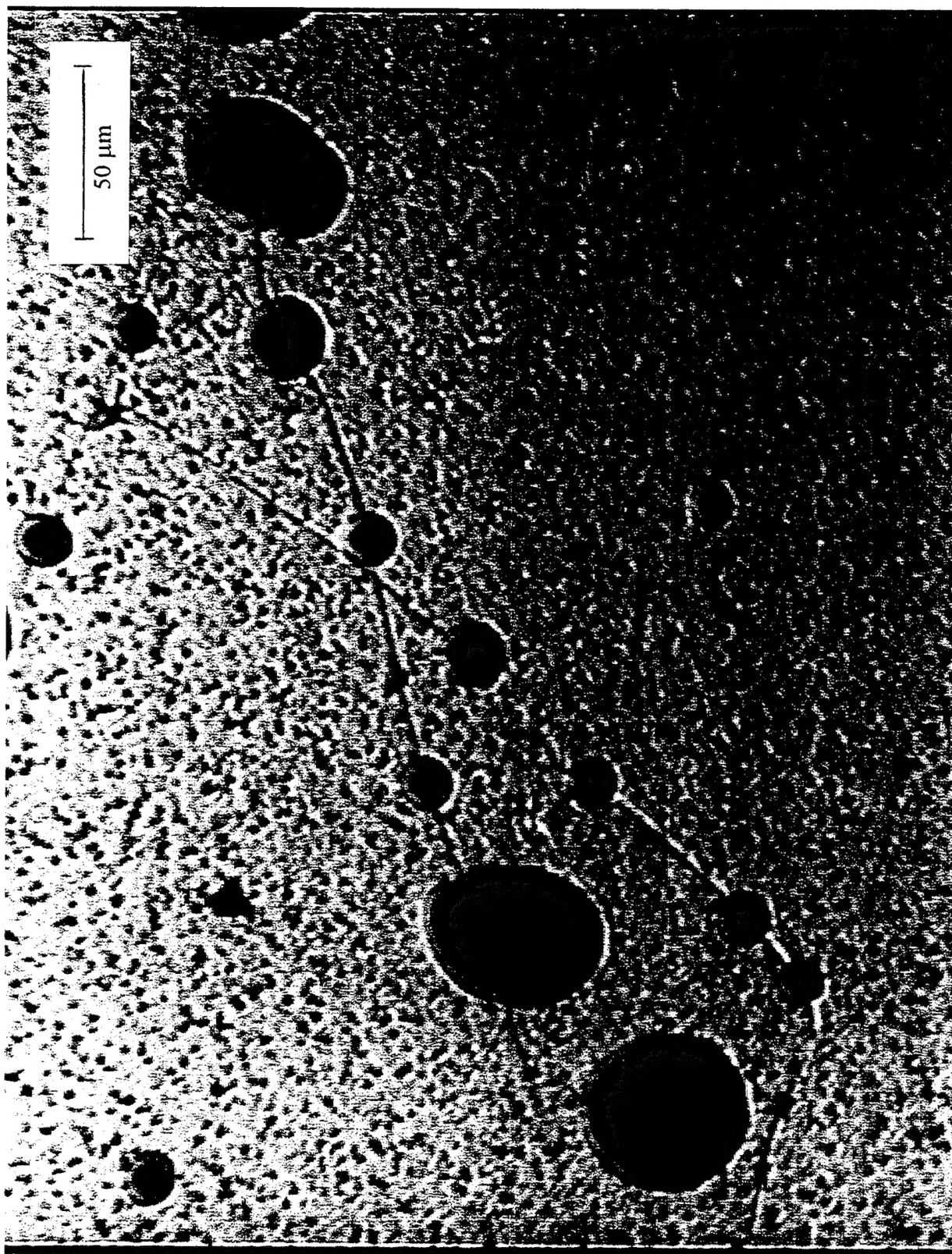
Figure 8. In-situ scanning laser micrograph showing the formation of pits along scratches in a thin film alloy during polarization in 0.1 M NaCl.
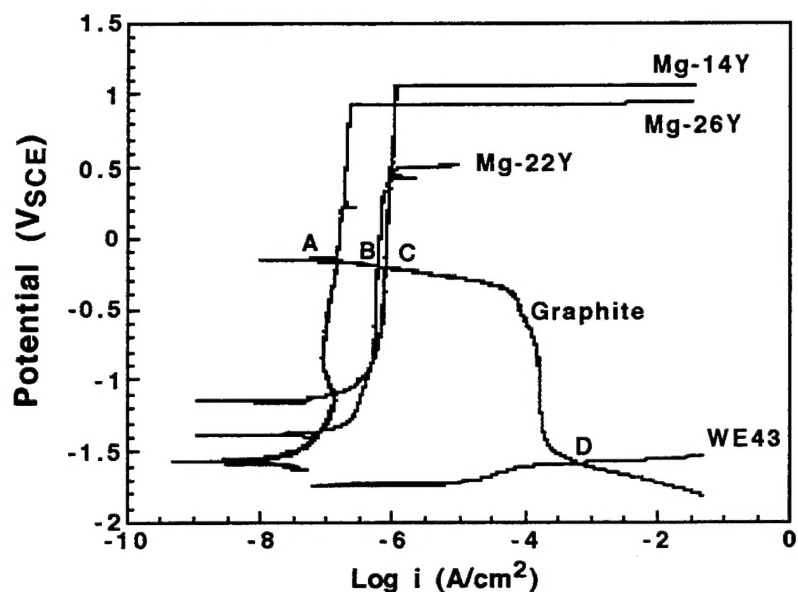
Figure 9. Galvanic diagrams for Mg-13.7Y, Mg-22Y, Mg-25.4 Y, and WE43 individually coupled to P75-Gr assuming equal areas for anode and cathode. Curves were generated in 0.1 M NaCl (pH = 12) at a scan rate of 0.05 mV/s. Points A through D are the estimated i_{galv} values for each galvanic couple. These values are approximately 630 $\mu A/cm^2$ for WE43, 0.8 $\mu A/cm^2$ for Mg-22Y, 0.6 $\mu A/cm^2$ for Mg-26Y, and 0.1 $\mu A/cm^2$ for Mg-14Y.
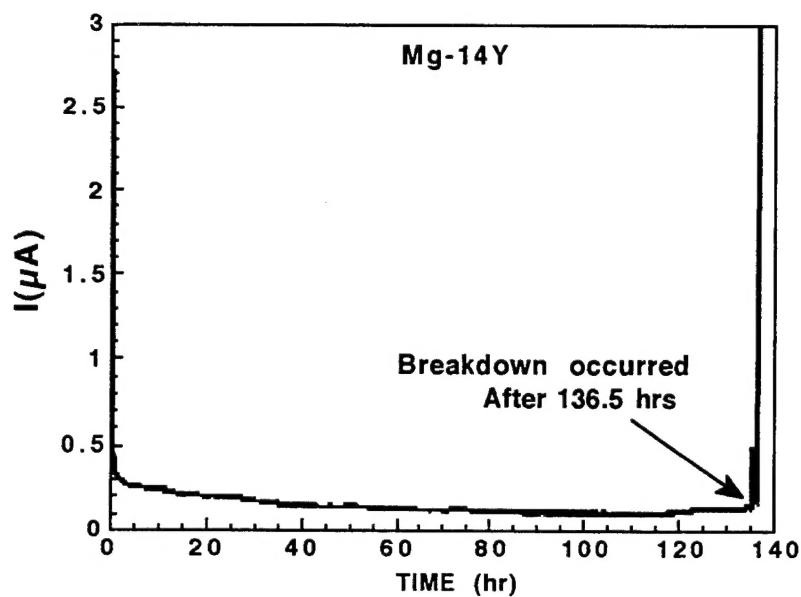
Figure 10. Current versus time plot for Mg-14Y in 0.1 M Cl- buffered to pH 12. Breakdown of the alloy occurred at 136.5 (c:a ratio = 0.067) hours into the test.
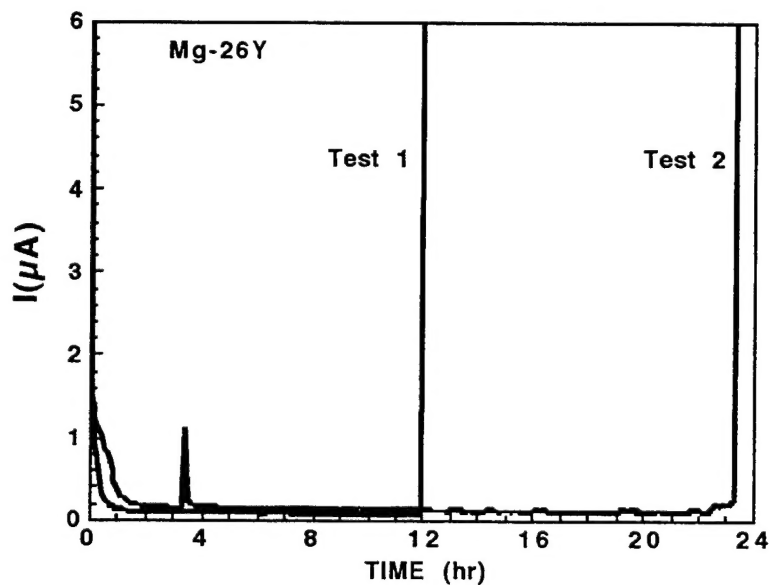

Figure 11. Current versus time plot for two Mg-26Y alloys tested in 0.1 M Cl- buffered to pH 12. Breakdown of the alloys occurred at 12 (c:a ratio = 0.025) and 23.4 (c:a ratio = 0.015) hours into the test.
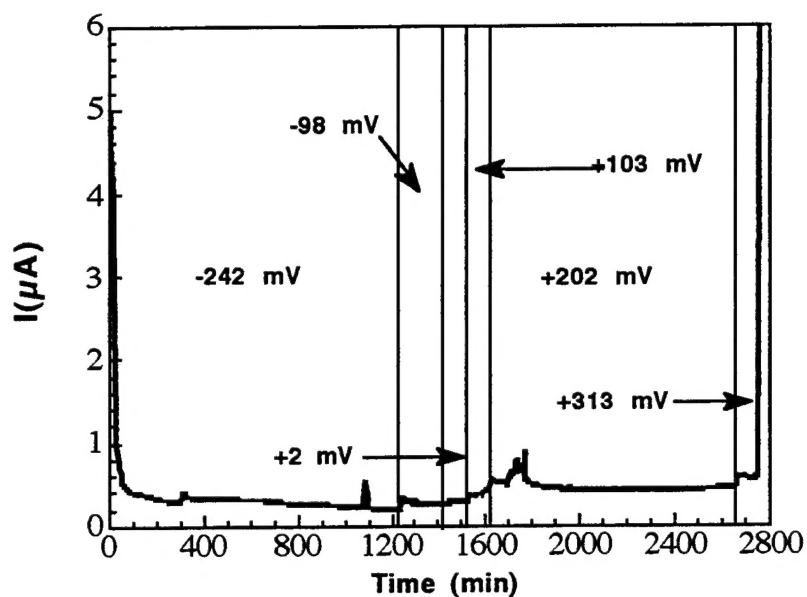
Figure 12. Potentiostatic testing results for Mg-14Y showing when potential increases were incurred.
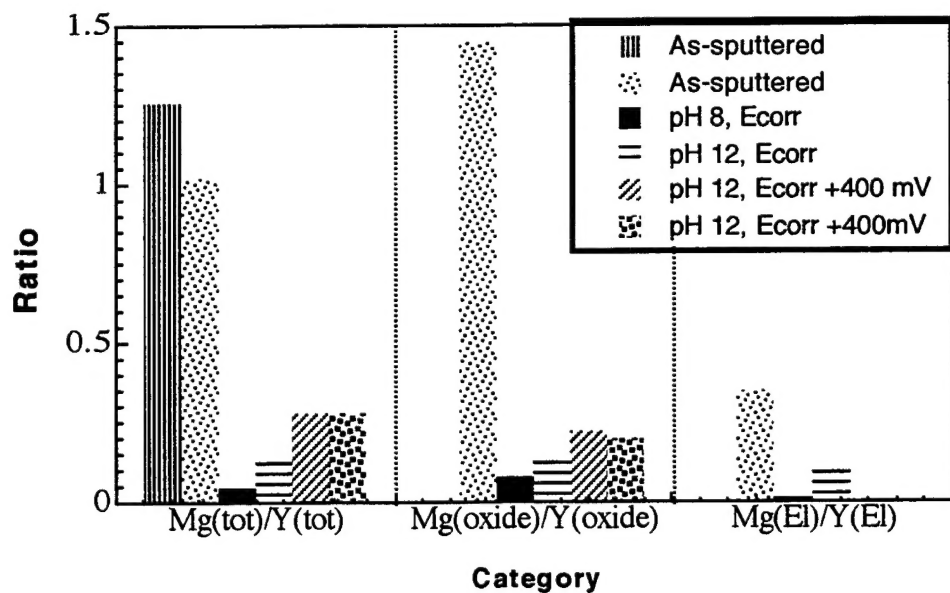

Figure 13. Plot of Mg/Y elemental, oxide, and total ratios obtained from XPS analysis. A decrease in height of a bar indicates an increase in yttrium content.